UNIVERSITÀ DEGLI STUDI ROMA TRE
Department of Mathematics and Physics

Doctoral School in Mathematics and Physics

XXVIII Cycle

Ph.D. Thesis in Physics

A polarimeter to observe exoplanets

by

Dedalo Marchetti

Supervisor Dr. Paolo Branchini _____

Co-supervisor Dr. Enrico Bernieri _____

Coordinator of PhD course Prof. Roberto Raimondi _____

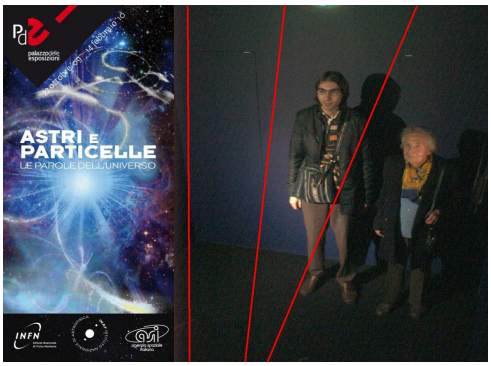

Dedicated to my grandmother Marcella Minieri Marchetti

A polarimeter to observe exoplanets

Dedalo Marchetti
Mathematics and Physics Department, RomaTre University of Rome, Italy

Contents

Preamble

In 1609, Galileo Galilei pointed for the first time a small telescope to the sky.
Few years before Giordano Bruno, an Italian Dominic friar philosopher was burned as heretic. One of his affirmations was that there are other universes (at that time the universe was only the Solar System with about 6000 fixed stars).
When Galileo pointed his telescope to Jupiter for the first time in the history, he discovered four moons (Io, Europa, Ganymede and Callisto). Iterating the observations of these moons, he understood that they orbit around Jupiter. Today this is not surprising, but at that time it was the first observation unequivocal of a system of some celestial bodies that don't orbit around the Earth. Galileo, who was a Catholic, reconsidered the affirmation of Giordano Bruno, as he had just found an independent system. Galileo promoted heliocentrism for the Solar System from this discovery (and others like Venus's phases) with experimental proofs of this theory.
Galileo wrote in a letter (dated 21st December 1613) to the abbot of the Benedectine monastery of Monte Cassino "Benedetto Castelli" that Bible cannot be wrong, but the interpretation of the Bible could be wrong.
Some years later (in 1633), Galileo was forced to recant his affirmations (the most important is that the Earth orbits around the Sun and not the contrary).
In 1992, the Pope, Saint Ioannes Paulus II, apologized for the Catholic Church error against Galileo (speech of Pope Saint Ioannes Paulus II Saturday 31st of October 1992). In particular, the Pope appointed a commission of theologians, scientists and philosophers who founded some errors on the analysis performed in 1633. The most important statement is to interpret the Bible not as a scientific text but as a religious one, so the descriptions in the Sacred Text are not "physically detailed" descriptions of the world. The scientific knowledge of the physical world is performed by the scientists, the God's Revelation of the world is described in the Bible.
Respect to XVII century the scientific knowledge of the universe is very extended. Nowadays we know more than 400 planetary systems in our galaxy (The Milky Way)...
Our Galaxy is one of the billions of observed galaxies in the today known universe...
Probably also the affirmations of Giordano Bruno must be revisited...

Introduction

The work of this thesis is based on the study and the measurement of the polarization of exoplanets.
Exoplanets are planets revolving around stars other than the Sun.
The first exoplanet was discovered in 1995 [5].
At the time of writing of this work (15 April 2016) 2107 exoplanets have been discovered[2].
The characteristics of these exoplanets are various and, in some cases, very different from the planets of the solar system.
There are different methods to discover exoplanets. The main methods are called "radial velocity method"and "transit method". The first is based on measuring the radial velocity of the star to detect the variations induced on the same planet during its period of revolution of the star. The "radial velocity method"is able to measure the oscillation of the star around the center of gravity of the star-planet system. The "transit method"measures the decrease in the brightness of light (by the light curves) due to the planet's transit in front of the star (if the orbital characteristics allow transit).
The new scientific challenge does not only consist in discovering new exoplanets, but it consist also in characterizing those already discovered. To characterize an exoplanet means to derive primarily physical parameters such as density and surface gravitational acceleration, but also to characterize the composition of its atmosphere (if it is present), and the features of the solid surface (if it is present).
Currently, some characteristics of planetary atmospheres are known by spectroscopic techniques (for example by comparing the two transits, in front and behind the star).

Theoretical studies [43] highlight polarimetry has been recognized as a powerful technique for enhancing the contrast between a star and an exoplanet, hence to directly detect it. Moreover, polarimetry can also be used for characterizing exoplanets, because the planet's degree of polarization as a function of wavelength and/or planetary phase angle is sensitive to the structure and to the composition of the planetary atmosphere and to the surface type . The polarization in the range of visible light depends strongly on the surface characteristics, weather and meteorology (clouds or clear) of the exoplanet [44].

A polarimeter is an instrument that through a spatial or temporal modulation (or both) allows to measure the polarization of the test source.
Some telescopes host polarimeters getting into the light path, as FOCAS [71], PEPSI [73], TURPOL [48]... (see tables 1, 2, 3, 4, 5 in cap. 3 for a complete list). Typically these instruments are optimized for a specific purpose (for example a particular wavelength, a high spectral resolution, high temporal resolution).

Piirola et al. (2008, 2011)[45], [46] claim to have measured the polarization of exoplanet HD189733b measured by TURPOL polarimeter, reporting a degree of polarization of about $2 \cdot 10^{-5}$, but another paper by Wiktorowiticz (2010) [49] denied the discovery, reporting a more

sensitive measurement performed by POLISH polarimeter.
Current difficulties in such kind of measurements underline the need of polarimetric instrumentation having sufficient sensitivity.

The aim of this thesis is to design a new kind of a polarimeter for characterizing exoplanets and to realize a prototype of the instrument.
The optical scheme proposed for this polarimeter has never been used before. The optical scheme is composed of a Brewster window and a wire-grid polarizing beamsplitter.
The polarimeter is projected to work in the visible light and near infrared wavelengths.

The thesis is divided in eight chapters and an appendix:

- In **Chapter 1** the most important historical exoplanet's discoveries and some methods used to detect and to characterize exoplanets have been illustrated. There is also some information about exoplanet's atmospheres.

- In **Chapter 2** some basics of polarimetry in astrophysics have been introduced. In particular some exoplanet's reflected flux simulations which are useful to evaluate exoplanet's degree of polarization and which have been useful to elaborate this thesis are reported in this part.

- In **Chapter 3** some simple calculations which have been performed in this thesis on the expected fluxes in the channels of a polarimeter are shown.
  Furthermore, the scientific requirement by a polarimeter to observe exoplanets are defined.

- In **Chapter 4** an optical scheme for a polarimeter is proposed in order to make it reach the required features. A ray tracing simulation is also presented. Moreover, some supports are illustrated in this chapter in order to perform the first optical test.

- In **Chapter 5** the experimental set up used for optical test is shown. Furthermore verification of the general behavior of the optical scheme (light patches and intensity versus polarization of the light source) is presented.

- In **Chapter 6** the project of a complete layout of a polarimeter's prototype is presented. Moreover the description of each component of the instrument are described. The characteristics of the used detector and some parameters, which have been experimentally verified, are illustrated.

- In **Chapter 7** the results of the calibration of the instrument using an artificial source of light are shown. For this purpose it has also been written a program in order to analyze

the measurements. The program performs a multi-parametric fit of three curves to find the best coefficients of transmission and reflection of the optics which best agree with obtained experimental data. The results allow confirmation of the operation of the optical scheme and the entire prototype polarimeter.

- In **Chapter 8** observations of some celestial bodies are shown. In particular the celestial bodies observed are planets in the solar system, the moon and some stars. Furthermore a review of the program developed to analyze observation is illustrated.

- In the **appendix** mechanical projects, program code, additional calculus and extra optical test are reported.

The thesis has achieved the goal to provide a working prototype of a polarimeter. The polarimeter has been calibrated successfully with a small telescope.

1 The exoplanets

The main scientific topics of this thesis are the polarization of the exoplanets. This chapter introduces some aspects of the discovery and study of planets orbiting other stars (exoplanets). In paragraph 2.1 some notes on the discovery and characterization of exoplanets are remembered. The paragraph ended with a look at future missions in development to study exoplanets. Paragraphs 2.2, 2.3 and 2.4 are dedicated to the explanation of the main methods used to detect exoplanets.
Paragraph 2.5 refers to some aspects of the characterization of the atmospheres of exoplanets (if any).
Section 2.6 concludes the chapter with some brief remarks on the state of art about the research on exoplanets.

1.1 Important dates of historical discovery of exoplanets

In 1992, Wolszczan and Frail announced the discovery of the first planet orbiting around another star [1]. The star is very particular: it is the Pulsar PSR1257+12. This star has an intrinsic variability with a period of 6.2 ms. The authors analyzed the data taken with the Arecibo radio telescope of 305 meters of diameter at a frequency of 430 MHz. They noted a modulation of the period. They excluded *"any morphological changes that might indicate the presence of a free precession of the pulsar spin axis or any magnetospheric phenomena at the level that could lead to periodic TOA Time Of Arrival variations of the measured magnitude. Consequently, the most plausible remaining alternative is that PSR1257 +12 has two low-mass companions and that their orbital motion produces the TOA variations"* [1].
Nowadays it is known that PSR1257 +12 has at least three planets [2]. This possibility was considered in the original paper of 1992, but at that time the instrumental error was too large to discriminate this evidence.

In 1995, the first exoplanet was discovered orbiting around the solar-type star 51 Peg [5]. The authors monitored the radial velocity of 142 dwarf stars with a precision of $13ms^{-1}$ along 18 months of observations. The mass of this exoplanet (51 Peg b) is estimated between 0.5 and 2 Jupiter mass. The big difference with the Solar System is that the semi-major axis is 0.05 Astronomical Unit, that is very close to its star in comparison to Mercury (0.39 AU). This discovery was immediately a scientific case of significant interest: until that the giant planets were assumed located in an outer part of the planetary system.
The spectral class of 51 Peg is G2-3 V [7].
The temperature of the planet is expected above 1300 K: a very high temperature very close to Jeans thermal evaporation temperature limit [5].

The discovery of 51 Peg b was followed soon thereafter by the detection of planets around 47 UMa b and 70 Vir b. In a quite short time the search for extrasolar planets has evolved into a mature field in astrophysics [35].

In 2000, the first detection of an an exoplanet with the "transit method"was reported [6]. This planet (HD209458b) was previously discovered by means of the radial velocity method (see next sub-chapter for method explanation). This planet is at 0.05 AU from the star and has a radius of about $1.27 \pm 0.02 R_{Jup}$.

With the data from radial velocity and transit, an exoplanet can be better characterized.

These discoveries were the beginning of an intense exoplanet detection activity. About 200 exoplanets were known in 2007 [8].
Fig. 1 reports the mass, the orbital period and the size of confirmed exoplanets binned over discovery year. Note that in the last years the number of the known exoplanets is incremented very much. The enhancement in the exoplanet detection is due mainly to the two satellites (CoRoT and Kepler) dedicated to the exoplanet's detection. CoRoT satellite, a CNES mission, was launched in december 2006. Kepler satellite was launched in march 2009 by NASA.
CoRoT (French: COnvection, ROtation et Transits planétaires) is the first space survey dedicated to the photometric search for extrasolar planets [9].
CoRoT-Exo-1b is the first planet discovered by CoRoT in its initial run of observation. The planet orbits a middly metal-poor G0V star of magnitude V = 13.6 in 1.5 days. CoRoT-Exo-1b is a giant planet orbiting at ~ 5 stellar radii from its star. Its main characteristics are a large radius and a very low value for the mean density that may be consistent with a planet's metal deficiency [9] (2008).
CoRoT results are that stars are very diverse, more complex than the Sun. Stellar models have be revised and improved. Planetary systems are also very diverse than the Solar System. The major difficulty for the detection of small planets is the stellar variability. Stars and planetary systems have to be studied together [10].
The Kepler mission was designed to determine the frequency of Earth-sized planets in and near the habitable zone (defined as the zone where the temperature is compatible for liquid water on the planet surface) of Sun-like stars [14]. The data obtained by Kepler has provided high-precision, high cadence, continuous light curves of tens of thousand of stars [16].
Kepler 10b is the first rocky planet found by Kepler. It is a planet about one and half time the size of Earth, it si very hot with year lasting less then 1 Earth day. The density of this planet is 5.8 grams per cubic centimeter (Earth: $5.5 g/cm^3$). Temperature is about 1800 Kelvin. It is probably got a molten lava ocean.
Kepler founds about 4200 planetary candidates. A lot of planets are bigger than Jupiter. Some have density less than water. [17]
Kepler team found that Earth-size planets are common. Planets are being found in habitable zone (the zone where the water could be liquid on planet's surface). They estimate approximately 1 billion Earth-size planets in the habitable zone of Solar like stars in our galaxy. [17]
The loss of two reaction wheels on the Kepler spacecraft has ended the primary mission data collection. The K2 mission is driven by the spacecraft's ability to maintain pointing in all three axes with only two reaction wheels.

A new generation of space missions for the exploration of exoplanets are in preparation (ESA:

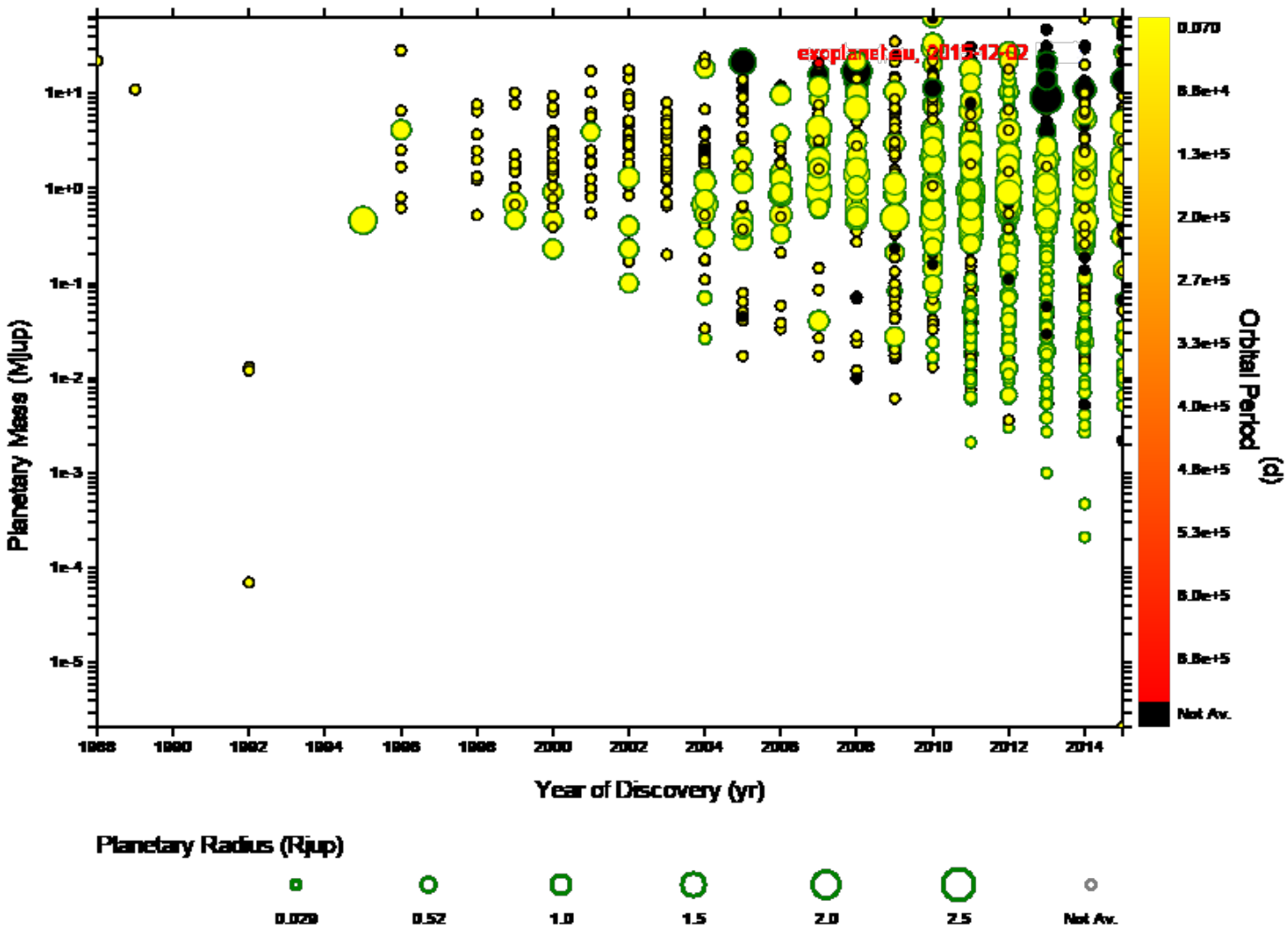

Figure 1: Graphs of discovered exoplanet as a function of the discovery year. The size of the spot on the diagram is proportional to the diameter of the planet.

CHEOPS, launch 2017 and PLATO) (NASA: James Webb Space Telescope, launch 2018 and TESS, launch 2018).

PLAnetary Transits and Oscillations of stars (PLATO) is the third medium-class mission in ESA's Cosmic Vision programme. Its objective is to find and study a large number of extrasolar planetary systems, with emphasis on the properties of terrestrial planets in the habitable zone around solar-like stars [18].

CHEOPS - CHaracterising ExOPlanet Satellite - is the first mission dedicated to searching for exoplanetary transits by performing ultra-high precision photometry on bright stars already known to host planets. The mission's main science goals are to measure the bulk density of super-Earths and Neptunes orbiting bright stars and provide suitable targets for future in-depth characterisation studies of exoplanets in these mass and size ranges [19].

James Webb Space Telescope (JWST) is a multi-purpose instrument that also will tell us more about the atmospheres of extrasolar planets, and perhaps even find the building blocks of life elsewhere in the universe.

JWST will study exoplanets during the transit. When a planet passes in front of a star, the starlight passes through the planet's atmosphere. During the transit some of the stellar rays are passing through the planet's atmosphere before arriving at the telescopes; those few stellar rays would now carry a faint imprint of the planetary gases they encountered in the planet's atmosphere. The capabilities of JWST's instruments will enable photometric and spectroscopic detection of both primary and secondary eclipses, measuring both atmospheric absorption and thermal emission from a wide variety of planets. The spectrum of the star, added to that of the planet, will have the "absorption line" of the planetary atmospheric elements. JWST will use a $R \sim 700$ grism to characterize the atmospheres, possibly even detecting the signature of liquid water on rocky planets.

JWST will also carry coronagraphs to enable direct imaging of exoplanets near bright stars [20].

The Transiting Exoplanet Survey Satellite (TESS) plan to discover thousands of exoplanets in orbit around the brightest stars in all-sky. This first-ever spaceborne all-sky transit survey will identify planets ranging from Earthsized to gas giants, around a wide range of stellar types and orbital distances. TESS will provide prime targets for detailed observation with the JWST, as well as with other large ground-based and space-based telescopes of the future [21].

1.2 The method of radial velocity to detect exoplanets

The radial velocity detection method is based on a dynamic effect. Supposing to have a two bodies system, composed of a star and a planet. The star "rotates"around the center of mass of the system. Theoretically It is possible to find exoplanets looking for the star moving in the sky, but most og the stars are so far away that the instrumentation often wouldn't be able to see their motion in this way. The projection of the star motion along the line of sight is an harmonic oscillation and produces a modulate radial velocity of the star. The term "radial" is referred to the observer - star line of sight. When the star moves toward the observer the light is blueshifted, else when the star moves away the observer is redshifted.
Often, the barycenter of the planetary system is located inside the star on the contrary example of what happens to the binary stars of similar mass.
The effect is larger for big mass planets closer to the star. The effect is modulated by orbital planet inclination, as the radial velocity is only in the line of sight. The velocity is very small, for example, the Sun moves at a max velocity of ~ 12.6m/s due to Jupiter [11].
In fig. 2 the historical graph of the radial velocity of 51 peg is reported. It was obtained by Mayor and Queloz. It has permitted to discover the first hot Jupiter around solar-type star.

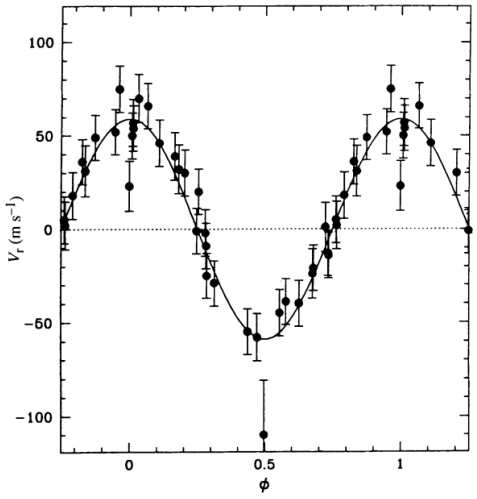

FIG. 4 Orbital motion of 51 Peg corrected from the long-term variation of the γ-velocity. The solid line represents the orbital motion computed from the parameters of Table 1.

Figure 2: Historical graph of the measure of the radial velocity of 51 Peg. It is evident the modulation of the radial velocity attributed to 51 peg b. Extracted from Nature paper [5].

The maximum shift in wavelength can be computed by the Doppler (non relativistic) equation:

$$\Delta\lambda = \frac{v}{c} \cdot \lambda \tag{1}$$

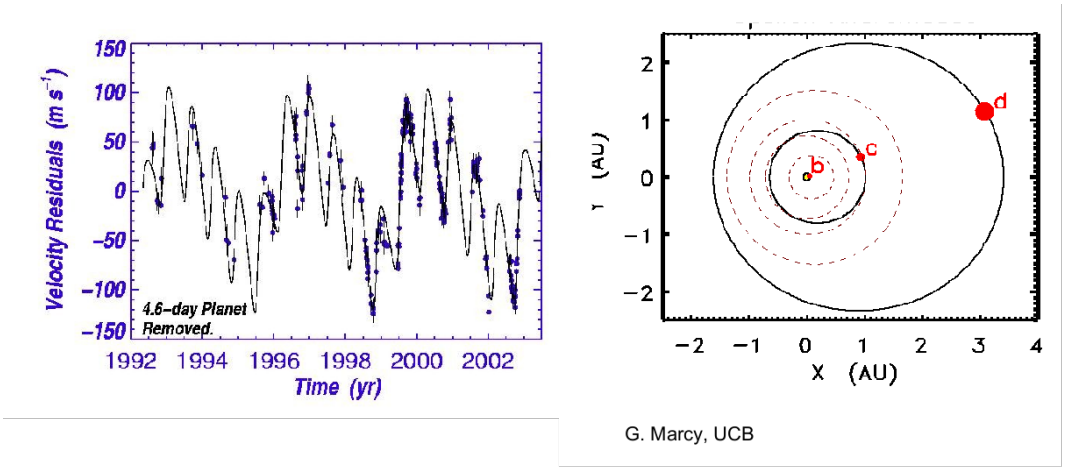

Figure 3: Radial velocity of Upsilon Andromedae. Measured data (left), computed hypothesis of 3 planets system (right). From [11].

In the case of the Hydrogen α Balmer line ($\lambda_0 = 6563\text{Å}$) on the Sun the shift due to Jupiter is:

$$\Delta\lambda = \frac{v}{c} \cdot \lambda = \frac{12.6\text{m/s}}{3 \cdot 10^8\text{m/s}} \cdot 6563\text{Å} = 2.8 \cdot 10^{-4}\text{Å} \tag{2}$$

this is a very favorable situation as in the case of earth-like situations is up to $v_r = 9.0\text{cm/s}$ and this requires a very large resolving power and spectroscopes very sophisticated.

The inclination of orbital plane changes the effect of measured velocity as the instruments are sensible only at the component of velocity vector project in the line of sight.

$$\Delta v = v \cdot \sin(i) \tag{3}$$

Where "i" is the angle between the "line of sight" and the direction of the orbital momentum. If the orbital plane is orthogonal to the "line of sight" the radial velocity is null. If the orbital plane is inclined at 45° the radial velocity is attenuated by a factor $\sqrt{2}$. If the "line of sight" is in the orbital plane the radial velocity is the real tangential velocity of the orbit (obviously the maximum and minimum in the radial velocity curve that is similar to a sinusoidal shape).
In the case of multiple planetary systems, the effect of the planets are added together with the star, and it is possible to have a graph like that reported in fig. 3. In these cases, a numerical simulation must be performed to analyze data. The variables of the numerical simulation are the number of planets, the orbital period, the inclination orbit plane angle and the eccentricity of the orbit.

A modern instrument developed to measure the radial velocity is HARPS (High Accuracy Radial Velocity Planet Searcher) commissioned in two telescopes: HARPS-North at "Telescopio Nazionale Galileo"(Islas Canarias) and HARPS-South at ESO La Silla (Chile) [12]. HARPS is a fibre-fed, cross-dispersed echelle spectrograph. The main characteristcs of HARPS is its extraordinary stability. HARPS is calibrated by a simultaneous ThAr reference lamp (fed by

2 fibers). The ThAr-reference technique is able to measure and correct the tiniest instrumental drifts. To make the spectrograph intrinsically stable it operates in vacuum, since ambient pressure variations would have produced huge drifts (typically 100 m/s per mbar). Two-stages air-conditioning around the vacuum vessel controls the air temperature to 17°C with long-term stability of the order of 0.01°C. The extraordinary stability translate directly into the stability of the radial velocity measurements [12]. To confirm the discovery of the detection of a radial velocity signal due to an exoplanet particular attention should be devoted to the study of the star as some stars pulsating like this effect, and it can be confused with planet'the same s radial velocity effect.

1.3 The transit method to detect exoplanets

The transit of an exoplanet in front of its star is another method used to detect exoplanets and to calculate some physical properties.
When a planet transits over a distant star, the amount of light coming from the star decreases. The larger the planet, the dimmer the star appears during the transit. In fact, the light from the star during a transit follows a characteristic curve known as a "light curve", from which it is possible to extract many informations (for example of a light curve see fig. 5). From the light curve it is possible to calculate the size of the planet, the radius of its orbit and many other factors [69].
The variations of the star flux induced by the exoplanets are very different and can be up to a few percent (see fig. 4 for the measured transit depth). There is no theoretical lower limit to the transit depth. The only limit is the sensitivity of the instrumentation.
For the observation of a transit of an exoplanet is not indispensable sophisticated instrumentation. There are some exoplanets easily observable with a small telescope (about 25 cm diameter), as reported in the next example.

> In an event for general public in 2009 the transit of an exoplanet in the center of Rome in Place "Campo dei Fiori" was observed in live with a telescope of an aperture of about 25 cm. The exoplanet observed is Tres-3 b that has a mass of 1.91 Jupiter-mass an orbital period of 1.31 day and a semi-major axis of 0.0226 AU [2]

In transit the main three parameters are [15]:

1. the period of recurrence of transit;
2. the duration of the transit;
3. the fractional change in brightness of the star.

The recurrence of the transit is the **planet orbital period** "P". If the mass "M" of the star is known (for example from the position of the star on Hertzsprung-Russell diagram) it is possible

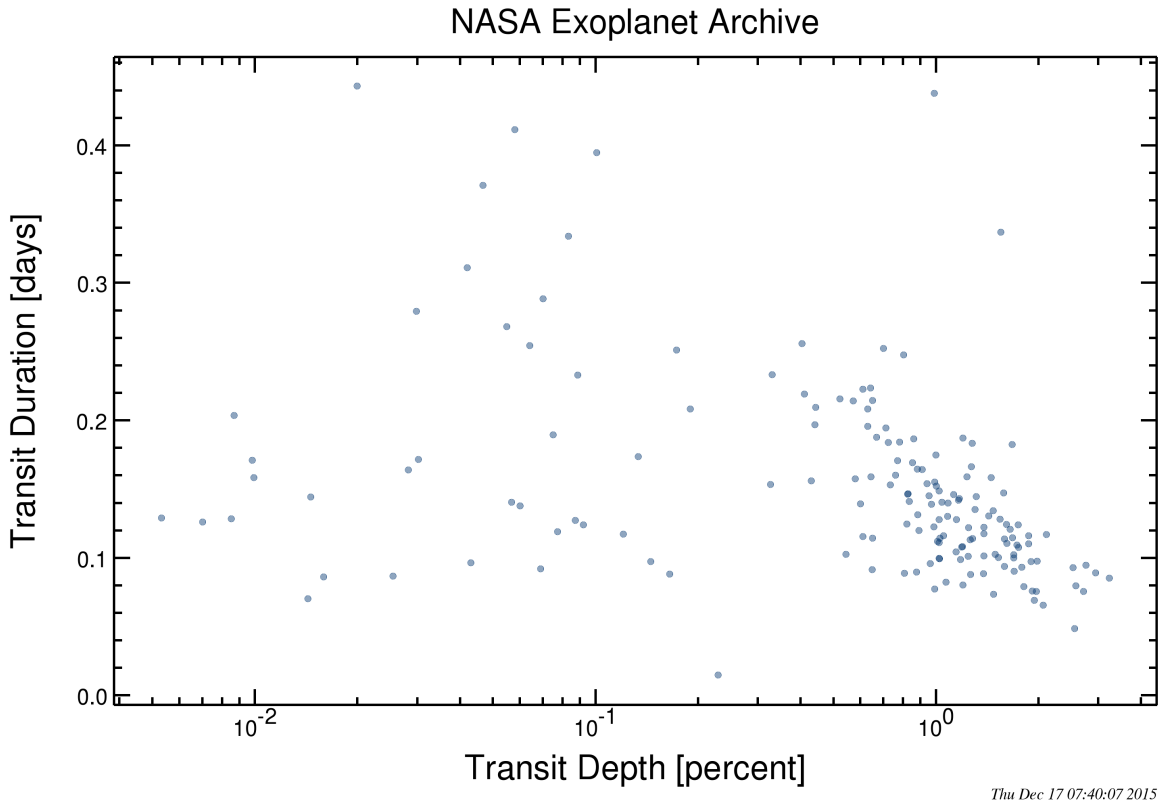

Figure 4: Plot of planets transit.The percentage of absorption of the starlight during transit and duration of transit itself are shown. Data elaborated from [4].

to determine the semi-major axis from Kepler's Third Law:

$$\frac{a^3}{P^2} = \frac{G \cdot M}{4\pi^2} \tag{4}$$

Where "a" is the semi-major axis and "G" is the Gravitational constant. The **semi major axis** is:

$$a = \sqrt[3]{\frac{P^2 \cdot G \cdot M}{4\pi^2}} \tag{5}$$

The fractional change in brightness is equal to the ratio of the area of the planet to the area of the star. As the radius of the star can be estimated from Stephan-Boltzmann equation or more precise from asteroseismology (the measure of oscillation of the star) the **planet radius** can be computed easily.
The transit occurs only if the planetary orbit is near the line of sight. The probability T_p of observing a star being transited by a planet is:

$$T_p = \frac{d}{2 \cdot a} \tag{6}$$

Where "d" is the stellar diameter and a is semi-maior orbital axis. The equation is get from [64] and in Appendix is reported a brief discussion.
For professional research of exoplanet was developed by ESA (European Spase Agency) the CoRoT space mission [13]. CoRoT ("Convection, Rotation and planetary Transits") is a space mission to perform stellar photometry in ultra-high precision condition. CoRoT is equipped width a telescope with a diameter of 27 cm and 4 wide field CCD-detectors. During a run CoRoT monitor about 12000 stars simultaneously and continuously over 150 days of observation. CoRoT can detect the exoplanets with an orbital period shorter than 50 days. The noise of light curve acquired is not far from the photon noise limit. The light curve measured with CoRoT are mixed with the ground-base observation of radial velocity, imaging and spectroscopy. The confirm of detection is given only with the match of telescope detection with ground base observations. This strategy allows to exclude almost all false positive case.
Another space-based mission to detect the transits of the exoplanets is Kepler developed by NASA [15]. The main scientific target of the Kepler mission is to find planets 30 to 600 times less massive than Jupiter. The Kepler satellite has a Schmidt telescope designed with a 0.95m aperture and about 12 degree diameter FOV (Field of View). The instrument onboard Kepler satellite is a photometer composed with 42 CCDs detectors. The images are intentionally defocused to improve the photometric precision (it permits to have an extended dynamic).
The probability to observe a Jupiter-like exoplanet in transit around its star is less than 0.1% [43].

1.4 Other methods to detect exoplanets

There are also many other systems to detect the exoplanets (see fig. 6). One of this is the **astrometry** [22]. The Astrometry consists in the measurement of the position of the stars repeated after some months and years to determine if there is also a signature of a planet that orbiting around the star in the proper motion. The principle is the same that radial velocity,

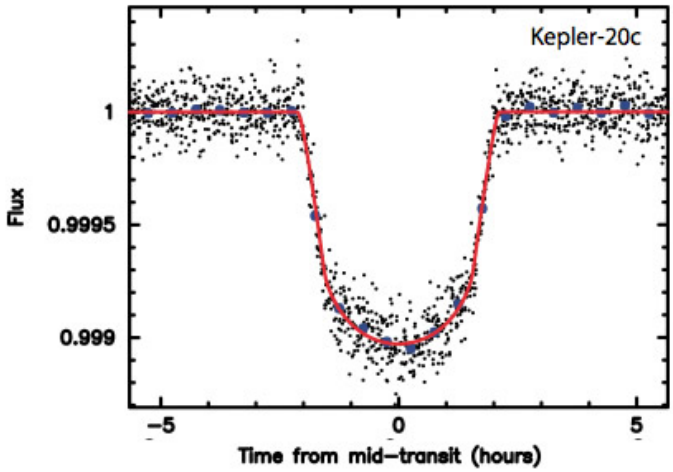

Figure 5: Light curve of Kepler 20c. The Flux measured is normalized at star flux. Credits: NASA / Kepler Mission.

but, in this case, the system is sensible also to a planet with the orbital plane orthogonal to the "line of sight". A current space-based mission that uses this principle is Gaia. Gaia scans all sky multiple times during 5 years of programmed activity. The precision is between 10 and 20 microarcsec at 15 mag. The data are useful also for the multiple scientific targets, as the 3-dimensions maps of Milky Way to investigate the origin and the evolution of our galaxy. Gaia is expected to detect all the Jupiter-mass planets with orbital period between 1.5 and 9 years within 150 light years from the Sun.

Microlensing is an advanced technique to detect exoplanets based on Einstein gravitational lens's effect predicted and verified by the theory of "general relativity". A source star is used as the reference, and it is observed during the passage of a "lens" star between the "source star" and the observer. If the lens star host a planet near the "Einstein ring" (it is about at 2-3 Astronomical Units) the magnification assumes a particular signature (see fig. 7).

From microlensing detection, it is possible to obtain the planetary mass ratio respect to star and the separation.

The **"direct imaging"** technique is a high-level proof of the detection of the exoplanets. This technique requires a very large diameter telescope for improving angular resolution, a system of adaptive optics for ground-base telescopes to reduce wavefront aberrations due to the atmospheric turbulence. A big problem is the high difference between the flux emitted by the star and the flux coming from the exoplanet. To avoid this issue, it is required a chronograph to occlude the starlight. This technique preferably reveals the big planets at a high distance from the star. The light coming from the exoplanet is due in part to its temperature (infrared black body emission) and in part is due to the reflection of light coming from the star. Planet black body emission is higher in young time of the planetary system as the planet is not yet cooled.

JWST (James Webb Space Telescope) will have the coronagraphic sensitivity to detect a Jupiter analog around a Solar-type star out to $\sim 30pc$. This would be a broadband detection, taking advantage of both the short-wavelength, as well as the more typically blackbody emission at longer wavelengths [24].

In the fig. 8 it is reported the first direct image of an exoplanet obtained by [25]. Authors imaged

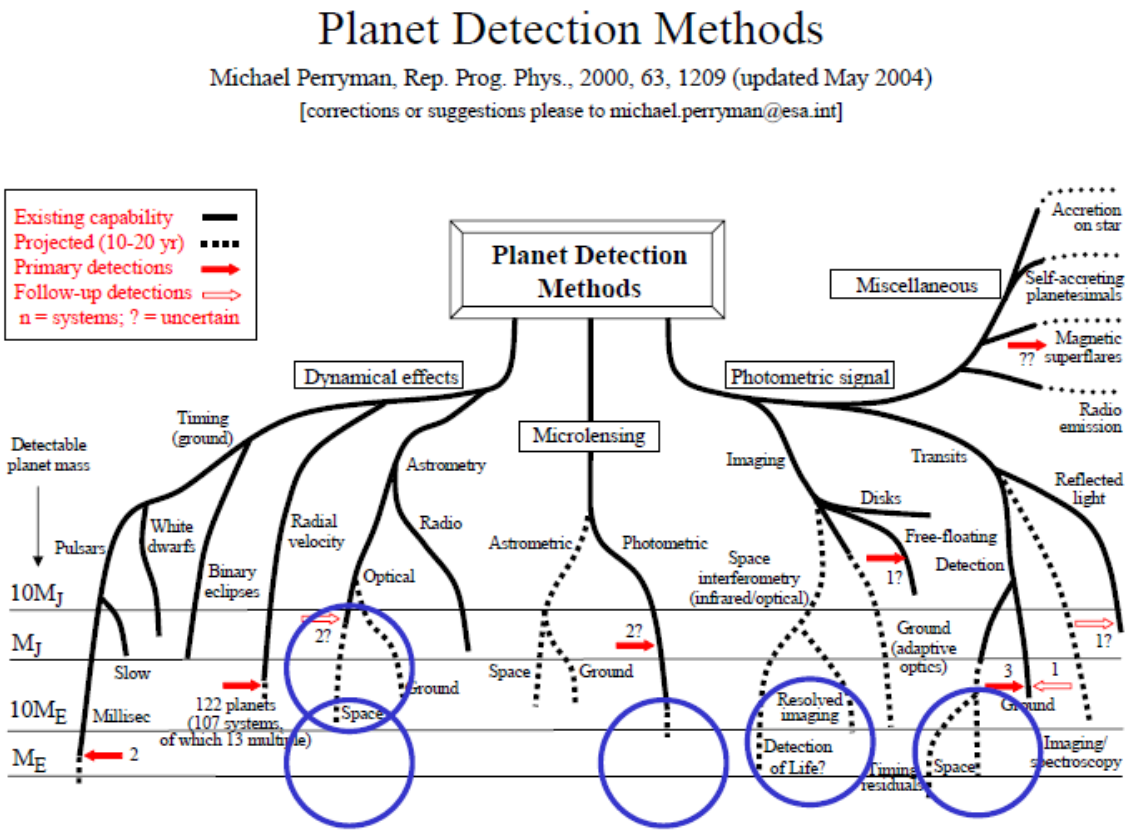

Figure 6: Exoplanets detection methods. Courtesy by [22].

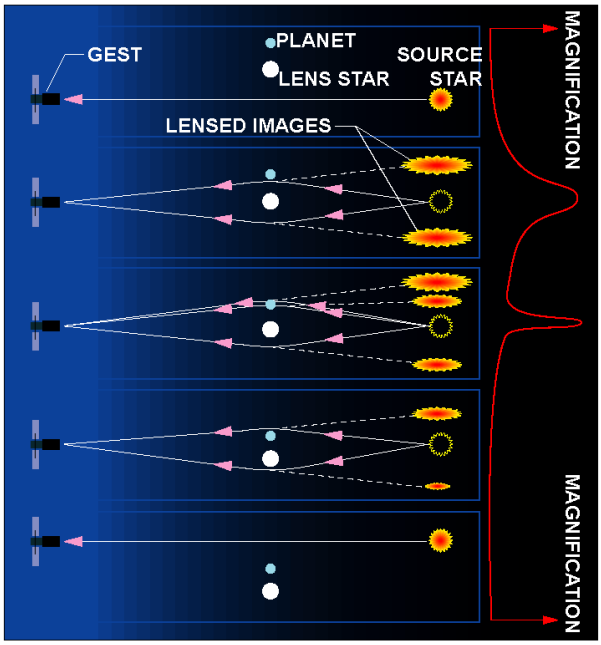

Figure 7: The Microlensing effect to detect exoplanets. Courtesy of D. Bennett, presentation of GEST (the Galactic Exoplanet Survey Telescope).

the young brown dwarf 2M1207 with the NACO adaptive optics instrument of the VLT-UT4 Telescope. The source 2M1207 was then imaged in J, H, K_s and L' bands. The AO (Adaptive Optics) IR sensing allowed to close the adaptive optics loop on the star 2M1207 and to detect in its close vicinity a faint and red object at 778 mas (milli-second of arc) [25].
In 2008 C. Doucurant et al. [26] measured the trigonometric parallax of the unresolved system 2M1207 with a precision better than 2%. This parallax puts 2M1207A and b at 52.4 ± 1.1 pc from our Sun [26].This implies that the distance of 2M1207b from the star is about 41 AU (little more of the distance of Pluto by Sun).
Fig 9 reports the Image of a multiple-planet system obtained with Keck telescope, a telescope located in the Hawaii's Island with primary mirror of 10m of diameter composed of 36 hexagonal segments and a 6 inch deformable mirror that adapts its shape even 2000 times per second to correct the atmospheric's turbulence [27].
A recent instrument developed to detect and characterized the exoplanets is SPHERE (Spectro-

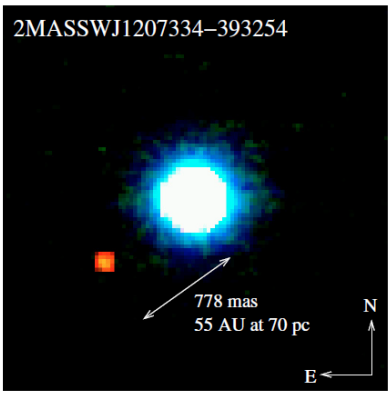

Fig. 1. Composite image of brown dwarf 2M1207 and its GPCC in *H* (*blue*), K_s (*green*) and *L'* (*red*). The companion appears clearly distinguishable in comparison to the color of the brown dwarf 2M1207.

Figure 8: Direct image of exoplanet Giant Planet companion of 2M1207 taken from [25]. H, K_s and L' are photometric bands utilized by [25].The distance of the star from us has been measured more accurately in the following paper [26].

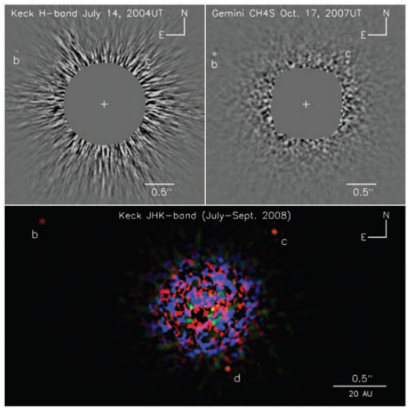

Fig. 1. HR 8799bcd discovery images after the light from the bright host star has been removed by ADI processing. **(Upper left)** A Keck image acquired in July 2004. **(Upper right)** Gemini discovery ADI image acquired in October 2007. Both b and c are detected at the two epochs. **(Bottom)** A color image of the planetary system produced by combining the J-, H-, and Ks-band images obtained at the Keck telescope in July (H) and September (J and Ks) 2008. The inner part of the H-band image has been rotated by 1° to compensate for the orbital motion of d between July and September. The central region is masked out in the upper images but left unmasked in the lower to clearly show the speckle noise level near d.

Figure 9: Direct image of multiple planetary systems obtained by Keck telescope [23].

Polarimetric High-contrast Exoplanet REsearch) [28]. In May 2014, the commissioning of

SPHERE starts at VLT. SPHERE is a combination of different instruments to detect and characterize the exoplanets. It includes a powerful extreme adaptive optics system, various chronographs, an infrared differential image camera, an infrared integral field spectrograph and a visible differential polarimeter (ZIMPOL). The imaging polarimeter ZIMPOL works in visual range (from 600nm to 900nm). It is based on a fast modulation, using a ferroelectric retarder and a demodulation technique described in paragraph **??** (page **??**). The modulation is faster than seeing variations. The instrument goal polarimetric precision is 10^{-5}.

Fig. 10 shows a graph of confirmed exoplanets, divided according to the method by which they were discovered.

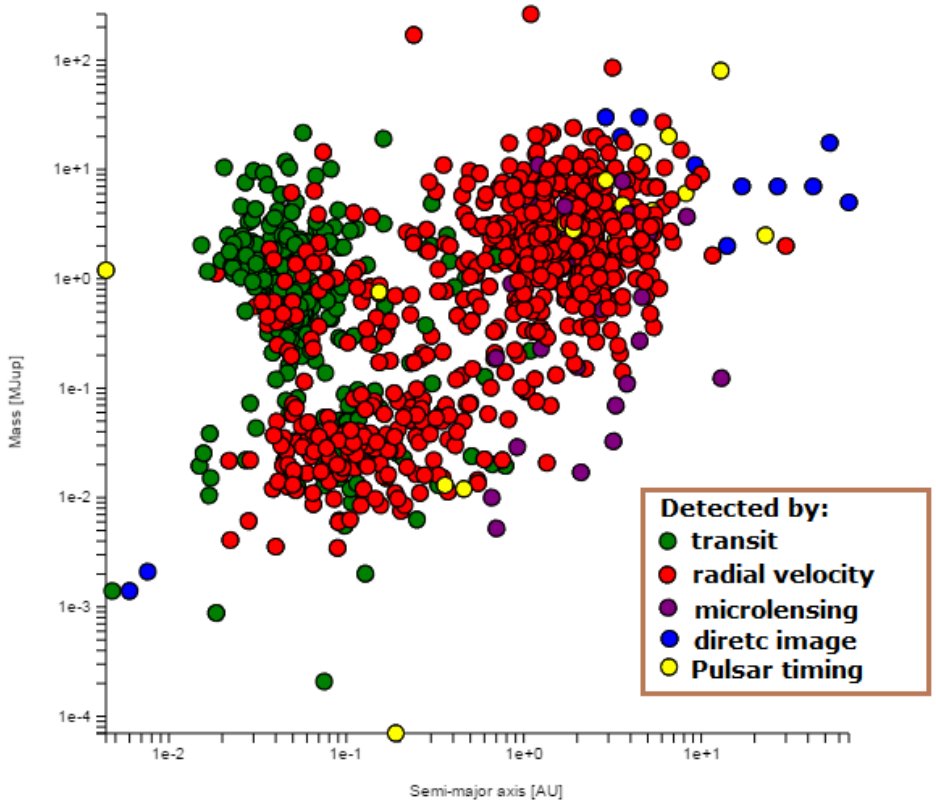

Figure 10: Graph of Mass of confirmed exoplanet versus semi-maior axis. The color of the spot shows the discovery method. The graph is recavated by plot tools of [3].

1.5 The atmospheres of exoplanets

A planetary atmosphere is defined as the layer of gas that overlays the planet's interior (a solid rock or ice crust, a liquid ocean, or a high-pressure gas envelope) and surrounds the planet. Its lower boundary is at either a solid or liquid interface, or (in planets such as gas giants) at a depth where no light or heat can escape directly to space. Its upper boundary is where gas molecules can move freely into space. Defining the boundaries in this way makes any atmosphere a gas layer of a relatively low mass compared to the total mass of a planet [69].
Understanding a planet's atmosphere is a necessary condition for understanding not only the planet itself, but also its formation, structure, evolution, and habitability. This requirement puts a premium on obtaining spectra and developing credible interpretative tools with which to retrieve vital planetary information [31].
A detailed study by photometry and spectroscopy must be performed to characterize the atmospheres of exoplanets. For about 50 exoplanets (mostly giant), the temperature, and atmospheric composition have been studied [29]. In some cases, this data are ambiguous. . The reason is that most of the data are low-resolution photometry at a few broad bands that retain major systematic uncertainties and large error bars. Moreover, the theory of their atmospheres has yet to converge to a robust and credible interpretive tool [31].
One method to characterize the atmosphere is to measure the radius of the planet in function of the wavelength during transit. This technique is based on measuring the transit radius as a function of wavelength. Because the opacity of molecules and atoms in a planet's atmosphere is a function of wavelength, the apparent size of the planet is also a function of wavelength — in a manner that is characteristic of atmospheric composition. Such a 'radius spectrum' can reveal the atmosphere's composition near the planet terminators. For this kind of measurements space-based telescopes like Spitzer or the Hubble Space Telescope or the largest ground-based telescopes are required [29].
Another technique is to compare the two transits (180° of difference in orbital phase): the first one is when the planet is transiting in front of the star and the second one when the planet passes behind the star. In the first case the spectrum is the sum of the star, the planet atmosphere, and the infrared planet emission; in the second case the spectrum is coming only from the star. The difference between the two spectra is only due to the planet. The significant problem with this technique is the instrumental stability of instrumentation and the low star flux passing in planet's atmosphere.
An important uncertainty of this technique derives from models and assumptions (like isotherm atmosphere).
It is known the high complexity of the Earth's atmosphere, and the difficulty to compute a weather forecast even with a big database of surface and satellite data upgraded continuously. The difficulty in modeling the Earth's atmosphere can show the difficulties to create and test the models of the atmospheres of exoplanets.

The atmospheric composition strongly depends from the temperature, as the molecules could be in a phase of gas or liquid/solid in function of the temperature. The UV light coming from the star can ionize some molecules and chemical reactions could be induced. Some exoplanets probably have an haze or cloud layer in the atmosphere. For example Deming et al. [30] re-

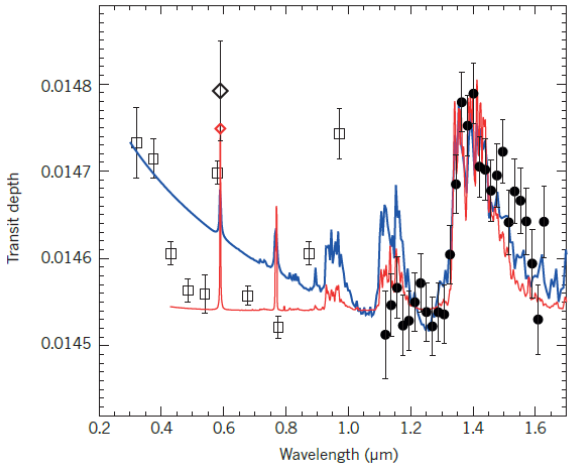

Figure 11: Transit depth spectrum of the Hot Jupiter HD209458b. Image from paper [30].

ported the presence of an absorption band by water in the atmosphere of HD 209458b at the wavelength around 1.4μm. Although the water also has an absorption line at 1.15μm, this line is not observed ((see fig. 11). This effect is interpreted as a superimposition of a continuum due to a haze layer.

Burrows [29] underlines the necessity of a model including condensation and atmospheric circulation for exoplanet with haze.

The presence of dust in the atmosphere is also a possible alternative to haze layer.

The molecules clearly identified, in exoplanets's atmosphere until now, are water, carbon monoxide, sodium, potassium and molecular Hydrogen and various ionized metals.

Some molecular detections reported in literature based on photometry are very model-dependent. Only with spectra it is possible to assure the evidence of a particular molecule.

These giant exoplanets are supposed to form in the outer region of the planetary system. As the temperature is colder than the actual temperature, they suppose to have an initial different atmosphere, also with ice (they form beyond the "ice-line"). The hypothesis is that when they approach the star, the atmosphere partially evaporates. This assumption is confirmed by the detection of wind in ultraviolet observation (Lyman-α of Hydrogen) during three transit of HD209458b by Vidal-Majdar et al. [32]. What they have estimeed is the radius of the exoplanet at the wavelength of 120nm and it is much larger than optical radius. So they have interpreted this as an hydrogen wind that flows out from the exoplanet.

The light curve of the star must contain the flux from the star, the flux reflected from the exoplanet (maximum emission in optical and ultraviolet) and the thermal emission flux from the exoplanet (maximum in infrared). They are modulated with the orbital phase of exoplanet and the reflect components depend on planet's albedo, that 's hard to determine and strongly depends on the presence of clouds. Night/day variation must modulate the infrared emission. A first measurement of this effect has been performed on HD 189733b [33]. The obtained difference between night and day temperature is about 240K, lower than expected. This suggests a mitigation of the night by super-rotational flows (like in Jupiter). A map of the temperature (with many assumptions) is extracted from these data, obtained with infrared space telescope Spitzer at wavelength of 8μm.

A significant improvement in atmosphere characterization could be achieved by the launch of JWST infrared space telescope and construction of the ground-base telescope EELT (with the diameter of the primary mirror of about 40m). Even measurements of the polarization of the reflected radiation of exoplanets will help characterize their atmospheres as shown in the next chapter.

1.6 Some significant results obtained in exoplanet research

At the time of writing of this work (15 April 2016) 2107 exoplanets have been discovered[2].
In addition to the confirmed planets, NASA's Kepler mission has published results on several thousands of planet candidates [18]. Together with radial velocity and microlensing survey detections, these results show that Earth-size planets are very numerous. The discovery of very low-mass planets so close to the detection threshold of radial-velocity surveys, and over a short period of time, suggests that this kind of object may be rather common. In particular rocky planets like our Earth, could be very common around solar-type stars [35]. This idea is fully supported by state-of-the-art planet formation models based on the core-accretion paradigm.
The range of terrestrial planets as found in our Solar System, with masses from Earth- down to Mercury-sized objects beyond 0.3 au, is still basically unexplored today.
Super-Earths are rocky planets with masses below $10 M_{\oplus}$ (Earth mass).
Fig. 12 shows the current status (update at 2013) of Super-Earth planet detections in comparison to the position of the Habitable Zone (defined as the region around a star where liquid water can exist on a planetary surface). Most super-Earths have been found at orbital distances to the star closer than the Habitable Zone. Detections in the Habitable Zone have been made by radial velocity or transit measurements. [18].
About 20 planets are found within the habitable zone .
CoRoT and Kepler, have provided more then 1000 planets, of which 100 of them are known to both the planetary radius that the mass simultaneously, from hot gas giants to a few hot super-Earths [18].
The formation of planets is presently believed to result from two different scenarios, which may or may not be mutually exclusive. In the core-accretion scenario, a planetary core is first formed by the accretion of solids that mutually collide. In the second scenario, the disk instability model, the formation of a giant planet is the result of the presence of a gravitational instability in a cold and massive protoplanetary disk [18].
The low-mass planets have a wide range of densities (more than an order-of-magnitude). Planets at low masses and densities are indicative for planet with large H-atmosphere envelopes.
planets [18].
Only seven exoplanets with orbital periods > 50 days are currently known [18]. For rocky exoplanets, the numerical models have to be consistent with the observed planetary masses and radii. Such models have been used to derive mass-radius relationships for exoplanets assuming a range of different mineralogical compositions to gain insight into the interior structure and possible bulk compositions of these planets [18].
For the smallest planets, radii are better constrained than masses. These planets are usually detected by space missions providing photometrically accurate light curves, and hence radii, but the target objects are too faint to permit an accurate mass determination. In many cases, even a rocky or icy nature cannot be distinguished within 1 sigma error. The knowledge of mean planet density is foremost dependent on the quality of the stellar mass and radius determinations. Typical current uncertainties for radius and mass determinations of small planets are around $\pm 6\%$ and $\pm 20\%$, respectively, leading to uncertainties of 30 to 50% in mean density.

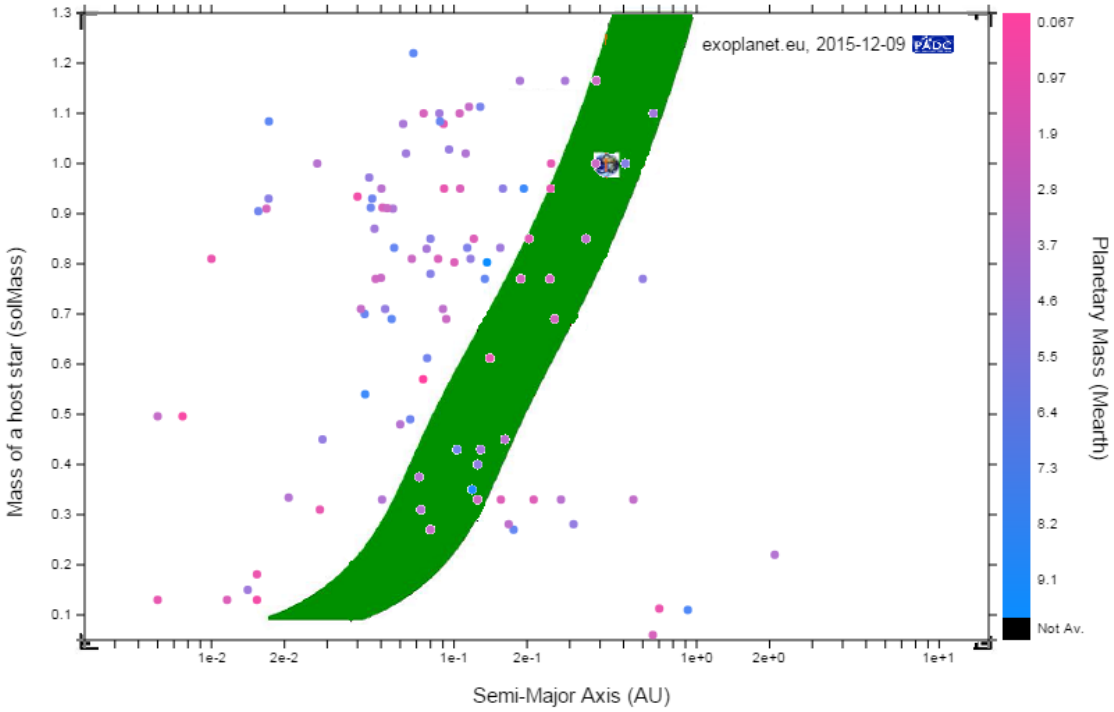

Figure 12: Graph of discovered Super-Earth exoplanets (mass $<$ 10 Earth mass). The graph was derived from the data in [2]. The y-axis shows the mass of the star in solar masses. The x-axis shows the semi major axis in astronomical units of the planet orbit. The habitable zone is superimposed in green (taken from [18]).

Giant planets are planetary bodies primarily consisting of hydrogen and helium as well as a small fraction of heavy elements. The Solar System gas giants are Jupiter and Saturn.
The icy planets of the Solar System are Uranus and Neptune, and standard interior models suggest that they consist of three main layers: 1) an inner rocky core; 2) a water-rich envelope; 3) a thin atmosphere composed mostly of hydrogen and helium with some heavier elements. However, it should be noted that due to the uncertainties of the measurements it is still unclear whether Uranus and Neptune are truly 'icy planets' [18].
The compositions and internal structures of extrasolar giant and Neptune-sized planets are less constrained than the planets in the Solar System, but they offer the opportunity to study giant planets as a class. The diversity of gas giant and 'icy' exoplanets is much larger than expected from our Solar System.
Although the majority of transiting giant planets are composed mostly of hydrogen and helium. their internal constitution is not necessarily similar to that of the gas giants in our Solar System. In fact, exoplanets show a large diversity of masses and radii, yet to be explained [18].
Extrasolar giant planets can differ significantly from Jupiter and Saturn, for example giant planets close to their parent stars are exposed to an intense stellar radiation.
Although our understanding of "hot Jupiters" is still incomplete, substantial progress in studying these objects has been made. Interior models including the effects of irradiation have been computed [18].
The compositions of gas giant planets can reveal important information on giant planet formation.

The number of planets known to orbit giant stars (≈ 50) is still small compared to those known to orbit main-sequence stars, but their number has dramatically increased in recent years and is expected to do so in the near future [18].

The discovery of 7 circumbinary planets in 6 systems has been announced to date [18]. Doyle et al. [36] report the detection of the first planet whose orbit surrounds a pair of low-mass stars (Kepler-16b). The planet is comparable to Saturn in mass and size and is on a nearly circular 229-day orbit around its two parent stars. The eclipsing stars are 20 and 69% as massive as the Sun and have an eccentric 41-day orbit. The motions of all three bodies are confined to within 0.5° of a single plane, suggesting that the planet formed within a circumbinary disk.

In the past decade, numerous studies have been published on the use of wavelength-dependent primary transits and secondary eclipses to characterise the atmospheres of exoplanets. Highlights include the claimed detections of molecular features in the infrared to the inferred presence of clouds/hazes in the visible in the atmospheres of hot Jupiters, and even the detection of the exosphere. Visible data determine the albedo, the identity of the major spectroscopically inert molecule and the relative abundance of clouds/hazes of the atmosphere [18]. The spectroscopically active molecules of an atmosphere typically contribute spectral features in the infrared, but these molecules are often minor constituents of an atmosphere (by mass).
Phase curves show the flux as a function of orbital phase, which may be deconvolved to obtain the flux versus longitude on the exoplanet, known as a "brightness map". Infrared phase curves

contain information about the efficiency of heat redistribution from the dayside to the nightside of an exoplanet. By contrast, visible phase curves encode the reflectivity of the atmosphere versus longitude, which in turn constrains the relative abundance of clouds or hazes if they are present.
Examples of exoplanets where clouds are likely to be present include Kepler-7b, which has a high albedo (≈ 0.3) and a phase curve containing a surprising amount of structure. The feasibility of obtaining visible phase curves has already been demonstrated for the CoRoT and Kepler missions [18].

Observations around bright enough stars with the Hubble (HST) and Spitzer Space Telescopes, combined with theoretical studies of transiting exoplanets, have indicated that obtained UV spectra related to the upper atmospheres can be used to study a number of issues, for example: space weather events on exoplanets, properties such as the thermospheric structure, the exosphere-magnetosphere-stellar plasma environment, outflow of planetary gas including hydrogen atoms and heavy species such as carbon, oxygen and metals [18].

Modulations in the transit light curve also allows for the detection of planetary rings and large moons. There is a well-developed project searching for moons around transiting extrasolar planets in the Kepler mission, but so far the search has proven to be elusive [18].

2 The polarization

In this chapter, the definition of the polarization of an electromagnetic wave is introduced.
Some general concepts about the tools used to measure the polarization (the polarimeters) are explained and examples of instruments for astrophysics uses are presented.
A small report on polarization data reduction is provided.
The physical reasons, that show why the light reflected from an exoplanet should be partially polarized, are discussed and some numerical simulations that support this hypothesis are reported.
In conclusion a controversial measure of the polarization of the star HD189733 perhaps due to its exoplanet HD189733b is presented.

2.1 Polarization basics

A basic feature of Maxwell equations is the existence of traveling wave solutions that carry energy. Let us now consider solutions of the form:

$$\begin{aligned} \vec{E} &= \hat{a_1} \cdot E_0 \cdot e^{i(k' \cdot r - \omega \cdot t)} \\ \vec{B} &= \hat{a_2} \cdot B_0 \cdot e^{i(k' \cdot r - \omega \cdot t)} \end{aligned} \tag{7}$$

where $\hat{a_1}$, and $\hat{a_2}$, are unit vectors, E_0 and B_0 are complex constants, and $\vec{k} = k' \cdot \vec{n}$ and ω are the "wave vector" and frequency, respectively. Such solutions represent waves traveling in the $\vec{n}$ direction, orthogonal to $\hat{a_1}$, and $\hat{a_2}$, since surfaces of constant phase advance with time in the $\vec{n}$ direction [40].
The polarization of light is connected with the oscillating direction ($\hat{a_1}$) of electric field. We need consider only the electric vector E; the magnetic vector simply stays perpendicular to E and has the same magnitude as E.
Light is called **unpolarized** if the direction of its electric field fluctuates randomly in the time. The monochromatic plane waves described in Eq. 7, and represented in fig. 13, are linearly polarized; that is, the electric vector simply oscillates in the direction $\hat{a_1}$, which, with the propagation direction, defines the *plane of polarization* [40].
In a realistic case, the direction of oscillation of electric field could be fixed or not. For example in a thermic emission process (Planck radiation) there isn't a favored direction for the electric field, and so the thermic emission process is unpolarized. Lasers are the most common source of polarized light. In everyday life, a mobile phone LCD screen or the computer's screen is very common source of linear polarized light.
The Stokes parameters are used to quantify the polarization.
Consider a parallel beam of light traveling in a certain direction, which it is chosen to call the positive x direction. The components of the electric field in any two mutually perpendicular directions (represented by unit vector $\hat{r}$ and $\hat{l}$ may be written in term of the amplitudes (a_l) and

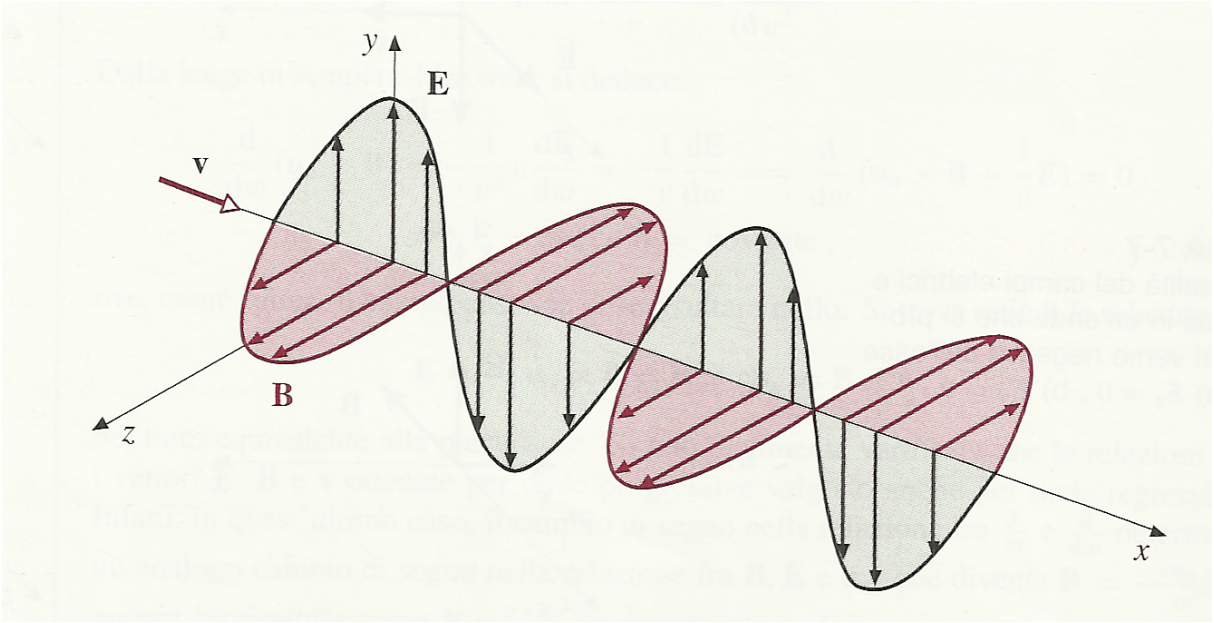

Figure 13: Representation of a monochromatic electromagnetic wave. The electric field oscillates in the y-axis, and the magnetic field in the z-axis (as a consequence of Maxwell equation). The wave propagates along x-axis. From university general physics book "Fisica Generale - Elettromagnetismo" by Focardi, Massa and Ugonozzi

(a_r) and phases (ϵ_l) and (ϵ_r) as [65]

$$\begin{aligned} E_l &= a_l \cdot e^{i(\omega \cdot t - k \cdot y - \epsilon_l)} \\ E_r &= a_r \cdot e^{i(\omega \cdot t - k \cdot y - \epsilon_r)} \end{aligned} \tag{8}$$

t represent time, $k = \frac{2 \cdot \pi}{\lambda}$ is the wave number and $\hat{r} \times \hat{l}$ is the direction of propagation.
The Stokes parameter are the time average [65]

$$\begin{aligned} I &= \langle E_l E_l^* + E_r E_r^* \rangle = \langle a_l^2 + a_r^2 \rangle \\ Q &= \langle E_l E_l^* - E_r E_r^* \rangle = \langle a_l^2 - a_r^2 \rangle \\ U &= \langle E_l E_r^* + E_r E_l^* \rangle = 2\langle a_l a_r \cos\delta \rangle \\ V &= \langle E_l E_r^* - E_r E_l^* \rangle = 2\langle a_l a_r \sin\delta \rangle \end{aligned} \tag{9}$$

where $\delta = \epsilon_l - \epsilon_r$ and asterisk represents the complex conjugate.
The Stokes parameters of a mixture of independent waves are sums of the respective Stokes parameters of the separate waves.
Suppose that E_r is subjected to a constant retardation ϵ with respect to E_l and let $I(\Psi, \epsilon)$ be the intensity of light due to vibrations in the direction making an angle Ψ with the $\hat{l}$ direction. So, Stokes parameters can be obtained from the following "measurements"[65]:

$$\begin{aligned} I &= I(0°, 0) + I(90°, 0) \\ Q &= I(0°, 0) - I(90°, 0) \\ U &= I(45°, 0) - I(135°, 0) \\ V &= I(45°, \pi/2) + I(135°, \pi/2) \end{aligned} \tag{10}$$

"I"is the total intensity. Q is the excess in the intensity of light transmitted by a polarizer which passes linear polarization in the "l"direction ($\Psi = 0°$), over the intensity of light transmitted by polarizer which passes linear polarization in the $\hat{r}$ direction ($\Psi = 90°$). "U"has an analogous interpretation with intensity for $\Psi = 45°$ compared to that for $\Psi = 135°$.
"V"is the excess in intensity of light transmitted by an instrument which passes left-handed circular polarization [65].
An arbitrary beam of radiation can be *mathematically* decomposed into two parts, one unpolarized with Stokes parameters $\{I - \sqrt{Q^2 + U^2 + V^2}, 0, 0, 0\}$ and one polarized with Stokes parameters $\{\sqrt{Q^2 + U^2 + V^2}, Q, U, V\}$ [65].
Thus the intensity of polarized light is $I_{pol} = \sqrt{Q^2 + U^2 + V^2}$. The degree of polarization is

$$P = \frac{I_{pol}}{I} = \frac{\sqrt{Q^2 + U^2 + V^2}}{I} \tag{11}$$

The intensity of linearly polarized light is defined as $I_{lp} = \sqrt{Q^2 + U^2}$ and the intensity of circularly polarized light as $I_{CP} = V$ [65].

The principal optical components used to manipulate the polarization are:

- **Polarizers** - In order to select a specific polarization of light, polarizers are used. Polarizers can be broadly divided into reflective, dichroic, and birefringent polarizers.

  - **Reflective polarizers** transmit the desired polarization while reflecting the rest. Wire-grid polarizers consist of narrowly separated metal wire grids deposited on an optical surface that are available for shorter wavelengths due to the great advances made in micro-lithography. Wire-grid polarizers can also be used in polarizing beamsplitter cubes with much improved performance compared to thin-film cube beamsplitters [60].
  - **Dichroic polarizers (*Polaroid*)** absorb a specific polarization of light, transmitting the rest; modern nanoparticle polarizers are dichroic polarizers.
    More recent types, such as the HN42 line, provide higher transmission (42 % for unpolarized light) with better environmental stability then the common HN38 line.
    Dichroic glass polarizer are based on the alignment of elongated metal particles in glass. *Polarcolor* covers the 600 to 2100 nm range, *colorPol* covers the 375 to 2000 nm [60].

  - **Birefringent polarizers** rely on the dependence of the refractive index on the polarization of light. Different polarizations will refract at different angles and this can be used to select certain polarizations of light.
    Historically, birefringent crystals have been the material of choice to build polarizers and polarizing beamsplitter and they are often found in astronomical instruments.
    The most frequently used polarizing beamsplitter is the Wollaston prism, which uses prisms with crossd optic axes. As the the birefringence exhibits dispersion, there can be some reduction in image quality in broadband and/or diffraction-limited applica-

tions [60].

  - **Thin-film polarizers** consist of a thin-film coating on an inclined substrate, which forms a polarizing beamsplitter. In most astronomical cases, thin-film polarizers are used in the form of cube beamsplitter. They are mainly used in broadband polarimetry, where crystal-based components exhibit unacceptable chromatic effects [60].

- **Retarders** - While polarizers select certain polarizations of light, discarding the other polarizations, ideal retarders modify existing polarizations without attenuating, deviating, or displacing the beam. They do this by retarding (or delaying) one component of polarization with respect to its orthogonal component.
  - **HWP fixed retarders** - An Half Wave Plate (HWP) changes the direction of linear polarization: It rotates the direction of the linear polarization by twice the angle between the input polarization and the fast axis. Linear polarization parallel to either the fast or the slow axis is unaffected, as these are the eigenvectors of the retarder [60].
  - **QWP fixed retarders** - A Quarter Wave Plate (QWP) converts circular into linear polarization at $\pm 45^\circ$ from retarder's fast axis, and vice versa.
  - **Liquid crystals variable retarders** - Liquid crystals offer a new approach to modulate the polarization without the need for a mechanical motion. Liquid crystals are birefringent materials, where the retardation and/or fast axis can be manipulated on a microscopy level by applying an external electric field. The switching times of liquid crystal are relative fast ($\sim$ 10ms) [60].
  - **PEM variable modulator** - PhotoElastic Modulator (PEM) is a variable retarder, which relies on a regular glass becoming birefringent when external stress is applied. A PEM applies this stress at the mechanical resonance frequency, which minimizes the energy needed to produce the stress. Typical resonance frequencies are $\sim 20 - 50$kHz [60].

2.2 Polarimeters for astrophysics in visible wavelengths

Polarimeters contain optical elements such as retarders and polarizers, that change the polarization state of incoming light in a controlled way. Detectors only measures intensities [60].
A polarimeter that measures Stokes parameters sequentially in time, such as polarimeter with a rotating retarder or a rotating polarizer, uses a **temporal modulation scheme**. A polarimeter that measures two or more polarization parameters simultaneously by splitting the incoming light into several channels employs a **spatial modulation scheme**. Both modulation schemes have advantages and disadvantages. Indeed, the two schemes are rather complementary, for this reason the modern sensitive polarimeters often combine the advantages of modulation schemes and minimize the disadvantages [60].
Tables 1, 2, 3, 4 and 5 list polarimetric instruments for visible astronomy that are currently or will shortly be in operation for Ground telescopes. The only space telescope that can make measurements of polarimetry is the Hubble Space Telescope using the tool ACS/WFC through 3 polarizing filters mounted on a filter wheel.

Detailed descriptions of 5 different polarimeters: FOCAS, PEPSI, SPHERE - ZIMPOL, GASP and TURPOL are now illustrated in order to show the main features of some polarimeters.

2.2.1 FOCAS Polarimeter

The Faint Object Camera and Spectrograph (FOCAS) is one of the seven common-use instruments of the 8.2-m Subaru Telescope on Mauna Kea. FOCAS is mounted at the F12.2 Cassegrein focus of the Telescope, where the image scale is 2."06/mm, given the telescope focal length of 100 m. The collimator lens unit consists of 8 lenses with 8 surfaces and has a focal length of 1097.7 mm, while the camera lens unit consists of 6 lenses with 8 surfaces and has a focal length of 329.4 mm (see fig. 14) [72].
The r.m.s. diameter of the PSF, averaged over the optimized wavelength range, has been found to be as small as 0."11 at the field center and smaller than 0."14 over the field of view.
For polarimetric observations, a half-wave plate, a quarter-wave plate and a Wollaston prism manufactured by B. Halle Nachfl. are available. Both of the wave plates are Pancharatnam-type super-achromatic retarders, and the deviation of the retardations is less than 3° in the wavelength range between 350 nm and 1200 nm.
The crystal quartz Wollaston prism, consisting of three elements, splits the incident light into two orthogonally polarized beams, ordinary o- and extraordinary e-rays, with a separation angle of 32.'17 at 633 nm. This separation angle produces a spatial shift of the two beams that amounts to 11.1 mm at the entrance mask and gives a 3.7 mm separation of the two images at the detector. Therefore, to avoid blending of the o- and e-images, the spatial opening of each slot in the polarimetric mask should be narrower than 10.7 mm, while the gap between neighboring slits should be wider than 10.7 mm in the direction of the beam splitting.

The whole FOCAS instrument has a diameter of 2 m and a height of 2 m, and its weight is approximately 2.1 t. A schematic view of the optics and structure of FOCAS is shown in fig. 14. FOCAS is attached to the Subaru Telescope on the Cassegrain flange surface by the automatic

	Instrument	Telescope	Modulation	Analyzer	Specifics
General purpose polarimeter	LRISp	Keck (10m) Cassegrain	rotating superchromatic (quartz+MgF_2) HWP, QWP	calcite Foster prism with folding prism	320-1100 nm imaging, spetroscopy
	RSS	SALT ($\sim$ 10m) prime focus	rotating superchromatic (quartz+MgF_2) HWP, QWP	calcite Wollastone prisme	320 - 850 nm imaging spestroscopy, Fabry Perot
	Fors 1/2	VLT (8.2 m) Cassegrain	rotating superchromatic (quartz+MgF_2) HWP, QWP	quartz Wollastone prism	330 - 1100 nm imaging spetroscopy
	FOCAS	Subaru (8.2 m) Cassegrain	rotating superchromatic (quartz+MgF_2) HWP, QWP	quartz Wollastone prism	370 - 1000 nm imaging spetroscopy
	ISIS	WHT (4.2 m) Cassegrain	rotating superchromatic (quartz+MgF_2) HWP, QWP	calcite Savart plate	330 - 1100 nm imaging spetroscopy
	PAOLO / DOLORES	TNG (3.6 m) Nasmyth	rotating HWP, QWP	MgF_2 double Wollastone prism	320 - 1200 nm imaging spetroscopy
	EFOSC2	NTT (3.6 m) Nasmyth	rotating superchromatic (quartz+MgF_2, polymer) HWP, QWP	Wollastone prism	305 - 1100 nm imaging spetroscopy
	ALFOSC	NOT (2.5 m) Cassegrain	rotating QWP, HWP	calcite Wollaston polaroid	320 - 1100 nm imaging, spetroscopy
	DBIP	UH 88" (2.2 m)Cassegrain	rotating polymer zero-order HWP	calcite Savart plate	400 - 700 nm imaging
	SPARC4*	Pico dos Dias (1.6 m) Cassegrain	rotating QWP, HWP	Savart plate	simultaneous U, B, V, I imaging
	HPOL*	Mt. Lemmon 60" (1.5 m)Cassegrain	rotating HWP	Wollastone prism	320-1050 nm spetroscopy
	HOWpol	Kanata (1.5 m) Cassegrain	-	rutile, MgF_2 wedged double Wollastone	450 - 1100 nm imaging, spetroscopy
	CAPS*	C2PU (1 m) Cassegrain	-	wedged double Wollastone	500 - 730 nm imaging
	SouthPol	T80S (0.80 m) Cassegrain	rotating HWP	calcite Savart plate	V band survey

Table 1: General purpose polarimetric instruments for visible astronomy that are currently or will shortly be in operation. Table get from [60].

	Instrument	Telescope	Modulation	Analyzer	Specifics
High spectral resolution polarimeter	**PEPSI***	LBT (2 x 8.4m)	rotating superchromatic polymer QWP	Foster prism + folding prism	383 - 907 nm R_λ = 120000 identical units on both telescopes
	EsPaDOnS	CFHT (3.6 m) Cassegrain	rotating Fresnel rhomb combination	calcite Wollastone prisme	370 - 1050 nm $R_\lambda = 68000$
	HARPSpol	ESO (3.6 m) Cassegrain	rotating superchromatic polymer QWP, HWP	Foster prism + folding prism	378 - 690 nm $R_\lambda = 110$
	HiVIS	AEOS (3.6 m) Coudé	2 Liquid Crystal Variable Retarders, rotating achromatic QWP, HWP	Savart plate	550 - 1000 nm + 1000 - 2500 nm $R_\lambda = 49000$
	SOFIN	NOT (2.5 m) Cassegrain	rotating achromatic QWP	calcite plate	320 - 1080 nm $R_\lambda = 27000$
	NARVAL	TBL (2 m) Cassegrain	rotating Fresnel rhomb combination	calcite Wollaston prism	375 - 1050 nm $R_\lambda = 68000$
	dimaPol	Plaskett (1.8 m) Cassegrain	QWP + HW Ferroelectric liquid Crystal	Calcite Savart	visible R_λ = 15000

Table 2: High spectral resolution polarimetric instruments for visible astronomy that are currently or will shortly be in operation. Table get from [60].

	Instrument	Telescope	Modulation	Analyzer	Specifics
High contrast imaging polarimeters	SPHERE - ZIMPOL	VLT (8.2 m)	Ferroelectric liquid Crystal + achromatic HWP switches	cube beam-splitter	600 - 900 nm
	ExPo	WHT (4.2 m) Nasmyth	2 Ferroelectric liquid Crystal + 2 wave plates polychromatic	cube splitter + prisms, polarization grating	500 - 900 nm
	PolCor	NOT (2.5 m) Cassegrain	-	rotating polarizer	410 - 750 nm

Table 3: High contrast imaging polarimetric instruments for visible astronomy that are currently or will shortly be in operation. Table get from [60].

	Instrument	Telescope	Modulation	Analyzer	Specifics
High time resolution polarimeters	RINGO (1, 2, 3)	Liverpool Tel. (2 m), Cassegrain	Rapidly rotating analyzer + wedge	Polaroid	350 - 1000 nm $\sim$ 0.1Hz
	OPTIMA	various	-	double Wollaston + fiber system	450 - 950 nm $\sim$ 1kHz
	HIPPO	SAAO (1.9 m) Cassegrain	rotating superchromatic QWP, HWP	Foster prism	350 - 900 nm $\sim$ 0.1Hz
	ROBOPOL	Skinakas (1.3 m)	-	Wollaston prism + HWP	V, I bands $\sim$ 1Hz
	GASP*	Cassini (1.2 m) Cassegrain	-	full-Stokes beamsplitter prism assembly	400 - 800 nm $\sim$ 400Hz

Table 4: High time resolution polarimetric instruments for visible astronomy that are currently or will shortly be in operation. Table get from [60].

	Instrument	Telescope	Modulation	Analyzer	Specifics
Aperture photopolarimetry	POLISH	Hale (5 m), Cassegrain	PEM	3-segment Wollaston prism	B, V, R bands
	PlanetPol	WHT (4.2 m), Cassegrain	PEM	3-segment Wollaston prism	R band
	single-channell polarimeter	ZTSh (2.6 m)	rotating QWP	Polaroid	visible range
	TurPol	NOT (2.5 m) Cassegrain	rotating QWP, HWP, chopping	Savart plate	U, B, V, R and I bands

Table 5: Aperture photopolarimetry instruments for visible astronomy that are currently or will shortly be in operation. Table get from [60].

htbp

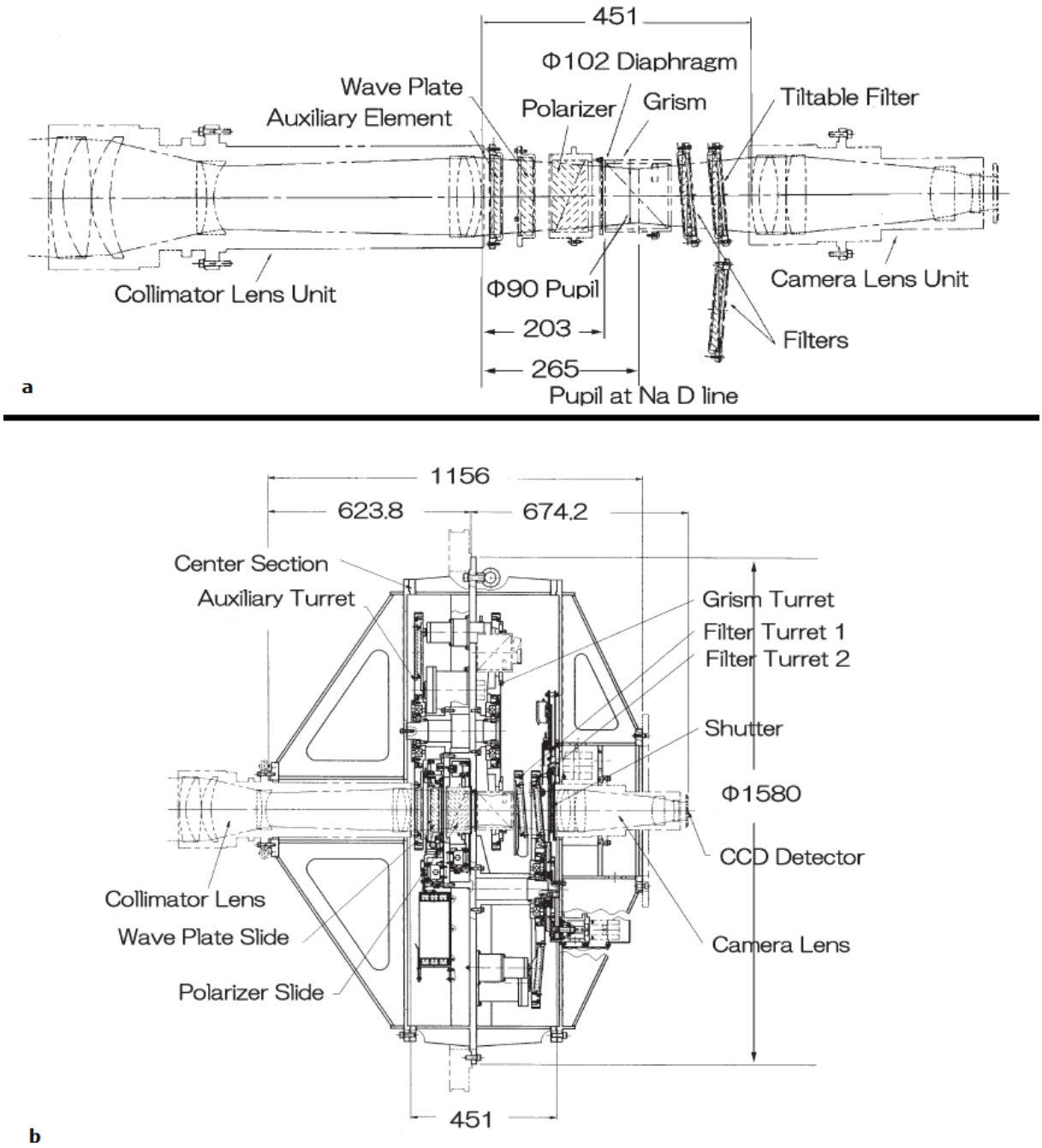

Figure 14: Overview of FOCAS Polarimeter. a) Optical train of the main optics of FOCAS. The collimator part consists of 8 elements i 4 groups, while camera part consists of 6 elements in 4 groups. b)Internal view of the FOCAS turret section (the turret section contains various optical elements). The Subaru telescope is on the left. figures taken from [71].

instrument exchanger (CIAX).
Various optical elements, such as grism, filters, and polarizers, can be inserted in the 451-mm turret section between the collimator lenses and the camera lenses using three turrets or two slides. A quarter-wave retarder plate and a Wollaston prism are on the slide. Both a half-wave retarder plate and a quarter-wave retarder plate can be mounted on the retarder-plate slide.
Rotation of these wave plates is driven by stepper motors with absolute potenziometers, controlled to an accurancy of $\simeq 0.025°$ [71].
To suppress ghost images produced by reflections internal to the optical surfaces the filters are tilted by 5° (see fig. 14 a).
The FOCAS CCD camera consists of a pair of abuttable CCDs of 2048 × 4096 pixels with 15μm square pixels. The CCDs cover the entire Subaru Cassegrain 6'-diameter FOV, and the pixel scale is 0.103"/pix, which yields good sampling of the image at the best seeing size available at the summit of Mauna-Kea. The CCDs are cooled to -100°C with a commercial cryocooler. The conversion factor of the CCD chips is $1.9e^-/ADU$ [71].
The response to the input light flux is linear in the range 0 to 40000 e^- with a 0.5% r.m.s. fluctuation. The readout noise is 4.1–5.1 ADU, which corresponds to 9–10 e^-. Although the bias level shows some chip-to-chip variance, it is quite stable, with the amplitude fluctuations being smaller than the readout noise. The dark current is negligible at CCD temperatures of -90°C to -100°C [71].
The stability of instrumental Q and U is good and the variation is less than 0.05 %. The degree of the instrumental polarization itself is not negligible in case of observation apart from the center of the field of view (FOV). The degree of polarization increases as approximately $\propto r^{-4}$, where r is the distance between the image position and the center of FOV, and shows a weak wavelength dependence. Instrumental polarization reaches $\sim 1\%$ around the edge of FOV. The position angle of instrumental polarization is almost radial. Anyway, the stability is still less than 0.05 % at each position and authors can remove the instrumental polarization with a proper calibrating observation [72].

2.2.2 PEPSI Spectropolarimeter

The PEPSI IQUV spectropolarimeter is designed to be mounted at the direct Gregorian focii of the 2×8.4 m Large Binocular Telescope (LBT) on Mt. Graham in Arizona [79].
Two identical instruments are fiber fed to the joint échelle spectrograph located in a stabilized chamber within the pier of the telescope. The polarizing units is based on interference-suppressed super-achromatic retarder plates and Foster prisms, and it is in a thermally controlled environment and kept constant at $+20 \pm 0.5$°C. The spectrograph receives light from the polarimeters and permanent focus stations via 45m long fibers, coupled with image slicers. [73]. Each polarimeter provides simultaneous spectra of the ordinary and the extra-ordinary beam. A total of four fibers will simultaneously direct two ordinary and two extraordinary light beams to the spectrograph. Both polarimetric units are layed out in a modular design, each one optimized to the polarization state in which it is used. A number of observing modes can be chosen that are optimized to the type of polarization that is expected from the target, e.g. circularly and linearly

polarized light simultaneously, or linearly polarized light in both polarimeters, or integral light from one and polarized light from the other telescope.
Calibration would be provided for each polarimeter separately.
The calibration optics are located on a rotary stage within the collimated beam and are interchangeable via two linear stages. The optics consist of a Glan-Thompson polarizing prism and two QWRs optimized for the red and the blue wavelength range, respectively. Calibration light is brought up to the telescope focus via a dedicated fibre and is injected into the polarimeter through a set of f/ratio-matching optics [79]. The design of the modified Foster prism (see fig. 15) allows to form two parallel orthogonally-polarized beams at the exit of the prism. The extraordinary beam transmits straight through the two blocks while the ordinary beam is reflected and passes through the interface layer into the second calcite block where it is again totally reflected. A third prism made of N-BK7 is used to redirect the ordinary beam in the same direction as the straight-through extraordinary beam [79].
The PEPSI optical train contains up to 66 optical surfaces from the telescope's primary mirror down to the CCDs [79].
PEPSI will attain a resolving power of 120'000 with a sky aperture of 1.64 arcsecond.
The overall PEPSI peak efficiency, including the telescope but excluding the atmosphere, is 15% at 650 nm and still 11 % at 390 nm and 10% at 900 nm [79].

The design of the modified Foster prism (see fig. 15) allows to form two parallel orthogonally-polarized beams at the exit of the prism.
Entrance diaphragm in the focal plane of the telescope to reduce the stray light and sky background polarization. Anti-reflection coated, polarization-grade, doublet collimator with a stress-free mount in a thermostabilized environment. The collimator is located on a rotary stage for calibration of its stress-birefringence. Calibration-optics unit on rotary stages retracted in and out of the beam with linear stages. Super-achromatic QWR are based on the Pancharatnam design and consist of five stretched acrylic PMMA zero-order retarder layers with their optical axes oriented at the specific angles.
The observation polarimetric modes of PEPSI are circular polarization and linear polarization modes. Circular observational mode allows to determine Stokes V in two exposures made with quarter-wave retarder angles $0°/90°$ in order to compensate for small second-order deviations in retardation angle and optical axis orientation of the retarder. Linear polarization observational mode allows to determine Stokes Q and U in four exposures made with angles of the polarizing beam-splitter at $0°/90°$ and $45°/135°$, respectively to compensate for the Foster prism cross-talk effect.
In 1 hour integration time, the PEPSI polarimeter would attain a precision in Stokes IQUV measurements of 10^{-4} for a star of 4th magnitude, and 10^{-3} for 9th magnitude. The accuracy of such measurements will be limited by the cross-talk between Stokes Q and U induced by a slight misalignment of the Wollaston prism; the entrance collimator lens birefringence can be caused by the mechanical and thermal stresses, anti-reflection coating, and the intrinsic structure of the glass which may lead to a severe cross-talk between Stokes U and V. Spurious polarization may arise due to CCD fringes and cannot be canceled out: a high quality flat fielding is essential, although, no optical fringes were detected from the PMMA retarders at the level of 10^{-4}. The

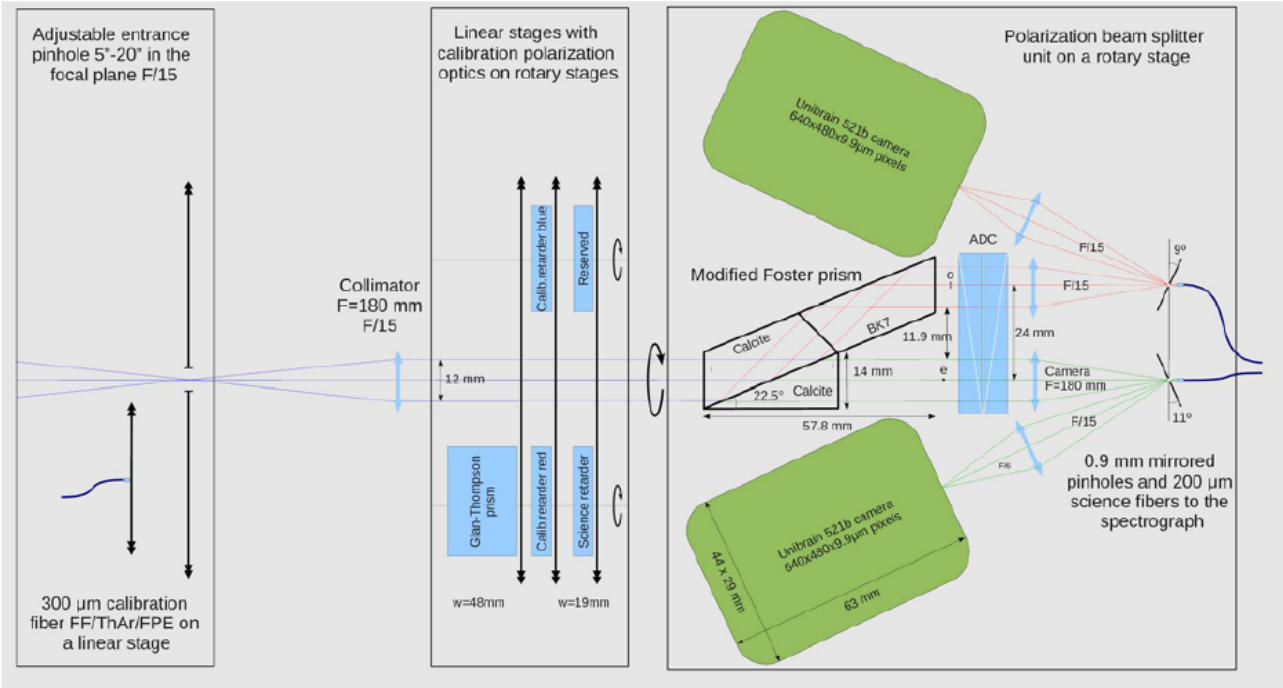

Figure 15: Schematic drawing of the principal components of the PEPSI polarimeter. The telescope is on the left side. The spectrograph is not shown. Image get from [73]

Earth's atmosphere changes the polarization state of the refracted light at large angles of incidence; the effect is of order of only 10^{-5} at zenith distance of 87°. The spectrograph stability is essential for the subsequent combination of the polarized spectra obtained in exposures with different configurations of the polarization optics [74].
The PEPSI spectropolarimeter is under commissioning/early science phase (December 2015).

2.2.3 SPHERE - ZIMPOL

SPHERE (Spectro-Polarimetric High-contrast Exoplanet REsearch) at VLT is an extreme adaptive optics system and coronagraphic facility feeding three science instruments: IRDIS, IFS, and ZIMPOL. ZIMPOL is the imaging polarimeter. one of three focal plane instruments of the SPHERE / VLT [28].
The design of SPHERE is divided into four subsystems: the Common Path and Infrastructure (CPI) and the three science channels (a differential imaging camera IRDIS, InfraRed Dual Imaging Spectrograph, an Integral Field Spectrograph (IFS) and the visible imaging polarimeter ZIMPOL). Fig. 16 reports the scheme of the main components of the SPHERE and detail of Common Path Infrastructure.
Common path Infrastructure (CPI) includes the main optical bench, connects the other subsystems to the light path, and guarantees a static alignment of SPHERE to the VLT focus.
CPI also includes half-wave plates for polarization switching/modulation.
The adaptive optics module is called SAXO. It is designed to correct for the turbulence perturbation at high frequency (1.2 kHz).
The coronagraphs are set-up by a mask in the focal plane, a Lyot stop in the downstream pupil,

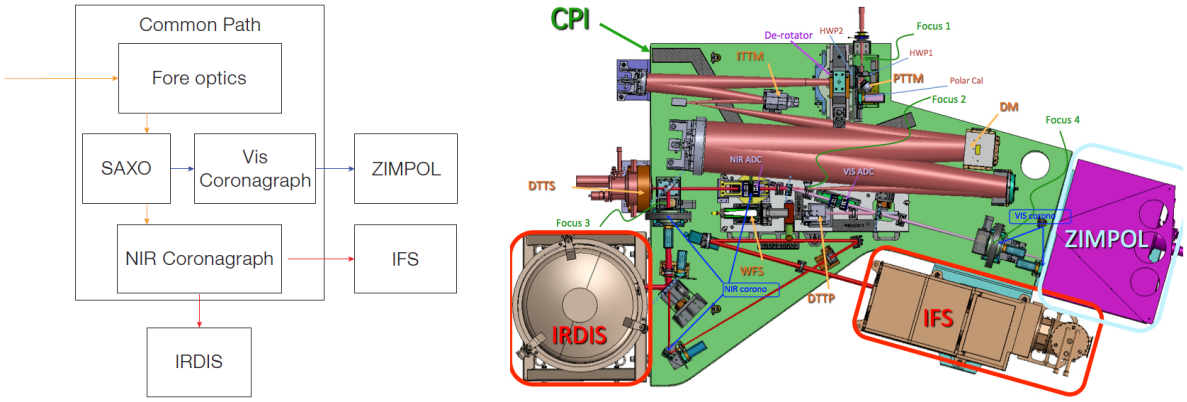

Figure 16: Left: Global concept of the SPHERE instrument, indicating its four sub-systems: Common Path Optics,IRDIS, IFS, and ZIMPOL. Get from [28]. Right: layout of the SPHERE Common Path Infrastructure.

and an apodizer in the upstream pupil (before the focal mask). The wheels for the coronagraphs include also field stops.
ZIMPOL is a diffraction limited imaging polarimeter with a very small field of view centered on a bright target. Because ZIMPOL is a Nasmyth instrument, it provides only a limited absolute polarimetric accuracy (0.5%). The reason is that Nasmyth mirror is responsible for strong po-

larization of the incoming light in the envisaged spectral range. In addition it rotates with time and changes therefore the induced polarization orientation [77].

The basic observing strategy for ZIMPOL is a relative polarization measurement of the im-

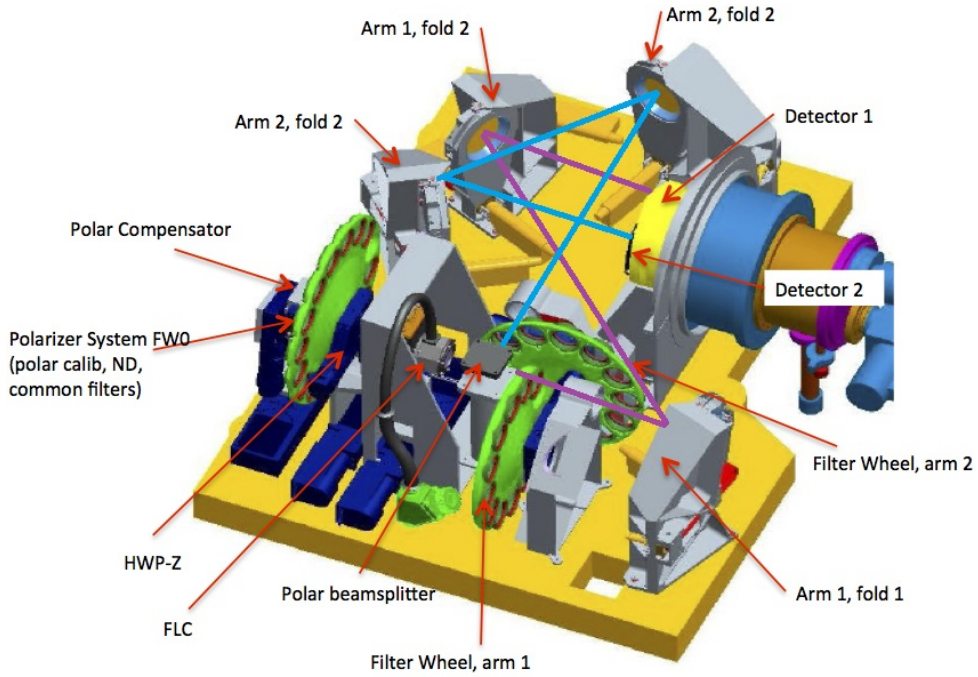

Figure 17: Optical scheme of ZIMPOL polarimeter. Arm 1 optical path is purple, arm 2 optical path is light blue.

mediate surroundings of a central star, which is used as a (zero)-polarization reference for the correction of the instrument polarization.

Fig. 17 reports the optical scheme of ZIMPOL. A single arm of ZIMPOL provides a full polarimetric measurement. Because a polarizing beamsplitter is used for the polarization analysis, half of the light goes to the other arm which can perform polarimetry for the same or another filter.

ZIMPOL measures the linear polarization based on a fast modulation – demodulation principle using a charge-shifting technique on a masked CCD for separating the photons with opposite polarization direction.

For the polarimeters that use a fast modulation frequency ($>$ 1kHz) the standard CCD detectors common used in astronomy are not suitable (their frame rate it is not sufficient). For this reason, special CCD detector was developed for polarimeter ZIMPOL (it was developed for solar polarimetry, but then it was upgraded for stellar polarimetry) [60]. The CCD detector has a row optical free (with deposition of micro-lenses) alternate to a row obscured to light (with a deposition of optical depth material). The obscured rows are used to storage the charge during the acquisition. The charge is shifted many times in obscured pixel during the exposure time synchronously with the polarizing optical modulator in front of the system (see fig. 18). In the astronomy, the micro-lens on the detectors are often deprecated, as they absorb light, and they could be not homogeneous. Contrary in photographic consumer cameras the micro-lenses are largely used. In the case of ZIMPOL, the micro-lenses permit to minimize the area lost on the detector due to obscured pixels.

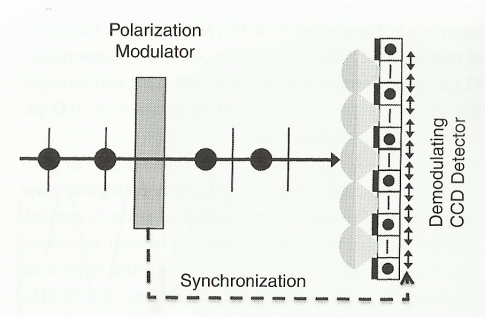

Figure 18: Simplified scheme of the CCD detector of ZIMPOL polarimeter. The charge is shifted synchronously with the polarization modulator. Image get from [60].

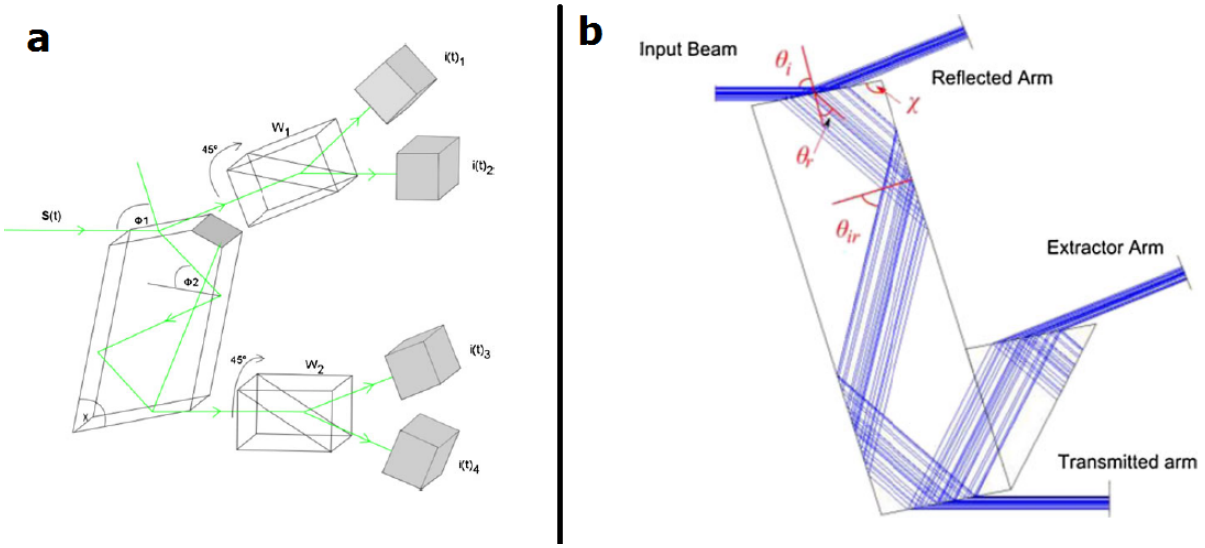

Figure 19: Polarization optics of GASP polarimeter. (a) Principle of a visible "Division of Amplitude"dielectric prism. (b) Layout of the retarding beam splitter and the extractor prism used in GASP showing the input, reflected, transmitted and extracted beams

2.2.4 GASP - The Galway astronomical Stokes polarimeter

The GASP polarimeter works by splitting the beam into two components, and then using a suitably oriented polarizing beam splitter in each of the two beams, dividing them again into two orthogonal linearly polarized beams (4 beams in all, see fig. 19, a) [66].
The design of GASP is based on a Division Of Amplitude Polarimeters (DOPA) concept using partial reflection from the uncoated end surfaces of a rhomb-type prism, similar to a Fresnel rhomb. Two internal reflections within the rhomb introduce a relative phase delay between the p and s waves of the transmitted light, which is dependent upon the refractive index of the glass and the angle of total internal reflection.
The collimated beam of incoming light is separated into two beams: reflected, and transmitted. They are each subsequently divided into two by two polarising prisms (Wollaston prisms) (see fig. 19, b). The Stokes vector can then be determined from the intensities of 4 final transmitted and reflected beams.

GASP potential targets are faint, consequently it is required to operate as efficiently as pos-

sible – precluding therefore the use of filters - and over a wide wavelength range (400–800 nm is a practical limit, set by detector spectral response).
Various optical designs of GASP have been explored, in which the four beams have been detected in various ways. These include a single imaging detector design, a double imaging detector design, and a multiple non-imaging detector design (using an array of photon counting avalanche photodiodes). These different solutions are appropriate to different astronomical targets, because whilst the imaging solutions offer high efficiency and the ability to perform polarimetry on point or extended sources in complex field regions, under varying atmospheric seeing conditions, they have limited time resolution. For the highest time resolution photon counting detectors are required.
Photon counts from counters are individually time-tagged to GPS time with a resolution of 250 ns. This enables GASP to investigate polarisation variations in the microsecond time regime, and to synchronize observations with those from other instruments or observatories, such as radio or other optical telescopes.
GASP was used on the 1.2 m Cassini Telescope at Loiano Observatory to observe the highly polarized source CRL2668 (Proto-planetary neabula, mag V = 12.7). The brightest (centre) source has linear polarization $\sim 50\%$ and circular polarization $\sim -0.6\%$.
The measured degrees of polarization were: linear polarization 51.0 % ($\pm 0.04\%$ statistical precision), and circular polarisation -0.1 % ($\pm 0.05\%$ statistical precision) [66].
The absolute values of the degrees of polarisation cannot be determined, but temporal variations of the order of the statistical precision could be determined.
The components of the Stokes vector can be measured to $< 1\%$ in conditions of poor atmospheric stability [66].

2.2.5 TURPOL

The principal characteristic of Turku UBVRI Photopolarimeter (TURPOL) is to use the same detector to acquire the two orthogonal polarization states [48]. An essential part of this polarimeter is a single plane parallel calcite prism. The scheme of the instrument is shown in fig. 20 got from [48].

The calcite prism divides the light into two parallel components, labeled ordinary and extraordinary. The state of polarization of the extraordinary component is orthogonal to the ordinary component. The distance between the two components depends on the thickness of the prism. After the prism, the two components pass through a chopper that alternates the real component passing toward the detector. The chopper has two IR emitters and two photodiodes to generate the synchronization signal for the acquisition board.
After the chopper, there is a focal plane diaphragms and a field lens that refocus the light onto the detector. An important feature of this lens is that the two polarization components are focused on the same point of the detector. The detector is a photomultiplier, and the sensitivity of this detector varies greatly in its different points. The transmission coefficient is different for ordinary and extraordinary beam light, so the intensity is slightly different. These differences could be eliminated rotating the whole instrument around the optical axis. In fact, rotating the

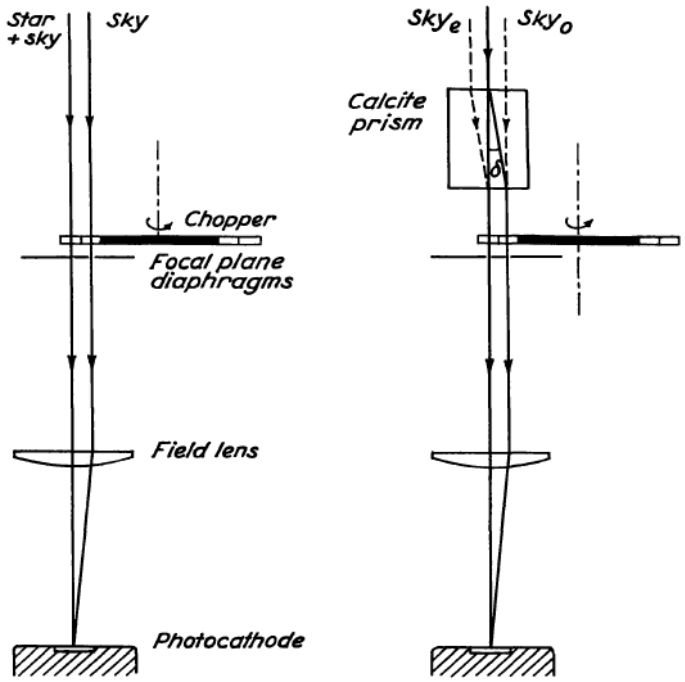

Figure 20: "Principle of operation of the polarimeter" from [48]. On the right without calcite prism the polarimeter can be transformed in a chopping photometer.

polarimeter by 90° the ordinary component became the extraordinary and vice versa. So, in data reduction the systematics are canceled.
Precise quartz oscillator generates the signal to synchronize the photomultiplier's counters. The photodiode signal is used only as a start to avoid errors due to mechanical imperfections of the slots of the chopper. The length of the period is calculated slightly shorter than optical free windows to avoid edge effects.
A great advantage to using a calcite prism is that it eliminates the sky background polarization. In fact the extraordinary component of sky polarization sum to the ordinary components of the signal (the signal is star plus sky background) and sky polarization ordinary component is added to the extraordinary component of the signal (see fig. 20 for the sketch by authors). In formulas it is:

$$beam_{ordinary} = signal_{ordinary} + sky_{extraord} = star_{ordinary} + sky_{ordinary} + sky_{extraord} \quad (12)$$

$$beam_{extraord} = signal_{extrord} + sky_{ordinary} = star_{extraord} + sky_{extraord} + sky_{ordinary} \quad (13)$$

So the sky adds the same quantity to each polarization components. Subtracting the components, the sky background is automatically removed.
Another advantage of the Turpol polarimeter is that there aren't optical polarizing components rotating respect to the detector. For photomultiplier, this is important as the beam hits every time in the same point of the photocathode. The modulation does not depend on wavelength, and the losses are reduced to minimum as the number of optical components are few.
Some drawbacks are that the refraction of the extraordinary beam introduces some astigmatisms, and it is wavelength dependent (chromatic aberration). The focus of the ordinary and

extraordinary beam is slightly different, but for a telescope with focal ratio of f/15 or greater there aren't problems (the difference in the diameter of least confusion of the spots are very smaller than diaphragms used by the author of [48]).
To measure the sky extended objects the diaphragm must be adjusted by some Polaroid to eliminate the background, so this type of polarimeter is not suitable for observation of extended objects.
The polarimeter was tested with 72 observations of stars with zero polarization. The measurements were analyzed to determine the instrumental polarization and to check the stability of the instrument. The results are $P_x = -0.00004 \pm 0.00005$ and $P_y = 0.00006 \pm 0.00004$. If the stars are not polarized this result introduces a $\Delta P = 0.017\%$ in the linear degree of polarization. A contribute to this error is due to scintillation at frequency greater than 25 Hz (the modulation period for test observations) [48].

2.3 Polarimetry data reduction

A general method for analyzing data of linear polarization is presented in this paragraph.
As described by [53] the next method can be used for data reduction to analyze linear polarimetry information. Note that for this analysis the polarization is linear so the eventually circular polarization is indistinguishable from the unpolarized light.
The polarization of a source can be represented by a vector oriented in the direction of oscillation of the electric field. The vector forms an angle ϕ respect to an arbitrary reference direction R in the plane orthogonal to the direction of light propagation.
To rotate the polarization vector, it is possible to place a "half wave plate" in front of polarimeter rotating the plate or rotating the whole polarimeter (or the polarization optical element as the Wollaston prism).

In agreement with [53] the direction of the polarization vector is η from "R"(see fig. 21).

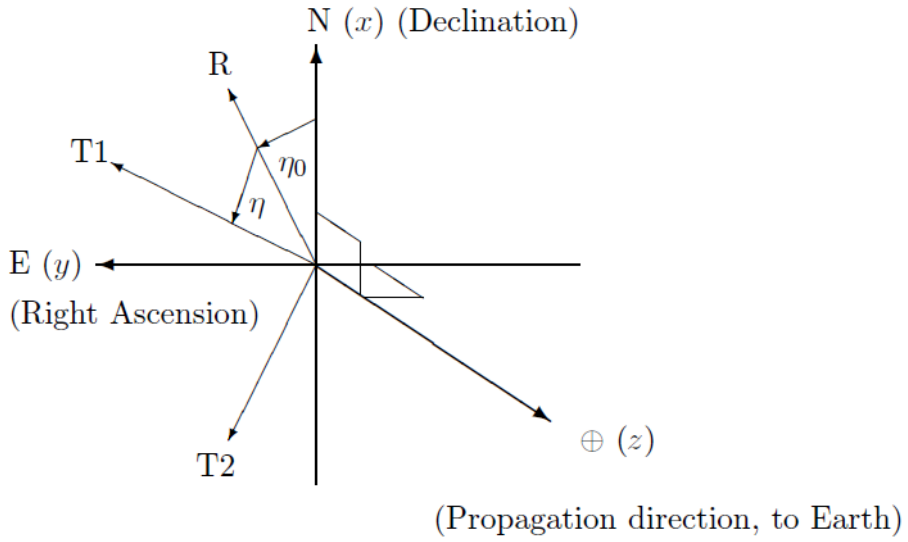

Figure 21: Scheme of polarization components and angles, image taken from [53].

"T1" and "T2" are two orthogonal reference system of the instrument. If the instrument has two-channels, like Turpol polarimeter (described in 3.2.5), T1 and T2 are the two channel of acquisition. In the thesis's polarimeter, T2 is the channel reflected by the Brewster window and polarizing beamsplitter. T1 is the channel transmitted by the beamsplitter (see chapter 5 for optical instrument detailed description).
$n_1(\theta)$ is the intensity measured in channel 1 at T1 axis, $n_2(\theta)$ is the intensity of the channel 2 at T2 axis.

$$\begin{aligned} n_1(\eta) &= \tfrac{1}{2} \cdot I_U + I_p \cdot \cos^2(\phi - \eta) \\ n_2(\eta) &= \tfrac{1}{2} \cdot I_U + I_p \cdot \sin^2(\phi - \eta) \end{aligned} \tag{14}$$

Where "ϕ" is the direction of polarization vector. Total intensity at an angle η is:

$$I(\eta) = n_1(\eta) + n_2(\eta) = I_U + I_p \tag{15}$$

The degree of linear polarization is defined by:

$$P = \frac{I_p}{I} = \frac{I_P}{I_P + I_U} \tag{16}$$

In [53] it is underlined that the degree of polarization is a biased indicator as it is a definite-positive quantity. So a source with no polarization has $P = 0$, and its fluctuations could be only positive. For a non-polarized source, the direction of the polarization vector ϕ is also not defined.

The polarimetric measurement consists in the estimation of photons counts of $n_1(\eta)$ and $n_2(\eta)$. The estimation of intensity of $n_1(\eta)$ and $n_2(\eta)$ could be performed by aperture photometry. Aperture photometry is a technique that use 3 concentric circles (see fig. 22) . The inner circle must be centered on the centroid of the PSF of the star. All the pixel in the circle with the radius r_1 are used to estimate the intensity of the star. The annulus of thickness "B"is used to estimate the mean sky background. The gap between the inner circle and the annulus assure that the stars's PSF doesn't reach the bakground estimation region. This technique can not be used for stars that have one or more nearby stars that interfere with aperture circles.

The sources of sky noise could be three: photon shot noise; pixel-to-pixel variations in the sky valued superimposed on the target object and imperfect estimation of the modal sky background.

The photons are recorded in the detector according to the Poisson distribution. The shot noise

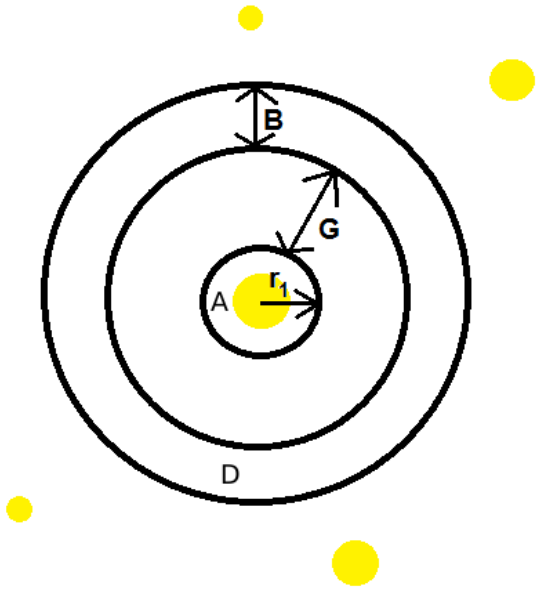

Figure 22: Sketch of the aperture photometry. The yellow circles are the star spots. r_1 is the inner radius called "aperture radius"; "A" is its area expressed in pixels. "G" is the gap width between the circle of star counts and the sky background annulus. "B" is the thickness of the sky background annulus; "D" is its area expressed in pixels.

is the square root of the number of photons. The shot noise is:

$$\sigma_{SN} = \sqrt{n \cdot \tau} \tag{17}$$

Where τ is the integration time for a given angle and "n" the measured flux of carriers on the detector expressed in counts per time unit.
The modal value "n_{sky}"of sky background could be estimated integrating the pixel values in an annulus with an area of "D" pixels. The root-mean-square deviation of these pixels in the annulus is σ_{sky}. The Sky background on an aperture photometry of area "A" in pixels is $A \cdot n_{sky}$, its error is [53]:

$$\sigma_{skysub} = \frac{A \cdot \sigma_{sky}}{\sqrt{D}} \tag{18}$$

The fluctuation of the sky on each pixel produce a sum in quadrature of the σ_{sky} with a total contribution of:

$$\sigma_{skyfluc} = \sqrt{A} \cdot \sigma_{sky} \tag{19}$$

The total error due to the sky and shot noise on $n_i(\eta)$ is the sum in quadrature of these three errors:

$$\sigma_n = \sqrt{\sigma_{SN}^2 + \sigma_{skysub}^2 + \sigma_{skyfluc}^2} \tag{20}$$

In practice, for long time exposures, the shot noise is much smaller than sky noise [53].

2.4 Why the exoplanet should be polarized?

The exoplanet with orbital plane orthogonal to the line of sight does not produce a modulation in photometric intensity, as the amount of planet scatter light is always the same during the whole orbital phase (see fig. 23, a). Also, the degree of polarization is constant as the surface exposed to the star's light has the same area at the same surface scattering angle. In a non-uniform superficial exoplanet the degree of polarization could be modulated by the surface characteristics. Also, the weather on the exoplanet could change the degree of polarization. Instead in uniform exoplanet case the polarization vector direction is modulated with orbital phase as the scattering plane rotates in function of the orbital period of the exoplanet.

The exoplanet, with the orbital plane with a small angle with the line of sight, produces a

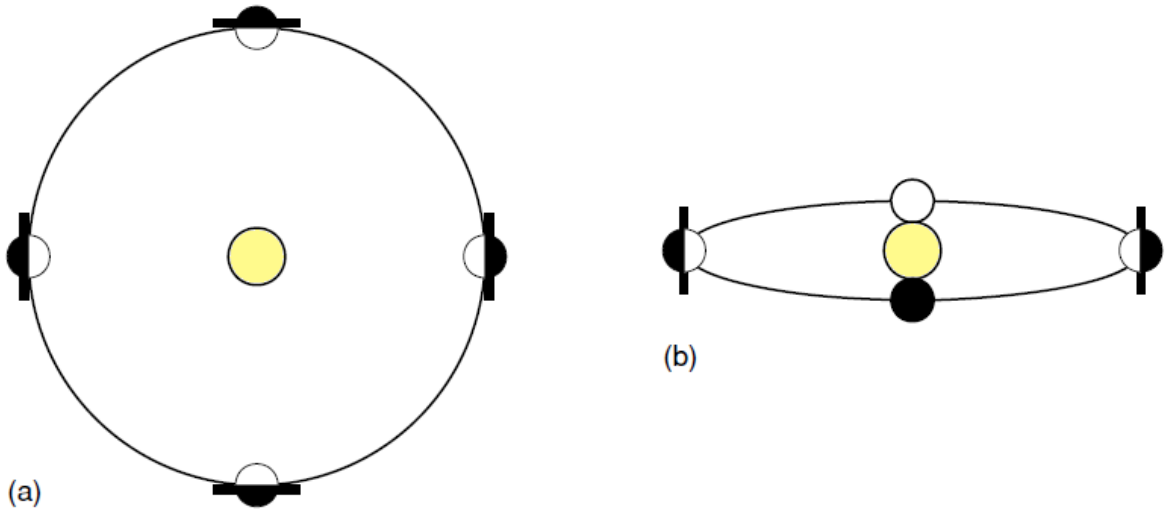

Figure 23: Schematic orbital modulation of polarization for an exoplanet by [49]. (a) The orbital plane of exoplanet is perpendicular to line of sight. (b) An exoplanet with a small angle between its orbital plane and the line of sight. The light portion of the exoplanet reflects light toward the observer. The black line is the orientation of polarization vector.

modulation either in photometry then in polarimetry (see fig. 23, b). The photometric intensity is modulated with orbital phase, as it is maximum at the opposition of the planet, and it is null in conjunction (if the planet transits the star during transit and occultation the intensity is also different). The polarization of the reflected light is maximum when the planet is in quadrature, as the scattering angle is 90°. The geometric polarization is null when the planet is aligned with the star. Note that the maximums of the photometric intensity and the degree of polarization are shifted in orbital phase of 90°.

In the alignment, there could be a polarization of the light for scattering in the atmosphere of the exoplanet.

The measure of the possible modulation in the orientation of the polarization vector could be used to estimate the orbital inclination. In fact for small orbital inclinations the scattering plane has a significance variation, else with high orbital inclination it has not big variations. For

example, for orbital inclination of 90° the vector rotates of 360° in function of the orbital phase. The presence of an atmosphere, its composition, the presence of clouds could change the polarization and the measure of exoplanet's polarization could be a constraint to characterize the exoplanets.

2.5 Numerical simulations of polarizations of exoplanets

Many numerical simulations on polarization of the light scattered by exoplanets are performed by D. M. Stam [43] and [44], both for giant gaseous exoplanets and for Earth-like exoplanets. The polarimetry could help to facilitate the detection of some particular exoplanets with a small mass and without the transit the star [43]. This is due as the star light integrated over the stellar disc could be considered unpolarized, while light reflected by the exoplanet will be generally polarized.
The most important feature of the polarimetry is the characterization of the planet as the degree of polarization strongly depends on the composition and on the structure of planetary atmosphere. These characteristics are measured in Solar System planets, for example in Venus's atmosphere.
Stam simulates the polarization signal from Jupiter-like exoplanet at a distance of some astronomical units from the parent star (like Jupiter in Solar System).
The Flux reflected by the exoplanet and its polarization depends on the wavelength and phase angle α. The phase angle has the vertex on the exoplanet and is placed between the Star and the Earth (or the observatory, but for a ground telescope or a space-based telescope this angle is the same as the stars are very distance from us). The Flux can be described with the Stokes vector:

$$\mathbf{F}(\lambda, \alpha) = [F(\lambda, \alpha), Q(\lambda, \alpha), U(\lambda, \alpha), V(\lambda, \alpha)] \tag{21}$$

"F" describes the total flux, "Q" and "U" describe the linearly polarized flux and "V" the circularly polarized flux. "Q" and "U" are defined respect to a plane, in fact:

$$\begin{aligned} Q &= F_{0^\circ} - F_{90^\circ} \\ U &= F_{45^\circ} - F_{135^\circ} \end{aligned} \tag{22}$$

These angles are defined in the plane orthogonal to the direction of the wave propagation. The "0" is arbitrary. Stam refers "Q" and "U" to the planetary scattering plane (the plane with star, exoplanet and observer). To rotate clockwise the "0" orientation of "Q" and "U" plane of an angle β following rotation matrix must be applied at the Stoke vector:

$$R(\beta) = \begin{bmatrix} 1 & 0 & 0 & 0 \\ 0 & \cos(2\beta) & \sin(2\beta) & 0 \\ 0 & -\sin(2\beta) & \cos(2\beta) & 0 \\ 0 & 0 & 0 & 1 \end{bmatrix} \tag{23}$$

The most general definition of the degree of polarization is:

$$P(\lambda, \alpha) = \frac{\sqrt{Q^2(\lambda, \alpha) + U^2(\lambda, \alpha) + V^2(\lambda, \alpha)}}{F(\lambda, \alpha)} \tag{24}$$

Stam in [43] and [44] uses the next equation to calculate the degree of polarization as she assumes the planet mirror-symmetric respect reference plane and so the integration of U and V is null. The minus sign is manually added to consider the direction of polarization vector ($P < 0$: light polarized parallel to the scattering plane, $P > 0$: perpendicular to scattering plane).

$$P(\lambda, \alpha) = -\frac{Q(\lambda, \alpha)}{F(\lambda, \alpha)} \tag{25}$$

An important parameter to characterize the exoplanet is the Bond albedo A_B. The Bond albedo is the fraction of the irradiance of the incident starlight that is reflected by the planet in all directions. This is important because the energy absorbed by the planet is proportional at $(1 - A_B)$. Practically it is possible to measure the geometric albedo, the amount of light scattered to the observer and it can be computed by the measurements of the reflect light in planet opposition. Notice that in this configuration phase, the degree of polarization is null and the light is reflect by Lambertian surface, so it reflects light isotropically and totally depolarized. From geometric albedo it is possible to compute the Bond albedo, but other parameters as planet radius, stellar flux, planet semi-axis and stellar radius must be known.
The planet emits also a thermal radiation due to the planet's temperature. The degree of polarization of the reflected plus the thermal planetary radiation equals [43]

$$P(\lambda, \alpha) = -\frac{Q_{ref}(\lambda, \alpha)}{F_{ref}(\lambda, \alpha) + F_{th}(\lambda, \alpha)} \tag{26}$$

$Q_{ref}(\lambda, \alpha)$ is the Stokes Q reflected flux by exoplanet, $F_{ref}(\lambda, \alpha)$ is the total Star flux reflected by exoplanet and $F_{th}(\lambda, \alpha)$ is the thermal planetary radiation.
The temperature changes the amount of thermal emitted radiation, and this change the total flux and so the degree of polarization (in equation 26 F_{th} decreases at the denominator).
At the shortest wavelengths, the planetary spectrum is dominated by reflected stellar radiation, and at the longest wavelengths by the planet's thermal radiation. For very hot planets the thermally emitted radiation will limit the use of polarimetry to visible wavelengths. Jupiter-like planets cool down relatively rapidly. The wavelength region available for polarimetry thus increases relatively rapidly towards the infrared [43].
Stam in [43] ignores the thermally emitted planetary radiation as it is negligible at optical wavelength. The atmosphere is modeled as divided in many shells locally plane parallel homogeneous layers that contain gaseous molecules and optionally aerosol particles, absorbing between 0.4µm and 1.0µm of wavelength.
Stam uses 38 layers with a Jupiter-like temperature and pressure profiles, composed mainly of methane (CH_4).
Three models are simulated in [43]: in the first model the atmosphere is clear: the layers contain only the gaseous molecules. In the second model a tropospheric cloud layer was added. In model 3 also a haze layer was added. The clouds are simulated by spherical particles with mean radius of 1.0µm and variance of 0.1µm distributed in size according to the standard distribution described by J. Hansen and L. Travis in [65]. In fig 24 some result of numerical simulations by Stam are reported. The flux is normalized by stellar incident flux on exoplanet. The degree of polarization is independent from semi-mayor axis of planet, star radius, planet radius as it

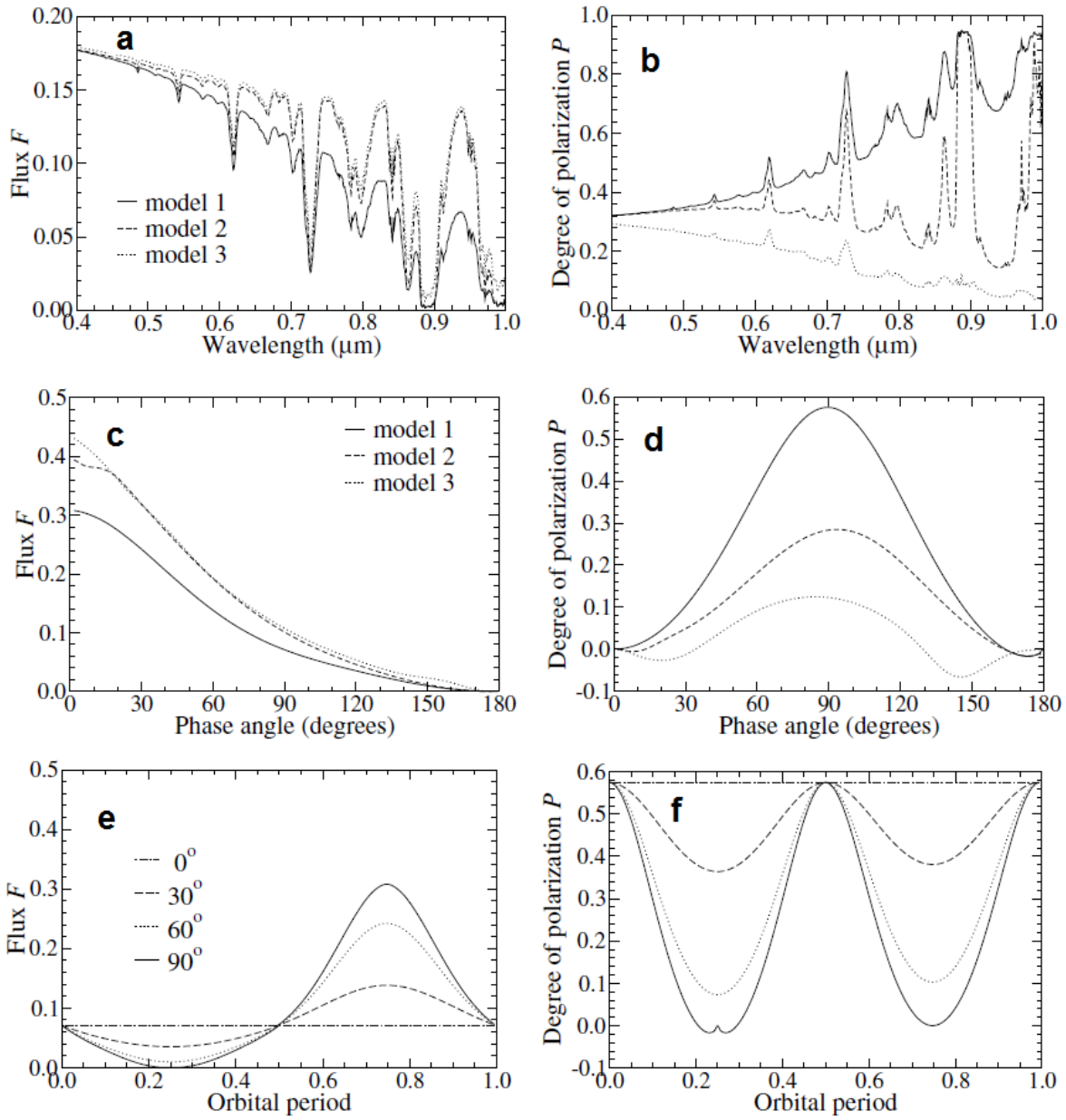

Figure 24: Numerical simulation of a Jupiter like exoplanet. Solid lines represent "model 1" with only molecules, dashed lines represent "model 2" with also the cloud layer and dotted lines represent "model 3" like model 2 with adding a haze layer. In graph "a" e "b" the Flux and degree of polarization in function of the wavelength are reported. The phase angle is fixed at 90°. In "c" e "d" the same quantities in function of phase angle of the exoplanet along the orbit are reported. Graphs "e" and "f" report the simulation performed for 4 different orbital inclinations for "model 1" atmosphere. For graphs "c", "d", "e" and "f" the light intensity is integrated in wavelength between 650nm and 950nm. Graphs get from [43].

is a relative measure. Note that in a real measure, if the measured flux is the sum of the flux reflected by the exoplanet plus the star flux, the degree of polarization strongly depend on semi-mayor axis of planet, star radius and planet radius. Otherwise if in the measurement the star is occluded (chronograph configuration), the previous affirmation is correct. In graph "a" of fig. 24 the continuum of the flux decreases with the wavelength, as the molecular scatter decreases with the wavelength.The continuum of the degree of polarization of the model 1 (graph "b" in fig. 24, solid line) increases with wavelength, because the smaller molecular optical thickness implies less multiple scattering within the atmosphere, and multiple scattering tends to lower the degree of polarization of the reflected light. The absorption lines are due to CH_4, the most evident line is the absorption at 0.89μm. The degree of polarization is predicted to be very high ($P = 95\%$) in this band (875nm $\sim$ 900nm), but experimentally there are two main problems. The first is that the flux is very low (about 7 times lower than continuum) so the flux of the received photons is very low and to accumulate a statistically sufficient number of photons must be integrated over a long time. If the flux from exoplanet is received in sum of stellar flux it is very arduous to distinguish the flux in this band coming from the exoplanet: the reflected flux is about 1 % of incident stellar flux incident on the planet that is in the best case 10^{-3} of the stellar flux, so the flux scattered by planet in this band is (in the best case) about 10^{-5} of the stellar flux. The second difficulty is the narrow band required of about 20nm. The actual instruments have difficulties to detect polarimetric signal with some hundreds of nanometres of optical bandpass. It is not excluded that a second generation of polarimetry instruments for the exoplanets could achieve this ambitious target.

By numerical simulation, it is evident that the presence or not of a haze layer doesn't influence the reflected fluxes, but the polarization of light scattered change radically. This is due to the haze layer reflects back to the space the incoming radiation without polarizing.

In graphs "c" and "d" of fig. 24 are reported the phase modulation computed for a virtual bandpass filter between the wavelength of 650nm and 950nm, that is I-band of SPHERE at VLT [28].

The flux reflected by exoplanet is modulated by the phase angle, but it doesn't depend on atmosphere model (it depends weakly on albedo). Else the polarization profile depends heavily on atmosphere's model. This underlines the necessity of a polarization measurement to understand something about the atmosphere of the exoplanets. For small phase angles (and for angles near 180°), the degree of polarization is negative for scattering of cloud's particles. This is in agreement with the observation of solar system asteroids and gaseous planets that are observable only at small phase angle from Earth (about maximum 11° for Jupiter and 6° for Saturn).

The maximum degree of polarization that can be measured along the planetary orbit is independent of the orbital inclination angle (see graph "f" of fig. 24). Because this maximum value does depend on the planetary atmosphere (see graph "d" of fig. 24), polarimetry could thus provide information about the planetary atmosphere without knowledge on the inclination angle.

The simulation reflects the intuitive concept that modulation of the degree of polarization is the highest for orbital plane aligned with the line of sight and null for orbital plane orthogonal to the line of sight.

These simulations illustrate the importance of a polarimetry information to characterize the atmosphere of an exoplanet. First observation will be probably made by a wide bandpass filter

and will be sensible only to continuum.
Stam performs also numerical simulations on flux reflected and its degree of polarization by **Earth-like exoplanets** [44]. These type of exoplanets is the most difficult to detect and to characterize but it is the most interesting in the research of the life on other planets.
Stam in [44] creates a planet model with an atmosphere composed of homogeneous layers of gaseous molecules and optionally clouds. The planet's model includes a uniformly flat surface. For each layer of the atmosphere 4 parameters are computed: optical thickness of absorption and scattering of molecules and clouds, temperature and pressure. The gases that have the most important role in wavelength absorption between 0.3μm and 1.0μm are ozone (O_3), oxygen (O_2) and water (H_2O). Each layer is a mixture of these 3 gases. Stam takes in account the rapid variation in wavelength of absorption cross section of O_2 and H_2O in the studied wavelengths. Clouds are modeled in the same manner of the Hot Jupiter simulations and they are placed in the second layer of the atmosphere between 802hPa and 628hPa of atmosphere pressure. The amount of pressure at the beginning and at the end of the layers derives from a division of the atmosphere in 16 layers with pressure and temperature vertical profiles.
The planet's surface is modeled flat to simplify the model and it is composed only of two homogeneous surface types: ocean and vegetation. This is a significant simplification respect the Earth situation, as the surface is not flat and it has a myriad of different albedos depending on moistness and seasons. The vegetation is assumed to depolarize the whole incident light and reflects light isotropically. This is in agreement with the measurements performed with Earth artificial satellite equipped with POLDER instrument. The new POLDER instrument is designed to collect accurate observations of the polarized and directional solar radiation reflected by the Earth-atmosphere system [67]. POLDER estimates the degree of polarization of vegetation of about few percent [44]. In the model only the deciduous type of vegetation is considered (see fig. 25). It doesn't has many difference respect of grass and conifer vegetation. The albedo is higher in near infrared wavelength and the rapid increase is named "red edge". This characteristic of the Earth vegetation is not universally accepted as a universal feature and it could be different also for different spectral class of the star.

Ocean surface is assumed black for the all models. On Earth, there are some ocean regions

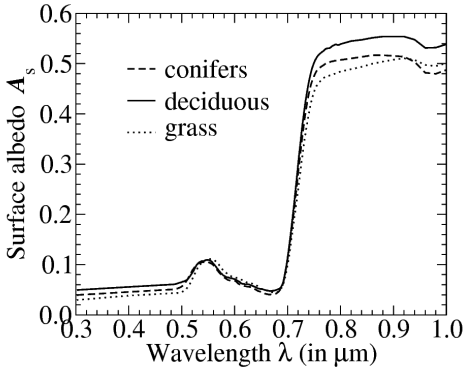

Figure 25: Graph of the surface albedo for different type of vegetation. Graph taken from [44].

colored by algae and small organisms, but they are negligible for a simplified model. The albedo is assumed to be "0", but Stam calculates the amount of reflected light by Fresnell equation,

assuming the refraction index of 1.34 for all the wavelength analyzed (0.3μm - 1.0μm). This light is also polarized. In the model, the ocean is flat without any waves.
In fig. 26 some graphs of the results of D.M. Stam's numerical simulations for Earth-like exoplanets are reported. The continuum of the flux (graph "a" and "c") and the degree of polarization (graph "b" and "d") are due to scattering in atmosphere by gaseous molecules and by surface (in function of the albedo). The absorption lines are due to gases in the atmosphere (O_3, O_2 and H_2O). The shape and the intensity of the absorption line are influenced by numerical wavelength resolution of 1nm. In graph "b" of fig. 26 the high degree of polarization at short wavelength (0.3μm), and at 0.95μm is due to the absorption lines of O_3 and H_2O, the absorption lines reduce the multiple scattering that depolarizes the light. In these bands the flux is also reduced. The increment of the degree of polarization in absorption lines has been measured in Solar System planets: Jupiter, Uranus and Neptune in the absorption lines of methane.
D.M. Stam affirms that the polarization is an excellent tool to analyze the exoplanet atmosphere as it is a relative measure and it isn't affected by Earth atmosphere and interstellar dust.
In fig. 26 "c" the dependence of the flux reflected by exoplanet in function of phase angle is reported. The amount of reflected flux largely depends on the variation in the illuminated and visible fraction of planetary disk with the phase angle. In graph "d" of fig. 26 the dependence of the degree of polarization by phase angle is reported. For a black surface planet (albedo = 0) the degree of polarization is totally symmetric respect to phase angle (maximum at $\alpha = 90°$). For a planet with a reflecting surface, the maximum degree of polarization occurs when the phase angle is greater than 90°. Remember that phase angle equals to 0 is for the planet's opposition and phase angle equals to 180° corresponds to planet placed in orbit between the star and the observer (for some planetary systems at this angle there is the transit). The shift in maximum of the degree of polarization is due to a decrease of scattering with a depolarizing surface for increasing phase angles.
In fig. 27 the results of numerical simulation for a more realistic model are plotted. The surface of the exoplanet is simulated totally covered by deciduous forests or specular reflective oceans. The results flux and degree of polarization are correctly comprise between albedo extreme cases: albedo = 0 (black surface) and albedo = 1 (white surface).
For each models are simulated a clear atmosphere (without cloud particles) and a cloudy atmosphere (with a cloud particles layer). The exoplanet cloudy has a very similar profiles of the degree of polarization with different surfaces (this is obviously as the cloud layer covers the surface). The cloud layer increases the reflected flux. The degree of polarization is lower respect a clear exoplanet as the cloud particles produce a multiple scattering with a depolarization effect. In a clear exoplanet the degree of polarization profile (graph "b" of fig. 27) is modulated by vegetation scattering and at shorter wavelengths by atmospheric gaseous molecules.
Stam affirms in [44] that the strength of the absorption bands in the flux and the degree of polarization depends on the altitude of the cloud layer as some molecules could be upward or downward this layer.
In graphs "d" and "f" of fig. 27 the dependence of the degree of polarization in function of the phase angle is reported. For a cloudy planet the degree of polarization is lower than in a clear exoplanet. At about $\alpha = 30°$ the polarization shows the effect namely "primary rainbow", which is due to light that has been reflected inside the droplets once [44]. The occurrence of a rain-

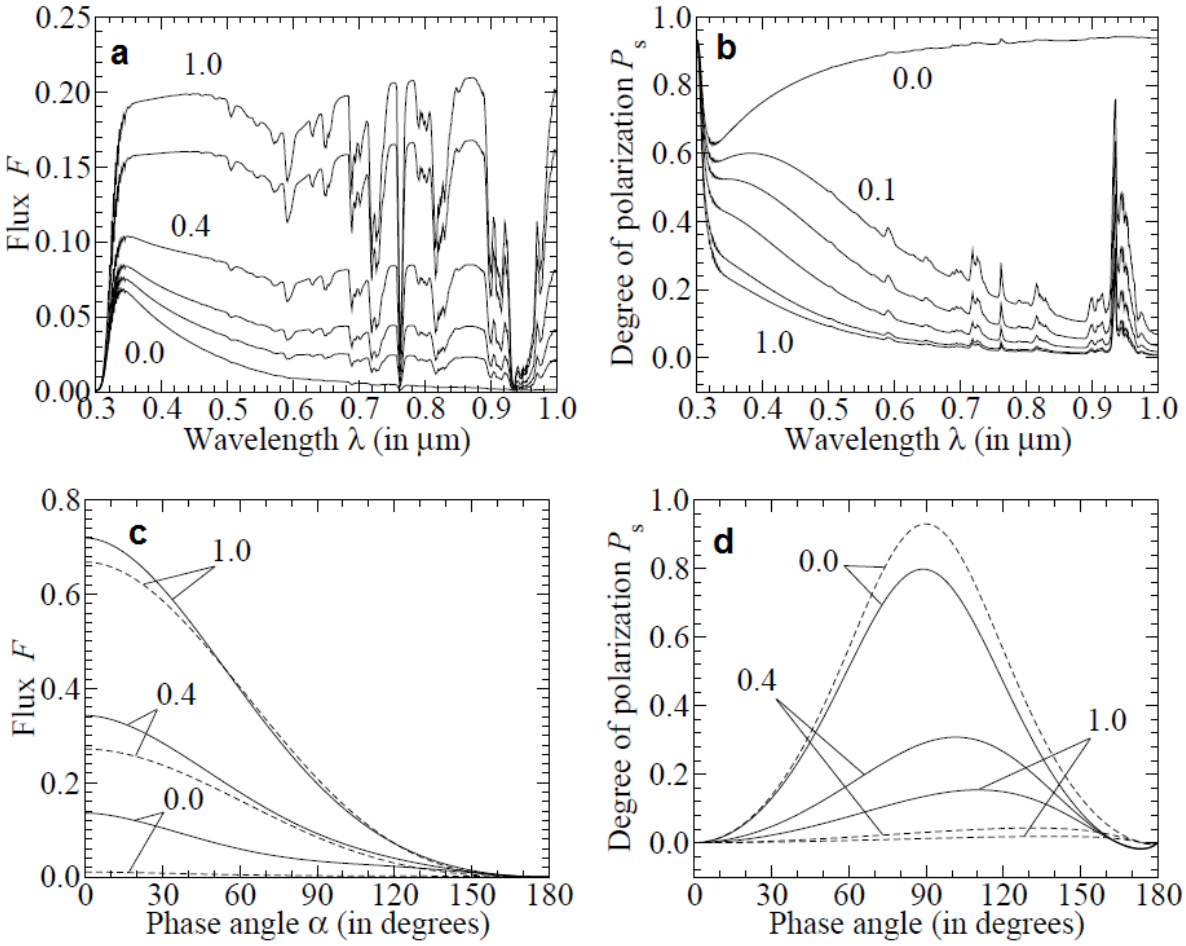

Figure 26: Result of simulation performed by D. M. Stam of Earth-like exoplanet. Graphs "a" and "b" are computed for 90° phase for different surface albedo from 0.0 to 1.0. Graphs "c" and "d" represented the flux and the degree of polarization in function of phase angle for 3 different albedos and for wavelength of 0.44μm (solid lines) and 0.87μm (dashed lines). Graphs taken from [44]

bow in reflected light is a strong and well-known indicator for spherically shaped atmospheric particles [65].

As the Earth has surface covered by lands and oceans, an observer looking at the Earth in a point on the Earth equator could measure variations in polarization during the day, as the polarization is modulated by ocean / land surface coverage. Stam simulated a very simplified planet composed of vertical stripes of lands supposing that is vertical homogeneous and like Earth equatorial distribution of water/lands at equator (represented in fig. 28)

The results of the simulation are reported in fig. 29. The simulation are performed for different phase angle ($\alpha = 50°$, $\alpha = 90°$ and $\alpha = 130°$). The maximum effect is expected at an observation phase of 130°, but in this situation the flux is minimum as the amount of visible surface exposed to starlight is little for this phase. Probably the best condition to perform this measure will be the quadrature phase ($\alpha = 90°$). This observation is very ambitions as it need the capability to measure the polarization integrating in only an hour for an exoplanet with an Earth-like rotational period. Also with this measure capability the weather on exoplanet could alter the polarization measure (the presence of clouds blinds the surface reflected light).

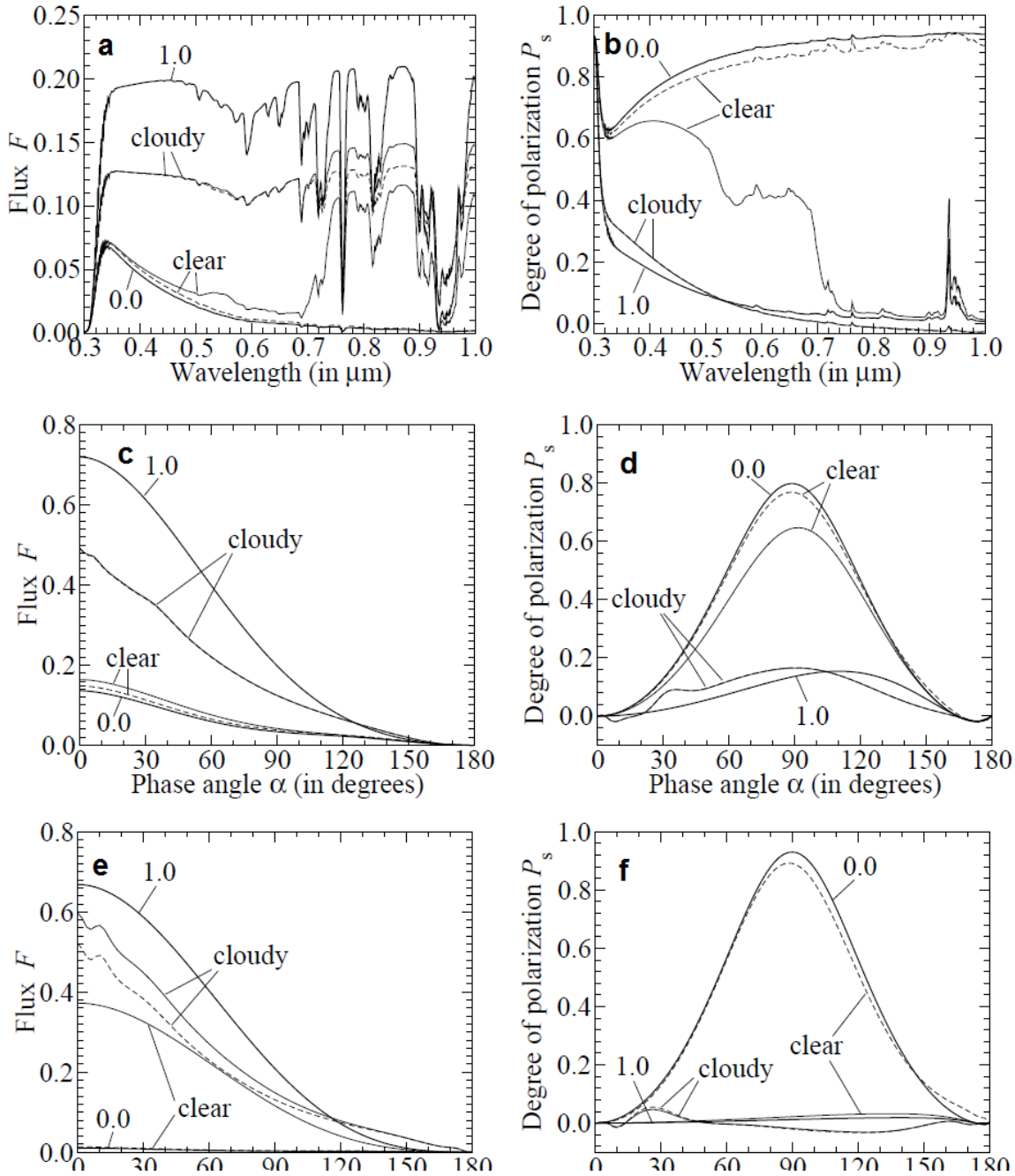

Figure 27: Graphs of the D.M. Stam simulation of an Earth-like exoplanet covered by deciduous forest (thin solid lines) or a specular reflective oceans (thin dashed lines). In graphs are included the white (albedo = 1) and black (albedo = 0) surface models. In graphs "a" and "b" are reported the flux and degree of polarization in function of the wavelength for a phase angle fixed at 90°. In graps "c", "d", "e", and "f" are reported the flux and degree of polarization in function of phase angle for the wavelength of $\lambda = 0.44\mu$m ("c" and "d") and $\lambda = 0.87\mu$m ("e" and "f"). Graphs taken from [44].

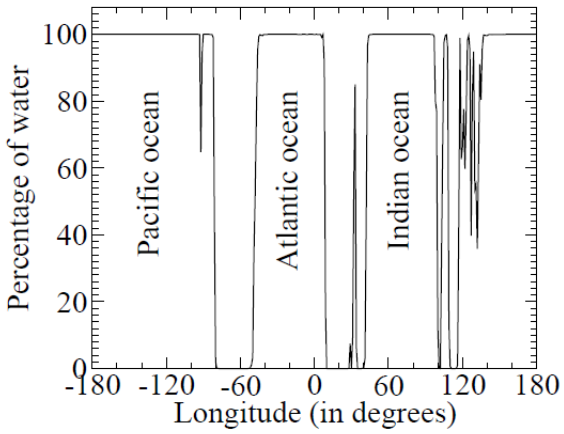

Figure 28: Graph of percentage of surface covered by water along the equator of Earth. Graph taken from [44].

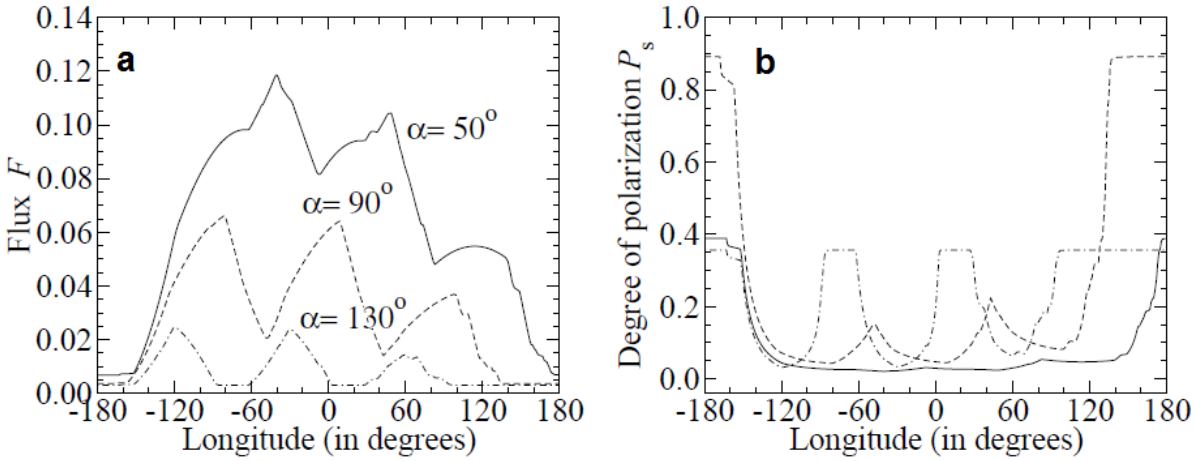

Figure 29: Graphs of the simulation of Earth-like exoplanet flux and degree of polarization modulated by longitude. Noticed that longitude regularly varies with the time for a fixed observer, in the Earth case the Period is 24 hours. The simulation is performed for the wavelength of $\lambda = 0.87\mu$m. In the paper is also reported the results for $\lambda = 0.44\mu$m, but they do not present particular signatures. Graphs taken from [44].

2.6 A measure of polarization of the exoplanet HD 189733b

A reliable measure of the polarization signal induced by an exoplanet has never yet been undertaken. However, some attempts have been made in the literature and there are some papers ([45], [46], [49], [50]) about the attempts to measure the polarization of some exoplanets including HD189733b presented here.

In 2011 Berdyugina et al. [46] published an observation and a detection of a polarimetry signal in the radiation of the star HD 189733 modulated with an orbital period of its exoplanet HD 189733b (nowadays is the only known planet orbiting around HD 189733) of slightly more than two days. The mass of the planet is about Jupiter's mass ($1.138 M_J$), the star is K1-K2 spectral type, 7.67 Visual apparent magnitude, mass of $(0.8 \pm 0.4) M_\odot$, radius of $(0.805 \pm 0.016) R_\odot$ and effective temperature of (4875 ± 43)K [2].
The authors observed in the Johnson B band ($370\text{nm} - 550\text{nm}$) the star HD 189733 in 100 night, so with a high number of measurements (this number must be compared to the Period of revolution of exoplanet). They measured a max peak of the degree of polarization of $2 \cdot 10^{-4} = 0.02\%$ modulated with the exoplanet's orbital period.
The measure was acquired by the polarimeter Turpol (described in the section 3.2.5), mounted at the Cassegrain focus at the Nordic Optical Telescope (primary mirror diameter of 2.5m) .
To determine the instrumental polarization authors observed 26 nearby stars with a visual magnitude of 4^m - 6^m, distance minor of 50 pc, of spectral classes A-G and without expected polarization. They considered the rotation of the telescope respect to the sky due to the alt-azimuth mount of the telescope. Some of these stars are observed multiple times on the same night to control the stability of the instrument. Also, they observe also three high polarized stars: HD 132052, HD 161056 and HD 204827. Notice that high polarized star corresponds to a degree of polarization of few percent. HD 161056 has a polarization of $(4.08 \pm 0.07)\%$ and HD 204827 has $(5.70 \pm 0.03)\%$ [47].
Table 6 reports the instrumental polarization in the photometric bands U, B, V measured by Berdyugina et al. in [46] in the two periods that they observed the exoplanet HD 189733b (April 2008 and August 2008).

Authors underlines that the instrumental polarization estimated independently after four

photometric band	April 2008	August 2008
U	$(23.1 \pm 2.7) \cdot 10^{-5}$	$(24.2 \pm 1.4) \cdot 10^{-5}$
B	$(13.4 \pm 1.6) \cdot 10^{-5}$	$(13.8 \pm 1.1) \cdot 10^{-5}$
V	$(11.8 \pm 2.5) \cdot 10^{-5}$	$(11.9 \pm 1.3) \cdot 10^{-5}$

Table 6: Instrumental degree of polarization of Turpol during the observation of exoplanet HD 189733b.

months are compatible with previous estimates, so the instrument has a good stability and the selected controls stars are an excellent standard set. In the August are reported Sahara dust particles in the atmosphere, but the Turpol polarimeter use a technique that is insensible to the

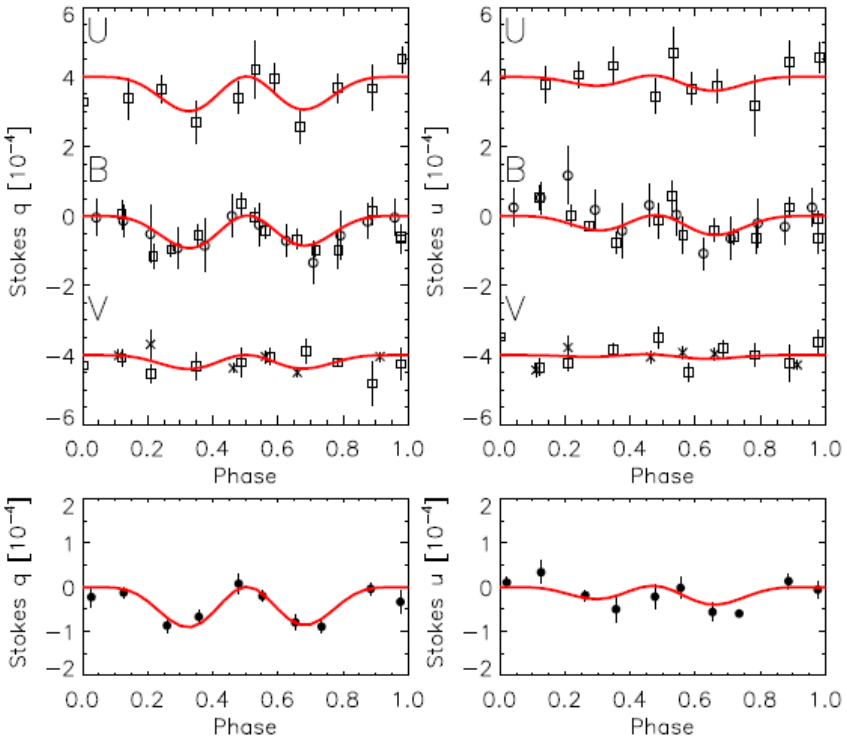

Figure 30: The measurements of the polarization of the star HD 189733 with at least an hot-Jupiter exoplanet. In uppers graphs are reported more datasets: new measurements by authors of [46] are represented by a square. Open circles are previous measurements of the same authors and crosses represent the measurements of Wiktorowicz [49]. Curves are the best fit of the authors of [46]. Measurements and graphs taken from Fig. 1 of [46].

sky background contamination.

They collected 35 measurements simultaneously in "U", "B" and "V" photometric bands, and they found a residual polarization after they subtract the instrumental contribute. They attribute this polarization to scattering in the exoplanet's atmosphere. The position of the polarization peaks near the elongation favors this hypothesis (see fig. 30). Authors exclude the possibility that the polarization is due to starspots, as they estimate these effect at a level of $\sim 5 \cdot 10^{-7}$. Another origin of the polarization could be a tidal effect on the star due to the planet (note that the exoplanet is very close to the star). They evaluate a possible ellipticity of the star of about 10^{-6} with a contribute to the polarization of 10^{-9} totally negligible.

The λ^{-4} law fits well the BVRI polarization amplitudes. Thus, it appears that most optical photons ($\lambda > 400$nm) are scattered only once in the atmosphere of HD189733b, because in such a case the polarization amplitude is proportional to the scattering cross section [46]. At the shorter wavelength the measure is lower than expected by Rayleigh scattering, this could be due to a Raman effect or to a molecule that absorbs the red light like methane. Raman effect has observed in the atmosphere of Neptune in Solar System. Interestingly, even though the effective temperature of the Solar system planets are cooler than this planet, [46] find that $p(\lambda)$ for Neptune is quite similar to HD189733b.

planet	
mass	$(1.138 \pm 0.025) M_J$
Semi-major axis	(0.03142 ± 0.00052) AU
Orbital period	$(2.21857312 \pm 7.6 \cdot 10^{-07})$ day
Radius	$(1.138 \pm 0.077) R_J$
Inclination of orbit	(85.51 ± 0.05) deg

star	
Distance	(19.3 ± 0.2) pc
Spectral type	K1 - K2
Mass	$(0.8 \pm 0.4) M_\odot$
Effective temperature	(4875 ± 43) K
Radius	$(0.805 \pm 0.016) R_\odot$

Table 7: Principal characteristics of the exoplanet HD 189733b and its star. Data taken from [2].

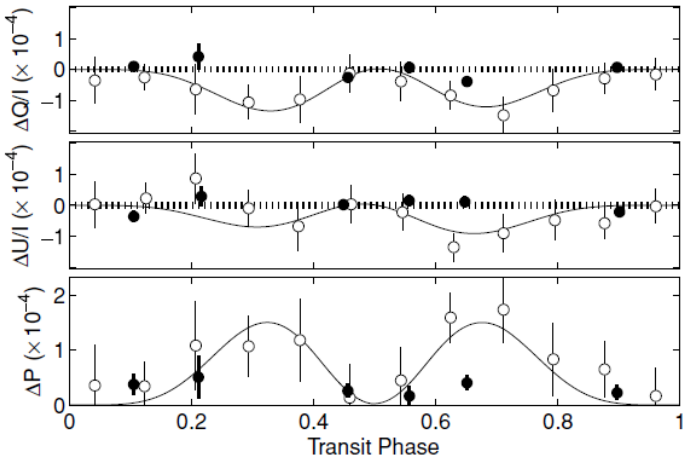

Figure 31: Graphs reported by [49]. The black dots are the data measured by Wiktorowicz in its paper of 2009. The open circles are the data measured by Berdyugina in 2008. The black curve is the model of exoplanet HD 189733b made by B08.

2.7 Controversy about the polarimetry signal detection of HD 189733b

Wiktorowicz [49] excludes the result of Berdyugina et al. as they exclude a degree of polarization of the planetary system around HD 189733 until $7.9 \cdot 10^{-5} = 0.0079\%$. Berdyugina et al. cite the paper of Wiktorowicz, but they affirm that the number of the observations is too small and in the maximum elongation there are only six measurements. The two measurements sets are also observed at different wavelengths. The conclusion of Berdyugina is that the measurements of Wiktorowicz are compatible with their measurements, and they cannot exclude the detection. Wiktorowicz has used POLISH instrument (POLarimeter for Inclination Studies of High mass x-ray binaries/Hot Jupiters) mounted at the Cassegrain focus of the Hale telescope of 5m of diameter at Palomar Observatory. POLISH uses a photoelastic modulator (PEM) to modulate polarization, a Wollaston Prism, a lock-in amplifier and a couple of Avalanche PhotoDiode (APD) or a couple of Photomultiplier (PMT).

The polarization limit of detection of POLISH instrument was measured in a previous work of the same author of about $2 \cdot 10{-}6$. The correct detection of polarization was controlled observing Cygnus X1, a star with a polarization of 4.98% with a variability of about 10^{-3}. The observations of Cygnus X1 detect a variability of $5.1 \cdot 10^{-4}$ and a non-detection of variability for HD 149026, HD 175541 and HD 189733.

The variability of the stars with exoplanets is excluded by a K-S (Kolmogorov-Smirnov) test. The variability of all the targets is compatible with Gaussian nature statistic oscillation at 99%

of confidence level for all the nights.
A chapter of the paper [49] is dedicated to HD 189733. The author excludes any variability of the star, and he tries to make a χ^2 test between his dataset and Berdyugina 2008 (see fig. 31 for a visual comparison of the two datasets). It concludes that the two data sets are incompatible at a confidence level of 99.99%. The author suggests that the polarization observed by Berdyugina could be due to starspots. The presence of the starspots on the surface of the star HD 189733 is reported in the literature with a variability of 11.8 days.

In July 2015 Wiktromicz et al. [50] have submitted to Astrophysical Journal a new paper about an upper limit for the albedo of HD 189733b computed by polarimetric data. In this paper Wiktromicz et al. contradict the albedo reported by Berdyugina et al. [46]. The authors underline the presence of some particle of sulfuric acid in Venus's atmosphere that scattering the Sun's light polarize them. A similar phenomenon is probably present in Titan as a signal of 50% of linear degree of polarization has been measured by Pioneer 11 and Voyager 1 and 2.
They observe HD 189733 in B band during 50 night distributed over three years by POLISH2 polarimeter at Lick telescope (primary mirror diameter of about 3m). POLISH2 is based on photoelastic modulator with a resonant frequency of 40Hz and 50Hz. It can measure simultaneously linear and circular polarization (Q, U, and V Stokes parameters) by demodulation software algorithm. Since POLISH2 is an AC-coupled polarimeter, a lock-in amplifier approach is taken in software. Briefly, both a sine and cosine are constructed for each modulation frequency, and the products of these sinusoids with mean-subtracted raw data from each PMT are calculated over 0.1 s data segments. The time average of each product is then taken, which removes the contribution of raw data varying at frequencies other than the modulation frequency. These time-averaged values, the so-called "in-phase" (X_i) and "quadrature" (Y_i) components of the power modulated at each frequency i. The polarized intensity (Stokes Q, U, or V) scales with $R_i = \sqrt{X_i^2 + Y_i^2}$ while total intensity (Stokes I) scales with DC [51]. Three frequencies "i"are selected appropriately to measure Q, U and V Stokes parameters.
To calibrate instrumental efficiency factors in each UBV filter, a linear polarizer and quarter-wave Fresnel rhomb are used to polarize and inject lamp light into POLISH2 with $\sim$ 100% Stokes q, u, and v sequentially [51]. They observe 20 standard calibration stars for a total of 1229 observations to determine the telescope polarization and the galactic magnetic field near the Sun. They do not found the polarization signal measured by Berdyugina 2011 [46] and with their measurements they found an upper limit for the albedo of HD 733189b of 0.37 in B band not compatible with $A = 0.61 \pm 0.12$ Berdyugina [46]. Graph of fig. 32 reports the measurements obtained for HD 189733 and a model of this exoplanet with different albedos.

By observing far-ultraviolet variability of HD 189733, it is supposed that HD 189733b partially evaporates, and the gas accretes the star [52]. Authors observe HD 189733 by Hubble Space Telescope and COS spectrograph in the wavelength of $115 - 145$nm. They divided the information from spectrograph in small time intervals ($\sim$ 200s) to control the variability of spectral lines, using algorithms of IRAF software. Data are taken during five consecutive orbits of HST. In the first orbit, HD 189733b was in eclipse behind the star, so the measured spectrum is the spectra of the star without a possible contribution by the planet. By the ratio of the intensity of lines in spectra are estimated the temperature of the emitting plasma. The temperature is

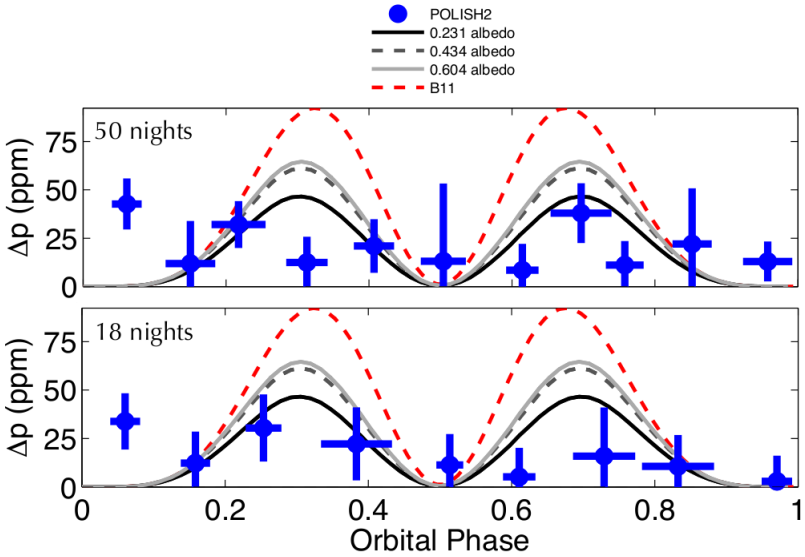

Figure 32: Graphs reported by [50]. The blue dots with error bars are data obtained by POLISH2. The curves are the best fit with different albedos.

computed for different time intervals obtaining a thermal profile in function of the time. The temperatures obtained for the quite plasma are 25,000K, 50,000K and 80,000K. Two activity episodes of increasing flux are recorded. The first episode is just after the eclipse. During the rise in activity, the centroid of the elements lines is red-shifted of a velocity compatible with the orbital velocity of the exoplanet (about 20km/s). The fluxes decrease in a time of 400s, restoring the basal level of the quiescent flux. These episodes are compatible with hot plasma accreting on the surface of the star, that produce some flares. In this orbital phase also X/ray emission are recorded. A magnetohydrodynamic model could explain all the observations with a magnetized stellar wind and material evaporating from the exoplanet and accreting the star. The outflow from the exoplanet could be supersonic, interact with stellar wind and fall in a spiral/shaped trajectory onto the star. The accretion could have time intervals, as the plasma could before accumulates and then falls in the form of dense fragments.
It is possible that such phenomena could modify the polarization profile expected and also it could explicate the controversy on the detection of polarization signal by HD 189733b. In the exoplanet simulations founded in literature the accreting phenomena are not included, a simulation must be performed. It is possible that light could be scattered by stellar wind and accreting disc. The flares observed by [52] are too time short to has a direct role in polarization as the measurements taken in polarization are integrated in a time of the order of the hour. The presence of the quiescent periods and the activity periods must be also considered to analyze the polarization results.

Based on these presented results, it is clear that it is necessary to refine the polarization measurements of the stars, to be able to measure with certainty the polarization of exoplanets. The development of new instruments can help to achieve this goal. The rest of the thesis therefore presents the design of a polarimeter to observe exoplanets and the realization of a prototype.

3 Scientific requirements for a polarimeter to observe exoplanets

This chapter defines the scientific requirements for a polarimeter to observe exoplanets.
The first section is dedicated to a preliminary analysis of a catalog of exoplanets in order to make a selection of exoplanets that should produce a stronger polarimetric signal.
The second paragraph reports the estimated fluxes of photons that can be expected in the channels of a polarimeter.
Based also on these calculations, the third paragraph defines the scientific requirements.

3.1 Estimation of fluxes analyzing an exoplanets catalog

A preliminary analysis of an exoplanets catalog is performed to estimate the number of photons received on Earth's surface.
About 1900 confirmed exoplanets are acquired by www.exoplanet.eu [2]. Only those planet with known radius and orbital separation have been selected. These two parameters regulate the intensity of scattered light by the exoplanet.
To calculate the number of photons expected from the planet, some star data must also be known. There are more ways to perform this calculus. One of these is to get the visual magnitude of the star and by the inverse of the Pogson law to estimate the flux:

$$F_s = F_{\odot} \cdot 10^{\frac{m_s - m_{\odot}}{-2.5}} \tag{27}$$

Where F_s is the flux of the star, m_s is the magnitude of the star, $F_{\odot}$ and $m_{\odot}$ are the flux and the magnitude of the Sun (or of an another reference star).
As in the catalog the magnitude of the stars is reported for different photometric band and the data are incomplete, another method is used. For the stars with enough data, the two methods are compared. For all stars in catalog the effective temperature and radius have reported, so by Stephan-Boltzmann equation it is possible to estimate the luminosity:

$$L_s = 4 \cdot \pi \cdot r_s^2 \cdot \sigma \cdot T_{eff}^4 \tag{28}$$

Where L_s, r_s and T_{eff} are the luminosity, the radius and the effective temperature of the star. As energy on a sphere centered on the star is conserved at the planet distance "d"the luminosity of the star is divided for the surface $4 \cdot \pi \cdot d^2$. The cross section of the planet of a radius "r_p"is about πr_p^2. If P is the degree of polarization of the exoplanet, the amount of polarized luminosity reflected by exoplanet "L_r"is about:

$$L_r = P \cdot 4 \cdot \pi \cdot r_s^2 \cdot \sigma \cdot T_{eff}^4 \cdot \frac{1}{4 \cdot \pi \cdot d^2} \cdot \pi r_p^2 \cdot B \tag{29}$$

$$L_r = P \cdot \pi \cdot r_s^2 \cdot \sigma \cdot T_{eff}^4 \cdot \frac{r_p^2}{d^2} \cdot B \tag{30}$$

Where B is the Bond albedo of the planet (the fraction of the irradiance of the incident starlight that is reflected by the planet in all directions).
It is evident that the highest flux is provided by giant exoplanets orbiting near the star.
The polarization of the reflected light by exoplanets could change between 1% and 80% (as numerical simulations suggest [43] and [44]). Here a minimum polarization of 1% is assumed.
The flux arriving on the Earth surface is reduced as the exoplanetary system has a distance "D"from Solar system:

$$F_E = \frac{L_r}{4 \cdot \pi \cdot D^2} \tag{31}$$

Where F_E is the flux incoming to the Earth.
Table 8 reports the estimated 30 most intense fluxes reflected by exoplanets. The calculation is a rough estimation. To perform a more realistic calculus, exoplanet's informations must be provided from future experiments.
In these calculus, it is assumed a transmission of Earth's atmosphere of $T_a = 80\%$ [75], reflectance of planet of 50% (Bond albedo) and a polarization of 1%. The calculus is performed for the exoplanets in quadrature phase of their orbit.
To convert the energy in a number of photons, the correct approach is to integrate the spectrum of the star to estimate mean photon energy. Here to simplify calculus, a mean energy of $E_\gamma = 3.19 \cdot 10^{-19} J$ (corresponding to a wavelength of of 550 nm), is assumed.
The estimate the number of photons "N_γ"collected by a telescope with an aperture diameter "A"in "Δt "integration time is given by:

$$N_\gamma = \frac{F_E \cdot T_a \cdot \Delta t \cdot A}{E_\gamma} \tag{32}$$

One of the telescopes located at the Department of Physics of RomaTre has a diameter of 0.2m. So, to estimate the number of photons received, a 0.2 meter telescope diameter and an hour of integration time are selected. No filter is inserted in the optical chain.
The number of photons estimated by 32 with the telescop of our Department of Physics is reported in table 8.
The observable is the modulation of the degree of polarization of the received flux to Earth with the period of revolution of the exoplanet. For not resolved exoplanets the received flux to Earth is the sum of the stellar flux and the reflected flux by the same exoplanet. To understand the intensity of the modulation, the ratio between the luminosity reflected by the by exoplanet (eq. 30) and the luminosity emitted by star (eq. 28) must be estimated. Notice that the ratio of the flux of the exoplanet and the star star flux is independent of the size of the telescope and also from the integration time.

The modulation of the polarization of exoplanet with the orbital period is fundamental to assure that the polarization signal is coming from the exoplanet and not from star (for example induced by a magnetic field in the star).
As shown by the numbers reported in table 8 the ratio between polarized flux from exoplanet and star flux is very low, so measuring this flux is a high difficult challenge.
These calculations are carried out whereas a low degree of polarization of the reflected light amount by (1%). In case the degree of polarization, induced by the exoplanet, is greater there are more possibilities to reveal this signal as shown in the next section.

3.2 Expected flux from the exoplanets in a polarimeter

The purpose of this section is to quantify the photon fluxes expected in a polarimeter for study exoplanet.
Telescope with three different apertures 0.2 m, 1.8 m and 10 m have been considered.
The figures 33, 34, 35, 36, 36, 37 and 38 show the Signal to noise expected from exoplanets for three degree of polarization (1 %, 25% and 50%) by 3 different diameter of telescope. They were taken into account only the 6 exoplanets of the table 8 with more favorable geometric conditions to produce a polarization signal detectable. In all graphs the horizontal black line is the minimum threshold to produce a signal greater than noise. Only the photon shot noise is considered. Only graphs with S/N greater than 1 for at least a few exoplanets have been reported.
Comparing the graphs it can be seen that measuring a degree of polarization of 1 % of an exoplanet by a telescope of 10 diameter is comparable to measure the polarization of an exoplanet with a degree of polarization of 50 % by a telescope of 0.2 m diameter.

Table 9 report the estimation of the number of photons entering the channels of a spatial modulation polarimeter (2-channel) for the 3 telescopes and for 3 different degrees of polarization of the exoplanets: 50 %, 25 % and 1%.

The differences between the two orthogonal channels are very small. In a limit case the 2 components of polarization are not distinguishable (case of low polarization: 1% and small telescopes: 0.20 m). In this case the source would be seen as a non-polarized.

Planet name	Planet radius [R_Ψ]	Planet orbital period [days]	semi maior axis [A.U.]	star distance [pc]	star radius [$R_\odot$]	star Teff [K]	Boltzmann luminosity [W]	Luminosity reflexted by planet [W]	flux from planet received at Earth [W/m^2]	planet polarized photons in telescope	star photons in telescope	planet vs star flux ratio
WASP-33 b	1.438	1.22	0.026	116	1.44	7400	2.16E+27	9.30E+20	2.89E-18	903	2.09E+09	4.31E-07
HD 189733 b	1.138	2.22	0.031	19.3	0.79	4980	1.32E+26	2.36E+19	2.64E-18	827	4.62E+09	1.79E-07
WASP-76 b	1.830	1.81	0.033	120	1.73	6250	1.57E+27	6.61E+20	1.92E-18	600	1.43E+09	4.20E-07
WASP-18 b	1.165	0.94	0.020	100	1.23	6400	8.75E+26	3.87E+20	1.62E-18	505	1.14E+09	4.41E-07
HD 209458 b	1.380	3.52	0.047	47	1.15	6075	6.17E+26	7.11E+19	1.35E-18	421	3.65E+09	1.15E-07
55 Cnc e	0.178	0.74	0.016	12.34	0.94	5196	2.23E+26	3.95E+18	1.08E-18	339	1.92E+10	1.77E-08
WASP-82 b	1.670	2.71	0.045	200	2.18	6490	2.91E+27	5.54E+20	5.78E-19	181	9.50E+08	1.91E-07
WASP-71 b	1.500	2.90	0.046	200	2.32	6050	2.49E+27	3.56E+20	3.72E-19	116	8.13E+08	1.43E-07
KELT-2A b	1.306	4.11	0.055	128.9	1.84	6148	1.67E+27	1.29E+20	3.24E-19	101	1.32E+09	7.68E-08
WASP-14 b	1.281	2.24	0.036	160	1.31	6475	1.03E+27	1.79E+20	2.92E-19	91	5.28E+08	1.72E-07
HD 149026 b	0.718	2.88	0.043	78.9	1.50	6147	1.10E+27	4.22E+19	2.83E-19	88	2.32E+09	3.80E-08
WASP-12 b	1.736	1.09	0.023	427	1.60	6300	1.39E+27	1.09E+21	2.49E-19	77	9.96E+07	7.73E-07
WASP-3 b	1.454	1.85	0.031	223	1.31	6400	9.92E+26	2.92E+20	2.46E-19	76	2.61E+08	2.91E-07
KELT-3 b	1.333	2.70	0.041	178	1.48	6304	1.20E+27	1.71E+20	2.26E-19	70	4.93E+08	1.42E-07
KELT-1 b	1.116	1.22	0.025	263	1.34	6516	1.11E+27	3.08E+20	1.86E-19	58	2.09E+08	2.77E-07
WASP-79 b	1.700	3.66	0.054	240	1.64	6600	1.76E+27	2.39E+20	1.73E-19	54	3.99E+08	1.35E-07
HAT-P-22 b	1.080	3.21	0.041	82	1.04	5302	2.95E+26	2.74E+19	1.70E-19	53	5.73E+08	9.25E-08
HAT-P-32 b	2.037	2.15	0.034	320	1.39	6001	8.60E+26	4.12E+20	1.68E-19	52	1.10E+08	4.74E-07
WASP-7 b	1.330	4.95	0.062	140	1.43	6400	1.19E+27	7.52E+19	1.60E-19	50	7.91E+08	6.32E-08
HAT-P-8 b	1.500	3.08	0.045	230	1.58	6200	1.27E+27	1.94E+20	1.53E-19	47	3.14E+08	1.50E-07
HAT-P-7 b	1.421	2.20	0.038	320	1.84	6350	1.90E+27	3.64E+20	1.49E-19	46	2.42E+08	1.90E-07
HAT-P-30 -WASP-51 b	1.340	2.81	0.042	193	1.33	6250	9.30E+26	1.30E+20	1.46E-19	45	3.27E+08	1.38E-07
HAT-P-6 b	1.330	3.85	0.052	200	1.46	6570	1.37E+27	1.21E+20	1.26E-19	39	4.48E+08	8.71E-08
HAT-P-2 b	0.951	5.63	0.067	118	1.64	6290	1.45E+27	3.94E+19	1.18E-19	37	1.36E+09	2.71E-08
GJ 436 b	0.365	2.64	0.029	10.2	0.46	3684	1.37E+25	2.98E+17	1.20E-19	37	1.72E+09	2.15E-08
WASP-62 b	1.390	4.41	0.057	160	1.28	6230	8.51E+26	6.98E+19	1.14E-19	35	4.35E+08	8.05E-08
HAT-P-41 b	1.529	2.69	0.042	311	1.53	6390	1.34E+27	2.37E+20	1.02E-19	32	1.81E+08	1.77E-07
HAT-P-1 b	1.319	4.47	0.056	139	1.17	5980	6.08E+26	4.67E+19	1.01E-19	31	4.11E+08	7.54E-08
WASP-90 b	1.630	3.92	0.056	340	1.98	6430	2.31E+27	2.65E+20	9.59E-20	30	2.61E+08	1.15E-07

Table 8: Estimated photon number received by exoplanet in a telescope of 0.2 m of diameter in one hour. The last column reports the ratio of the flux of the exoplanet and the star star flux and it is independent of the size of the telescope and also from the integration time.

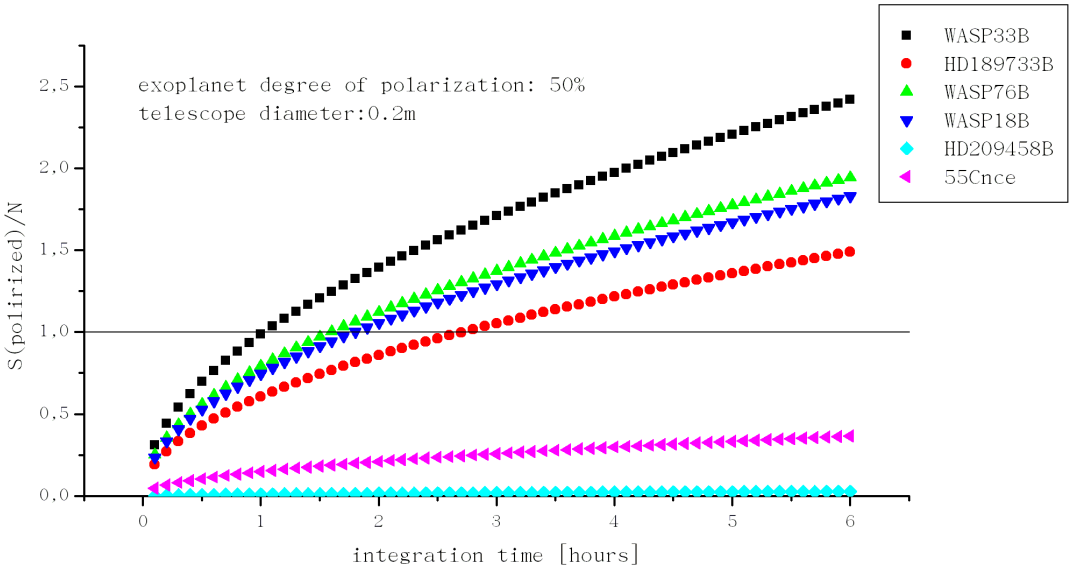

Figure 33: Graph of the signal to noise expected in a 0.2 m diameter telescope for an exoplanet with 50 % degree of polarization. The signal is produced by polarized photons. The noise is just the photonic shot noise due to star flux. They were taken into account only the 6 exoplanets of the table 8 with more favorable geometric conditions to produce a polarization signal detectable.

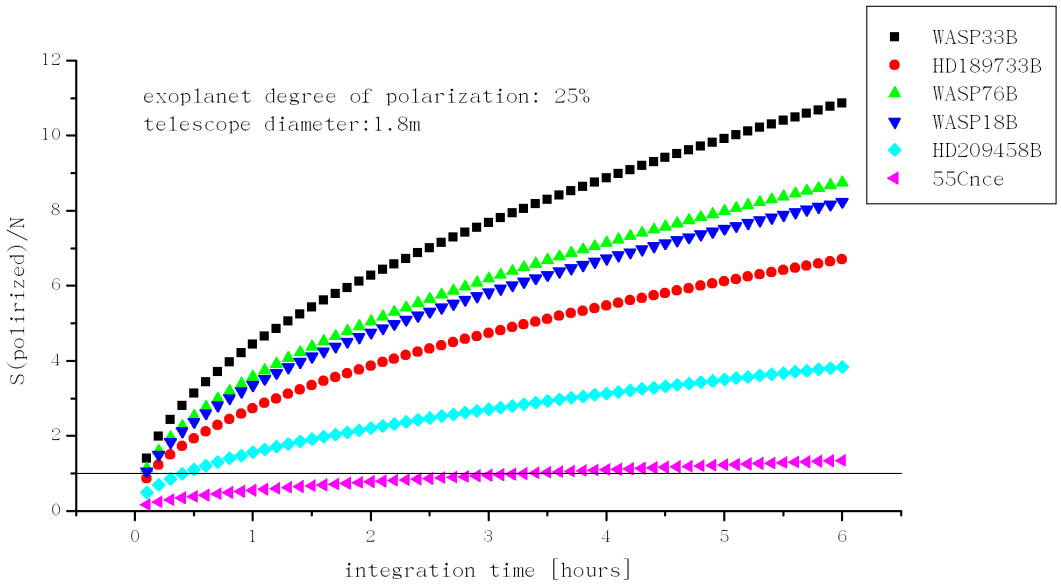

Figure 34: Graph of the signal to noise expected in a 1.8 m diameter telescope for an exoplanet with 25 % degree of polarization. The signal is produced by polarized photons. The noise is just the photonic shot noise due to star flux. They were taken into account only the 6 exoplanets of the table 8 with more favorable geometric conditions to produce a polarization signal detectable.

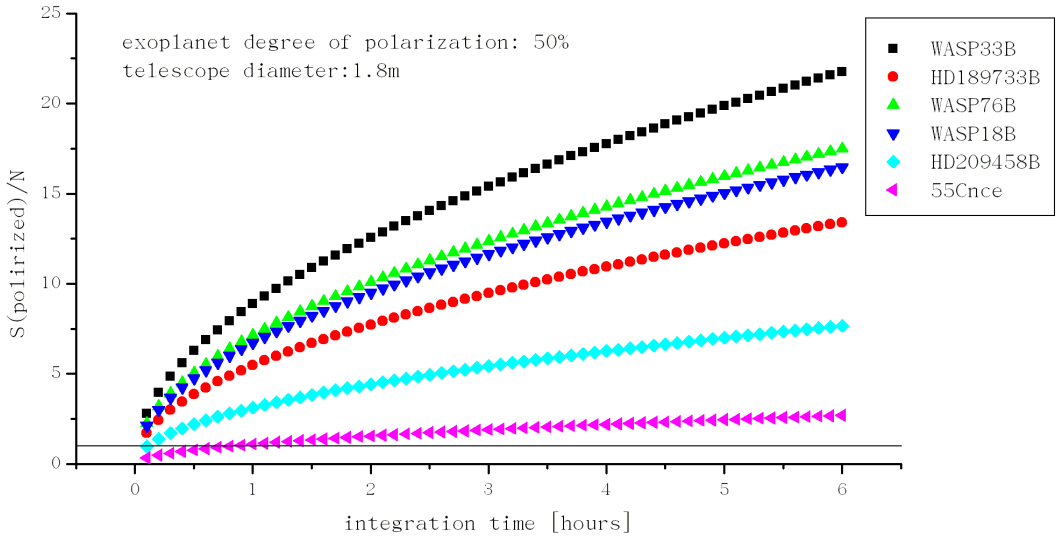

Figure 35: Graph of the signal to noise expected in a 1.8 m diameter telescope for an exoplanet with 50 % degree of polarization. The signal is produced by polarized photons. The noise is just the photonic shot noise due to star flux. They were taken into account only the 6 exoplanets of the table 8 with more favorable geometric conditions to produce a polarization signal detectable.

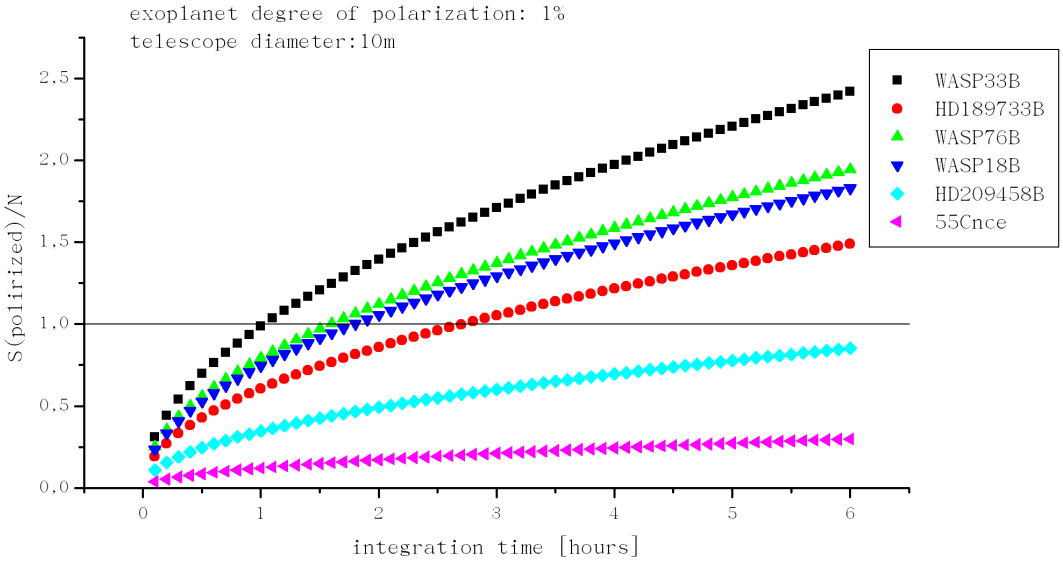

Figure 36: Graph of the signal to noise expected in a 10 m diameter telescope for an exoplanet with 1 % degree of polarization. The signal is produced by polarized photons. The noise is just the photonic shot noise due to star flux. They were taken into account only the 6 exoplanets of the table 8 with more favorable geometric conditions to produce a polarization signal detectable.

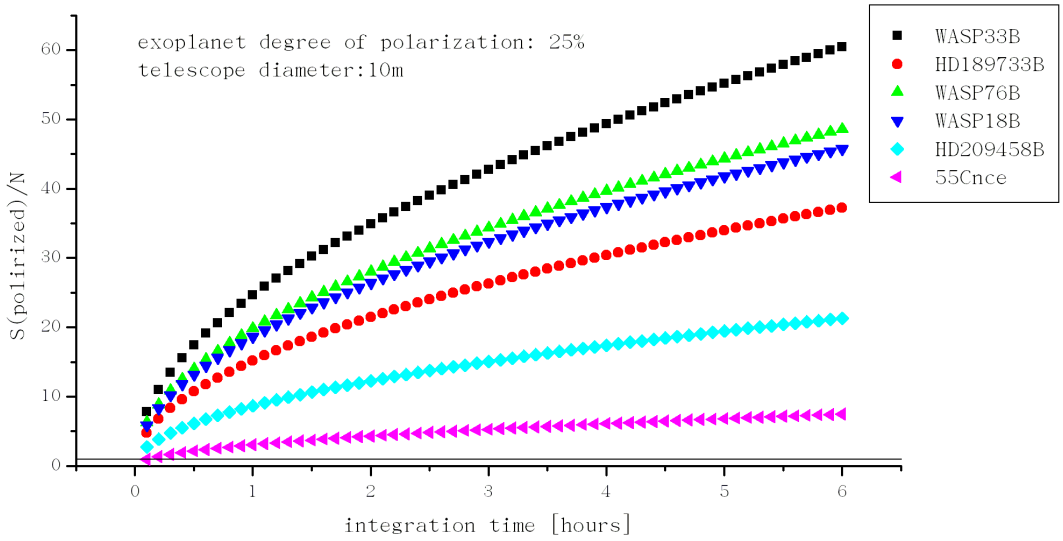

Figure 37: Graph of the signal to noise expected in a 10 m diameter telescope for an exoplanet with 25 % degree of polarization. The signal is produced by polarized photons. The noise is just the photonic shot noise due to star flux. They were taken into account only the 6 exoplanets of the table 8 with more favorable geometric conditions to produce a polarization signal detectable.

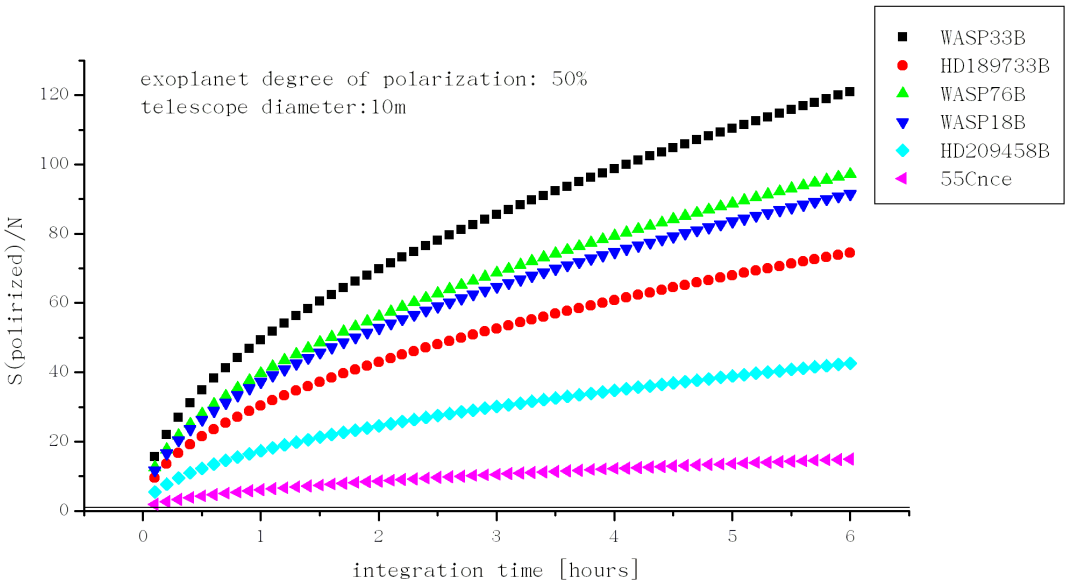

Figure 38: Graph of the signal to noise expected in a 10 m diameter telescope for an exoplanet with 50 % degree of polarization. The signal is produced by polarized photons. The noise is just the photonic shot noise due to star flux. They were taken into account only the 6 exoplanets of the table 8 with more favorable geometric conditions to produce a polarization signal detectable.

telescope diameter		**0.2 m**	**1.8 m**	**10 m**
P = 50 %	$F_0 =$	580562 / s	47025508 / s	1451404566 / s
	$F_{90} =$	580574 / s	47026524 / s	1451435920 / s
P = 25 %	$F_0 =$	580565 /s	47025762 / s	1451412404 / s
	$F_{90} =$	580571 / s	47026269 / s	1451428081 / s
P = 1%	$F_0 =$	580568 / s	47026016 / s	1451420243 / s
	$F_{90} =$	580568 / s	47026036 / s	1451420870 / s

Table 9: Expected fluxes in a polarimeter for the exoplanet WASP-33b observed with three different telescopes. The system is not angularly resolved. 3 different degrees of polarization of the reflected radiation by exoplanet are estimated. It is supposed to not put filters in the optical chain.

3.3 Scientific requirements

The table 10 shows the minimum requirements for the polarimeter and those ideals (goal). The final polarimeter must reach at least the minimum targets. Below are explained all the features required.

	minimum requirement	**goal**
polarization sensitivity	10^{-5}	10^{-7}
wavelenght band	visible	visible + near infrared
temporal resolution	1.5 hours	5 minutes
temporal stability	1 month	$\sim$ 5 years
minimum dynamic	10^6	10^8

Table 10: Scientific requirement for the polarimeter to observe exoplanets. The minimum to be achieved and the ideal characteristics are listed.

3.3.1 Polarization sensitivity

The polarization sensitivity must allow to measure the estimated flows. 10^{-7} would be the ideal sensitivity of the polarimeter, since this, for a low degree of polarization, is equal to the degree of polarization of a planetary system with a planet with 1% of polarizing effect. If this sensitivity can't be achieved and the sources are so few polarized, only an upper limit can be placed (see for example the article by Wiktorowicz [50]).

3.3.2 Wavelength's response

Exoplanet polarization effects are induced by the reflection of starlight. The range of wavelengths of interest is therefore that of emission of the stars: between infrared and ultraviolet light.

Since the atmosphere is however only transparent to visible light and near infrared, the instrument's response will be limited to this band. A polarimeter on satellite instead could be work in a more extended bandwidth.
If the purpose is to study planets capable of hosting life, the ultraviolet is in general less interesting because stars with strong ultraviolet emission are not suited to the development of life as we know it. In fact, the ultraviolet radiation damages the biological activity and also the stars emitting strong ultraviolet emission are typically more massive and thus combustion period lower standard (still a little time on the main sequence).
For these considerations, **the polarimeter is required to respond to visible and near infrared**.
Information in narrow photometric bands (or better high resolution spectroscopic), could help to constrain models on the planet. However a narrow photometric band reduces strongly the number of photons.
Therefore, the polarimeter will be used without filters, or with broadband filters (few hundred nanometers bandwidth).

3.3.3 Temporal resolution

As explained in the previous chapter, the polarization is modulated by the orbital period of the exoplanet.
The smallest orbital period known (to 18-01-2016) for exoplanets is to PSR J1807-2459 A b equal to 1h 41m [2].
Until 18-01-2016, 77 exoplanets are known with period of less than 2.5 days[2].
Note that exoplanets with small orbital period if giants are the best candidates to detect a polarization signal (according to the accounts of paragraph 4.1).
Taking 2.5 days exoplanet's orbital period and assuming 20 measurements during that time, a time resolution of 1.5 hours is required.
For some exoplanets more ambitious (orbital period of about 2 hours) a resolution of 5 minutes is required.

3.3.4 Temporal stability

In order to observe exoplanets with the rotation period of a few years (orbital radius of some astronomical unit) is necessary that the polarimeter has a stability for at least half of the orbit of rotation of the exoplanet. In the case of a planet like Jupiter this is equivalent to having a stability of the instrument of at least five years.

The stability means that the polarimeter maintains its efficiency and the same response for all the time required. The observing conditions may change, and this must be taken into account by finding a method of controlling and / or reducing data suitable.
Note that the temporal stability for such a long period is only a requirement goals as to observe the polarization of an exoplanet with a shorter orbital period (for example 2 days) it is sufficient that the instrument maintains the stability for at least 2 consecutive observational nights.

Already to observe a good number of exoplanets a minimum stability of a month is enough.

3.3.5 Dynamic

The dynamics required to measure the expected fluxes in the previous paragraph can reach 10^8 to each polarimeter channel. Using a detector composed of more pixels you can spread the source on more pixels, otherwise with a single pixel detector is difficult to achieve a such dynamic.
On a modern CCD the full well capacity of a pixel is of the order of 10^5 electrons and a read noise of about $10e^-$. The dynamic range is:

$$RD = \frac{FWC}{RN} \tag{33}$$

The dynamic D of a measurement divided on N pixels is:

$$D = \frac{N \cdot FWC}{\sqrt{N \cdot RN}} = \frac{\sqrt{N} \cdot FWC}{\sqrt{RN}} \rightarrow N = \left(\frac{D}{FWC}\right)^2 \cdot RN = \left(\frac{10^8}{10^5}\right)^2 \cdot 10 = 10^7 \tag{34}$$

In order to achieve a dynamic of 10^8 it is necessary to divide the light at least 10^7 pixels (corresponding to a minimum diameter of ~ 1780 pixels).
For a most favorable measurement (higher degree of polarization of the exoplanet) a dynamic of 10^6 is sufficient. In this case the number of pixels is:

$$N = \left(\frac{D}{FWC}\right)^2 \cdot RN = \left(\frac{10^6}{10^5}\right)^2 \cdot 10 = 10^3 \tag{35}$$

Note that the diameter must be greater if the light of the source is distributed non-homogeneous pattern in the collecting area (typically at the center is more intense than at the edges of the spot, but of course this depends from the polarimeter optics and of focusing condition). An example of non-homogeneous source is an annular defocused PSF (this might be convenient to deploy the image on more pixels rather than concentrating on a few pixels, but taking into account that the contribution to the noise increases.

3.3.6 Temperature and mechanical stability

To achieve such sensitivity (and in order to ensure to keep them during the exoplanet's orbit) is also an important thermal and mechanical stability of the instrument. Note that the orbit of the exoplanet could extend over several days.
A change in temperature can lead to mechanical deformation of the instrument with a consequent misalignment and/or deformation of the optics. The efficiency and characteristics of the optics themselves can depend on the temperature.
Even the mechanical stress of the instrument must be carefully assessed, the more so that the polarimeter must move with the telescope, so it must maintain the same mechanical properties in different inclinations of the instrument (assuming you use the Cassegrain focus).
This section can not be put a numerical constraints on these characteristics as strongly depen-

dent on the optical design that will be chosen.

3.3.7 Field Of View

The polarimeter works only on a single stellar source. Accordingly, the field of view required for the polarimeter is constrained by the size of the star on the telescope focal plane which is the plane where the light of the star is selected to be analyzed.
Since all the stars (except the Sun) seen with any telescope in the world are point-like objects, the size occupied by a star on the focal plane of the telescope is then due solely to the diameter of the telescope, the quality of the optics of the telescope and observation conditions (transmission of the atmosphere).
In general, the distribution of light from a point source on the focal plane of a telescope is called PSF (Point Spread Function).
The optical quality can be improved until reaching the diffraction limit, and in this case it can supply the diameter of a point source as the diameter of the first ring of the Airy diffraction pattern. The diameter in arc-seconds of the first Airy disk is [68]:

$$\theta[arcsec] = 2.5 \cdot 10^5 \cdot \frac{\lambda}{D} \tag{36}$$

Where "λ"is the wavelength and "D"is the telescope diameter.
For the three telescopes considered in the previous paragraph the Airy disc is:

$$\begin{aligned} \theta(0.2\text{m}) &= 2.5 \cdot 10^5 \cdot \tfrac{550 \cdot 10^{-9} m}{0.20 m} = 0.6875" \\ \theta(1.8\text{m}) &= 2.5 \cdot 10^5 \cdot \tfrac{550 \cdot 10^{-9} m}{1.8 m} = 0.0764" \\ \theta(10\text{m}) &= 2.5 \cdot 10^5 \cdot \tfrac{550 \cdot 10^{-9} m}{10 m} = 0.0138" \end{aligned} \tag{37}$$

The observing conditions can affect the quality of optical performance, and that's why the bigger telescopes using adaptive optics systems to sample the wavefront in real time and using deformable optics they correct the optical path to rebuild the front wave of a point source (so a spherical wave front).
The field of view selected for the polarimeter must be greater than the diameter of the star on the focal plane of the telescope, to use an annular region around the star in order to estimate the sky background intensity.

The pointed region of sky will be controlled from field camera. The "field of view"of this camera is not a critical parameter. With a larger field of view in the control chamber must be less the exposure time because it is statistically more likely that there are brightest stars in the control field.

3.3.8 Telescope coupling

All polarimeters must be placed directly at the focus of the telescope, at least for the first part of the optics that break or select the polarization of the incoming light. The optical fibers can

be possibly used to bring light to the detector or to the eventual spectroscope (such as PEPSI at LBT).
The polarimeter must be able to rotate around the axis of the telescope. This feature is easy to implement on professional telescopes since most of them already provides a field rotator on the connection flange between the telescope and the instrumentation. If there isn't a field rotator on the telescope it must be implemented in the connection of the polarimeter to the telescope.
One full rotation of the polarimeter allows to reduce the instrumental polarization.
In addition it is necessary to perform at least a 45° rotation to be able to characterize all the linear components of the Stokes vector (I, Q, U).
Both rotations can be made simultaneously by performing 8 observations spaced each 45° of rotation of the polarimeter around the optical axis of the telescope.

4 Optical proposal to build a polarimeter

The purpose of this chapter is to present the proposal for the optical polarimeter to observe exoplanets.
An optical pattern composed of the Brewster window and a polarizing beamsplitter is presented.
The characterics of the selected optical components are described.
It is shown that the combination of the 2 optics potentially reduces the measurement polarization error with respect to the single Brewster window.
A ray tracing simulation of the optical design is presented.
The projects of some mechanical supports to hold the optics are illustrated.

4.1 Optical proposal to split light into polarization components

The main purpose of a linear polarimeter is to divide the light into its polarization components. The polarization components are called "s" and "p". These two characters are the beginning of German world "senkrecht" (perpendicular) and "parallel" (parallel). The geometry is referred to the direction of the electric field respect to the plane of the incident light. P-polarized light has the electric field parallel to the plane of incidence; s-polarized light has the electric field orthogonal to the incident plane.
In other case, as reported in [58], the definition of the "s" and "p" plane of polarization is referred to the optical bench, so "p" is horizontal and "s" is vertical. Note that these definitions are arbitrary. For the wire-grid polarizers, the "s" and "p" direction is referred as perpendicular to the grid or parallel to the grid.
For the linear polarimeter proposed in this thesis, the light is divided by a Brewster Windows and a wire-grid polarizing beamsplitter.
A Brewster window is a normal planar glass oriented at a particular angle. The angle of Brewster can be computed by the next formula:

$$\theta_{Brewster} = \arctan\left(\frac{n_{glass}}{n_1}\right) \tag{38}$$

Where n_{glass} is the index of refraction of the glass of the windows, n_1 is the index of refraction of the substance where the window is inserted (the most common substance is the air with the index of about 1). If the window is oriented at this angle, the reflected light is totally polarized (s-polarization). So this Brewster Windows can be used to extract s-polarization component from a light source. Note that the reflected light is only a part of the s-polarized incident light, since a fraction of the s-light is transmitted.
By Fresnel equations, it is possible to compute the amount of the light reflected and transmitted. Two interfaces must be considered to model a real "Brewster window correctly" by these equations. The first interface partially reflects the light. The part that is not reflected is transmitted into the glass. The second interface reflects a part of the transmitted light by the first interface. The part that is not reflected is transmitted out of the glass. These two interfaces produce two

Brewster spots of a point collimated source. The distance between the two spots depends only on the thickness of the Brewster window.

In principle, a Brewster window can be enough to measure the linear polarization, but in order to obtain a more accurate measurement, the transmitted light can be split again to constrain better the polarization of the source. A wire grid polarizing beamsplitter is selected to achieve this purpose. The fig. 39 represents a logic diagram of a polarimetric decomposition of the light according with this scheme.

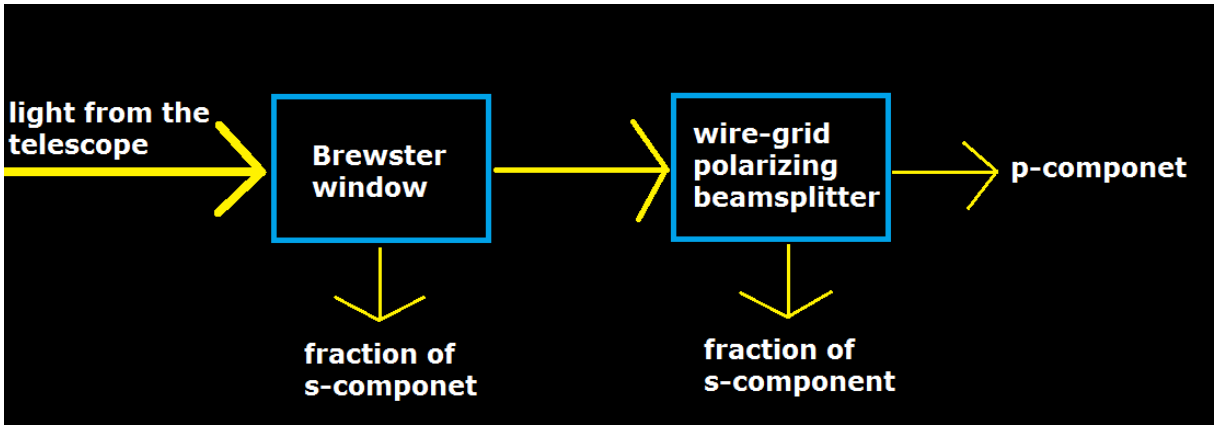

Figure 39: Logical scheme of polarimetric decomposition of light from the telescope

4.2 Selected optical components

The optical component of EDMUND ♯65 − 823 was chosen as Brewster window. When it is used at 55.57° has a 10 mm diameter circular profile. The surface quality limits the transmitted wavefront distortion to $\lambda/10$ at 632 nm. The thickness of this Brewster window is 2.0 ± 0.2mm. The selected Brewster windows is made by uncoated "Fused Silica"glass. The design wavelength is 632.8 nm and working wavelength range is from 200 to 2000 nm.

The polarizing beamsplitter is made by Edmund Optics (part number: ♯48 − 544); its common use is in 3D video projector.
The shape is square window with the side of (12.5 ± 0.2) mm. The thickness is (0.70 ± 0.07) mm. The substrate of the beamsplitter is made by "Corning Eagle XG Industrial Grade"glass. The operating temperature is from -40°C to $+200$°C.
Fig. 40 reports the curves of transmission and reflection of the polarizing beam splitter as a function of wavelength, supplied by the manufacturer. Broadband Polarizing Plate Beamsplitters consist of a thin layer of aluminum MicroWires adhered to a substrate glass window.
An Anti Reflecting (AR) coating has applied to the polarizing beamsplitter by manufacturer. The index of Refraction of this glass is 1.5255 at 430nm and 1.5056 at 1000nm. Unlike normal incidence optics, the purpose of AR coatings on polarizing beam splitters is not to increase transmission. In an imaging application, an AR coating will often provide improved contrast but may have little or no effect on system efficiency.

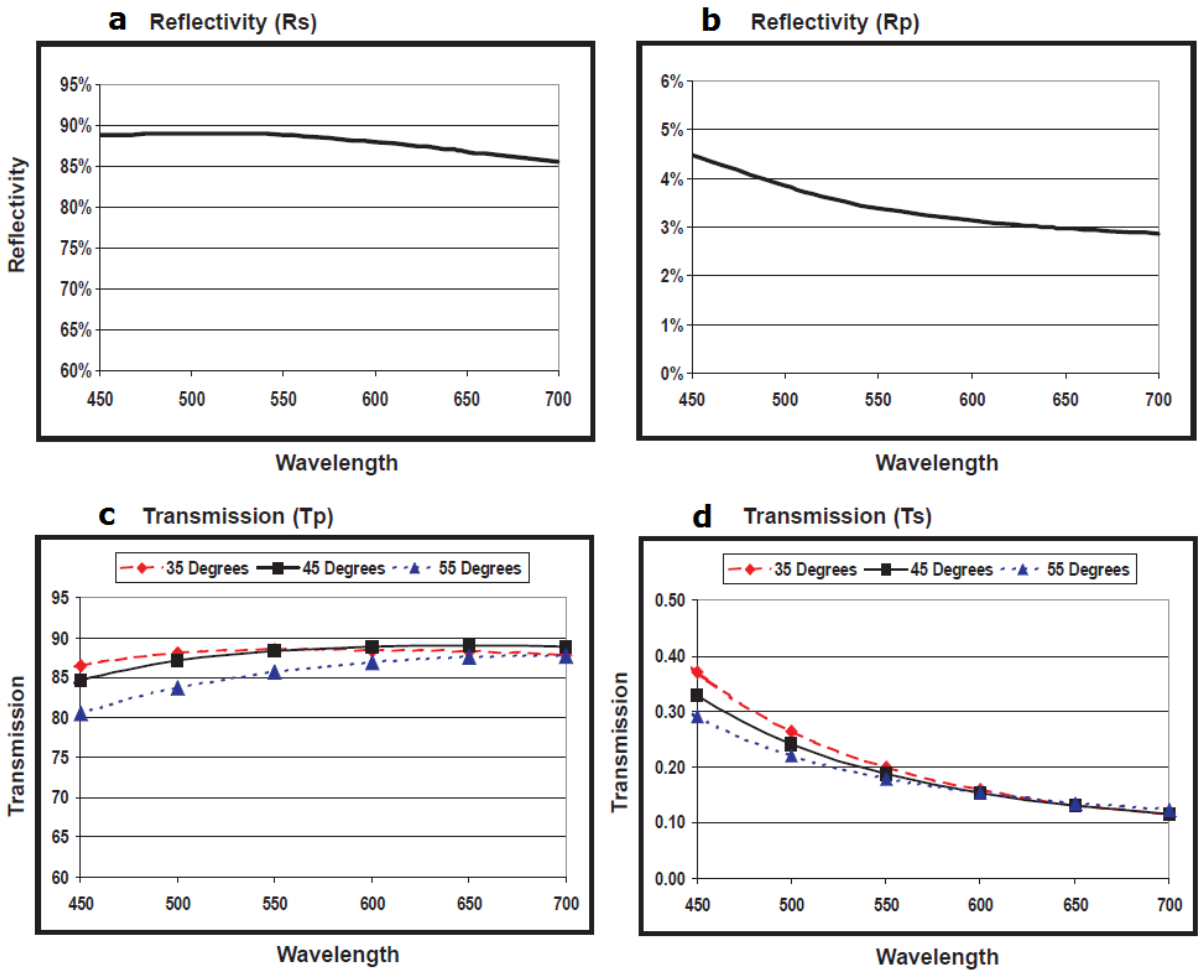

Figure 40: Curves of transmission and reflection of the polarizing beam splitter as a function of wavelength, supplied by the manufacturer. Graph "**a**"shows the reflectivity of a typical polarizing beamsplitter at 45°; graph "**b**"shows the reflectivity of the unwanted p-polarization of a typical polarizing beamsplitter at 45°; graph "**c**"shows the transmissivity of a typical polarizing beamsplitter; graph "**d**"shows the transmission of the unwanted s polarization of the polarizing beamsplitter. Graphs "c"and "d"are provided for more incident angles.

Both in the transmitted component that in the reflected component there is a contamination of the not desired polarization (see graphs "b"and "c"of Fig.40). In the specifications of the manufacturer, there is a 0.33% of s-component transmitted and 4.5% of p-component reflected (the polarizing beamsplitter transmits the p-component and reflects the s-component). The p-component transmittance is about 84.6%, and s-component reflectance is about 88.8%.
Using only the beamsplitter is impossible to measure the polarization of source better than contamination. The uncertainty on the transmitted and the reflected components (due to contamination) are for unpolarized light:

$$\Delta transmitted = \frac{s_{transmitted}}{p_{transmitted}} = \frac{0.33\%}{84.6\%} = 0.39\% \tag{39}$$

$$\Delta reflected = \frac{p_{reflected}}{s_{reflected}} = \frac{4.5\%}{88.8\%} = 5.1\% \tag{40}$$

So an uncertainty of few percent is at a minimum level. Using a Brewster window in combination with a polarizing beamsplitter, three independent measurements of 2 components of polarization are acquired. It is also possible in this case to take into account the contamination of the components of the polarization in signals. The three measurements will be fitted with 2 polarized and one unpolarized component of the light intensity that could generate these 3 spots.

Table 11 reports the expected coefficient of transmission and reflection divided by the polarization components relating to the incident light on the optics. They were calculated for the Brewster window and acquired by the manufacturer's specifications for the polarizing beamsplitter. Table 12 reports the expected intensity of the 3 spots produced by the proposed optical

	Brewster reflected	Brewster transmitted	Beamsplitter reflected	Beamsplitter transmitted
s	25.96%	75.73%	88.00%	0.13%
p	0.00%	100.00%	3.50%	89.00%

Table 11: Table of the expected coefficients of transmission and reflection divided by the polarization components relating to the incident light on the optics.

scheme.The intensities are divided in the polarization components and they are referred to the incident light in the optical scheme. The last raw reports the intensity of the 3 spots for a non-polarized light source.

	Spot 1	Spot 2	Spot 3
s	25.96%	66.64%	0.10%
p	0.00%	3.50%	89.00%
total light for the spot (for unpolarized source)	12.98%	35.07%	44.55%

Table 12: Table of the expected intensity of the 3 spots produced by the proposed optical scheme.The intensities are divided in the polarization components and they are referred to the incident light in the optical scheme. The last raw reports the intensity of the 3 spots for a non-polarized light source.

The overall transmission of this optical scheme is estimated to be about 92.6% for a non-polarized source.

$$T = 50\% \cdot (BR_{rs}+BR_{ts} \cdot BS_{rs}+BR_{ts} \cdot BS_{ts})+50\% \cdot (BR_{rp}+BR_{tp} \cdot BS_{rp}+BR_{tp} \cdot BS_{tp}) = 92.6\% \tag{41}$$

Where "BR"is a coefficient related to the Brewster window, "BS"is a coefficient related to the beamsplitter polarizer, the subscript "t"indicates a transmission coefficient, "r"a reflection coefficient and "p"and "s"subscript letters indicate the polarization components.
The high percentage of global transmission is an advantage of this optical scheme that uses thin glasses. Other polarimeters often include a calcite block or a glass prism which have a lower transmission.
In this optical scheme the total transmission depends on the polarization of the source. The

account of the total transmission reported in the table has been made to a non-polarized source. The target sources (stars with exoplanets) are not polarized sources to the level of 10^{-4} (used in the calculations), so the transmission efficiency of this optical scheme for the main scientific objective is precisely estimated in this calculation.

4.3 Comparison of the uncertainty obtained from a measurement carried out with the only Brewster window respect to one performed with the optical scheme proposed

In the next calculus, there is the prove that a polarimeter that uses two lenses (the Brewster window and the polarizing beamsplitter) produces a minor uncertainty respect to a polarimeter that uses only the Brewster window to analyze the polarization. The advantage of using two optics is to have about a half noise of the degree of polarization respect using only Brewster window.

A calculation for deriving the flow of photons from a degree of polarization is shown in Appendix (appendix A.3). A source, with a degree of polarization of $\alpha = 2 \cdot 10^{-5}$, has the intensity expressed in the orthogonal polarization components equal to $F_{90} = 1.59097 \cdot 10^{10} photons$ and $F_0 = 1.59101 \cdot 10^{10} photons$.

Next, is calculated the signal and the error of a polarimeter composed only by a Brewster window. The obtained error for the degree of polarization is about equal to the measurement.

Now suppose to utilize only the Brewster window as polarization optic analyzer. The reflected light is:

$$F_r = BR_{RP} \cdot F_0 = 0.2596 \cdot 1.59101 \cdot 10^{10} = 4.1298 \cdot 10^9 \tag{42}$$

Its error for statistic can be estimated as:

$$\Delta F_r = \sqrt{F_r} = 64263 \tag{43}$$

The flux transmitted by Brewster window is:

$$F_t = BR_{TP} \cdot F_0 + F_{90} = 2.7690 \cdot 10^{10} \tag{44}$$

Its error for statistic can be estimated as:

$$\Delta F_t = \sqrt{F_t} = 1.664 \cdot 10^5 \tag{45}$$

In a real measure, to estimated the fluxes with these counts (F_r and F_r), the inverse operations are performed:

$$\begin{aligned} F_0 &= \tfrac{F_r}{BR_{RP}} \\ F_{90} &= F_t - BR_{TP} \cdot F_0 \end{aligned} \tag{46}$$

The errors propagates as:

$$\begin{aligned} \Delta F_0 &= \frac{\Delta F_r}{BR_{RP}} = 2.476 \cdot 10^5 \\ \Delta F_{90} &= \Delta F_t + \Delta F_0 \cdot BR_{TP} = 2.140 \cdot 10^5 \end{aligned} \tag{47}$$

The degree of polarization and its error is:

$$\begin{aligned} P &= \frac{(F_0 - F_{90})}{\sqrt{F_0^2 + F_{90}^2}} = 2.00 \cdot 10^{-5} \\ \Delta P &= \frac{\left| \sqrt{F_0^2+F_{90}^2} - \frac{(F_0 - F_{90}) \cdot F_0}{\sqrt{F_0^2+F_{90}^2}} \right|}{F_0^2+F_{90}^2} \cdot \Delta F_0 + \frac{\left| -\sqrt{F_0^2+F_{90}^2} - \frac{(F_0 - F_{90}) \cdot F_{90}}{\sqrt{F_0^2+F_{90}^2}} \right|}{F_0^2+F_{90}^2} \cdot \Delta F_{90} \end{aligned} \tag{48}$$

The equation of the error obtained by partial derivatives of the other equation can be simplified:

$$\Delta P = \frac{F_{90}^2 + F_0 \cdot F_{90}}{(F_0^2 + F_{90}^2)^{\frac{3}{2}}} \cdot \Delta F_0 + \frac{F_0^2 + F_0 \cdot F_{90}}{(F_0^2 + F_{90}^2)^{\frac{3}{2}}} \cdot \Delta F_{90} = 2.05 \cdot 10^{-5} \tag{49}$$

The final result of the polarimeter built with the only Brewster window is $P = (2.00 \pm 2.05) \cdot 10^{-5}$**.**

Obviously this result is not significant as the uncertainty is comparable to the measure.
In next calculus are analyzed a virtual measurement of the same source by a polarimeter with a Brewster Windows and a polarizing beamsplitter. The final result has a minor error respect previous case.

If it is put a polarizing beamsplitter after the Brewster window, F_t is splitted in two components: BS_r (the reflected component and BS_t (the transmitted component). The Flux reflected and transmitted are:

$$\begin{aligned} BS_r &= F_0 \cdot BR_{TP} \cdot BS_{RP} + F_{90} \cdot BS_{RS} = 1.1177 \cdot 10^{10} \\ BS_t &= F_0 \cdot BR_{TP} \cdot BS_{TP} + F_{90} \cdot BS_{TS} = 1.3499 \cdot 10^{10} \end{aligned} \tag{50}$$

To estimate the beamsplitter incoming components (F_0' and F_{90}') the next equation system can be used (note that the variables are only F_0' and F_{90}', the other coefficients are supplied by manufacturer or they are the result of an instrumental calibration).
F_0' and F_{90}' are the incoming flux to the Beasmplitter.

$$\begin{cases} BS_r = F_0' \cdot BS_{RP} + F_{90}' \cdot BS_{RS} \\ BS_t = F_0' \cdot BS_{TP} + F_{90}' \cdot BS_{TS} \end{cases} \tag{51}$$

Solving for F_0' and F_{90}' and substituting the values of flows calculated in 50 you get:

$$\begin{cases} F_0' = \frac{BS_r - \frac{BS_t \cdot BS_{RP} - BS_r \cdot BS_{TP}}{BS_{TS} \cdot BS_{RP} - BS_{RS} \cdot BS_{TP}} \cdot BS_{RS}}{BS_{RP}} = 1.1780 \cdot 10^{10} \\ F_{90}' = F_{90} = \frac{BS_t \cdot BS_{RP} - BS_r \cdot BS_{TP}}{BS_{TS} \cdot BS_{RP} - BS_{RS} \cdot BS_{TP}} = 1.5910 \cdot 10^{10} \end{cases} \tag{52}$$

The F_{90}' is assumed to be equal to the F_{90} as the Brewster window is assume to transmit 100% of incoming radiation not-reflected (in a real windows there is a minimum absorption by

glass).

To estimate the error it is propagates the errors of BS_r and BS_t, the glass reflection and transmission coefficients are assumed to be perfect.

$$\begin{aligned} \Delta F_0' &= \left| \frac{1}{BS_{RP}} + \frac{BS_{TP} \cdot BS_{RS}}{BS_{TS} \cdot BS_{RP}^2 - BS_{RS} \cdot BS_{TP} \cdot BS_{RP}} \right| \cdot \Delta BS_r + \left| \frac{BS_{RS}}{BS_{TS} \cdot BS_{RP} - BS_{RS} \cdot BS_{TP}} \right| \cdot \Delta BS_t \\ \Delta F_{90}' &= \frac{BS_{RP}}{|BS_{TS} \cdot BS_{RP} - BS_{RS} \cdot BS_{TP}|} \cdot \Delta BS_t + \frac{BS_{TP}}{|BS_{TS} \cdot BS_{RP} - BS_{RS} \cdot BS_{TP}|} \cdot \Delta BS_r \end{aligned} \tag{53}$$

$$\begin{aligned} \Delta F_0' &= 1.260 \cdot 10^5 \\ \Delta F_{90}' &= 1.378 \cdot 10^5 \end{aligned} \tag{54}$$

To obtain the F_0 it is possible to divide F_0' for the coefficient of p-transmission of Brewster window.

$$\begin{aligned} F_0 &= \frac{F_0'}{BR_{TP}} = 1.5910 \cdot 10^{10} \\ \Delta F_0 &= \frac{\Delta F_0'}{BR_{TP}} = 1.260 \cdot 10^5 \end{aligned} \tag{55}$$

To compute the degree of polarization is used the mean value of F_0 obtained by Brewster reflected component and Beamsplitter. The errors of the main value is:

$$\Delta \langle F_0 \rangle = \frac{\sqrt{\Delta F_0(1)^2 + \Delta F_0(2)^2}}{2} = 1.50 \cdot 10^5 \tag{56}$$

The degree of polarization is $P = (2.00 \pm 1.28) \cdot 10^{-5}$.
The error is about the half of the configuration with the only Brewster window.
It is very big error, but if the integration time is 5 time greater the result obtained by same calculus is $P = (2.00 \pm 0.57) \cdot 10^{-5}$, that could be acceptable.

Remember that the importance is the comparison between the two configuration and not absolute numbers. The advantage of the use of the two optics: the Brewster window with the polarizing beamsplitter is about a factor 2 in reducing the uncertainty.

4.4 Response of the optics with the temperature

The polarimeter, depending on the place of observation and the season, may have an operating temperature between about $t_{min} = -40°C$ and about $t_{MAX} = +40°C$.
So, the maximum expected temperature variation for the instrument is 80°C.
This temperature excursion can occur only during the use of the instrument with telescopes located in different geographical locations and in different seasons. In a single evening observing run the expected temperature variation is significantly lower.
Now we calculate the Brewster angle variation due to variation index of refraction of the glass and air as the temperature changes.
The index of refraction of the silica glass for photons of 2.3 eV (546 nm) is 1.459949 at $-43.4°C$ and 1.460696 at $+45.2°C$ [76] (temperature and energy of the photons are extracted from Table 1 of that cited article).
The refraction index of the air is calculated using the database [78]. The index of refraction of the air is 1.00034 at $-40°C$ and 1.00025 at $+45°C$.
The Brewster angle is (equation 38) 55.58° at $-40°C$ and 55.60° at $+40°C$.
The table 13 summarizes the calculated results.

This variation of the Brewster angle involves a change of 0.18 % of the reflection coefficient

Temperature [°C]	n_{glass}	n_{air}	$\phi_{Brewster}$
-40	1.459949	1.00034	55.58°
+40	1.460696	1.00025	55.60°

Table 13: Table of refractive indexes of the air and the glass as a function of temperature and associated Brewster angle.

and $3.6 \cdot 10^{-5}$% of the transmission coefficient.
This uncertainty of the transmission coefficient is negligible, while that in the coefficient of reflection it is negligible only under some conditions. This shows that in case of use of the instrument in different environmental conditions you need to repeat the calibration procedure of the reflection coefficients and transmission of the optics.

4.5 Definition and ray tracing simulation of the optical scheme of the polarimeter

In the diagram a collimation lens has been added as the beam of light coming from the telescope after the focal plane diverges.
A mirror after the beamsplitter was also added to bring all the light beams on a single detector.
Fig. 41 reports the optical scheme of the polarimeter. An astronomical source is selected on the focal plane of the telescope. Only the light from this source passes to the collimation lens. Then, the light is decomposed respect polarization. The Brewster window reflects a part of the incident light producing the first light spot on the detector. A polarizing beamsplitter decomposes the light transmitted by Brewster window. The reflected light by beamsplitter produces the second light spot. The transmitted light by the beamsplitter is reflected toward the detector by a simple first-surface mirror.
In this way, all the three spots are produced on the same detector reducing the inter-calibration errors in the case of use 2 or 3 detectors.

The optical scheme has been verified with a simulation of ray tracing using the software

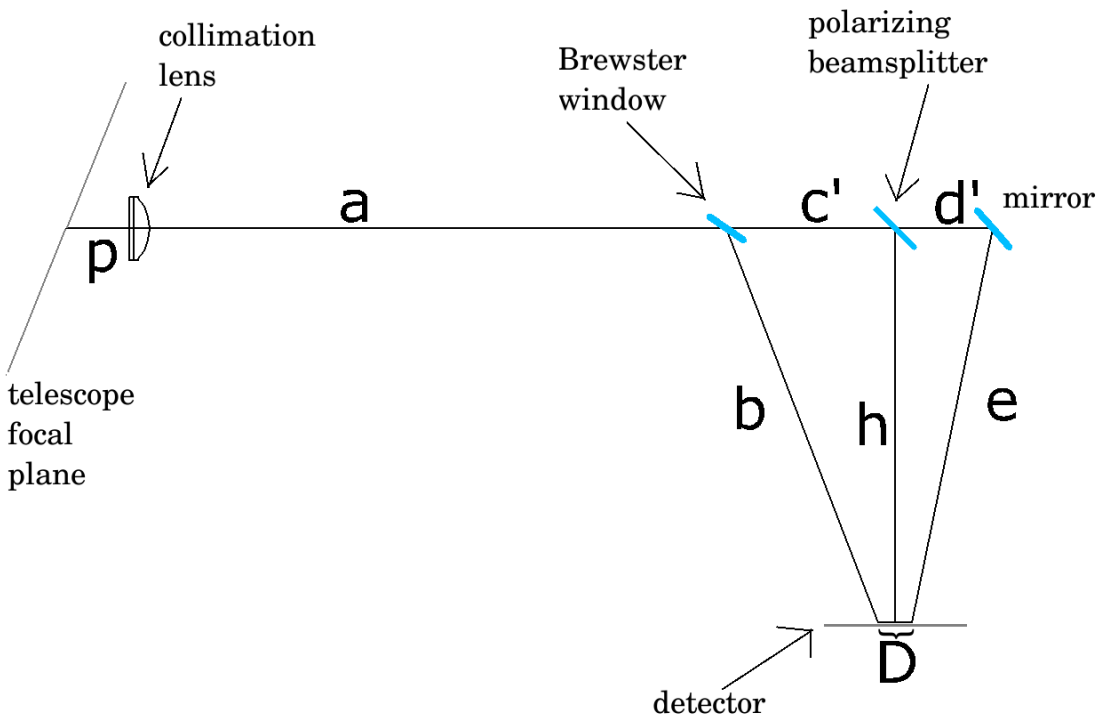

Figure 41: The optical scheme of the polarimeter..

ZEMAX.
ZEMAX uses two different ways of describing optical systems: "Sequential Mode"or "Non-Sequential Mode".
"Sequential ray tracing"means rays are traced from surface to surface in a predefined sequence. "Non-sequential ray tracing"means rays are traced only along a physically realizable path until they intercept an object. The ray then refracts, reflects, or is absorbed, depending upon the

properties of the object struck.
To this simulation was chosen non-sequential mode to reproduce all the physical interactions, and because the system is not describable in a sequential way. Fig. 42 reports a screen-shot of the optic simulation.

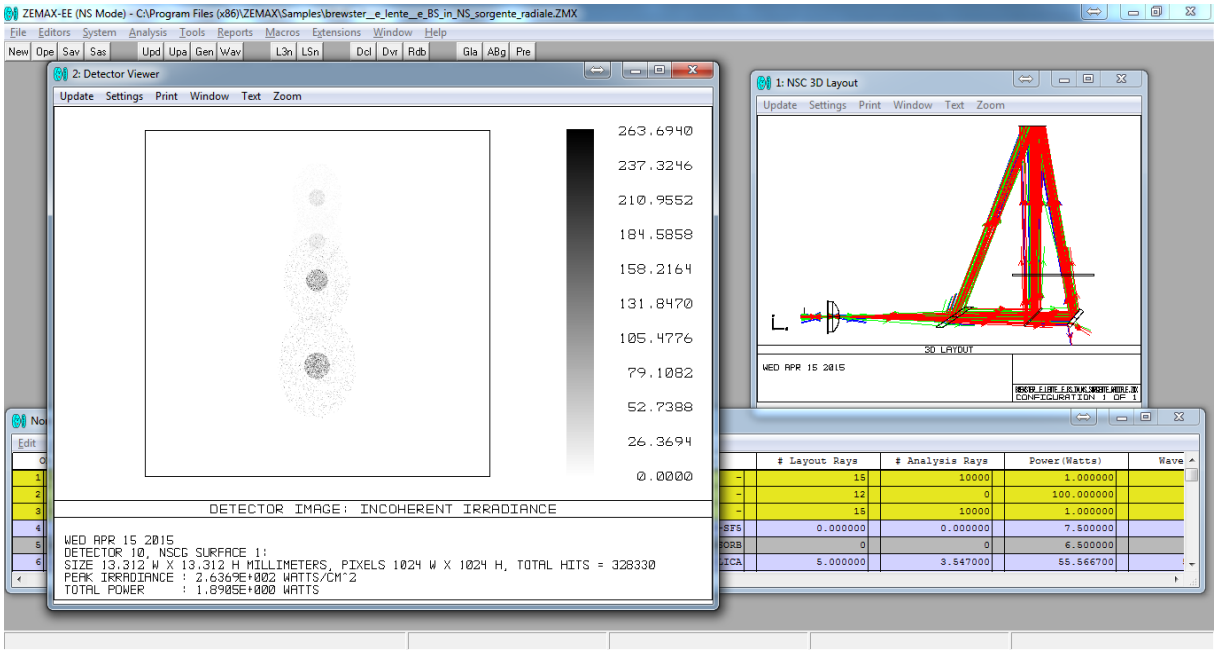

Figure 42: The Zemax simulation of the optical scheme.

In the simulation is included the focusing lens, the Brewster windows, the polarizing Beam-splitter and the mirror and a detector.
The lens is modeled by “Standard Lens”NSC object : a 5 surface lens object with two Standard faces, two flat edges, and a cylindrical outer edge. The back of the lens (the telescope) was set plan. The other side has received a radius of curvature equal to 10.09mm.
Behind the lens has also been added to a mat annular volume modeling support the lens.
The Brewster window is modeled by “Cylinder 2 Volume”NSC object. It consists of a solid cylinder of material with a cutting angle of the front and back. In this case it sets the cutting angle equal to the angle of Brewster.
The polarizing beamsplitter is modeled by “Rectangular Volume”. On the front face it was applied a coating specifically defined according to the specifications provided by Edmund Optics. On the back face it was applied a AR coating, as indicated by producer. The object was tilted by 45°.
The mirror is modeled by “Cylindrical Volume”NSC object, the material is set ti “MIRROR”.
The detector has 1024 x 1024 square pixels, their size is 13µm.
Other rectangular volumes have been inserted in the optical path to absorb some optical beams to assess the behavior of the different optical separately. These surfaces are perfect and are either completely transparent or completely absorbent.
The light Source is composed by a point source (the star) and an extended elliptic source (the sky background).

In “Non Sequential” mode the simulation uses the scattering laws of physics, and it propagates the light rays until they are absorbed by a surface (ex. the detector) or until the rays decreases below a minimum energy.
The table 14 shows the results of a simulation by setting a stellar source of at 1W and sky background of 0.01 W. This ratio of brightness between the star and the sky background is computed for a star of V mag with a sky background of 18 $mag/arcsec^2$ and a star selection area of the star of about 40 arcsec of diameter on telescope focal plane.
The intensity of the three spots are extracted by placing screens covering two beams of light on 3 and taking the value “Total power”in the summary of the results of ZEMAX. The simulation was made by setting the source with two different and orthogonal linear polarizations. Consider that the optical axis is the z axis, so Jx and Jy define the polarization on the plane orthogonal to the propagation of light.
The transmitted component by the beam splitter (BS) and then reflected from the mirror is called “BS Transmitted”. ZEMAX allows you to export the matrix of pixels as a text file with

	Brewster	**BS reflected**	**BS transmitted**
Jx = 0, Jy = 1	$1.37 \cdot 10^{-6}$W	$3.54 \cdot 10^{-2}$W	0.847W
Jx = 1, Jy = 0	0.228W	0.676W	0.138W

Table 14: Results of the ZEMAX ray tracing simulation of the optical scheme.

the number of photons that hit each pixel. It ’been analyzed this file by writing a script Matlab (see appendix A.4 for code). Since the detector is an ideal model, a photon of any energy produces a count. Therefore the number of photons that hit the detector is highly overestimated compared to a realistic CCD.
The choice of the power of the stellar source for the simulation of ZEMAX must be scaled on the real case to the light power collected by the telescope in the focal plane. The choice of 1 W allows you to scale very easily the simulation results with the real power from the star.
The ray tracing simulation is a useful tool to calculate expected flows and to optimize the choice of the detector.

4.6 Project and realization of the mechanical support for the optics

In order to test the optics were built of mechanical supports for them to manage and handle. Some of these supports were then used in the subsequent design of the prototype of the polarimeter.
See appendix A.5 for detailed mechanical design.

Brewster support.

Every window that is oriented at its Brewster angle is a Brewster window, but optical sup-

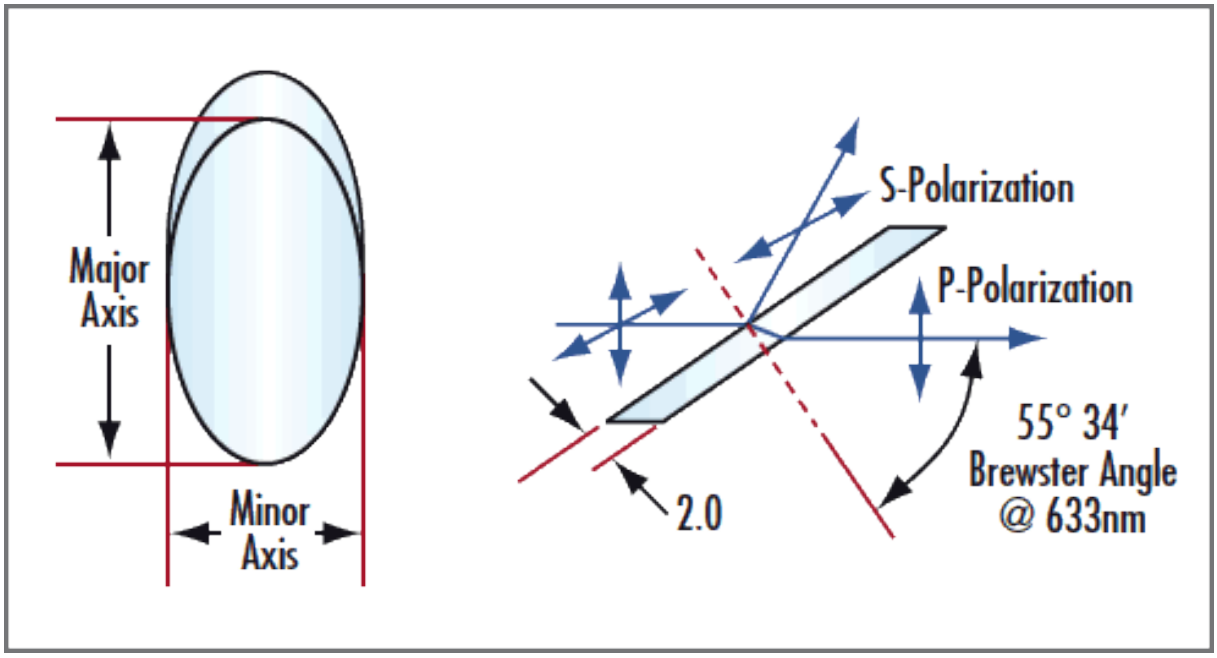

Figure 43: Brewster drawing by Edmund Optic (optical component manufacturer)

pliers sell the "Brewster Windows" as a special elliptic window with appropriate edge cut at the Brewster angle. So, the projection in the beam direction of this elliptic Windows is a circle when it is oriented at the Brewster angle. Its edge is inscribed into a tube and it is horizontal. Obviously a commercial Brewster Windows is intended to use in air or vacuum (the difference is very small), but not in other substances like oil, as the Brewster angle, in this case, is different. Fig. 43 shows the Edmund Optics drawing of Brewster Windows.
The principal purpose of the Brewster support is to ensure the correct inclination of Brewster angle. For the "Fused silica" glass and the air the Brewster angle is 55°34′.
A first support is designed as two black plastic cubes with a groove for the glass and cylindrical hole for the light (see fig. 44). The hole diameter is 9 mm because the optical diameter of the glass is 10 mm. The 0.5 mm of difference in each side is due to ensure the glass in the groove. The two cubic supports are joined with four screws M3 4cm of length.
The cubes are designed with a 3D CAD software (see fig. 104). The production of the cubes is made by 3d printer SD 300 Pro installed in mechanic service of INFN section of RomaTre.
It is possible to print more cubes at the same time, using the plane of the building of 3D printer, in this case, six cubes are printed at the same time.
The printer could realize a plastic object in 5 different colors: transparency, black, red, blue cream. For optic support Is is need the black plastic as it absorbs eventually scattered rays. In

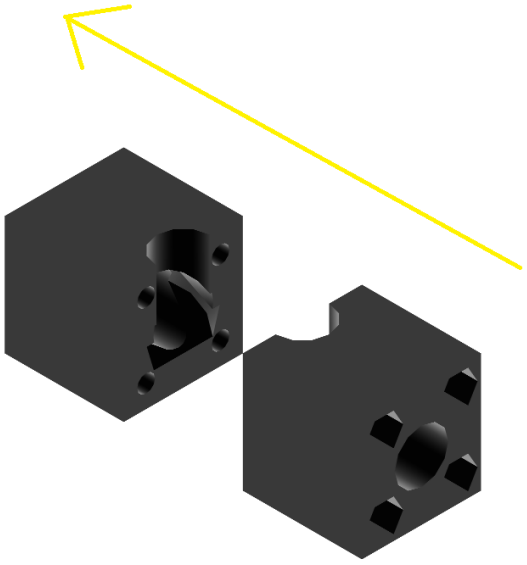

Figure 44: An isometric view of the optical supports for the Brewster window. The yellow arrow indicates the direction of light propagation.

fact, to avoid unwanted spot rays that exit from the optical patch, it must be absorbed by edge supports. For this reason, optical support must be matt black.
The supports have one hole for incoming radiation and two orthogonal holes for the outcoming radiation. Two cubes can be connected by four screws and in the middle they have a groove to insert the Brewster Windows. At the beginning of this thesis more optical schemes have been taken into account. For this reason it has been provided a housing for a circular mirror of 1cm of diameter behind the Brewster window. This mirror is never inserted in Brewster support.
For reflected radiation, the hole is not oriented in an optimal way, in fact, the out-coming reflected light exits with an angle of about 112°, but the out-coming hole has an angle of 90°. This problem is also found in laboratory measurements: the same support obstructs a part of the reflected light.

For this reason, a new support with a thinner edge has been projected (see fig. 45). It is lighter than precedent support. It permits the propagation of the reflected component of the light by Brewster without obstacles. It has squared external edge that assure the correct inclination of internal Brewster Windows. Externally the support has the shape of a rectangular parallelepiped. The external dimensions are 20mm (height), 22.6mm (width), 38.7mm (length). With this external shape, it is easy to position the optical components in an optical bench and also integrate the Brewster Window with other parts of the polarimeter. See fig. 105 in the appendix to see mechanical design with dimensions.

Polarizing beamsplitter support.
For the polarizing beamsplitter, a support with the same external shape and dimensions has projected and realized (see fig. 46). The external dimensions are 20mm (height), 22.6mm (width), 25.4mm (length). The box is dived into two triangular prisms with a wall inclined at

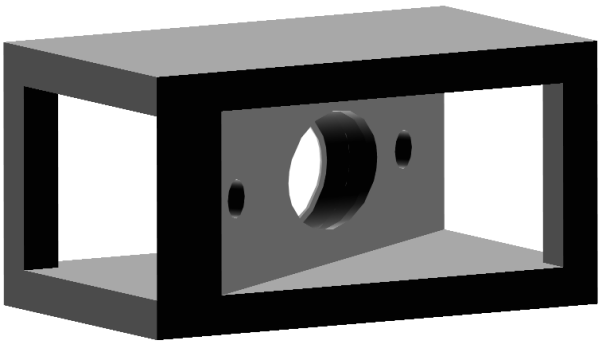

Figure 45: Isometric view of new Brewster window optical support.

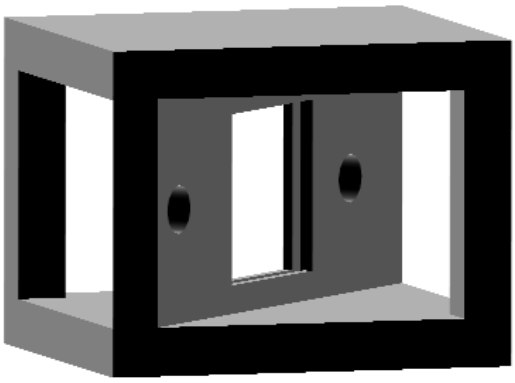

Figure 46: Isometric view of polarizing beamsplitter support.

45°. In the middle of this wall, there is the polarizing beamsplitter. The optic in inserted in a housing of 0.7mm of thickness. The correct inclination respect incoming light is assured by the inclined wall of the support. See fig. 106 in the appendix to see mechanical design with dimensions.

5 Laboratory test of optics

This chapter presents a functional test of the optical scheme proposed for the polarimeter.
In the first paragraph it is illustrated the laboratory setup used.
The second one reports the experimental verification of the optical paths.
The last paragraph shows the response of the optical system to different orientation of the incoming polarization in the optical system.

5.1 General set-up

The experimental set-up was assembled on a solid aluminum optical bench. The test was performed in a dark room.
To test the optical scheme, a collimated light source and a linear polarizing filter were used. Each optic is positioned on a rotating platform. Fig. 47 reports a scheme of the set-up used for the test.
The goals of the test are 1) to verify the expected light patches; 2) to measure the transmitted and reflected intensities by the optics in function of the angle of orientation of the linear polarization filter.

5.1.1 Optical bench

The optical bench has a rectangular shape. It is based on the imperial British standard (for the size, the spacing of the holes and threads). It is 18 inches width and 24 inches length (0.4572 m x 0.6096 m).
The optical bench was positioned inside a dark room of approximately cubic shape with a side of 1 meter.
The darkroom has a front door to place inside the experimental set-up. The door has a black rubber gasket that ensures darkness of the optical chamber.
In a part of the initial tests it was present a plexiglass case to preserve the cleanliness of the environment of measurement.
Fig.48 reports a photo of the set up positioned inside the dark room.

5.1.2 Light source

In order to test the optics, it is necessary to use a fairly collimated light beam. The source must be collimated because the light beam must remain inside the free optic diameter, and there are no focusing elements in the optical path (see fig. 49).
The length of the optical path is about $OP = 50$cm, the free optical diameter of the optics is about $O_D = 9$mm. The source diameter is about $S_D = 2$mm . To ensure that the light beam is

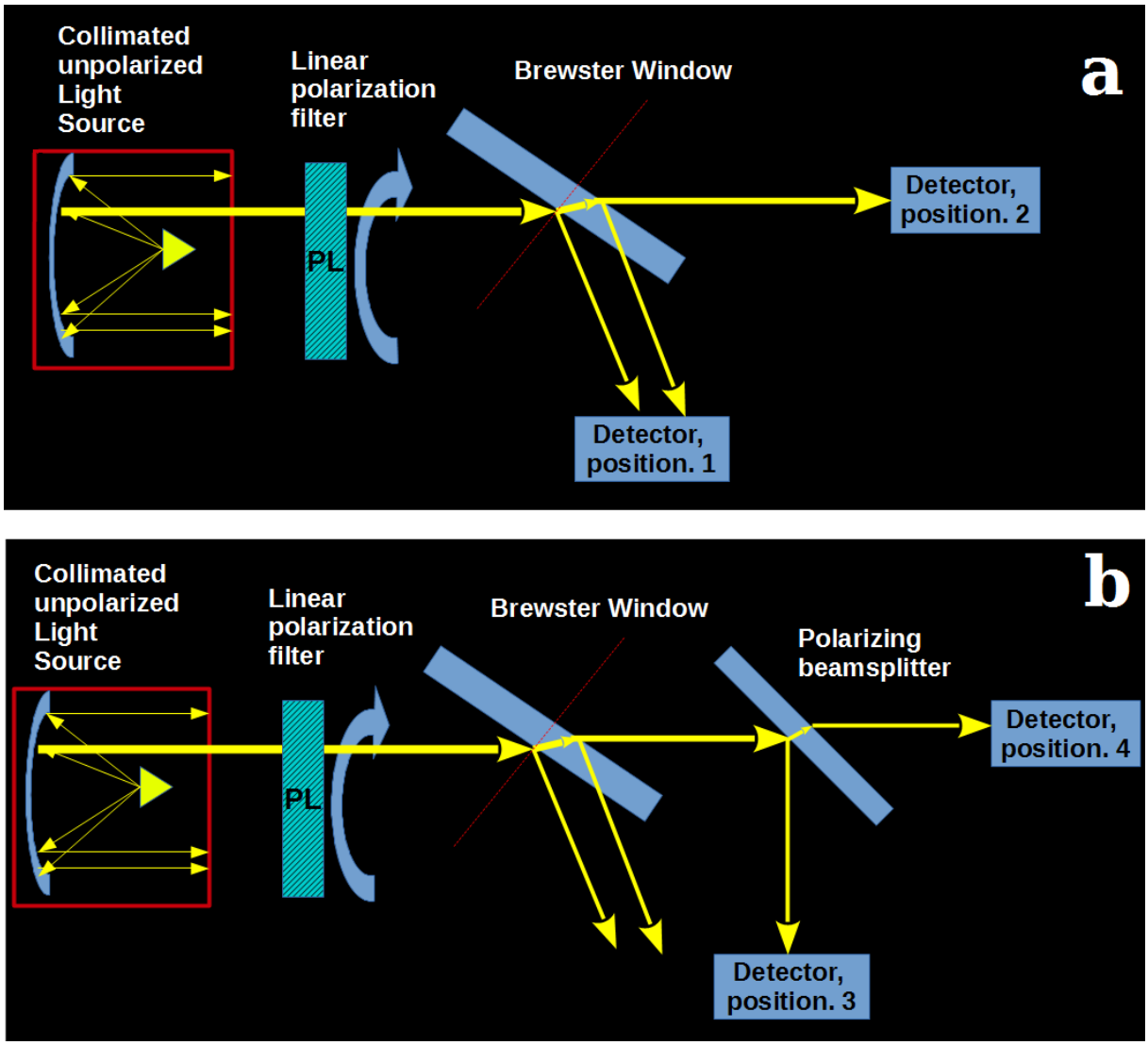

Figure 47: Configuration used to test the optical scheme. The detector was placed in 4 different positions. The intensity of each light beam for each position was acquired in function of the angle of rotation of the linear polarizing filter.

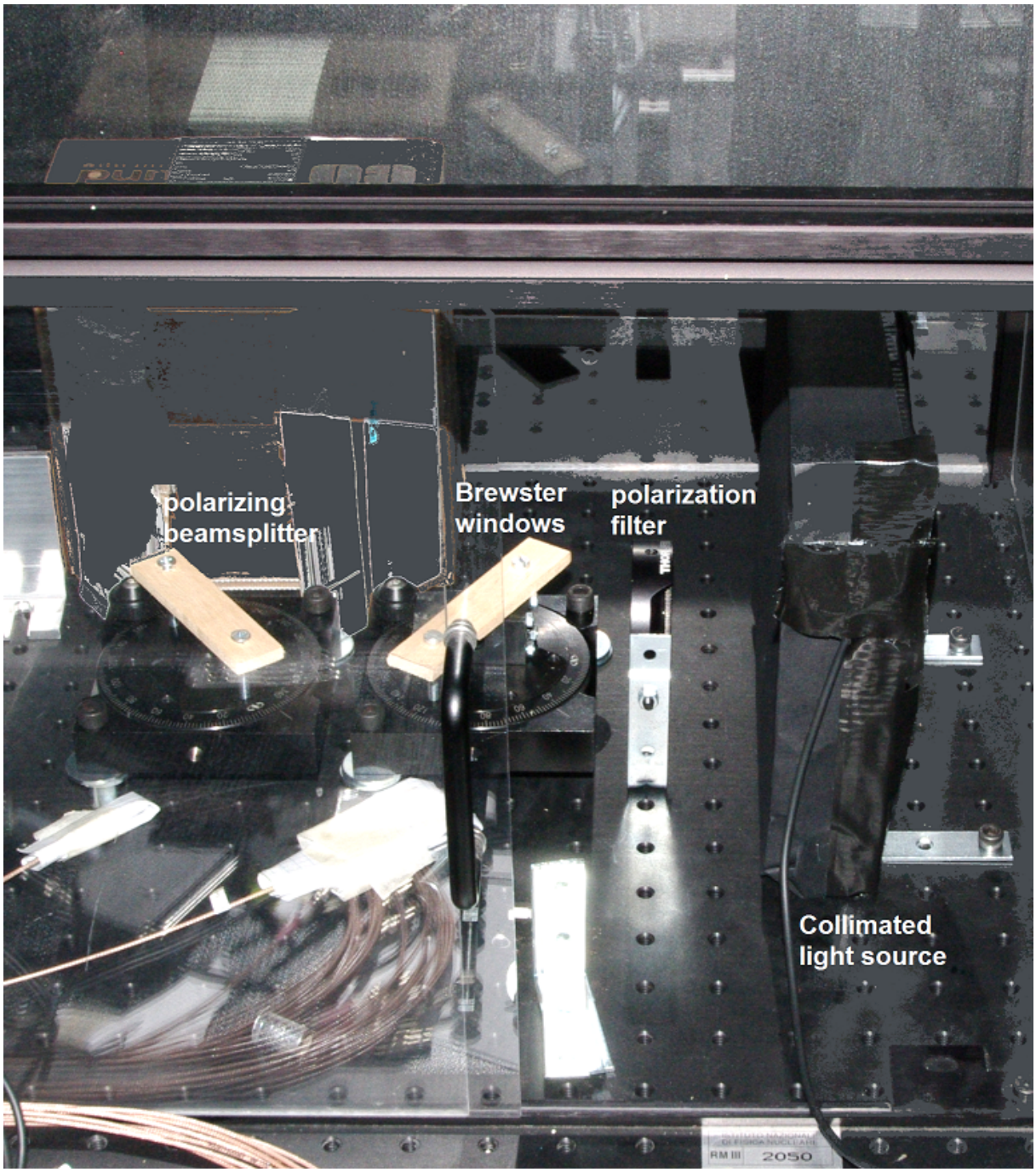

Figure 48: The setup used to test the optics and to verify the predicted coefficient of reflection and transmission of each glass. The optical bench is inside the dark room (open for the picture). In the picture the optics are mounted on rotating platforms used for this test.

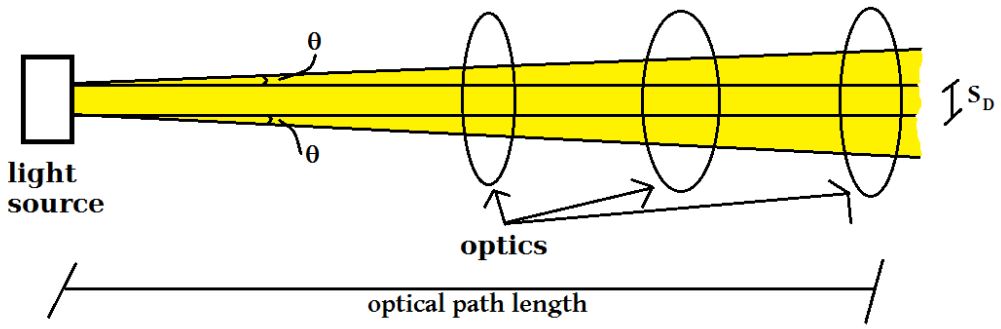

Figure 49: Scheme for the calculation of the maximum divergence allowed for the light source used for the optical test

contained within the diameter of the optics it is necessary that the divergence is less than

$$\theta = 2 \cdot \arctan\left(\frac{(O_D - S_D)/2}{OP}\right) = 2 \cdot \arctan\left(\frac{(9\text{mm} - 2\text{mm})/2}{500\text{mm}}\right) = 48' \tag{57}$$

The collimated light source was realized as follows.
A parabolic mirror is utilized to collimate the light. A parabolic mirror concentrates all the light rays parallel to its optical axis in the parabola focus point. The parabolic mirror can be utilized in inverse mode: putting a source of light in the focus point of the parabola to have an output collimated light beam.
Parabolic mirrors, in general, are very expensive and not so easy to find on the market. They are sold as a part of a telescope or as elementary optical components. A cheaper solution is to get the "physics toy" of the optic illusion, composed of two parabolic mirrors put one above the other with reflecting coating in the internal part (see fig. 50). The mirror is cheap as the support is plastic (and not glass). The surface is aluminum coated. There are no indications about surface quality and curvature tolerance, but this mirror is enough for the preliminary test purpose.

To produce the collimated source of light, one parabolic mirror is selected. A wood sandwich is built to contain the mirror and to have a structure to fasten the light source. A bracket is suspended over the mirror, to put a small light (see in fig. 51). In the beginning, a white led light was used, but this source is suspected to have an intrinsic polarization due to the geometric shape of anode and cathode and the verse of the electric field in the diode to polarize the PN junction. The LED was replaced with a small incandescent lamp of 5V of nominal tension and 2.5W of nominal electric power. The incandescent lamp is not polarized as the emission is due to a thermic process.
The wood support is coated with a matt black paint.
The diameter of the mirror is about 14cm, so the diameter of the output beam is about of the same dimension. It is verified that at a distance of 3m, the beam is enlarged of about 3cm. This implies a divergence of:

$$\theta_S = 2 \cdot \arctan\left(\frac{(3\text{cm})/2}{300\text{cm}}\right) = 34' \tag{58}$$

less than the required divergence of 48'.

Figure 50: The “physics toy” used to get a cheap parabolic mirror. Note that the plastic frog is inside the mirror and not above.

The whole mirror with the lamp is enclosed by a black cardboard (see fig. 52). The black cardboard is drilled with a pin to have a small diameter collimated light beam. In this way, a small diameter light beam exits from the source, and it is contained within the optics.

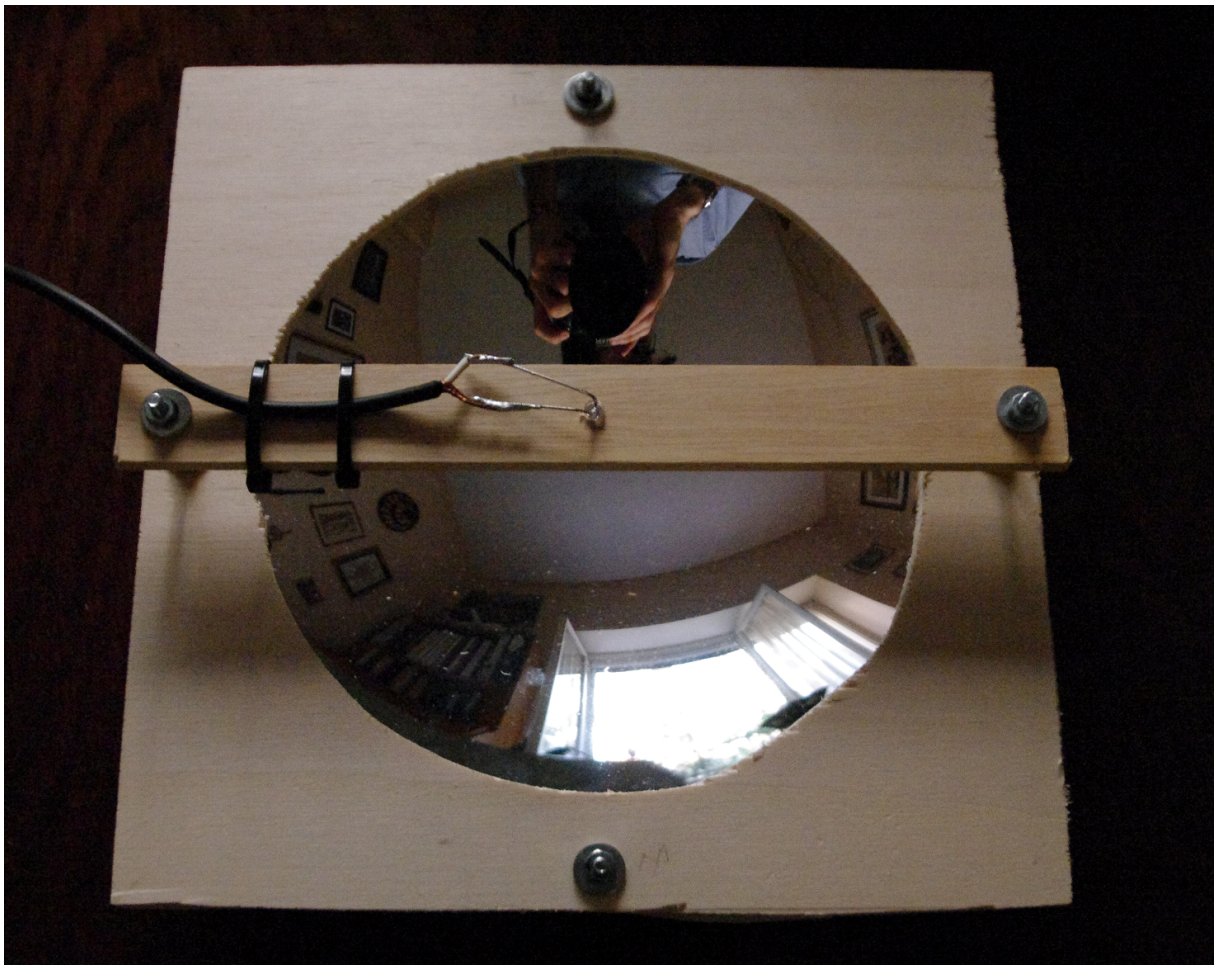

Figure 51: The parabolic mirror with the bracket support for the led.

Figure 52: The collimated light source. Back view. The metallic supports to screw the source light to desk are visible.

5.1.3 Polarization filter

In the test, the light passes through a photographic linear polarization filter.
The filter used is the CF-7590-PL 72mm Picture Plus Filter provided by Sunpak.
Putting this polarizing filter after the light source, a completely linearly polarized light source is obtained. Turning the filter, the polarization vector can be rotated.
The filter is vertically mounted on the optical bench by a mechanical support produced by the mechanical service of INFN-RomaTre. An angular graduated scale with the angle indication is mounted around the filter. The absolute orientation of the direction of the electric field transmitted by the filter is unknown. It is possible to measure the relative angle of the filter using the graduated scale.

5.1.4 Optics

A preliminary test of the Brewster window was carried out to check its behavior. The description of this test and the results are reported in Appendix A.6.

The Brewster window and the beamsplitter are hosted in plastic supports described in previous chapter project and realized in INFN-Sez. RomaTre.
Each optic is positioned on a rotating platform and is stopped by a crossbar. The rotating platform is screwed at the optical bench.
Initially it is only been positioned the Brewster window (see fig. 47,a).
It is verified that light was transmitted and reflected from the Brewster window without obstruction from the optics supports and from the holders for the optical bench.
A laser beam was used to align the optics. The use of lasers has facilitated the alignment because it was easily visible unlike the collimated source. The polarizing beamsplitter with its support has been included in the second phase of the test (see Fig. 47,b).

5.1.5 Detector

Some different types of detector are taken into account. For a preliminary optical test, a reflex photographic camera is used. This type of detector allows to have a complete working system, that does not require any acquisition system. The camera was used without any lens. The camera screen with the "LiveView" (real time image monitor) function facilitates a lot the alignment of the optics.
The used camera (Pentax K-7) is SLR incorporates a Samsung 23.4mm x 15.6mm CMOS sensor with a primary colour filter. The sensor has effective (light sensible) 4672 x 3104 square pixel with 5μm side. Around these pixels is present a darkened rectangular frame of 4 pixels thick.
The ADCs of the camera have a resolution of 12 bit.
To measure the dynamic range have been acquired ten image to the maximum shutter speed (1/8000 s exposure time) with the lens closed. Under these conditions the thermal noise (that is proportional to the root of time) is negligible and therefore almost all of the noise is due to the system read noise.

A mean image of bias was then determined as the median pixel to pixel of the 10 captured images. The read noise counts was determined as the average value up for all the pixels of the difference between an image of bias and the median.

$$RN = \frac{\sum_{i,j} B_i - \underset{k=1..10}{median}(B_i(k))}{N} \tag{59}$$

where Bi(k) is a bias frame, N is the total number of pixel i,j in the sensor ($\approx 14Mpx$).
The value obtained is a read noise equal to 102 counts.
The dynamic range "DR"is obtained as the ratio between the full well capacity "FWC "and the read noise "RN":

$$DR = \frac{FWC}{RN} \tag{60}$$

Here the dynamic range is approximated as the ratio between the maximum value that is of the ADC and the number of counts due to read noise:

$$DR \approx \frac{MAX_{count}}{RN} \tag{61}$$

The count values are saved in 16-bit variables. The most significant digit of the ADC (the twelfth) is saved at the sixteenth position in the variable of the counts of the image output file. Therefore the saturated pixels on the ADC produces a value equal to $(2^12 - 1)$ and the output file a count equals to $(2^16 - 1 - 2^1 - 2^2 - 2^3 - 2^4) = 65505$ (the subtracted numbers are due to the zeros inserted in the least significant bits of the 16-bit variable).
The DR dynamic range is about:

$$DR = \frac{FWC}{RN} \approx \frac{MAX_{count}}{RN(counts)} = \frac{65505}{102} = 642 \tag{62}$$

So, dynamic range is about $6 \cdot 10^2$.

For an image of dark images were acquired 10 with closed lens, ISO 400 sensitivity, with different exposure times (equal to the time of the light frame).
The Dark image is obtained with the median pixel to pixel. The dark image is subtructed from other images as data reduction procedure.
The mean value of 30s exposure time of the dark is about 340 counts.

5.1.6 Verification of light patches

The light paths are shown in fig. 53 by a green laser. The first goal of this test is to verify the projected optical patches illustrated in fig. 41. It is appropriate to point out that in fig. 53 light propagates from right to left.
In the set up of fig. 53 the mirror is absent, therefore, the beam transmitted by the beamsplitter is not then reflected. The other light beams meet the optical scheme.

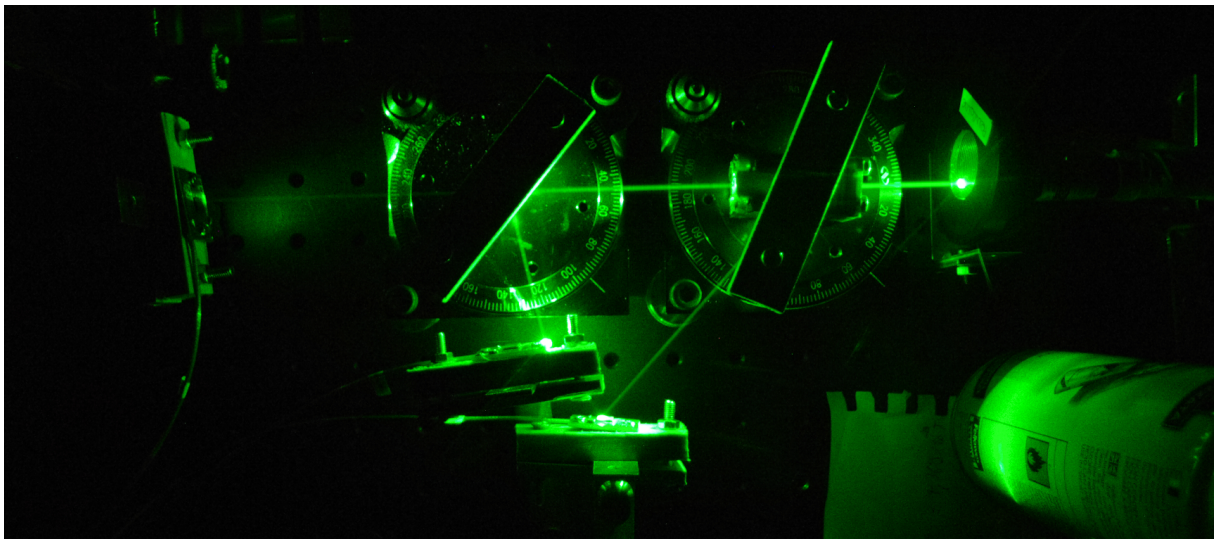

Figure 53: Light path produced by a green laser and enhanced with a cold air jet, produced with simple compressed air spray.

5.2 Measure of transmission and reflection coefficients of two orthogonal polarizations

5.2.1 Source polarization calibration

The measurements are acquired by the collimated source light described before.
The camera is used in RAW mode. The information about the counts of internal ADC (Analog to Digital Converter) is preserved without compression. In the JPEG format, this information is lost.
The polarization of the source is controlled putting the detector just after the polarization filter (without others optics). The measurements are acquired for different orientations of the filter rotated around its optical axis with a step of 20°. The filter used is photographic linear polarization filter of 72mm of diameter described in 6.1.3. Fig. 54 shows one acquired frame.
All the measurements are acquired with an exposure time of 1/100s.
During the measurement is controlled that no pixel of the image have reached the maximum value (saturation prevention).
The photo camera was controlled by IR remote controller to avoid movements in setup.
The images are analyzed with software by "Cyanogen": "Maxim DL".
The image has been removed from the image of dark obtained with the procedure described in section 6.1.5 that has the same shutter speed.
The flat field in this case is not necessary as the photographic camera was used without lens, then the system does not suffers from vignetting due to the optics and all the light coming from the source has been used. The pixels may have a different answer, but for the absence of optics is almost impossible to make a correct flat, for example the angle of incidence of light on the sensor is not well defined.
To calculate the counts "C ", a rectangular area is selected around the lamp filament image with N_l pixels. The value provided and then reported in the graph in fig. 55 is the sum of the values of the 3 RGB channels of the image file taken by "information window"of Maxim DL.

Figure 54: The photo of the collimated source at the angle of the polarization filter of 60°. The original frame is cut. Final dimension is 1500 x 1500 pixels equals to 7.5mm x 7.5mm. The photo was acquired by reflex camera Pentax K-7 without lens. The image is the incandescent filament of the small lamp.

The values are taken from the files saved with 16-bit depth (maximum value obtained with all pixels saturated: $3 \cdot 2^{16} \cdot 14Mpx = 2.75 \cdot 10^{12}$).
Even removing the dark, may remain a part of the noise for example due to a slight diffused light (not "perfect" dark). For this the average "bg"of the background is estimated in a dark area of the image and then subtracted to the area used to estimate the counts of the source.
The product of the noise for the number of the pixel used is subtracted from each frame.

$$I_\theta = \sum_{i,j \in N_l} (R_{i,j} + G_{i,j} + B_{i,j}) - N_l \cdot bg \tag{63}$$

The error "E"is estimated as the standard deviation "σ_p"of the counts measured in a rectangular area outside the image of the lamp multiplied by the number of pixels on which the measurements are made.

$$E = \sigma_p \cdot N_l \tag{64}$$

Fig. 55 reports the graph of the obtained measurements.

The obtained measurements are analyzed using the MicroCal Origin software. The curve is fitted with $y = 0.5I_U + I_P \cdot \cos^2(x - \eta)$ function (Malus law). The best fit is obtained with $I_U = (3.468 \pm 0.011) \cdot 10^{10}$, $I_P = (1.195 \pm 0.093) \cdot 10^9$ and $\eta = 0.319 \pm 0.040$. The chi-square is 5.29 and the degrees of freedom are 16 (19 fits points minus 3 fit curve parameters). The fit is good at 99.5 % of probability. The degree of polarization is $(3.33 \pm 0.26)\%$.
From these measurements it appears that the source has a small degree of polarization. This could be due to a partial polarization of the lamp for the same geometry of the filament.

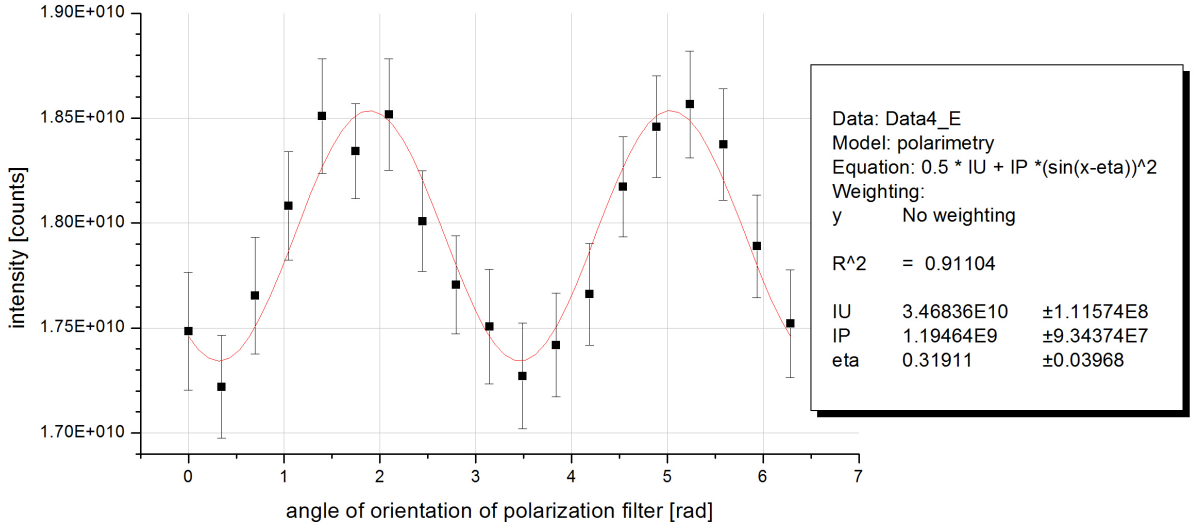

Figure 55: The intensity of light beam produced by collimated source with the incandescent lamp after pass through only the polarization filter. The curve is fitted with $y = 0.5I_U + I_P \cdot \cos^2(x - \eta)$. The best fit (red curve) is obtained with $I_U = (3.468 \pm 0.011) \cdot 10^{10}$, $I_P = (1.195 \pm 0.093) \cdot 10^9$ and $\eta = 0.319 \pm 0.040$. The chi-square is 5.29 and the degrees of freedom are 16 (19 fits points minus 3 fit curve parameters). The fit is good at 99.5 % of probability. The degree of polarization is $(3.33 \pm 0.26)\%$

5.2.2 measure of the transmission and reflection coefficients

Using the same measurement procedure used to calibrate the source the following measurements are made:

1. The Brewster window has been placed on the optical bench. The detector was placed laterally to measure the intensity of the reflected beam from the Brewster window. See fig. 47, a, detector position 1.

2. The detector was placed directly on the "main line of the light beam"behind the Brewster window. See fig. 47, a, detector position 2.

3. The polarizing beamsplitter has been added to the optical bench. The detector was placed laterally to the beamsplitter to measure the intensity reflected by the beamsplitter. See fig. 47, b, detector position 3.

4. The detector was placed at the end of the "main line of the light beam"for measuring the intensity transmitted by the beamsplitter. See fig. 47, b, detector position 4.

The acquired images are analyzed with the same methodology of reduction and data analysis of the source calibration of previous paragraph.
The data obtained are normalized with the calibration curve of the source is shown in fig 55. In this way the effect of the polarization of the source has been removed.
Fig. 56 reports the normalized measurements.

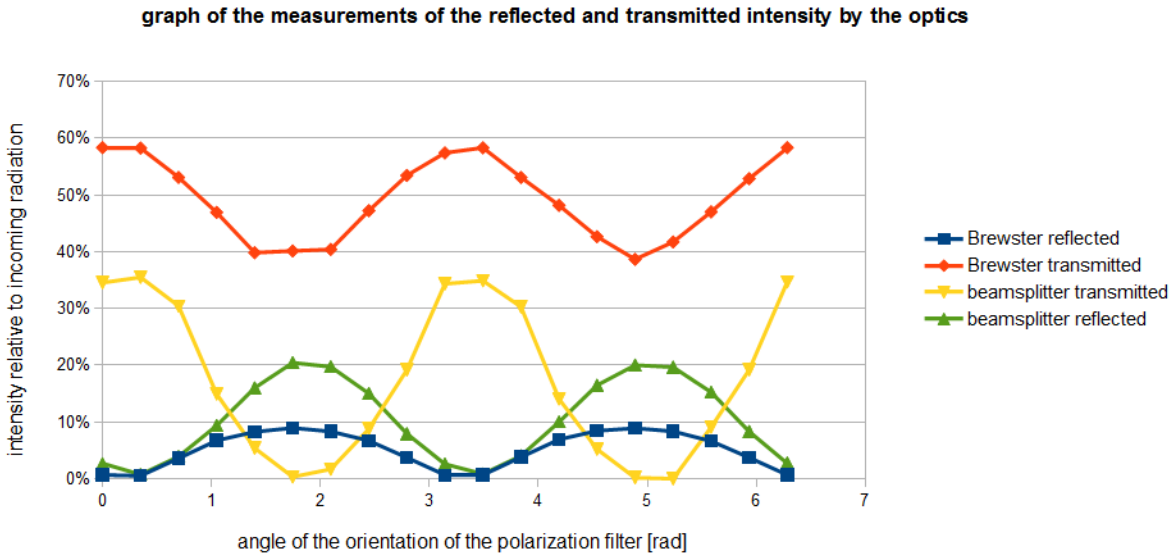

Figure 56: Graph of the measure obtained for the intensity reflected and transmitted for Brewster window and polarizing beamsplitter.

5.2.3 Comparison between measured and computed values

The expected values of the intensity "I_0"and "I_{90}", in the two orthogonal polarizations, were calculated using the law of Malus:

$$\begin{aligned} I_0 &= \tfrac{1}{2} \cdot I_U + I_P \cdot \cos^2(\theta) \\ I_{90} &= \tfrac{1}{2} \cdot I_U + I_P \cdot \sin^2(\theta) \end{aligned} \tag{65}$$

where "I_U"is the unpolarized light, "I_P"is the polarized light, "θ "is the angle of oriantation of the filter. In these calculations the angle θ is the independent variable and has been chosen between 0 and 2π with 145 steps.
Fig. 56 shows the values established with fully polarized light ($I_P = 1$, $I_U = 0$ in arbitrary units). The results were shifted of 1.31 rad to put them in phase with the experimental measurements of fig. 57.

The expected graph is the similar to the measured graph. The intensities are different, but the relative angles of the maximum and minimum are the same. Comparing these graphs, it is possible to see that the general behavior of the optics corresponds to the expected one.

In order to obtain from the experimental measurements (fig. 56) the reflection and transmission coefficient of the optical components (Brewster window and polarizing beamsplitter), following integral over the angle for each measured beam was computed.

$$I = \int_0^{2\pi} I_\theta d\theta \tag{66}$$

The integral is approximated by the sum of all the measured values. There are not problems of normalization as the number of the angles is equal for all the measurements, and the angles are the same. The exposure time is uniformed to $\tau = 1/80$s for all measurements by a simple

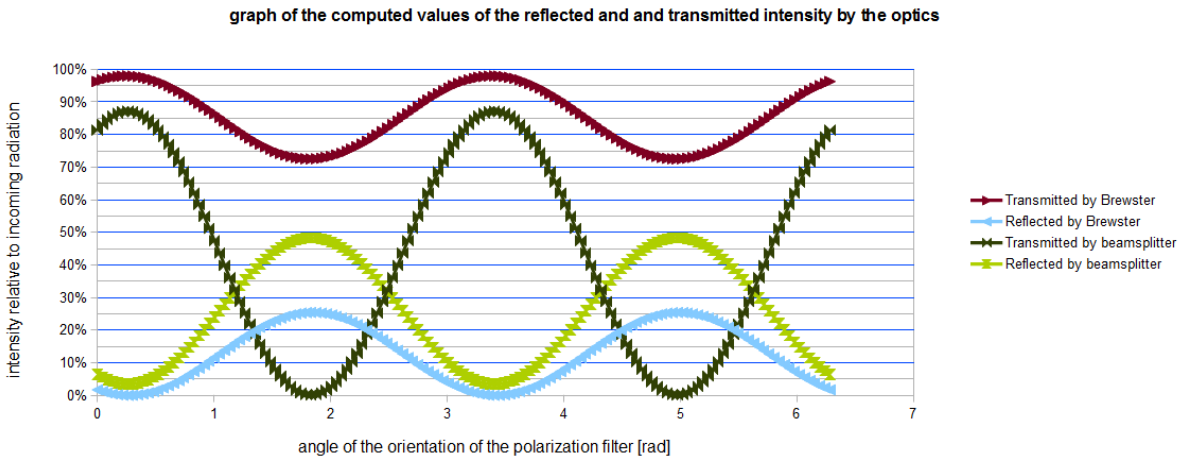

Figure 57: Graph of the computed values for the intensity reflected and transmitted for Brewster window and polarizing beamsplitter.

proportion.

Table 15 reports the obtained measurements of the intensity for different beams.

beam	Total intensity [counts]	ratio reflected over transmitted
reflected by Brewster	$(1.363 \pm 0.020) \cdot 10^9$	(0.1689 ± 0.0012)
transmitted by Brewster	$(1.166 \pm 0.097) \cdot 10^{10}$	
reflected by beamsplitter	$(2.78 \pm 0.17) \cdot 10^9$	(0.608 ± 0.037)
transmitted by beamsplitter	$(4.57 \pm 0.11) \cdot 10^9$	

Table 15: Measured intensity of the light reflected and transmitted by the Brewster window and by the polarizing beamsplitter. The ratio between reflected and transmitted intensity is in the second column.

6 Project of the prototype of the polarimeter

After verifying the correct operation of the optical design a project of a prototype polarimeter to observe exoplanets was performed.
In this chapter the design of a prototype of the polarimeter is presented with a general introductory description and then a detailed description of the various components of the polarimeter itself is illustrated.
The detectors used are finally presented and an overall estimate of the weight of the polarimeter is carried out to optimize the assembly with the telescope.

6.1 General overview

Fig. 58 reports a general scheme of the polarimeter. The project is modular, and the single boxes are described in a dedicated subsection. The figure is only a logical scheme, and it is not detailed or dimensional correct.

An astronomical source is selected by the light coming from the telescope through the "star

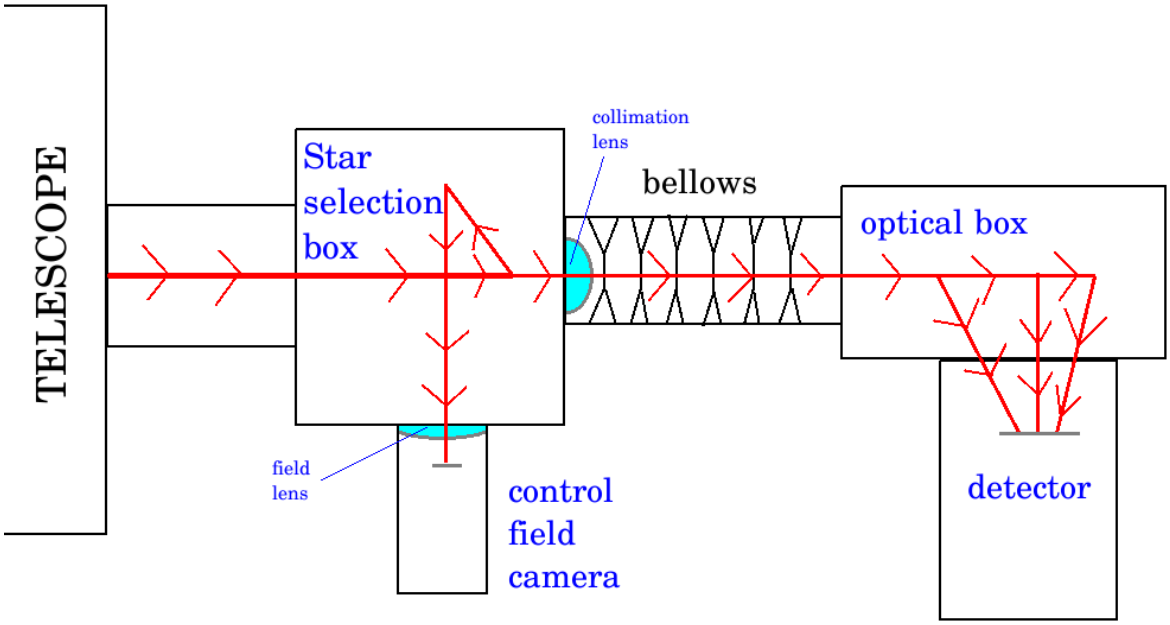

Figure 58: A general scheme of the polarimeter. In the scheme many optical components. are omitted. The optical paths are red lines.The dimensions are not in scale.

selection box". The focal plane of the telescope must be located inside this box. A field camera is connected to this box to control the telescope pointing and the orientation of the polarimeter respect to other celestial objects in the field.
The light of the selected source is decomposed within the "optical box"according to its polarization.
The "star selection box"and the "optical box"devices can be connected via a bellows to adjust

the focus distance, or directly joined to each other.
In the observations reported in the next chapter, it used the second configuration without the bellows.
A detector is placed in front of the "optical box"to acquire the information of polarization of the selected source. Fig. 59 shows the overall CAD project of the polarimeter. The design does

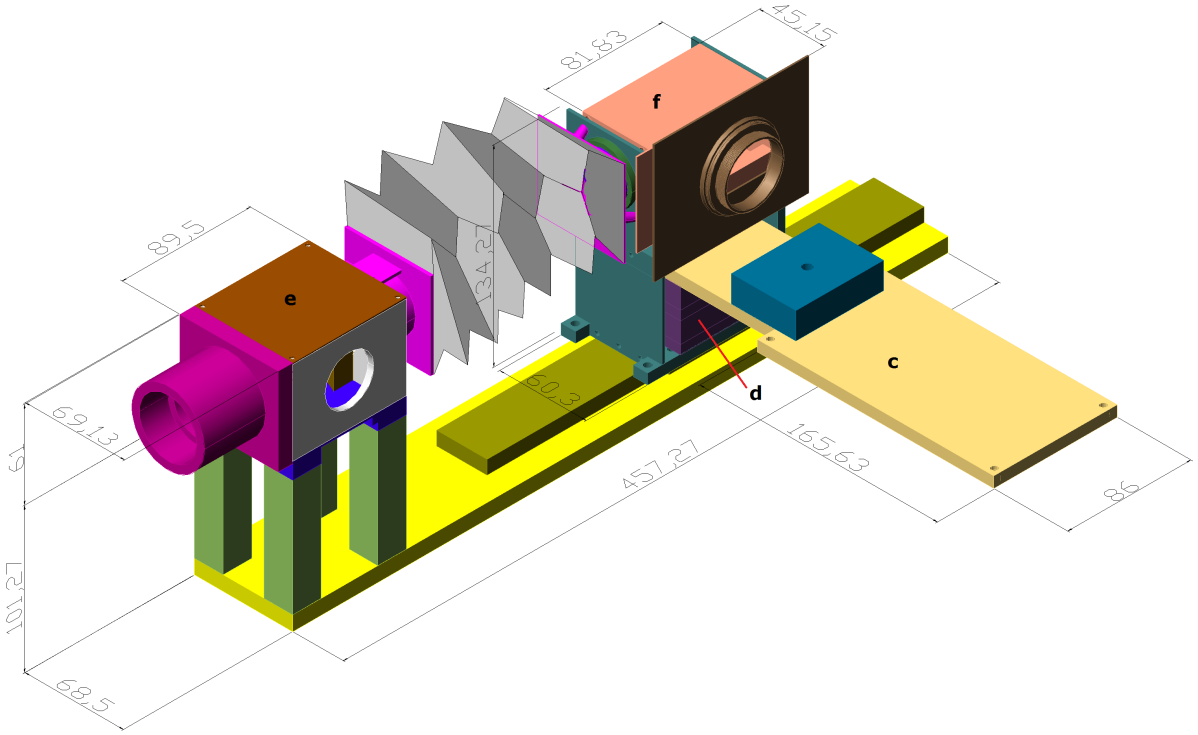

Figure 59: Isometric view of the projected in CAD of the polarimeter. The different colors are not realistic; they underline the different elements of the polarimeter. "c"bracket to support the detector; "d"slide rail to adjust the horizontal position of the detector; "e" "star selection box"; "f" "optical box".

not include the detector and camera control field.
A more detailed design is reported in fig. 110 in appendix A.7.

6.2 Optimization of the optical path length

The light exiting from the "star selection box" diverges (the angle depends by the focal ratio of the telescope). In order to refocus the light beam, a lens was added between the "star selection box" and the "optical box".
To select the lens optic calculus has been performed. Fig. 41 reports a scheme of the optic (replied in this chapter in fig. 60).
The distance between the telescope focal plane and the focus of the lens (the center of the lens

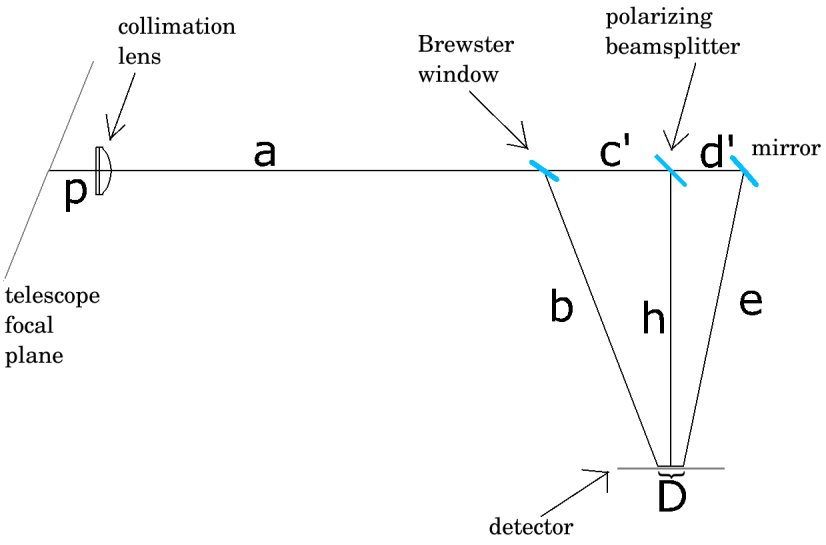

Figure 60: The optical scheme of the polarimeter. (The scheme is the same of fig. 41, here it is reported to facilitate the reader).

is inside the lens) is called "p".

- "a" is the distance between the focus of the lens and the Brewster window.
- "b is the distance between the Brewster window and the sensor.
- "c' " is the distance between the Brewster window and the polarizing beamsplitter.
- "d' " is the distance between the beamsplitter and the mirror.
- "e" is the distance between the mirror and the sensor.
- "h" is the distance between the beamsplitter and the sensor (it is equal to the distance between the telescope optical axis and the sensor).
- "D" is the distance between the spots on the sensor.

The mirror deflects the transmitted beam by beamsplitter. In this way it is possible to acquire with the same detector the all three beams.
The thin lens optical law is:

$$\frac{1}{f} = \frac{1}{p} + \frac{1}{q} \tag{67}$$

Where “f” is the focal length of the lens, “p” is the distance of the source from the lens and “q” is the distance of the image from the lens. In this optical scheme “q” is the sum of optical patches “a” and “b”.

$$q = a + b \tag{68}$$

The length of “b” is fixed as the scattering angle of reflected beam by Brewster window derives from physical laws. The orientation of the mirror could be changed. “p” could be changed screwing or unscrewing the lens. “a” could be adjusted moving all the “optical box”.

p [mm]	spot diameter on the lens [mm]	a [mm]	q [mm]	**f [mm]**	c [mm]	d [mm]	diameter BS refle. [mm]	diameter BS transm. [mm]
16	1.39	140.15	240	**15**	273.28	298.20	0.19	0.34
17	1.48	27.65	127.5	**15**	160.78	185.70	0.39	0.68
22.3	1.95	94.06	193.91	**20**	227.20	252.12	1.28	1.53
15	1.31	110.15	210.00	**14**	243.28	268.20	0.90	1.05

Table 16: Optical optimization of the focal length and the position of the focusing lens. “b”is equal to 99.85mm. “h”is equal to 93.14mm. “e”is equal to 95.05mm. The bold parameter are manually selected, the others are calculated. The last two columns are the diameter of the spot on the sensor for reflected and transmitted beams by beamsplitter. These diameters are computed for a point source. In case of an extended source the diameter of the source must be added. “c” is the total optical path of the beam reflected by the beamsplitter. “d” is the total optical path of the beam transmitted by the beamsplitter.

Table 16 reports four calculations for the optimization of the position of the lens. More cases are analyzed. Some are rejected as the focus is too close to the lens. It is impossible to get too close to the lens for the space occupied by the same supports of the optics. If the length “a” is too big, then the weight of the detector is shifted far from the back of the telescope, unbalancing the whole instrument. It would be preferable that the diameter of the spots was as small as possible. Note that the three beams have three different optical path lengths, so only one spot could be focused correctly. The beam reflected by Brewster window has the minor intensity (for unpolarized light), so it is better to focus it. The other two beams are defocused automatically. The defocus of the most intense beam helps to equalize the intensity specific for pixel of the three spots.

6.3 Components of the polarimeter

The various components that make up the polarimeter are described in detail in this section. For detailed mechanical drawings, see Appendix A.7.

6.3.1 Telescope connection adapter

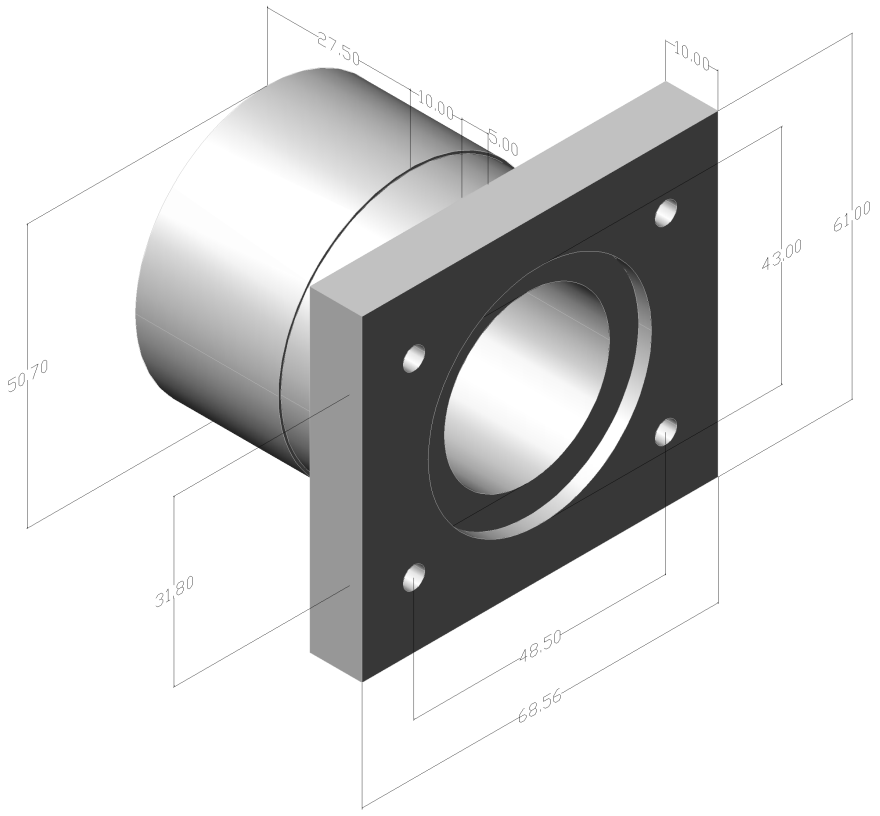

Figure 61: the project of the connection with the telescope. Dimensions are in millimeters.

Fig. 61 reports the design of the project of the connection with the telescope.
This connection has the task of connecting the polarimeter to 2-inch eyepiece opening of the telescope. This connection is intend to use only for the first tests. For the connection of the polarimeter to a professional telescope this connection will be completely re-designed according to the specifications of the telescope flange to which is to be connected.
Inside this connection it is possible to insert optical filters.

6.3.2 Project of box to select the celestial target and control the field of view

In order to select the source for polarimetry, the input section of a commercial spectrograph (Baader-DADOS, fig. 62) has been re-designed.

The system is based on two mirrors, that deviate the incoming path of 90°. The first mirror in spectrograph has a slit to select a portion of field, forwarding it to a grating.
In our case a circular hole was drilled in the first mirror. The diameter of the hole is 400µm,

Figure 62: "DADOS Slit - Spectrograph" produced by Baader Planetarium. The light enters on left side. A special system of mirrors select light of star by a slit in a mirror in a left box and a grating separates the light by wavelength in right box.

just more bigger than the diameter of the star in focal plane of a telescope with a 2m of focal length and a 20cm of aperture. The Airy disc in seconds of arc can be computed as:

$$D = 2.516 \cdot 10^5 \cdot \frac{\lambda}{Diameter} = 2.516 \cdot 10^5 \cdot \frac{550 \cdot 10^{-9}\text{m}}{0.20\text{m}} = 0.6919'' \tag{69}$$

The diameter in liner dimensions can be computed as:

$$Dia = f \cdot \tan D = 2\text{m} \cdot \tan 0.6919'' = 6.71\mu\text{m} \tag{70}$$

This diameter is the minimum diameter that a point source has on focal plane, but in realistic case the seeing enlarge this diameter until 50 or 100µm.
So a hole of 400µm was enough to pass the starlight. This diameter is different in 2 perpendicular directions because the circular hole is inclined, so the projection is an ellipse, and the thickness of the mirrors reduces partially the effective diameter.
The "star selection box" is composed of an external box and a support for two mirrors. The box has all the connections with the telescope, with the optics of the polarimeter and with the "star field camera".
Fig. 64 represents the support of the two mirrors. The production of this support is not possible in a monolithic piece as the spindle crashes against the same piece. For this reason, the mechanical service divides the piece into two parts, produced separately and after joined by two screws and two parallel pins.

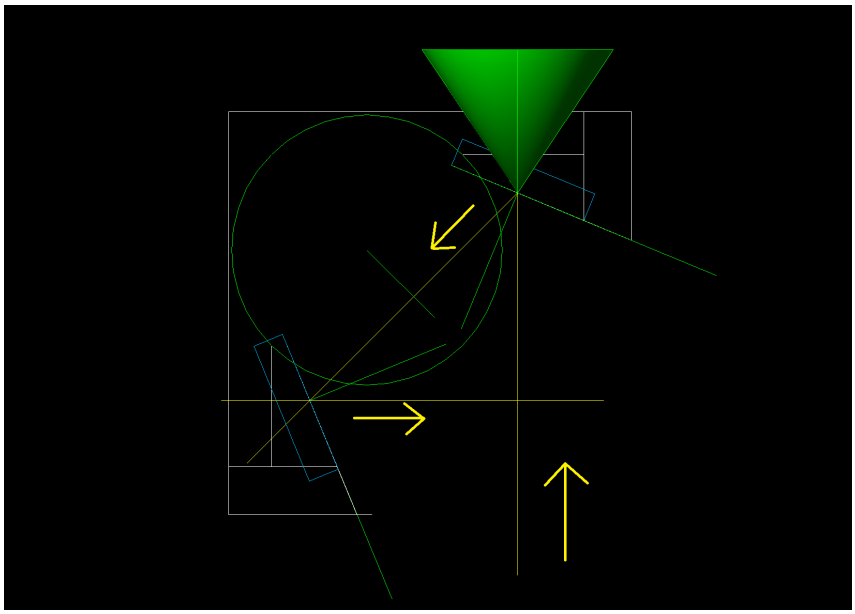

Figure 63: Design of the orientation of the mirror to reflect the star field toward the control camera or the eyepiece. The yellow arrows show the direction of propagation of the light. The green cone is the area that must be free to assure the right enlargement of the diameter of the spot as the light diverges exiting the focal plane of the telescope.

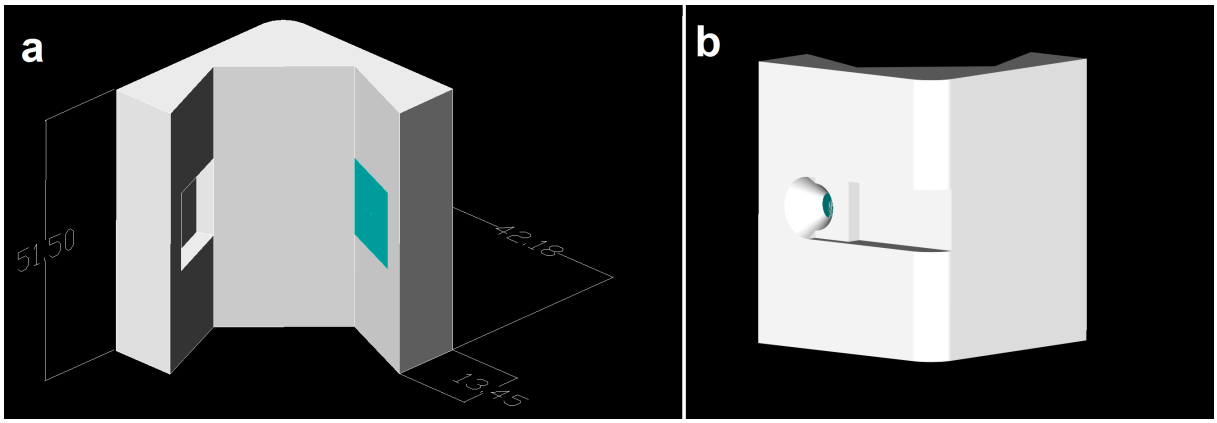

Figure 64: Project of the support for two mirrors. a) The right mirror was produced in the mechanical service with a central hole of 400µm of diameter. The left mirror is simple square plane mirror with a size of 15 mm of side and 3mm of thickness (not in figure). In figure dimensions are in mm. b) Back view of the support - The horizontal duct is necessary to pass light from illuminator.

The realization of the mirror with a hole was one of the most difficult mechanical steps in the realization of this polarimeter. Fig. 65 represents an ideal solution and a practical solution. The ideal solution has the hole parallel to the optical axis of the telescope. This solution is too complicated for the machine in our institution. The tip drill of 400µm of diameter bends and breaks when drilling is not perpendicular to the surface. So the practical solution adopted has the hole perpendicular to the surface and inclined respect to the telescope optical axis. At the back side of the mirror it was taken away a circular hole by a milling machine, leaving the last surface of about 300µm of thickness and a diameter of about 1mm. This last surface was drilled with the 400µm optical hole.
A first mirror was produced in aluminum. The most difficult work is to polish the mirror surface without a specific machine. The mirror is tried in a night by a test at a telescope. The control field camera (Sbig STi-I monochromatic CCD) is connected at the side exit. The surface anomalies are too big to have an acceptable star field images. In any case, it is verified the possibility of isolating a star and fitting it in the hole. A secondary CCD monitors this outlet. The light of the star passes trough the hole and produces a spot with a great diameter (it is comparable with the CCD sensor dimension of about 1cm). This big diameter is normal as the CCD is out of the focal plane of the telescope and there isn't yet a re-focusing lens. At the end of this test the "star selection box" could operate, but the quality of the holed mirror must be improved.
A second mirror was produced using an old hard-disk plate because these plates are very flat. This mirror has a sufficient flatness to monitor the star field.
The thickness of the hard disk (1.20mm) is less than the thickness of the aluminum mirror (3mm). For this reason, the support of the two mirrors is rebuilt by a 3D printer reducing the depth of the housing of the holed mirror.

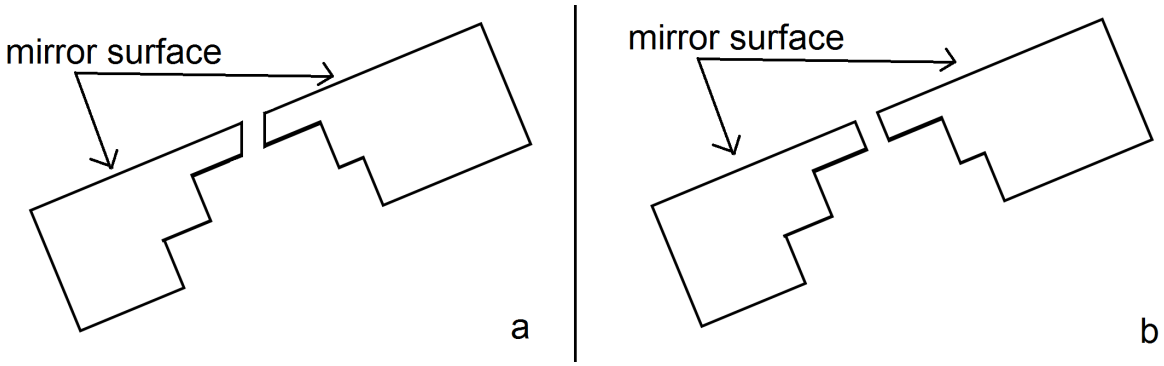

Figure 65: Sketch of mirror used to select a star for polarimetry. Two solutions are showed. a) an ideal solution. b) a practical solution. The dimensions are not in scale.

Fig. 66 shows the support of the two mirrors inside the "star selection box". The function of this box is to select the star, but also to interconnect mechanically the different parts of the polarimeter. The box has two covers: the upper cover is used to access to the inner parts, like the support of the two mirrors assuring that this support is in a fixed position. The bottom cover has the most important function, as it has four interconnections to support the weight of the detector. With the same interconnections, the bottom cover supports also the "optics box".

The weight of the "optics box" is about 200g, that is negligible respect to the weight of the detector (4kg). The bottom cover is assured at the box by eight screws.
The box has three threaded circular openings to connect an astronomical adapter. The front aperture has a diameter of 42mm to connect a standard adapter to the flange of the telescope. The side aperture has a diameter of 38mm. It is used to connect the control field camera with the lens to the "star selection box". The back aperture is not a standard photographic or astronomical thread. The back aperture is necessary to connect the lens to refocus the light of the celestial body selected, analyzing its polarization. Without this lens the light beam enlarges. The divergence is inversely proportional to the focal length of the telescope. Without the lens the diameter of the spot is too big to enter in polarization optics and in the detector. With this lens, it is possible to create a collimated light beam, or a focused light beam. To collimate the beam, the focus of the lens must coincide with the focal plane of the telescope (in this case is the "hole mirror" surface).
The dimensions and the thickness of the side walls of the star selection box are not standard numbers as the project was revisited many times, also during mechanical works.

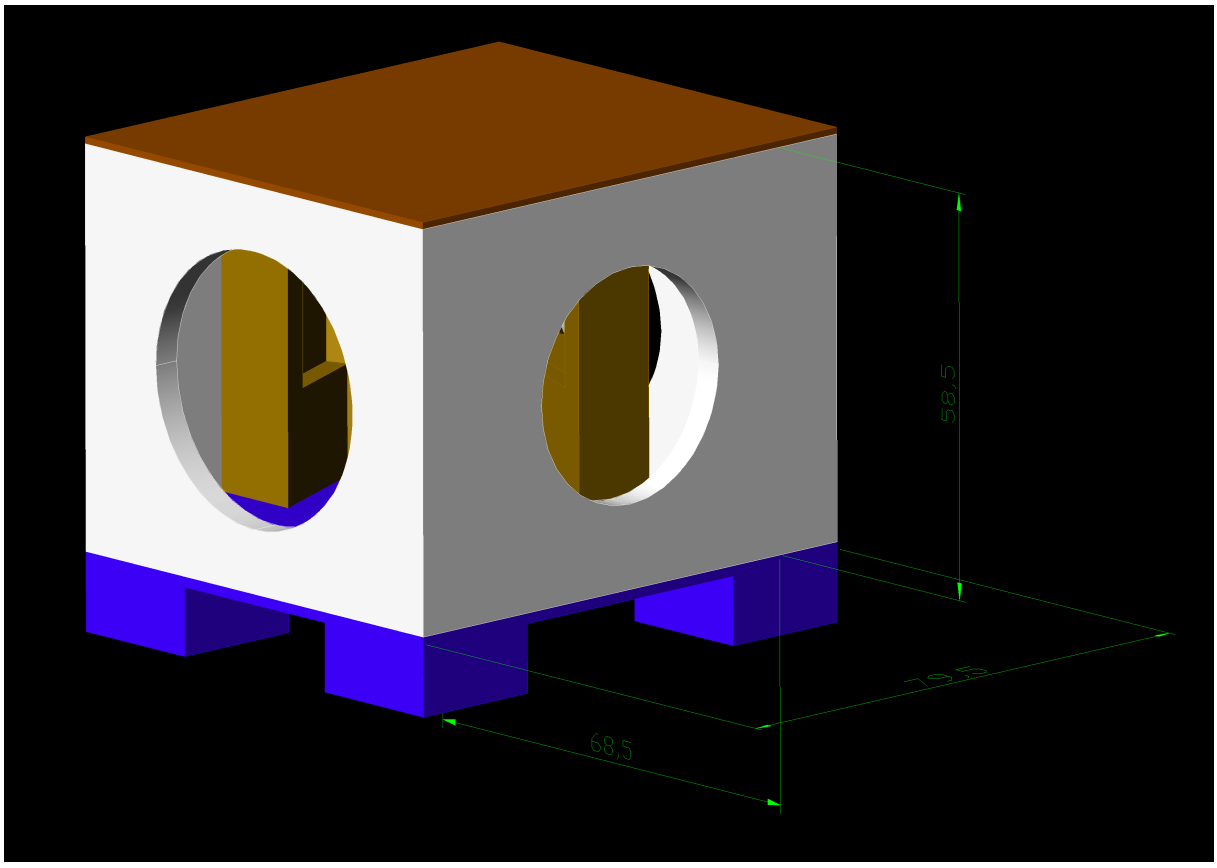

Figure 66: Isometric of the star selection box. The main function of this box is to select the star to analyze and to control the star field assuring the correct pointing of the telescope. This box has two covers: the top cover (brown) is used to access internal parts; the bottom cover is used to connect the other components and the detector of the polarimeter. Dimensions are in millimeters.

6.3.3 Collimation lens

As described in Chapter 5 after selecting the light source to analyze a collimating lens is necessary because the light beam after the focal plane of the telescope diverges.
Fig. 67 illustrate the project of the support of this lens. The support has an external thread to focus the lens. A lens of 15mm of focal length has been selected with three different coatings: the first optimized for visible wavelengths, the second for near infrared wavelengths and the last for visible extended to near infrared.

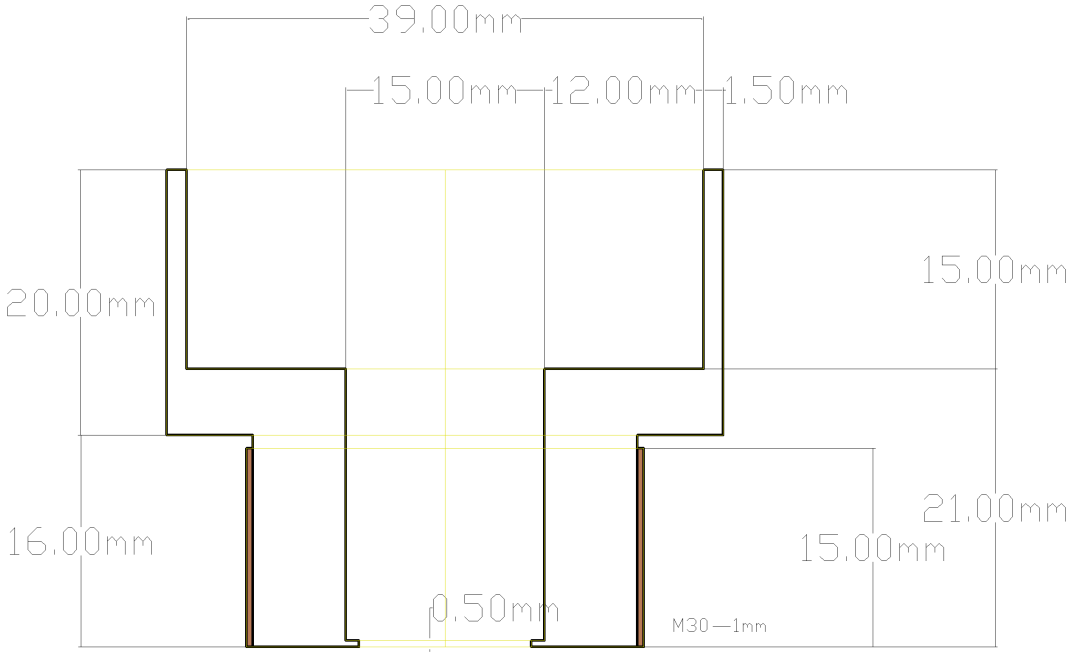

Figure 67: Section of the support for the lens putted after the "star selection box" to refocus the light beam after the telescope focal plane.

6.3.4 The bellows

Between the lens and the "optics box", there is a variable distance to optimize the spot diameter and focusing conditions. The "optics box" and detector can turn away from the lens of about 20cm. They can also come near few centimeters from the lens. A black bellows was built to exclude the light in all the situations.
The bellows was made by a black skin goat. An internal structure of black cardboard was glued to the skin shaping the creases. The skin was also glued to itself by a bench vise. Two special junctions have been designed. These junctions were realized by a 3D-printer. One of them is not realizable in the mechanical service with three or fuor axis milling machines without modifying the project (see fig. 69). The junctions connect on a side to the support of the lens and to the other side the optical box. The junctions are glued to the skin and screwed to the "star selection box" on a side and to the "optics box". The lens support rotates by hand around a cylindrical ring, visible in fig. 68. The horizontal brackets are external of the support lens, but they permit the hand access to the lens support but not a complete rotation of 360°.

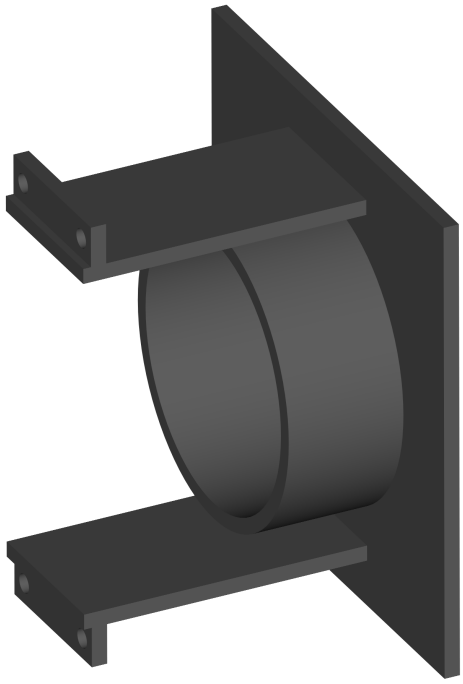

Figure 68: Design of the junction between the lens support and the bellows.

Fig. 69 shows the other junction. It has similar connection with the cylindrical support of the "Brewster support". The cylindrical support is around the long cylindrical ring and it is inward the little inner ring. The two holes on each cone are not perpendicular to the cone axis, and their function is to screw the support. The thread is not made by 3D printing, but it is engraved manually. By 3D printer, only two holes of 2.5mm of diameter were realized and then they were manually threaded with standard isometric M3. The screws connect with plastic thread are not very strong. In this case, the weight that these screws must support is very little (about one hectogram). In fact, these junctions do not support either the detector or the "optical box". Fig. 70 shows the bellows with two junctions glued together.

6.3.5 Slide rail

To move the "optics box" it was acquired a slide rail. The slide rail must be able to support the "optics box" and the detector. In the case of using the professional detector with the water cooling the weight could reach 5kg. The slide rail selected can support a weight of 30kg in horizontal mount and 25kg in the vertical mount. The polarimeter orientation is highly variable as the position of the slide rail (and all the other components) depends on the position of the celestial body in the sky. So, the orientation of the slide rail could not be estimated a priori: all the inclinations must be taken into account. In the worst case, the slide rail is stressed by a factor 1/5 respect to specification.
The slide rail is composed of a rail on which a small cart can move by the ball bearings. The

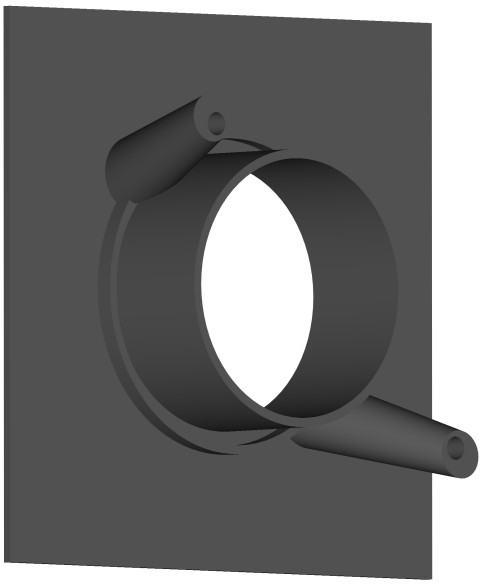

Figure 69: Design of the junction between the bellows and the “optical box”.

Figure 70: Photo of the bellow manually realized to interconnect the “star selection box” with the “optics box”.

rail has four screws M4 welded in the factory. The cart has four holes to connect user system with 4 M5 screws.

6.3.6 The optical box

The optical box has the task of supporting the main optics of the polarimeter. It allows to to regulate their collimation and to avoid the contamination from external light sources. Inside the box each optical component is supported by a suitable system in order to allowthe necessary geometrical adjustments.
The whole box can rotate, in this way you can adjust the height of the light beam reflected by the beamsplitter (see fig. 71).
The support of Brewster window has instead been inserted inside another cylindrical support (purple piece A in fig. 71) which allows it to rotate with respect to the beamsplitter. This rotation avoids the overlapping of the light beams so that they do not insist on the same plane. Supports to keep the Brewster glass and polarizing beamsplitter is the same described in chapter 7 (second version) and then used in the optical test provided in chapter 6.
Figure 72 reports an isometric view of the project of the rotatable support designed to orient

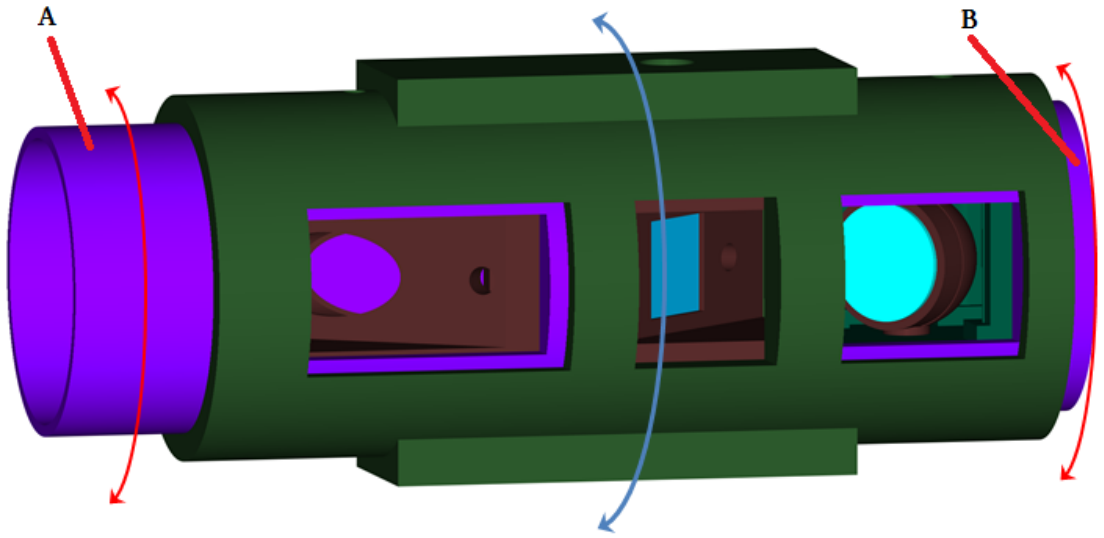

Figure 71: The Optical box. The arrows indicate the possible movements. The central blue arrow indicates the rotation of all the optical (used to adjust the height of the reflected beam from the beamsplitter). The side red arrows indicate the rotation of the supports of the Brewster window and the mirror. They are used to adjust the height of the beam reflected respectively from Brewster and that transmitted by beasmplitter.

the transmitted light beam from the beamsplitter towards the detector by a first surface mirror. A first reflective surface mirror has been chosen to avoid that the light beam passes into the the glass and so it is absorbed and subjected to aberrations.

The mirror is inserted by pressure in a holder (brown support in fig. 72) with 2 vertical cylindrical pins to rotate and slightly shift the mirror to be aligned with the light beam. This

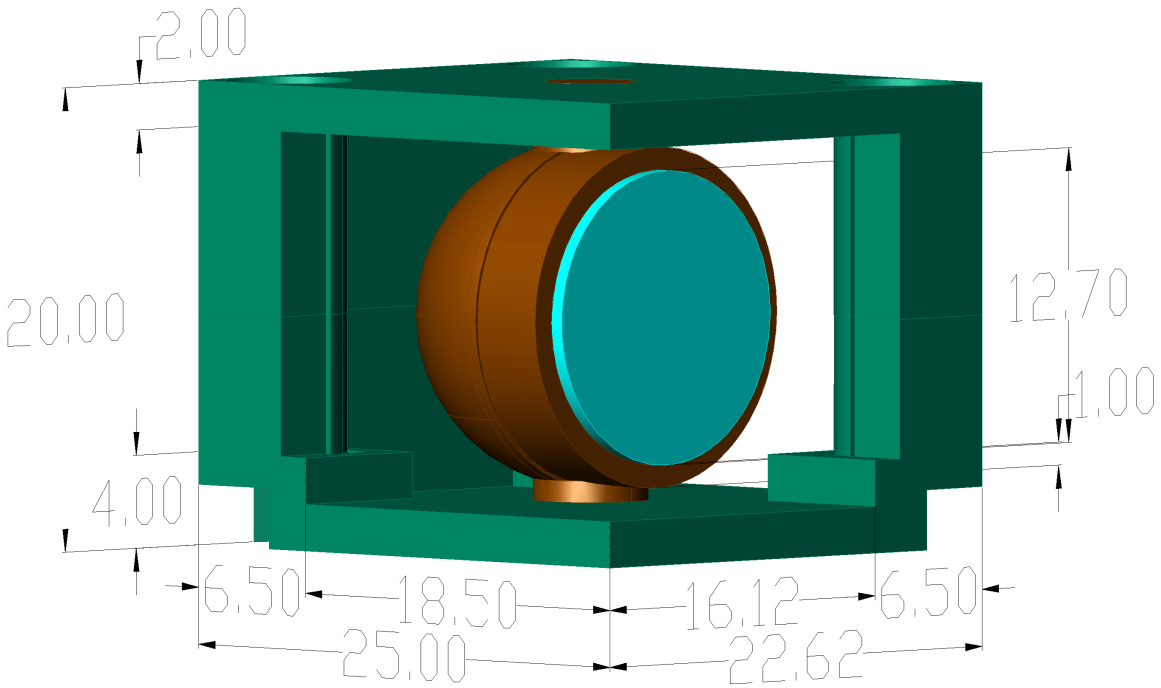

Figure 72: rotatable support designed to orient the transmitted light beam from the beamsplitter towards the detector by a mirror

rotation serves to adjust horizontally the light beam.
The external structure allows, instead, to insert this mirror in the rotating support B of fig. 71 that allows to adjust the vertical position on the detector of the transmitted light beam by the beamsplitter.
The adjustment of the position of the light beams must be carried out in advance before the observations then, once adjusted, the supports can be inserted and set by screws to stop the alignment of the optics. Then it is possible to close the polarimeter to prevent the entry of light. It is verified that by using a flexible cover is also possible to make small adjustments of the position of the light beams on the detector also during the observations.
These adjustments are made completely by hand. This approach is preferable in the prototype version of the polarimeter to facilitate improvement and learning in the early use of the new instrument. In next versions of the polarimeter some screws can be placed to adjust the position of optics manually or remotely, by using suited motors.

6.3.7 The Detectors

The detector is positioned on the "c"bracket of fig. 59. The horizontal position of the detector can be adjusted by the 2 Thorlabs slides indicated by the letter "d"in fig. 59. In particular, it is possible to move closer or farther away the detector to the optical box. Moving away the detector can approach the spots to fit them within the sensor. Approaching the detector, it is possible to move away spots on the sensor and can prevent overlapping of the spots on each other.
The other adjustment slide allows to move the detector in parallel to the optical axis to adjust the horizontal position (right / left) of the 3 spots.
Both of these movements act simultaneously on all spots.
The polarimeter is built with the possibility of utilizing more detectors.
In the polarimeter tests two detector was used: 1) A reflex photo camera Pentax K-7; 2) An Hamamatsu ORCA II Digital CCD camera C11090-22B.
The main advantage in the usage of the reflex camera during calibration and test are:

- It is light (the weight is less than 1kg).
- The reflex camera acquires at the same time three bands (Red, Green, and Blue) by a Bayer matrix deposed directly on the CCD Silicon wafer. This possibility was just used for lunar photometry and polarimetry [55] and [56].
- The acquisition system is tested in the factory. Therefore, its use is immediate.

On the other hand the reflex camera can't be utilized for high precision measurements because:

- The detector is not cooled. The noise depends in part on the sensor's temperature. This photo camera has a temperature sensor, but the temperature is not recorded in the header of the image file.
- The internal image processing algorithms are not known. For example, the camera subtracts a dark image for exposure time longer than 30s. For the shorter exposure time, it could be selected to activate/deactivate this function.
- The producer does not provide scientific specifications of the camera and its detector. A calibration could be performed to overpass this problem.

The Hamamatsu camera has a CCD back-thinned CCD with 1024 x 1024 square pixels each of 13µm of the side. The pixels can be binned in 2x2, 4x4 and 8x8. The readout noise is 6 electrons rms at the high-precision mode (the camera has two operating modes: high-speed readout or high-precision readout). Fig. 73 reports the graph of the quantum efficiency of the Hamamatsu camera in function of the wavelength.
Table 17 reports manufacturer's specifications of the camera.

The Hamamatsu camera is cooled by air system up to $-65°$C. The camera could also be cooled with water. The producer includes a fridge/pump to cool the water down of 10°C. In this way the sensor of the camera reach a temperature of $-90°$C and the dark current could be

Effective no. of pixels	1024 (H) × 1024 (V)
Pixel cell size	13µm (H) × 13µm (V)
Effective sensor area	13mm x 13 mm
Full well capacity	1×1: 80 000 electrons
Readout speed	3.15 frames/s
Readout noise	6 electrons rms
Exposure time	High-precision readout: 400 ms to 120 min High speed readout: 20 ms to 120 min
Cooling method / temperature	Forced-air cooled: -65 ℃, Water cooled: - 90°C
Dark current	Forced-air cooled (-65 ℃): 0.0065 electron/pixel/s Water cooled (-75 ℃): 0.0012 electron/pixel/s
Dynamic range	13 333:1
Analog gain	High-precision readout: ×1, ×4, ×18 High speed readout: ×1 to ×6
Binning	1 x 1, 2 × 2, 4 × 4, 8 × 8
A/D converter	16 bit
Lens mount	C-mount
Weight	approx. 3.6 kg

Table 17: Typical specification of the Hamamatsu C11090-22B camera.

also reduced.

The main advantages in the usage of the Hamamatsu camera are:

- The detector is cooled. The temperature of the sensor could be between $-90°$C (water cooling) and $-65°$C (air cooling). The noise is highly reduced.
- The Hamamatsu camera has a high quantum efficiency. This permits to have nearly one count for an incident photon.
- There are not absorbing filter in front of the sensor.
- The Hamamatsu camera has a wide dynamic of the analog to digital converters. ADCs use 16-bits rather than 12-bit of the Pentax's ADCs.

The main problems in the usage of the Hamamatsu camera are:

- Hamamatsu camera weight 3.6 kg without water cooling system (lighter configuration).
- The size of the sensor (13.3mm x 13.3mm) is smaller than the photo camera sensor (23.6mm x 15.7mm).

The reflex Pentax photo camera was useful for the first test of the polarimeter. The Hamamatsu camera is necessary to perform a high precision polarimetric measurement.

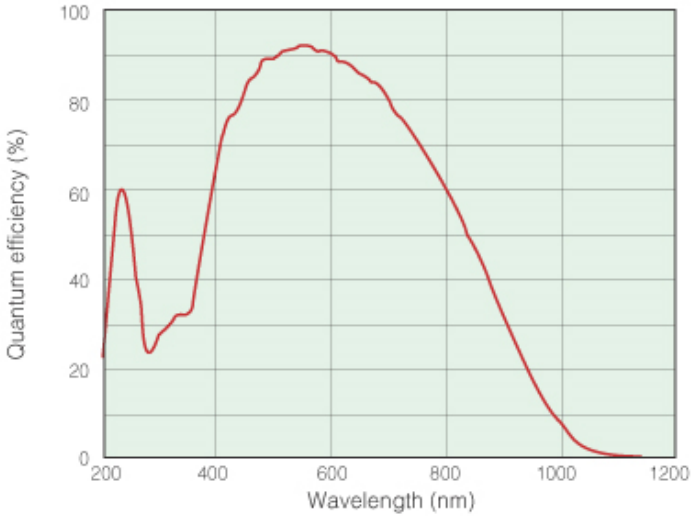

Figure 73: The response of the Hamamatsu C11090-22B camera in function of the wavelength. Credits: Hamamatsu.

6.3.8 Characterization of CCD Hamamtsu detector

In order to characterize the CCD camera in the best possible way some of its parameters (G, RN, linearity and Dark Current) has been directly measured.

The measurement of the gain is carried out starting from a bias frame and a flat frame. The standard deviation of an F frame is exposed to light:

$$\sigma_F = \sqrt{\left(\frac{\sigma_N}{G}\right)^2 + RN^2} \tag{71}$$

This camera does not have the bias acquisition mode. In order to acquire a Bias frame, it is necessary to set the exposure time to the minimum possible with the system covered to the light. In this way, the counts acquired will be mainly due to the reading system.
The flat has been acquired by a flat box piling up about 1/3 of the maximum of the counts of the CCD.
Table 18 reports the acquired measurements to compute the gain of the camera Hamamatsu

Frame tipe	exposition time [s]	mean value [counts]	standard deviation [counts]
Bias1 B1	0.400	2004.83	5.57
Bias2 B2	0.400	2003.63	5.53
Flat F1	1.2	23329	1440
Flat F2	1.2	22243	1368

Table 18: Frames acquired with Hamamatsu C11090-22B to compute the gain.

C11090-22B.
To avoid artifacts is preferable to use the standard deviation of the difference between the bias frame and the frame of Flat. First, the difference pixels to pixels of the frames is performed and then we calculate the standard deviation of difference frame.

According to Howell [70] the gain is given by:

$$G = \frac{(F1 + F2) - (B1 + B2)}{\sigma^2_{(F1-F2)} - \sigma^2_{(B1-B2)}} \tag{72}$$

Where $\sigma_{(F1-F2)}$ is the standard deviation of the difference between two flat frames and $\sigma_{(B1-B2)}$ is the standard deviation of the difference between two bias frames.
Substituting the measurements:

$$G = \frac{(23329 + 22243) - (2004.83 + 2003.63)}{(185)^2 - (7.78)^2} = 1.22e^-/ADU \tag{73}$$

The measured gain is $1.22e^-/ADU$.
The read noise can be estimate by [70]:

$$RN = \frac{G \cdot \sigma_{(B1-B2)}}{\sqrt{2}} \tag{74}$$

Using the same measurements used for compute the gain:

$$RN = \frac{1.22 \cdot 7.78}{\sqrt{2}} = 6.7e^- rms \tag{75}$$

This value is very near to the fabric value (of $6e^-$ rms).

The dark current was measured with the sensor cooled to -65°C through the air cooling system of which is equipped the camera. The dark current was measured with exposures time up to 30 minutes and was equal to $0.01\frac{e^-}{s \cdot pix}$. Also this value is similar to the fabric specifications ($0.0065e^-/(pix \cdot s)$).

We also verified the linearity of Hamamatsu C11090-22B camera acquiring light frames of a flat box with increasing exposure time between 0.4 s and 3.8 s.
The figure 74 shows the measured values. The intensity is the average of all the pixels, after subtracting the image of bias (the contribution of dark on these exposure times is negligible). Linearity is ensured up to about 60000 ADUs.

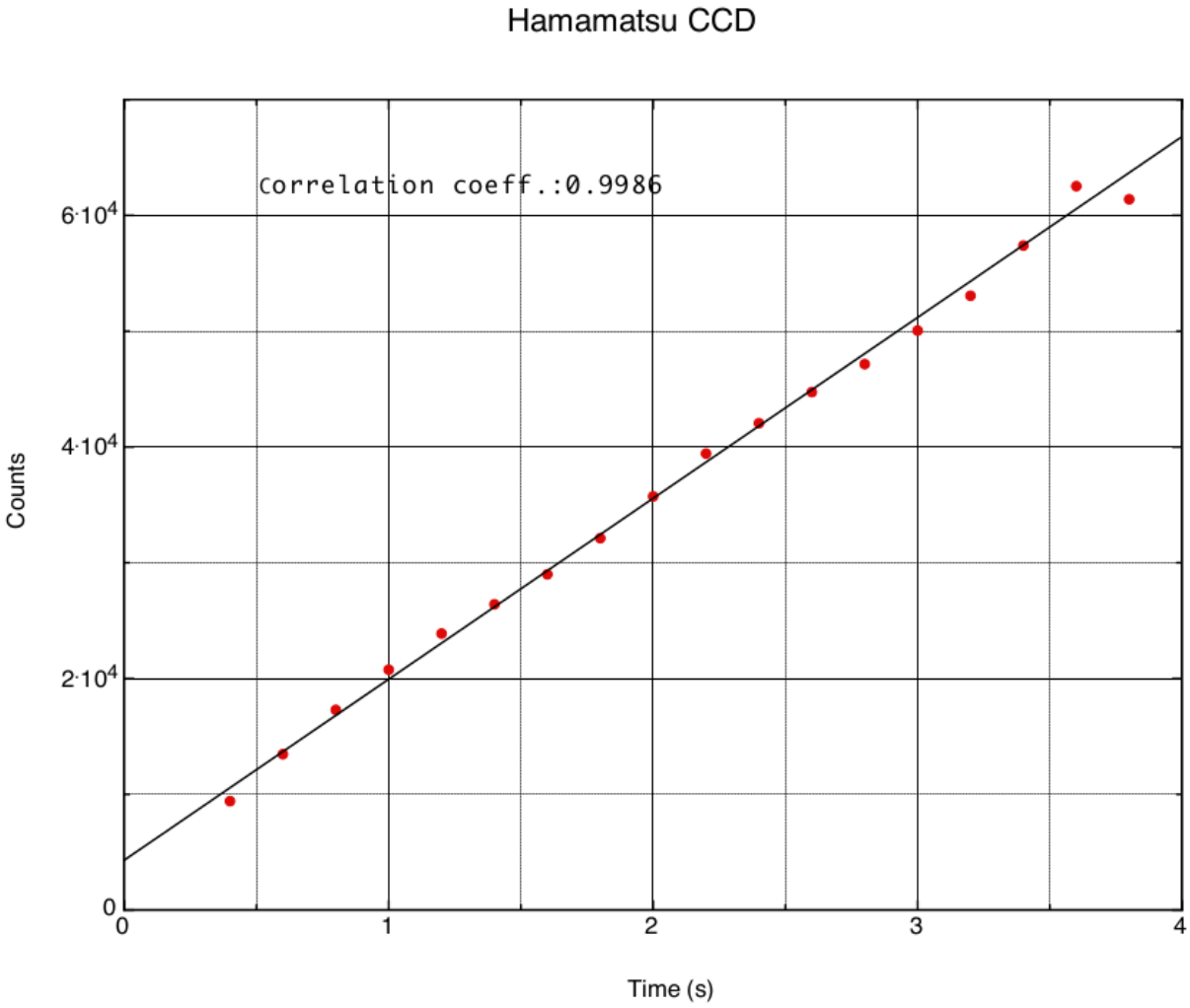

Figure 74: Measurement of the linearity of the CCD Hamamatsu C11090-22B camera. The line shows a linear best fit of the experimental data (red dots). The statistical fluctuation of the measured counts is too small to be represented.

6.4 Weight estimation

Table 19 reports the weight of the components of the polarimeter. The weight of some components is measured, and the other is estimated. The mass is estimated multiplying the volume of the component for the material density "ρ". Some part are made in aluminum ($\rho \approx 2.75\text{kg/dm}^3$), in steel ($\rho \approx 7.9\text{kg/dm}^3$) and others in 3D-printed plastic ($\rho \approx 0.92\text{kg/dm}^3$). The density of 3D printed plastic is taken from datasheet provided by the 3D-printer factory. The volume is derived from the CAD project by a software computation.

object	measured mass [kg]	extimed volume [cm^3]	extimed mass [kg]	material
star selectio box	0.641			Al
focusing lens with support	0.028			–
bottom cover of the box	0.108	0.0406	0.112	Al
fours columns		0.1319	0.363	Al
bottom bracket		0.2731	0.751	Al
bottom bracket excaveted		0.1390	0.382	Al
slide rail	0.274			steel
C bracket for optics		0.0687	0.189	Al
rack rail		0.0300	0.237	steel
rack wheel		0.0141	0.112	steel
Thorlabs supports	0.509			Al
Hamamatsu Bracket		0.1729	0.475	Al
bellows	0.072			–
bellows connections		0.0270	0.025	plas.
optical box	0.106			plas.
dark box		0.0239	0.022	plas.
Pentax connection		0.0451	0.042	plas.
Pentak K-7 body	0.806			–
Hamamatsu video camera	3.6			–
field CCD detector	0.150			–

Table 19: Weights of the components of the polarimeter. Some components are weighted; others are estimated. The volume is computed by a CAD software. The mass is the product of the volume for the density.

Table 20 reports the total weight estimated for the polarimeter. Four combinations are analyzed. The polarimeter can be used with two different detectors: a simpler and lighter photo camera and a professional cooled CCD. The bottom bracket (colored by yellow in fig. 59) could be excavated to reduce the total weight. The calculus is performed for the both situations.
The final decision was to excavate the base bracket to make the polarimeter lighter.
The prototype of the polarimeter was planned to be tested on a small commercial telescope, and the maximum weight that safety could be applied to the telescope is about 5kg in order to avoid mechanical flexures. With a Pentax photo camera, the weight is less than the safe weight. Another problem of this polarimeter is the distribution of the weight. The detector is located at a distance of about 40cm far from the back of the telescope and 20cm out of the telescope axis. A counter-weight could be applied in future to balance the weight, but the total weight

will increase.

	with Pentax	with Hamamatsu
solid bottom bracket	4.769 kg	7.563 kg
excavated bottom bracket	4.400 kg	7.194 kg

Table 20: Total weight calculated for the polarimeter used with the Pentax photo camera or the Hamamatsu video camera detector. Two solutions are analyzed for the bottom bracket: solid or excavated.

Fig. 75 reports a photo of the prototype of the polarimeter connected at the telescope of the RomaTre physics department. The optics are enclosed by a black cloth to assure the darkness.

Figure 75: The prototype polarimeter connected to the telescope of RomaTre physics department, observing some stars.

7 Calibration of the first prototype of polarimeter

This chapter presents the calibration of the prototype polarimeter.

7.1 Preliminary laboratory test of prototype of polarimeter

The first test is to assure the mechanical stability in the laboratory, before connecting the polarimeter to the telescope.
The cart on the slide rail supports the weight, but it has a backlash too high to assure a correct positioning of the detector. It is verified that the spots are smaller for the minimum distance of the "optical box" from the "star selection box" (for all the distances "p" of the lens of the fig. 60).
At the end of the laboratory test, the slide rail was substitute with a rigid slice of aluminum with the same thickness of the slide rail: 11mm. The bellows was removed and substitute with a simple sleeve bushing to fillet the two cylinders of different diameter.
In the future, a good upgrade could reduce the height of the four columns of 11mm. This upgrade could also help the rotation of the instrument around optical axis of the telescope.

The sensor of the Pentax camera could not be used in the whole area, as the inclination of the incoming rays is bigger than the maximum permitted from the market photographic lens. The lens holder mechanically stops some incoming rays (in particular the most difficult is the Brewster reflected image). Note that the only light beam perpendicular to the sensor is the beam reflected by the beamsplitter. The other two beams arrive inclined on the sensor. The beam reflected by the Brewster window has an incident angle of about 22° (respect to the perpendicular to the sensor's surface).
The Hamamatsu flange focal distance is 17.53mm, that is very less than reflex camera ($\approx$ 44mm). So, the geometric acceptance of the Hamamatsu camera is larger than the reflex camera. In the laboratory test of the polarimeter with the Hamamatsu camera, there are not obstruction problems.
Fig. 76 reports the detector's image of the first laboratory test with the Hamamatsu Camera.

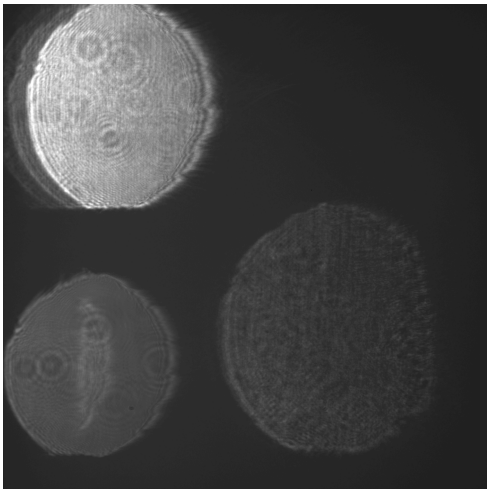

Figure 76: The first test in laboratory of the polarimeter.

The polarimeter is connected to the telescope (optical tube without mount), and a light torch is put in front of the telescope. This configuration is used to align the three spots into the detector. The diameter of the three spots is different, due to the different optical paths of the tree spots. Brewster reflected spot has the shorter path, so its spot is the smallest. The beamsplitter transmitted spot has the longest optical path and so its spot is the widest.
The diameter of the spots in laboratory is not the diameter of the star's spot as the used light source is not collimated, and it is not a point source.
The diameter of the spots is about 400 pixels ($\approx 375px$ for Brewster, $\approx 392px$ for reflected beamsplitter and $\approx 444px$ for transmitted beamsplitter). The thermal noise of the Hamamatsu camera at the temperature of $-65°$C is in a circle of 400 px of diameter is about (for producer's specifications):

$$\sigma_T(A) = A \cdot N_T = \pi \cdot \frac{D^2}{4} \cdot N_T = \pi \cdot \frac{400^2}{4} \cdot 0.0065e^-/px/s = 817e^-/s \tag{76}$$

In read out noise is:

$$\sigma_{N_r}(A) = A \cdot N_r^2 = \pi \cdot \frac{D^2}{4} \cdot N_r^2 = \pi \cdot \frac{400^2}{4} \cdot (6e^-)^2 = 4.52 \cdot 10^6 e^- \tag{77}$$

If the bin of the pixel of 8x8 is used the Read Noise is the same for the bigger pixel and the contribution to the measurement is reduced, else the dark noise is the same of the equation 73. The Read Noise in 8x8 cels bin is:

$$\sigma_{N_r}(A_{8x8}) = \pi \cdot \frac{50^2}{4} \cdot (6e^-)^2 = 7.07 \cdot 10^4 e^- \tag{78}$$

The total noise is the quadrature sum of the different independent noise. The photonic noise also give its contribution. The total noise of the spot is:

$$\sigma(A,t) = \sqrt{A \cdot {N_r}^2 + A \cdot N_T \cdot t + P \cdot t \cdot QE} \tag{79}$$

Where P is the star power collected by the telescope, QE is the quantum efficiency, and t is the integration time.
Without binning the read noise is predominant for time exposures until $\approx$ 90min (that is very close to maximum time exposure of the camera of 120 m) respect to dark noise. If the binning of 8x8 cells in CCD is activated the thermal noise predominant above $\approx$ 90s respect to dark noise.
The effective dynamic of a measure is now computed.
Supposing to see the star WASP-33 "W33"(first star in table 8) for an integration time of 180 s, using 8x8 binning. Suppose to use the $\eta = 50\%$ of the WC well capacity of each pixel. Laboratory test of the linearity of the detector could help to use higher value of η. The noise is:

$$\sigma_{W33} = \sqrt{\pi \cdot \frac{50^2}{4} \cdot (6e^-)^2 e^- + \pi \cdot \frac{400^2}{4} \cdot 0.0065 \cdot 180e^- + 1.04 \cdot 10^8 \cdot 0.75e^-} = 8844e^- \tag{80}$$

The signal acquirable is the intensity of the star:

$$S_{W33} = P \cdot t \cdot QE \cdot \eta = 3.92 \cdot 10^7 e^- \tag{81}$$

The signal to noise ratio is:

$$S/N_{W33} = \frac{S}{\sigma_{W33}} = \frac{3.92 \cdot 10^7 e^-}{8844 e^-} = 4432 \tag{82}$$

This S/N could be improved in the future using the full well capacity of the pixels of the detector (controlling in laboratory the linearity).

7.2 Source of calibration

The first analysis is to try to calibrate the instrument with one or more light sources. For a better result and to assure that we have not unwanted effects we also estimate fluxes and polarization. For astrophysical sources some effects that could alter the calibration are the polarization of sky, of the telescope, the interstellar medium etc...

Only a depolarized ($P = 0\%$) source is not sufficient to calibrate the polarimeter. With more sources, at least one of them must have a degree of polarization different from 0. The calibration consists in finding the response of the polarimeter to the polarization vector direction (not to the verse of this vector). At the input of the instruments enter photons that propagate along the z-axis, that is optical axis of the telescope. A reference frame is selected with plane "x-y" orthogonal to the optical axis, "y" is parallel to the minor axis of the Brewster Window and "x" points in positive versus toward the detector (see fig. 77). In the case of a depolarized light source the amount of photons that have Electric field aligned with x-axis "Ex" and those aligned with y-axis "Ey" are the same for each orientation of the polarimeter. With the same components in x and y-direction without a modulation with the orientation is logically impossible to estimate the dependence of response of the two optics by "Ex" and "Ey". In the same case from an optimization process could result the correct parameters of the optics from a depolarized source, but *"even a stopped clock gives the right time twice a day"* as a proverb says.

In others words, it is impossible to estimate the dependence of transmission and reflectance of polarimeter's optics by Ex and Ey field with a source that is independent by Ex and Ey.

A proper calibration could be performed in a laboratory using a light source and a linear polarization filter. In this case, the input of radiation of the polarimeter has the Electric field direction totally aligned in one direction. The problem is the efficiency of the filter that for photographic linear polarization filter is unknown.

Another solution, to calibrate the instrument in laboratory, is to use a totally polarized source of light.

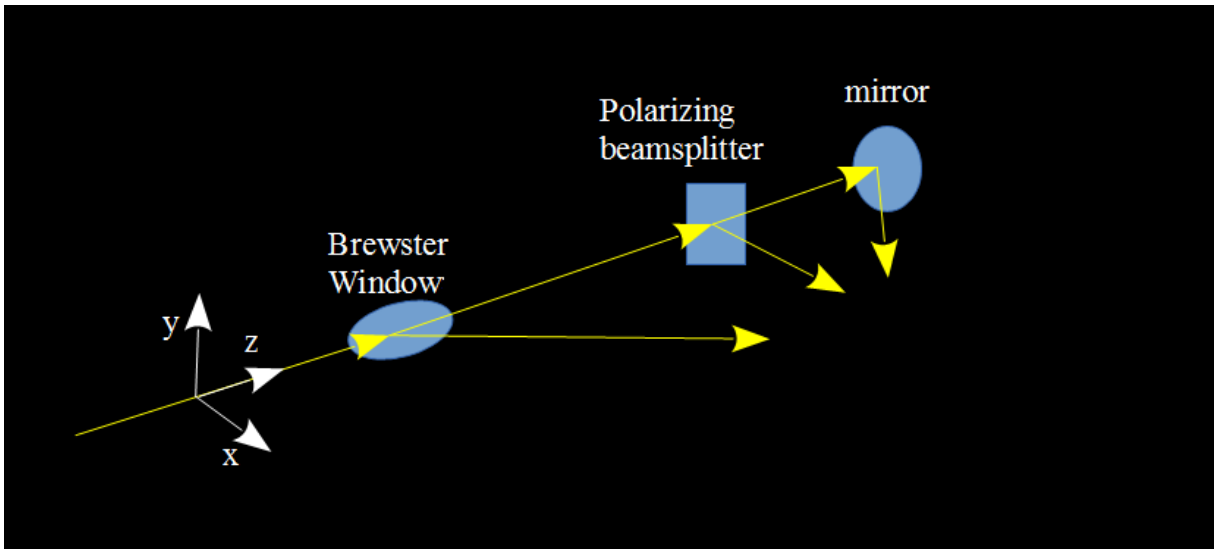

Figure 77: The disposition of optics. The yellow arrows represent the light rays.

7.3 Fitting software to analyze data

In order to calibrate and analyze the measurements of the polarimeter a software is written in C language. In the general version of the software it is optimized the transmission and reflection coefficients of the optics of the polarimeter, the polarization vector and the unpolarized light intensity.
The software uses a set of test parameters (in a defined range) to estimate the number of counts on the three spots. The calculated values are compared with the real value by the χ^2 (chi-square) statistical function. The software searches the parameters that give the minimum χ^2.
The program computes direct the statistical function χ^2. A subroutine nlopt (with the algorithm "NLOPT_GN_DIRECT_L") searches the global minimum of the χ^2 function.
The χ^2 is estimated as the quadratic difference between the real value and the expected value:

$$\chi^2 = \sum_{n=1}^{3} \frac{(mis_n - cal_n)^2}{(\sigma_n)^2} \tag{83}$$

Where mis_n is the measure of the spot number n, cal_n is the estimation of the measure, and σ_n is the error of the measure mis_n. The $n = 1$ is the spot produced by reflection of Brewster window, $n = 2$ is the spot produced by the reflected beamsplitter light beam, $n = 3$ is the spot produced by the reflection of the transmitted beamsplitter light beam. The formulas to calculate cal_n are:

$$\begin{aligned} F_s &= \tfrac{1}{2} \cdot I_u + I_p \cdot cos^2(\eta - \psi) \\ F_p &= \tfrac{1}{2} \cdot I_u + I_p \cdot sin^2(\eta - \psi) \\ cal_1 &= F_s[k] \cdot BR_{rs} + F_p[k] \cdot BR_{rp} \end{aligned} \tag{84}$$

Where I_U is the intensity of the unpolarized light, I_P is the intensity of polarization vector, η is the orientation of the polarization vector, ψ is the angle of orientation of the polarimeter, BR_{rs} and BR_{rp} are the coefficients of the p and s reflected components by Brewster.
Before calculate cal_2 and cal_3 the flux are projected to another reference system rotated by angle θ as in the polarimeter the beamsplitter is slightly rotated respect to the Brewster window to do not overlap the spots. The angle θ is estimated measuring the number of pixel of difference between Brewster spot and reflected beamsplitter spot multiplied by pixel dimension:

$$\theta = \arctan\left(\frac{N_{pixel} \cdot l_{pixel}}{distance_{sensor-optics}}\right) \tag{85}$$

The fluxes are computed in the new reference system rotated by θ:

$$\begin{aligned} F'_s &= \tfrac{1}{2} \cdot I_u + I_p \cdot cos^2(\eta - \psi + \theta) \\ F'_p &= \tfrac{1}{2} \cdot I_u + I_p \cdot sin^2(\eta - \psi + \theta) \end{aligned} \tag{86}$$

cal_2 and cal_3 are now calculated:

$$cal_2 = F'_s[k] \cdot BR_{ts} \cdot + F'_p[k] \cdot BR_{tp} \cdot BS_{rp} \tag{87}$$

$$cal_3 = F'_s[k] \cdot BR_{ts} \cdot BS_{ts} + F'_p[k] \cdot BR_{tp} \cdot BS_{tp} \tag{88}$$

Where BR_{ts} and BR_{tp} are the transmission coefficients of the Brewster window, BS_{rs}, BS_{rp}, BS_{ts} and BS_{tp} are the reflection and transmission coefficients of the polarizing beamsplitter.
The Brewster transmission coefficients "BR_tp", "BR_ts", are computed estimated as:

$$\begin{aligned} BR_{tp} &= \alpha_{BR} \cdot (1 - BR_{rp}) \\ BR_{ts} &= \alpha_{BR} \cdot (1 - BR_{rs}) \end{aligned} \tag{89}$$

Where α_{BR}, is the transmission coefficients of the Brewster window, supposed equally for each polarization components. Its value is supposed to be near 100 %. The advantage of this assumption are: 1) reducing the number of free parameters, 2) avoiding the possibility to have the sum of reflect and transmitted coefficients more than "1" corresponding to the creation of energy inside the glass (clear impossibly as the energy is one the quantity universally conserved). The disadvantage is to suppose that the transmission of the glasses is the same for each polarization status ("s" and "p").

To test the reliability of the program a set of "perfect" measurements are computed and analyzed. The only uncertainty of these measurements is the truncation and rounding error of the calculator.
The first test is to compute the χ^2 for the perfects coefficients to avoid simply writing errors. A null χ^2 is obtained.
With the virtual set of data two sub-algorithms of NLOPT are tested, that are "NLOPT_GN_ISRES" and "NLOPT_GN_DIRECT_L". The first algorithm uses a random research of values of the function; the second uses the previous calculus to estimate the minimum of the function. The second methods requires a lot of RAM memory as it must storage all partial results for all combinations of tested parameters. Each algorithm uses only one thread of the processor at the peak load permitted by the operating system. The angle θ computed in 85, is set equal to "0" in test environment.
The optics coefficients are searched between the boundary: the minimum equal to 0.00 (or -0.01) and the maximum of 1.00. The negative minimum is necessary for coefficients very close to 0 as the boundary solution for coefficients is a bad result of the software. In any case if one or more optimized coefficients are in boundary conditions the result is rejected.
To estimate the errors of the coefficients the Hessian matrix is computed by numerical second partial derivatives respect to the optimized coefficient. The errors are the square root of the double diagonal values of the inverted Hessian matrix.
Fig. 78 reports a flow diagram of the program.

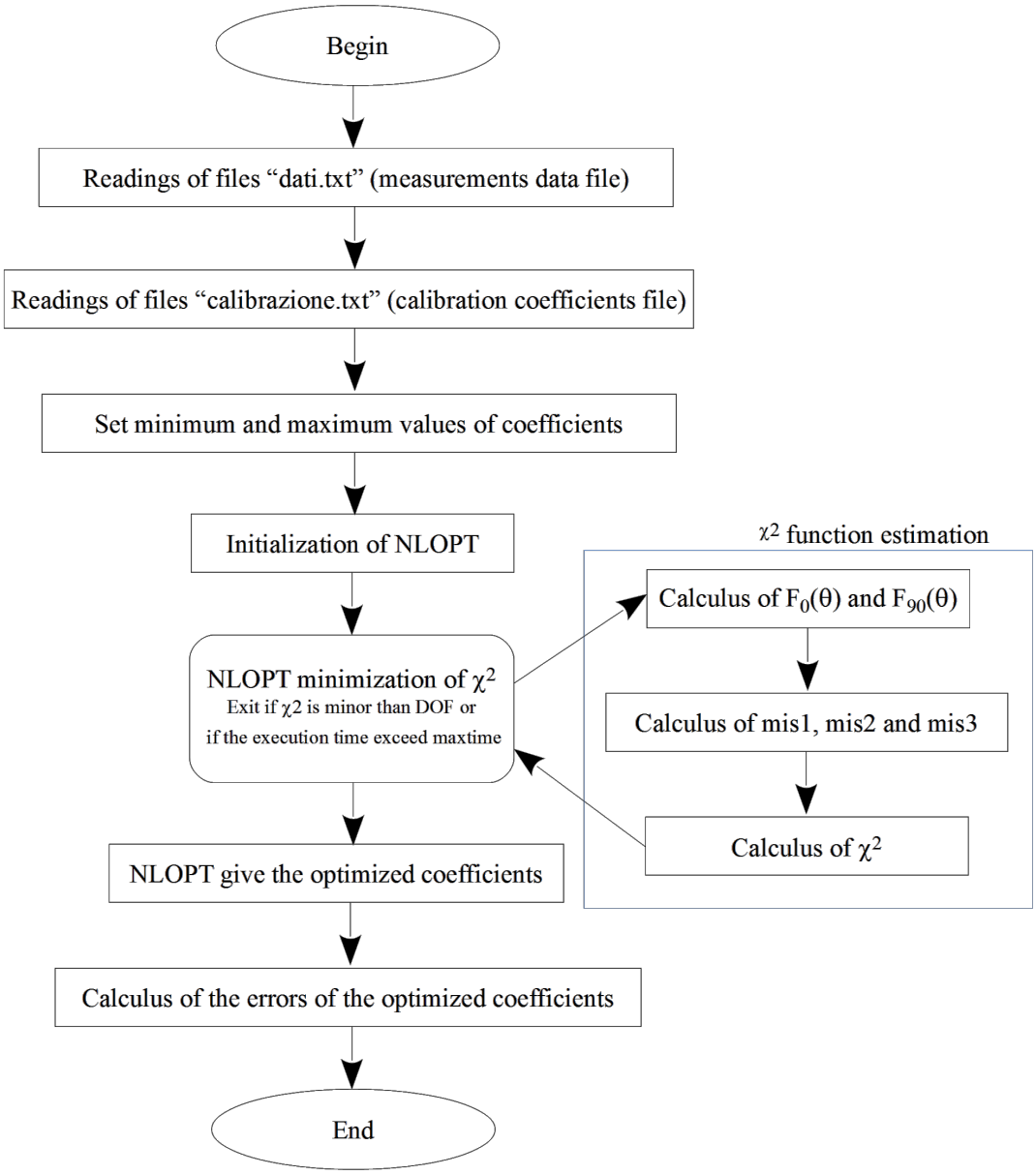

Figure 78: Flow diagram of the program written to optimized the coefficients of the polarimeter

7.4 Telescope Calibration

The polarimeter was tested at a small Schimidt-Cassegrein telescope with an aperture diameter of 20cm (Meade LXD75). The telescope is set on a Orion HDX110 EQ-G GoTo Equatorial Mount. The mount is screwed to a column of reinforced concrete, in order to assure the stability of the telescope.
A preliminary calibration test was performed. The light of a computer's screen was used as a light source. The computer's screen is high polarized. The degree of polarization is near 100 %.

Figure 79: The calibration setup. The computer used as source light is pointed out in the left red circle. The telescope with the polarimeter is in the red circle on the right.

Some boxes are drawn on the computer's screen to point the telescope to the same position of the screen and to determine the orientation of the polarimeter. The image is saved in a file without compression to avoid eventual shades. It is always important to point the same point of the screen as it is not ensured the perpendicularity of the screen to the optical axis of the telescope. A different inclination changes the polarization. To obtain a good calibration the polarization must be constant for all the measurements. If the observed polarization is not the real screen polarization it does not influence the calibration quality. The scope of these measurements is not to find screen polarization but to calibrate the polarimeter.

Fig. 80 shows the drawing utilized for calibration. During the calibration procedure, the "power saving" function of the operating system is disabled. It is highly deprecated that the screen power goes off, as it is not guaranteed that the luminosity is the same when it is again on. The source stability and eventually ripple in light intensity could be present. Analyzing more acquisitions these effects could be monitored.
The tracking of the telescope mount was turned off. Fig. 81 shows the control field camera pointed to computer's screen. The frame is the original frame not reduced. The only scope of the control field frames is to determine the inclination of the polarimetry for this kind of measure. No photometric information are obtained, so the image reduction (dark and bias subtraction and flat normalization) are not necessary. The screen of the computer is focused by Schmidt-Cassegrain primary mirror focuser. The mirror's hole is centered by "hand controller" of the mount.

The spots produced by this source are shown in fig. 83. The angle of orientation of the

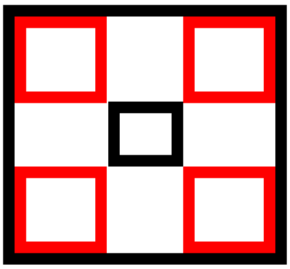

Figure 80: The calibration boxes utilized to point the telescope toward the computer screen.

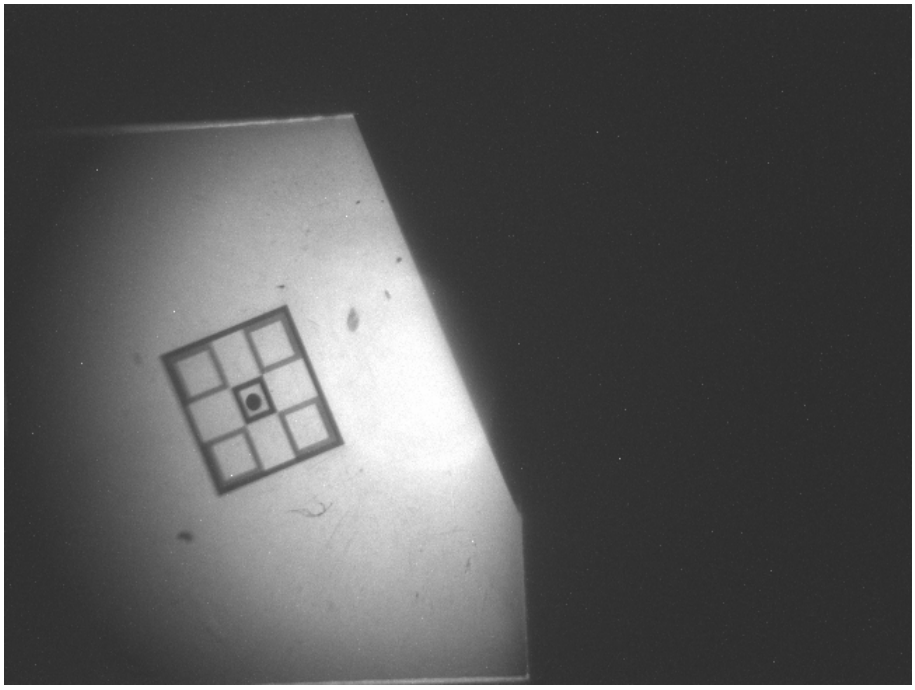

Figure 81: The field control during the calibration procedure. The black circle in the middle of the central box is the hole in the mirror. The light in the mirror goes to the polarimeter optics. The inclined black line is the edge of the computer.

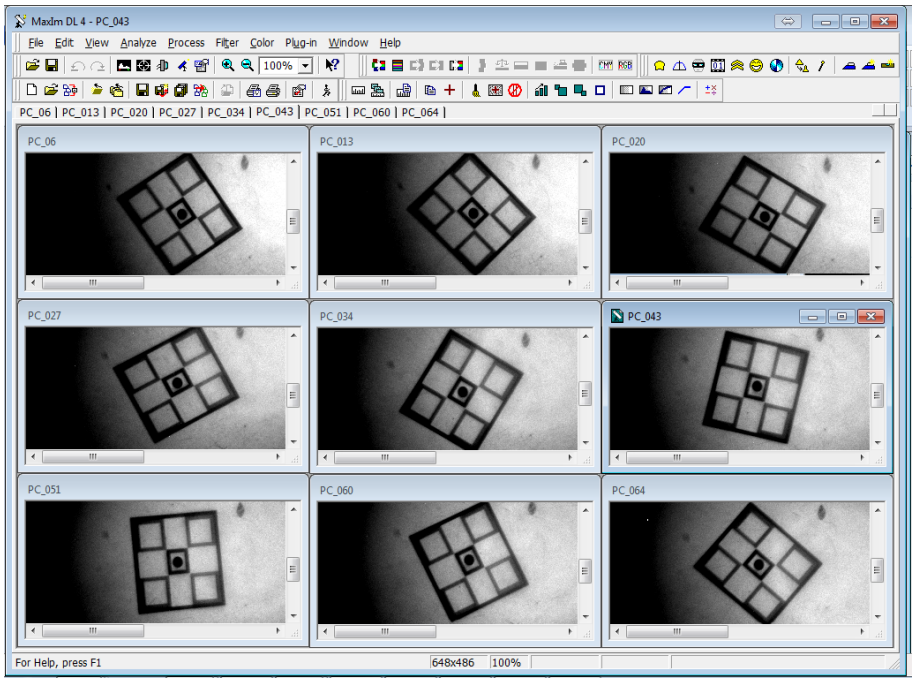

Figure 82: The image of the rotation angle of the polarimeter. The rotation is counterclockwise. Single rotation angle never exceed 45°.

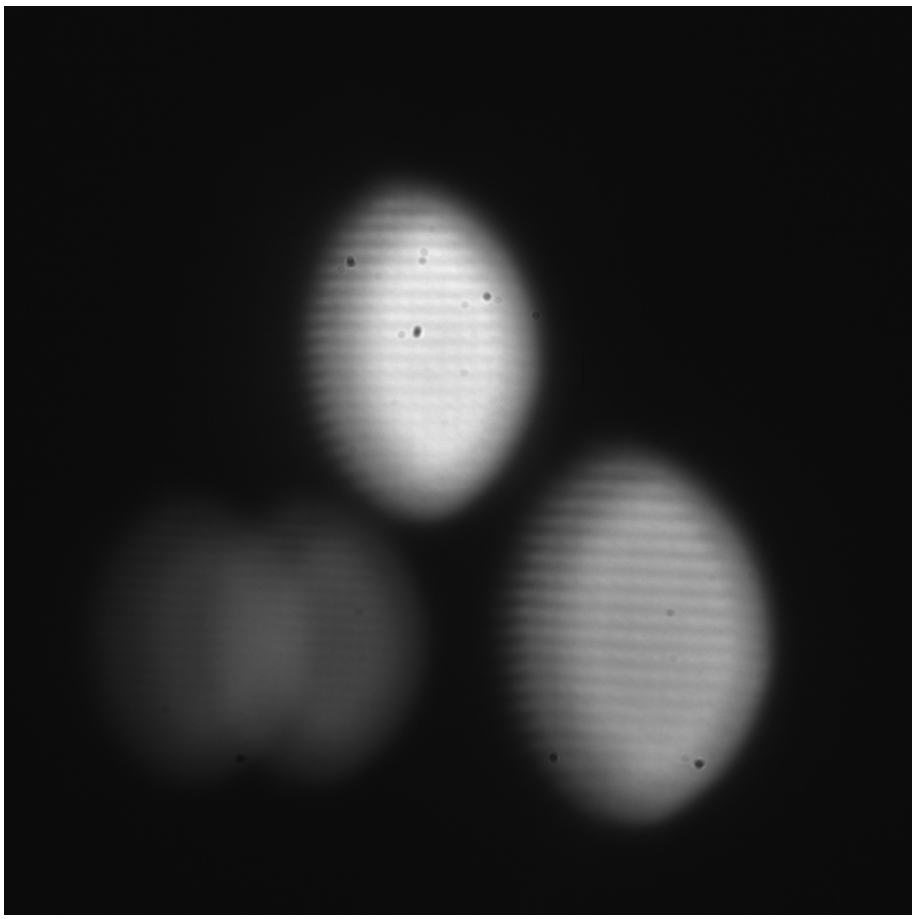

Figure 83: The 3 spots produced by calibration source on the Hamamatsu sensor. The polarimeter is oriented at 2.85 rad (respect to the first observation of this source). The mesh in the spot's images is the screen structure of the pixels of the same screen.

polarimeter is determined by pixel coordinates of two vertexes of the rectangular box. The error in angle determination is about 3 pixels for vertex. The length of the diagonal "d" is about 144 pixels.

$$\theta = \arctan \frac{\Delta l}{d} \approx 2.4^\circ \tag{90}$$

Each angle is measured with an uncertainness of $\pm 1.2^\circ$. The acquired images are analyzed by Hokawo software (made by Hamamatsu). The three spots are selected by the elliptic selection of the Hokawo software. A fourth ellipse is used in a dark area to estimate the noise level and the standard deviation of the noise. The selection is made by hand.
The mean noise multiplied by the number of the pixel of the ellipse is subtracted.

$$spot_n = Counts_{ellipse} - \langle dark \rangle \cdot Area_{ellipse}[pixels] \tag{91}$$

The noise is estimated multiplying the area of the ellipse used for select the n-spot for the standard deviation of the dark area.

$$\sigma spot_n = \sigma_{dark} \cdot Area_{ellipse}[pixels] \tag{92}$$

The intensity of the screen is observed at 10 angles (see fig. 81 and fig. 82). The values are inserting in the program of χ^2 minimization.
The program searches for a global minimum of the χ^2 function changing random all the free parameter in the given interval. The program stops if it is a minimum less than the number of degrees of freedom or if the execution time exceeds a maxtime (for this run it is set at 8 hours). The program stops for the maxtime. The result is compared which a shorter maxtime of 10 minutes. The results are the same, so the global minimum is reached. The χ^2 is statistically too big as it is 448 (10 degrees of freedom). Graph of fig. 84 reports the best fit with the optimization of the ten parameters (three parameters to characterize the light source and seven parameters to describe the reflect and transmission coefficients).

Brewster transm. p	Brewster transm. s	Brewster reflec. p	Brewster reflec. s	BS transm. p	BS transm. s	BS reflec. p	BS reflec. s	I_U 10^7	I_P 10^9	η
77.4%	101 %	22.8 %	-0.86 %	0.28 %	65.7 %	85.0 %	5.87 %	1.26	1.13	3.738

Table 21: Table of the coefficients of transmission and reflection estimated by optimization by software of the calibration dataset.

The table 21 reports the obtained parameters after the optimization. The negative parameter is changed to zero in next calculus and also the parameter that exceeds 100% is fixed to 100 %. The uncertainty in the intensity due to angle's error is now computed by obtained parameters. The angle's error is evaluated by the difference of a spot computed for the max angle shift.

$$\sigma spot_n(\Delta\theta) = |spot_n(\theta - \Delta\theta) - spot_n(\theta + \Delta\theta)| \tag{93}$$

For each angle and each spot is computed the quantity of equation 7.4.

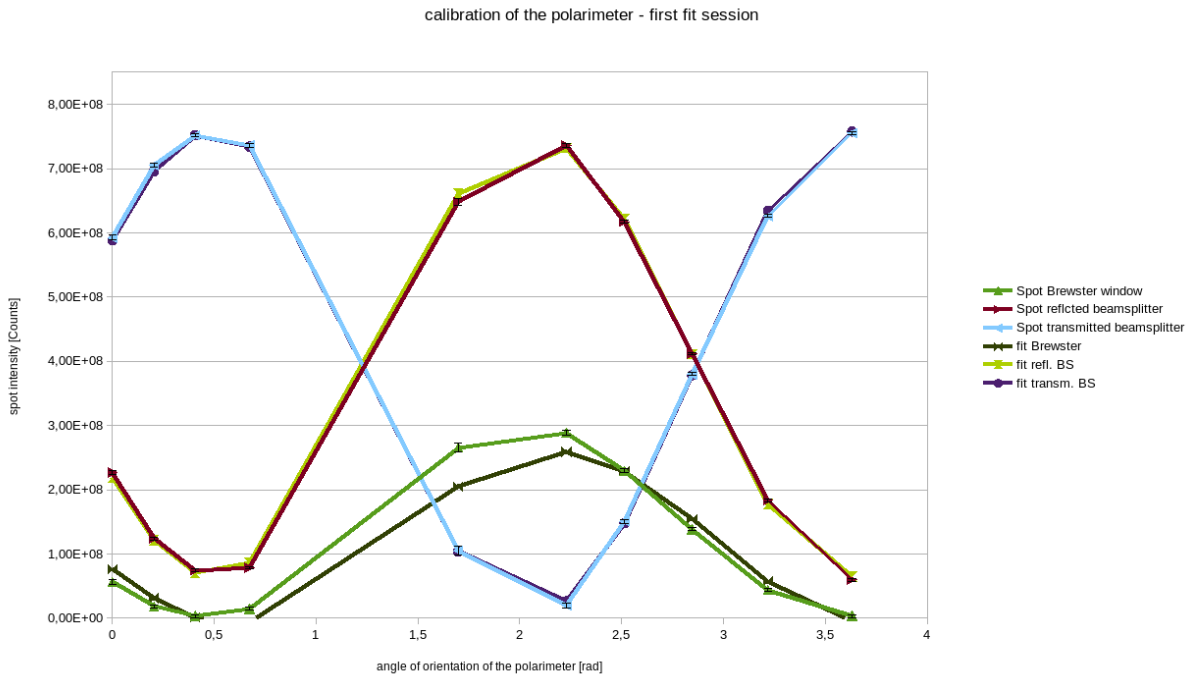

Figure 84: Measurements of calibration. The 3 spots curves are superimposed with the first fit.

The error of each spot is the sum of more errors:

$$\sigma spot_n = \sqrt{\sigma^2_{dark} + \sigma^2_{\Delta\theta} + \sigma^2_{reprodicibility} + \sigma^2_{photons}} \tag{94}$$

The new measurements are reanalyzed with the same program. The best chi-square is 12.95 with 10 degree of freedom.
The plot of fig. 85 reports the best second fit compared with the measurements with the total error bars. Table 22 reports the best parameter estimated by this fit. These parameters are realistic as they are similar to the expected value from physics laws and from Edmund specifications of the polarizing beamsplitter.

Brewster transm. p	Brewster transm. s	Brewster reflec. p	Brewster reflec. s	BS transm. p	BS transm. s	BS reflec. p	BS reflec. s	I_U 10^7	I_P 10^9
72.83%	98.85 %	26.22 %	-0.14 %	0.1 %	65.52 %	86.77 %	4.63 %	2.4414	1.15784022
±0.46%	±0.50%	±0.34%	±0.34%	±1.0%	±0.25%	±0.56%	±0.75%	±0.0014	±0.00000083

Table 22: Table of the coefficients of transmission and reflection estimated by the second optimization by software of the calibration dataset. The degree of polarization is $97.9350\% \pm 0.0012$.

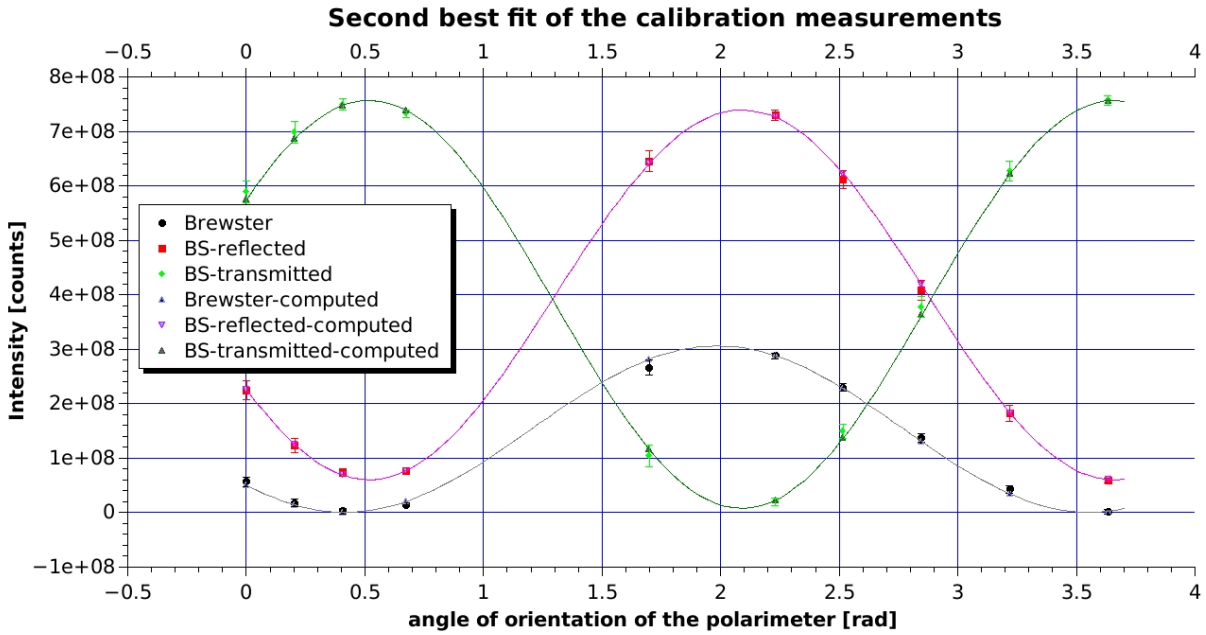

Figure 85: Measurements of calibration. The 3 spot curves are superimposed with the second fit. The vertical errors bar includes all contributions given in the formula 7.4.

8 Telescope observations

This chapter contains a number of tests carried out by the polarimeter mounted on one of the telescopes of the Department of Physics of RomaTre University.
The observation of the planets Saturn and Venus are shown.
A set of stars was analyzed.
Finally, a set of measurements of the Moon polarization was made at different phase angles, to control modulation of the polarization in function of the orbital position of the Moon.

8.1 Observations of planet and stars

The Solar System Planets are the first astronomical objected observed, as they are easily detectable and well pointing. It is also used the reflex photo camera detector.
Fig. 86 reports one of the first image of Saturn obtained. It is visible the ring of the planet. The image quality is not high, but the polarimeter is not projected (and optimized) for imaging. The capability of distinguishing the ring from the planet is just a good extra result.

Figure 86: Polarimetric images of Saturn acquired by Reflex photo camera detector in the 11th of June 2015. The camera acquires synchronously in the three bands: red, green and blue. Here is shown combined color images. In RAW images the three bands colors can be analyzed separately. Exposure time is 30 s, sensibility is ISO-1600.

Fig. 87 shown the image of Venus acquired by polarimeter on the 15 June 2015. The phase of the Venus is about 44 % as represented in virtual planetarium image created by Stellarium software (see fig. 88). The polarimeter image is highly similar to the virtual image. The rotation of the image is due to telescope optics and the particular angle of the orientation of the polarimeter.

Fig. 89 reports a first test of the polarimeter with the Hamamatsu detector. The observation

Figure 87: Polarimetric images of Venus acquired the 15th of June 2015 by reflex photo camera. It is evident the planet phase of about 44 % (see fig. 88). Exposure time is 1/3 s, sensibility is ISO-1600.

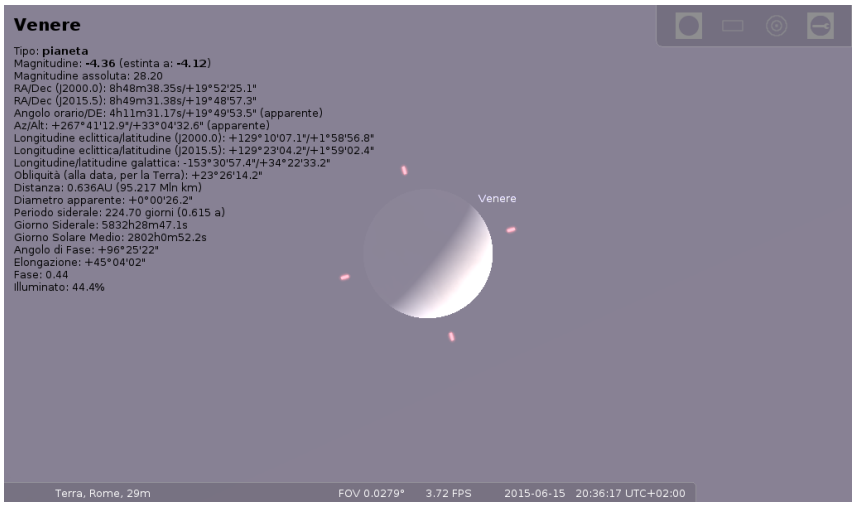

Figure 88: Virtual image of Venus in the 15th of June 2015 created by Stellarium planetarium software.

was performed the 27th of July 2015. The telescope is pointed to Saturn. In this configuration it is also visible Saturn's ring.

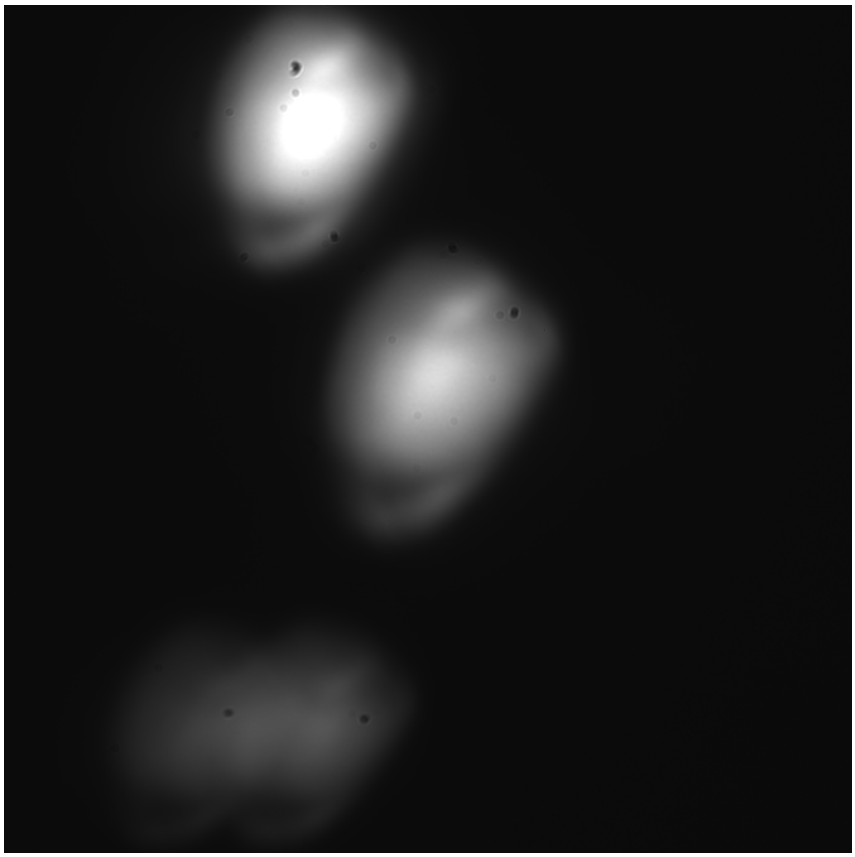

Figure 89: Polarimetric images of Saturn acquired the 27th of July 2015. The polar region is much intense in a polarization direction respect to the orthogonal direction as well known in literature.

Along July 2015 some stars were observed. The stars are pointed by telescope mount and next manually centered in the control field of view to assure that the star is in the mirror's hole. Table 23 reports some observation acquired by Hamamatsu video Camera C11090-22B. The observations are acquired in different days with different exposure time. The observed stars are:

- Sources 1,2 and 3 are the observation of the star HD 198237, RA 20° 47' 21", DEC +45° 34' 47" (J2000) acquired at different angle of the polarimeter. They are acquired in the 17th of July 2015 with 10min of exposure time.

- Source 4 is the star Tarazed, RA 19° 46' 16", DEC +10° 36' 48" (J2000). It is acquired the 27th of July 2015 with an exposure time of 1 s.

- Source 5 is the star Altair RA 19° 50' 47", DEC +08° 52' 6" (J2000). The observations are acquired the 27th of July 2015 with an exposure time of 1 s.

- Source 6 is the star Vega, RA 18° 36' 56", DEC +38° 47' 01" (J2000). It is acquired the 14th of July 2015 with 1s of exposure time.

The Counts are extracted with Hamamatsu Hokawo software manually selecting spot area with ellipses. Fig. 90 and fig. 91 report the Hokawo's windows of the stars frame analysis. The errors are estimated multiplying the standard deviation measured out of spots for the number of pixels (the same methods used for calibration, see equation: 91 and 92).
Notice that the total flux is not stable also for measurements of the same source. For long time expositions, this problem could be due partially to a de-pointing of the source. In fact, for the shorter exposition of Altair (source number 5) the total flux is more stable around $1.2 \cdot 10^8 counts$.

Table 24 reports the coefficients obtained by the program of minimization of the χ^2 function. In this case, only the intensities and polarization of the source are optimized, and the reflection and transmission coefficients are obtained from the previous calibration. The observations are corrupted by atmospheric turbulences, as the signal variations of the measurements are not compatible with expected polarization modulation. For example a rotation of the instrument of 180° must give the same value (it is verified in calibration), and in astronomical measurements the variations of atmospheric transmission change the signal. All the measurements could have a constant signal unpolarized plus a polarization signal modulate by square cosine in function of the angle of orientation of the polarimeter. This modulation is not observed in astronomical observations. The degree of polarization computed does not consider more angles of observation so that could be only an estimation.
If the observations are getting only at one angle only I_P (Polarized intensity) and θ are optimized, and I_U is set to null value. Physically is impossible determine these three source parameters with an observation at only one angle.
To determine the intensity F_0 and F_{90} is used the Malus law:

$$\begin{aligned} F_0 &= I_P \cdot \cos^2(\theta) \\ F_{90} &= I_P \cdot \sin^2(\theta) \end{aligned} \tag{95}$$

The degree of polarization is (in these measurements is impossible to determine the Stokes parameter U and V):

$$P \approx \frac{Q}{F} = \frac{F_0 - F_{90}}{F_0 + F_{90}} \tag{96}$$

star name	N	Brewster counts	Beamspl. reflected counts	Beamspl. transmit. counts	Brewster error	Beamspl. reflected error	Beamspl. transmit. error	Total intensity [counts]	Electric vector	Brewster over BS reflected	Brewster over BS transmit.	beamspl. reflect. over transmit.
HD 198237	1	66223954	201659456	148737261	1146657	770326	690802	4.17E+08	14433	0.328	0.445	1.356
	1	32860412	100938900	74944824	918507	617055	553353	2.09E+08	10216	0.326	0.438	1.347
	2	743807	2468847	1924912	646220	286922	486975	5.14E+06	1602	0.301	0.386	1.283
	2	42047848	121038342	94834933	1631110	724215	1229163	2.58E+08	11356	0.347	0.443	1.276
	3	341331	1457972	1141499	639348	283871	481796	2.94E+06	1213	0.234	0.299	1.277
	3	23919883	63967472	55985631	792236	351753	597008	1.44E+08	8482	0.374	0.427	1.143
Tarazed	4	4331536	12904082	10078231	536735	345257	363032	2.73E+07	3696	0.336	0.430	1.280
Altair	5	16110062	45226400	35611268	719975	452057	480533	9.69E+07	6962	0.356	0.452	1.270
	5	21247274	59560467	49787042	684335	429679	495207	1.31E+08	8081	0.357	0.427	1.196
	5	21966863	61738217	51512800	685692	430531	496189	1.35E+08	8222	0.356	0.426	1.199
	5	18218390	50936252	43740976	682655	428624	493991	1.13E+08	7513	0.358	0.417	1.164
2-13 Vega	6	19325589	56888244	52717428	1797354	1459365	1458239	1.29E+08	8029	0.340	0.367	1.079

Table 23: Table of the counts measured for four different stars. The number in first column represent the source. The same number indicates an observation repeated. 1,2 and 3 are the observation of HD 198237 at 3 different angles.

N	I_P	η	Mis_1	Mis_2	Mis_3	P(%)
1	370630602	5.464	45294075	140408533	103771837	6.7
2	50172960	2.3081	5941824	18584668	14514159	9.6
3	74764045	5.414	8165606	26143828	23337705	16.7
4	34528264	2.3052	4062699	12730714	10053485	10.2
5	127711459	2.2996	46673731	46673731	37642125	11.2
6	164757123	2.2713	17938269	57485480	51569884	16.9

Table 24: Table of the result of optimization by software of the data obtained by observation reported in table 23.

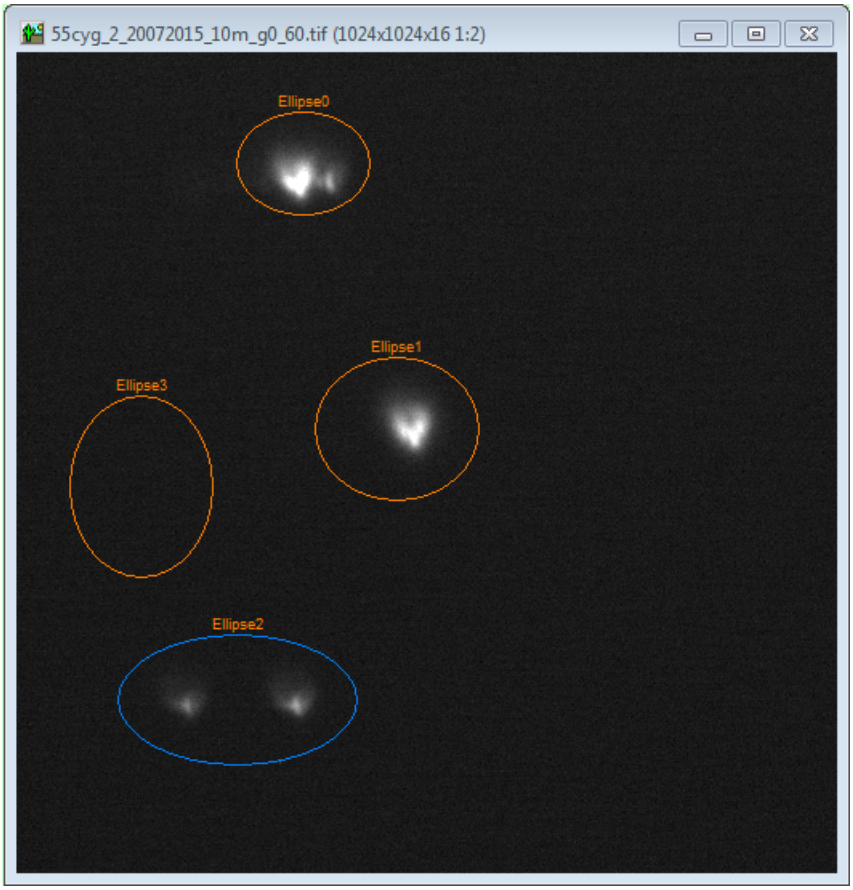

Figure 90: Image captured by Hamamatsu detector. The ellipses are the areas, where the intensity of 3 spots are measured. Ellipse0 is the spot produced by reflection of beamsplitter; ellipse1 is the spot produced by transmission of beamsplitter; Ellipse2 contains the two spot produced by reflection of the 2 surface of Brewster window; Ellipse3 is the area to estimate the background noise.

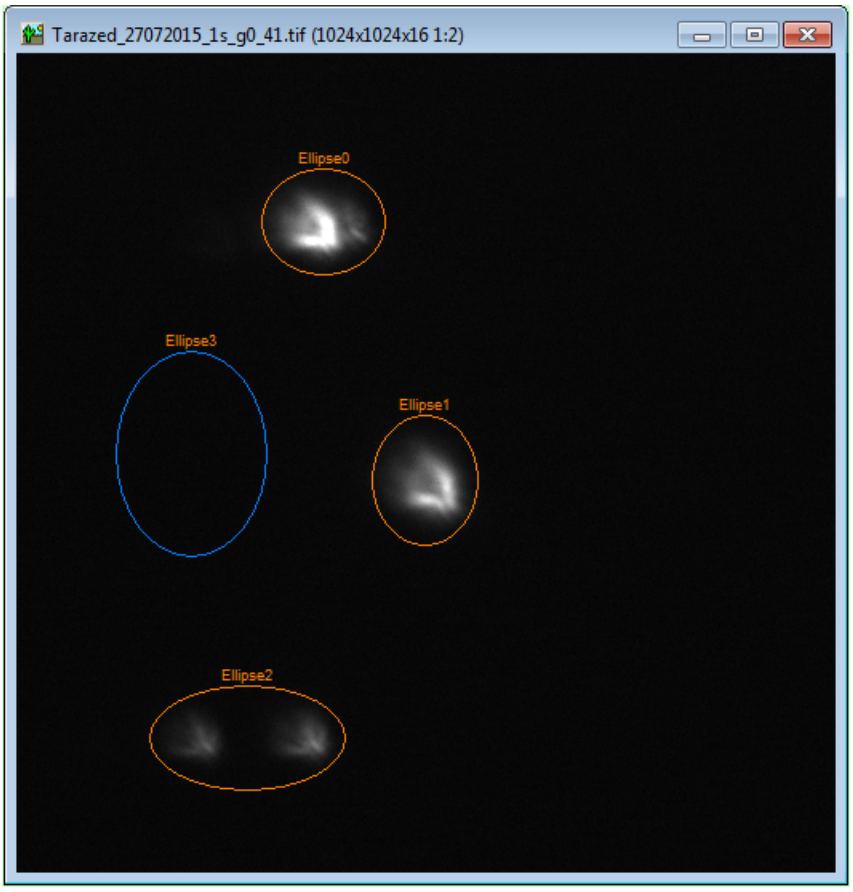

Figure 91: Image captured by Hamamatsu detector of light from Tarazed (gamma aquilae). This star is suspected to have circular polarization. As in previous figure, the ellipses are the areas, where the intensity of 3 spots are measured. Ellipse0 is the spot produced by reflection of beamsplitter; ellipse1 is the spot produced by transmission of beamsplitter; Ellipse2 contains the two spot produced by reflection of the 2 surface of Brewster window; Ellipse3 is the area to estimate the background noise.

8.2 Polarization of the Moon and biomarker in Earth-shine

The Moon is an extended object viewed from a ground telescope (even visually), so it is possible to make two types of polarimetric measures: point measure and image measure [54]. The first measure of polarization of the Moon was detected in 1858 by Araqo. The other measurements have been conducted from the ground (Lyot acquired the most relevant of these in 1929), but they have never got from a lunar orbiter, until now.
Most of the polarization of the Moon is linear, and only a small part is circularly polarized due only to geometrical factors and not to surface characteristics. Principal Stokes parameter measured are I and Q, utilized to characterize the surface. Also, Q is useful to determine the orientation of the polarization vector in Lunar map. Some measurements were compared with laboratory measurement of lunar samples.
The polarization of the Moon changes in a wide range from negative value of -1% at $\alpha_{Moon} = 11°$ to positive value of about 7% at $\alpha_{Moon} = 105°$ [55]. The phase angle of the Moon α_{Moon} is the angle formed by Sun-Moon-Earth. Its range is 0° - 180°. Note that not all the points of the surface of the Moon are visible at all the phase angles. The phase equal perfect to 0° corresponds to the lunar eclipse, and so the Earth stops the solar radiation, and it does not reach the lunar surface. Despite this, during the full Moon, the phase angle is very close to zero. The negative branch of the curve of the Moon polarization is not completely understood. The best hypothesis is that negative polarization is due to single scattering by regolith surface, as the size of the dust (regolith) has a size comparable with visible wavelength. In the phase in which the polarization is minimum, the surface polarization is in the range between -1.4% and -0.6%.
The absolute value of the degree of polarization has a linear correlation with albedo (for the low value of the albedo), or inverse correlation (for the high value of the albedo). These dependencies are obtained by empirical results.
The Moon also reflects the light coming from the Earth. Observing the dark side of the Moon, the light observed (Earthshine) is only due to the Earth light. The light reflected by Earth could be polarized up to 40%. The scatter light by the Moon surface depolarizing the radiation for a final polarization of about 10%. The study of this radiation is very interesting for characterization of the exoplanets. In fact we know that there is life on Earth planet (at this moment it is surely the only planet with life), so the study of radiation scattered by the dark side of the Moon could help tracing the biomarkers. The biomarkers are a signature of the presence of life in the spectrum and/or in the polarization signal (also the combination of more measurements could give a biomarker).The most promising candidates for biomarkers on distant planets are gases in their atmospheres. In exoplanet research, it is defined biomarker gases as gases produced by life that can accumulate in a planetary atmosphere to levels detectable remotely by large telescopes. We make the assumption that life uses chemistry to capture and store energy, and that life's chemistry generates gaseous products. Oxygen is Earth's most robust and abundant biomarker gas, produced by plants and photosynthetic bacteria. Oxygen fills Earth's atmosphere to 20 percent by volume, but without photosynthetic life, our planet would be virtually anoxic, with only the faintest trace of oxygen in its air. Living things do produce other gases in addition to oxygen, including methane, nitrous oxide, methyl chloride and dimethylsulfide. However, these

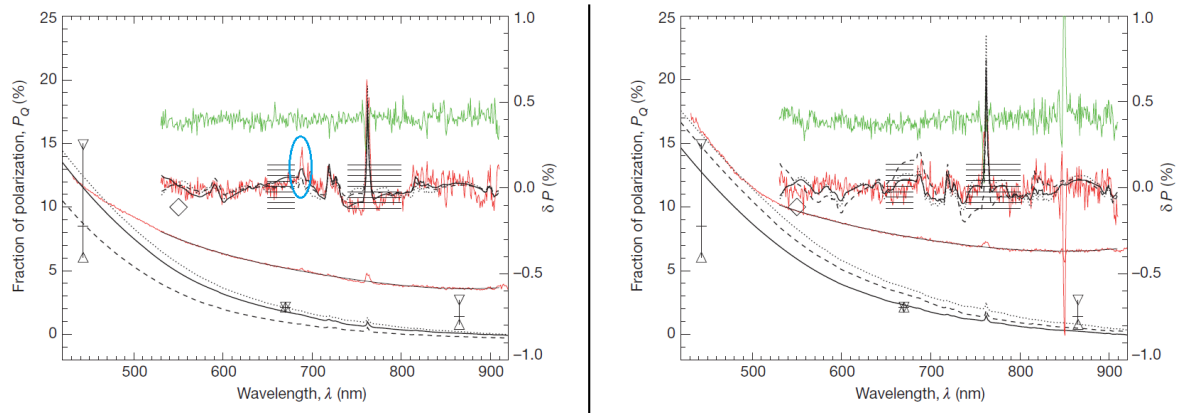

Figure 92: Two graphs from [57] of the spectropolarimeter of Moon Earthshine. Left graph. is Fig.1 and right graph is Fig.2 of [57]. All the graphs are Earthshine, but in the left graph the light scattered by the Earth toward the Moon has 7% of lands covered by vegetation, in the right graph has only 3%. The pick circled by light blue is due to vegetation. Red and green line are measures, dotted, dashed and solid lines are models with different ocean clouded or clear and vegetation cloud or clear.

gases are only produced in trace amounts, not enough to be detected by remote observation. Oxygen, or its by-product ozone, remains the best candidate for detecting life [69]. Sterzik and al. [57] observe Earthshine in two different situations: one in which the part of the Earth's surface that is visible from Moon has 7% of the surface covered by vegetation and one with 3%. To analyze radiation from the Moon they use the information of satellite-borne instrument POLDER as a measure of Earth's linear polarization in three bands (443nm, 670nm and 865nm). The polarization has a strong dependence on cloud cover. These observations are an excellent confirmation for numerical simulation of the exoplanets because there aren't until now any exoplanet measure having these characteristics. The Earth's measure from satellite could also adjust the numerical simulation for an Earth-like exoplanet.

The observations are fitted with a model that has four variable configurations: ocean covered by cloud, ocean clear, clouded vegetation surface and clear vegetation surface. The observations are reported in fig. 92. Data are processed by the authors. The most important curves are the residual Polarization (red and green lines) once authors subtract the continuum. These residuals are plotted by authors with the model described above, and they have found the best fit for a model with presence of vegetation for left graph and a model without vegetation for right graph in agreement with satellite observation of the Earth's surface visible from Moon and illuminated by Sun.

The authors conclude the paper asking for an improvement in radiative transfer models to describe better Earth's atmosphere and Earth's surface.

Biosignature could be also the estimation of molecular oxygen and methane abundances in the planetary atmospheres if they are away from chemical equilibrium they could indicate a life activity.

8.3 Moon observations

In the test observation of the polarimeter, some observing time is dedicated to the Moon. In particular, the Moon "Mare Humorum" is observed at two different angles of the polarimeter around the telescope optical axis (see fig. 93). The exposition time is 1 s.

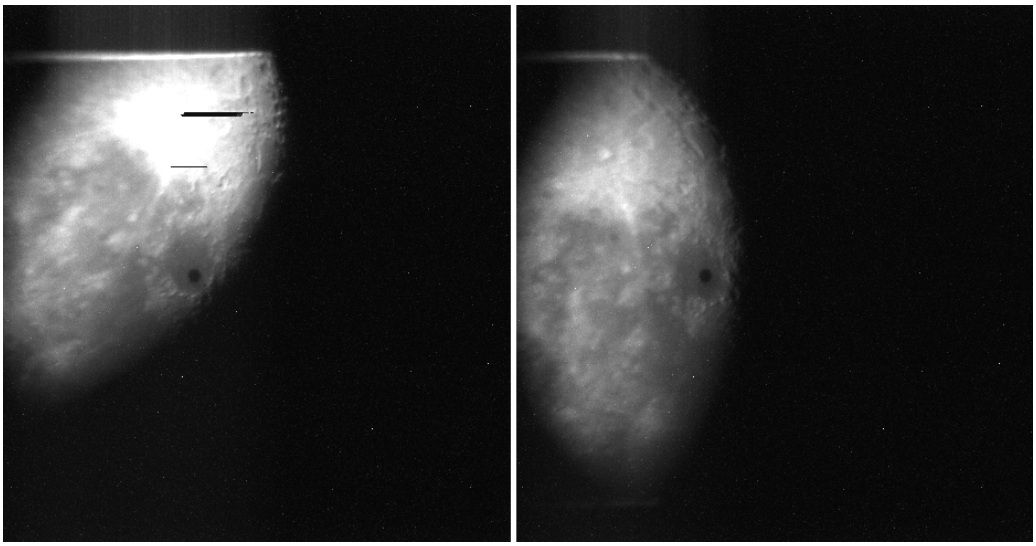

Figure 93: Control field images of the moon during the polarimetric measure of the "mare Humorum".

The observation of the "Mare Humorum" of the Moon was performed in the night between the 27 and the 28 of the July 2015.
The rotation angle was determined by the control field images of the Moon calculating the positions of the same lunar structure in the two frames. The rotation of the pixel coordinates is the same angle of rotation of the polarimeter.
In calculus in the Appendix A.8 the phase of the Moon was computed during these observations of the "*Mare Humorum*". The scope is to calculate the phase angle α represented in fig. 94.

The data extraction from the frame is performed by Hokawo Software in the same way of the stellar analysis (see fig. 95).
The spot signal is obtained subtracting the mean dark noise level measured out of the spot areas.
The measurements are analyzed by the optimization fitting software. The unpolarized flux and polarization vector is optimized. The reflection and transmission coefficients of the optics are obtained by previous calibration.
The obtained degree of polarization for "Mare Humorum" is $10.93\% \pm 0.39\%$. Although the quality of the measurement is low, the obtained value for polarization is compatible with literature measurements.
In addition, the polarization of the sky is not measured and subtracted.

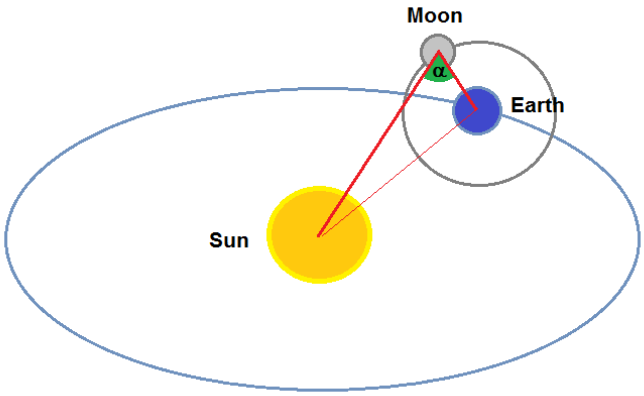

Figure 94: The scheme of the Moon phase α calculation. The distance and the celestial bodies diameters are not in scale.

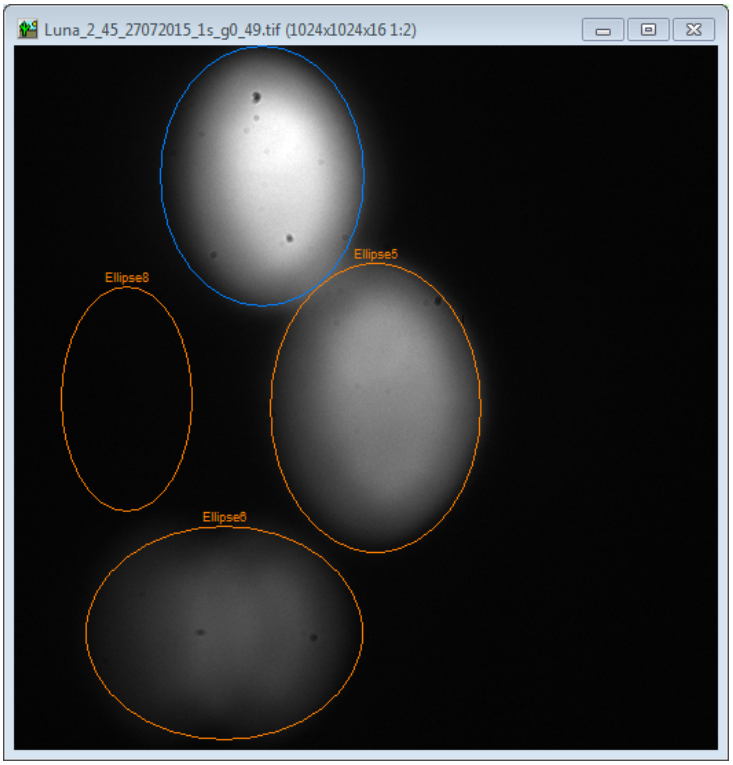

Figure 95: One of the six images captured in the polarimetric measure of the "Mare Humorum". On the image are superimposed the ellipses used for select the area of integration of the three spots and the area to characterize the background (Ellipse8).

8.4 Moon polarization in function of the orbital phase

The Moon was also observed during the growing phase from the 21st of September 2015 (≈ a quarter phase) to the 29th of September 2015 (≈ the full Moon). The target ot this measurement is to obtain the graph of the variation of the degree of polarization in function of the phase. In literature [63] is well known the shape of the degree of the Moon polarization in function of the phase (see fig. 96). The planned observation is to observe a Moon's crater every day during the

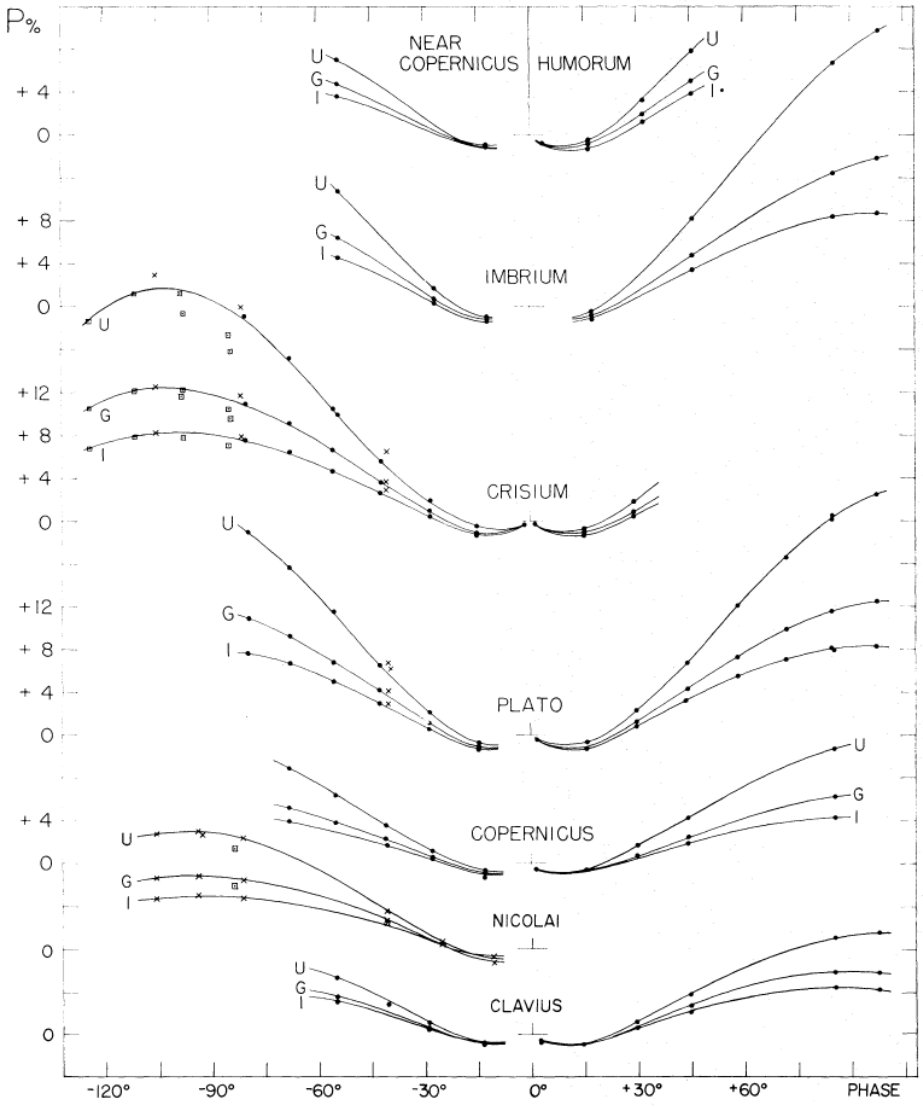

FIG. 7. The percentage polarization as a function of phase, observed with *U*ltraviolet (3600 Å), *G*reen (5400 Å), and *I*nfrared (9400 Å) filters. *Circles*, observations made in April 1959; *squares*, August 1959; and *crosses*, November 1963.

Figure 96: Degree of polarization of some Lunar structures in function of the Moon phase. Figure get from [63].

growing of the Moon. Four days of observation were performed as the meteorological conditions were bad in others day. The crater observed in the first two days is indistinguishable in the last two days, so a different crater was observed (the Copernicus crater is shown in fig. 97). The image contrast and structure recognition also depends on the angle of Solar incident rays on the Moon surface that changes during the Moon orbit. Each day the Moon was observed at different angles (from 5 to 10 angles) of the orientation of the polarimeter. The counts of the three spots

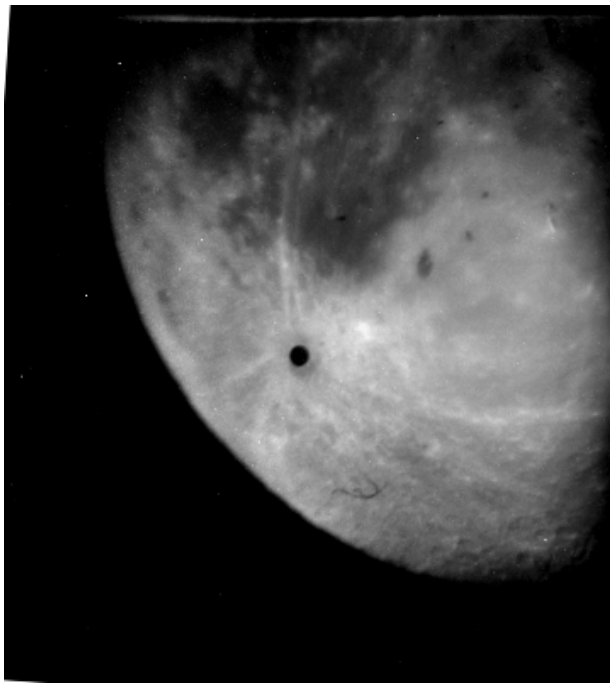

Figure 97: Field of view (cropped to mirror) of the Moon Copernicus's Crater.

are extracted in the usual way by Hokawo software. The area on which to measurement of the counts was performed using a threshold by an pattern recognition algorithms in the Hokawo program.
Each day is analyzed separately. The phase angle is calculated in the same way reported in appendix A.8.

Fig. 98, 99, 100 and 101 report the data aquired by the polarimeter in the 4 days of good meteorologic conditions (21/09/2015, 22/09/2015, 25/09/2015 and 29/09/2015).
In the upper graph shows the extracted counts for each of the three spots for each angle at which it was oriented polarimeter. The angle of the first measure has always been placed arbitrarily to zero, the other angles express the rotation of the polarimeter around the optical axis of the telescope counterclockwise.
The presented measurements show a strong influence of atmospheric conditions. All the single measurement (count versus angle) take about an hour. During this time you may notice that the transmission of the atmosphere changes, as all 3 spots have the same variations (from an angle to another it is required some time to rotated manually the polarimeter and to correct the telescope pointing).
The only difference of these measurements, compared with calibration measurement presented in Chapter 8, is the presence of the atmosphere and the difference of the source. Since the source (The Sun and the Moon, which reflects the radiation) cannot have such variations, it is clear that it is the atmosphere that changes the transmission during the measurement (for example a little cloud could pass during the measurement).
In order to meet these atmospheric turbulence, some coefficients "AT" were introduced in the fit program. The measurement angle "0" is taken as a reference. The measurements at angles > 0

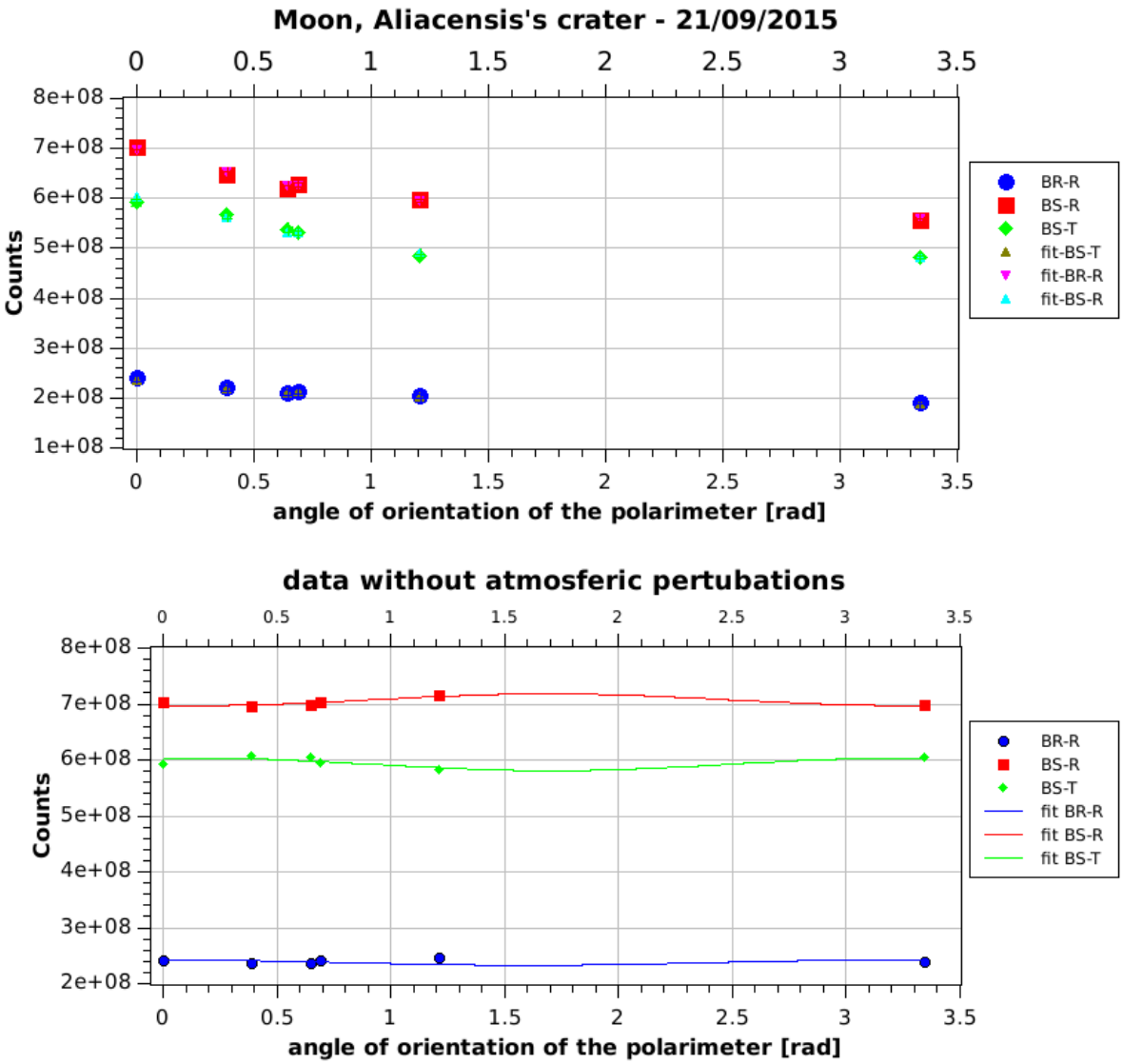

Figure 98: Measurement of the degree of polarization of the Moon's crater Alicensis. Data acquired in the 21/09/2015 at 85° of Moon phase angle. The data are fitted by a custom software. In the lower graph is reported the same data without the atmospheric variation (the atmospheric influence is estimated by the same fitting software).

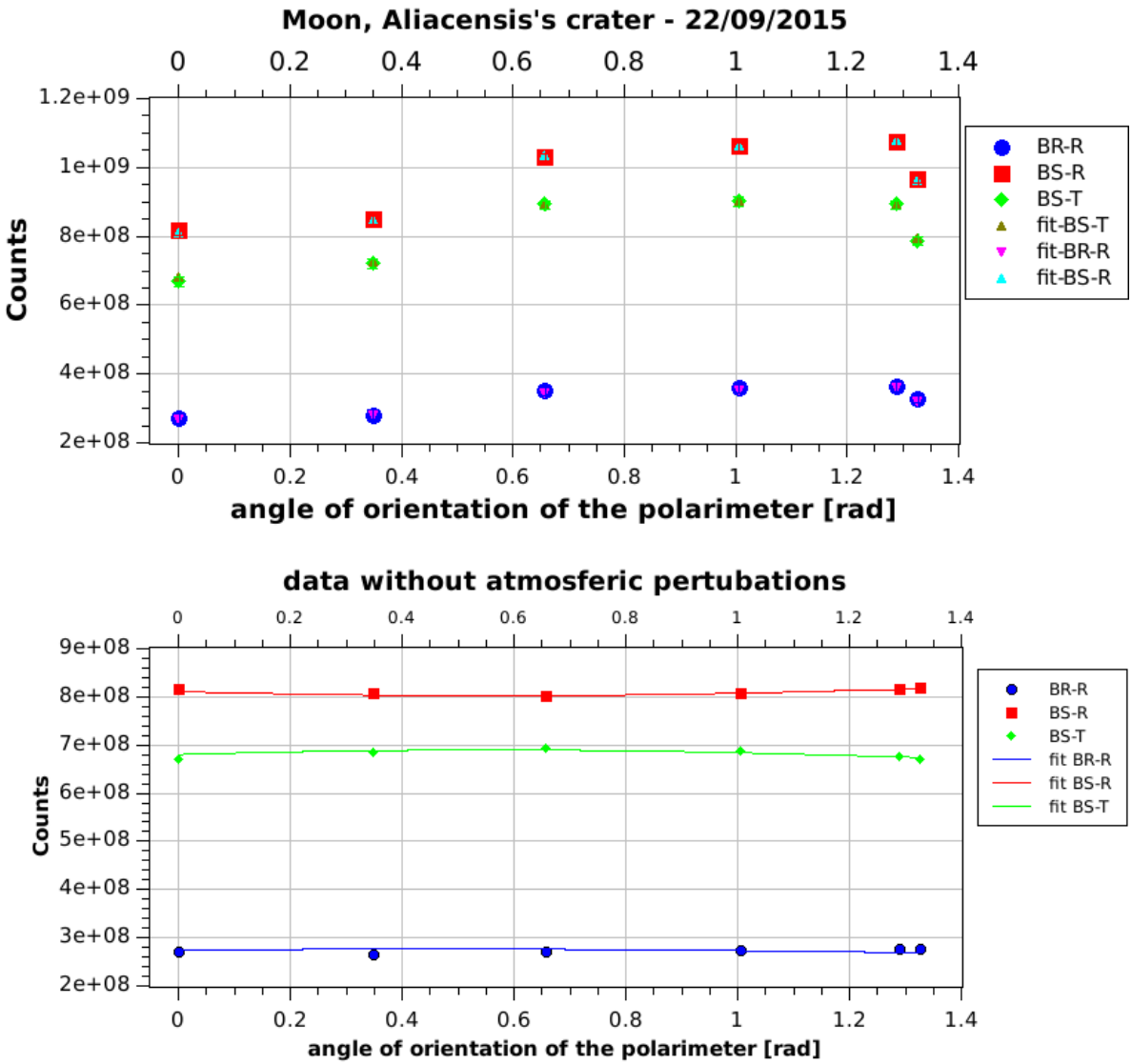

Figure 99: Measurement of the degree of polarization of the Moon's crater Alicensis. Data acquired in the 22/09/2015 at 73° of Moon phase angle. The data are fitted by a custom software. In the lower graph is reported the same data without the atmospheric variation (the atmospheric influence is estimated by the same fitting software).

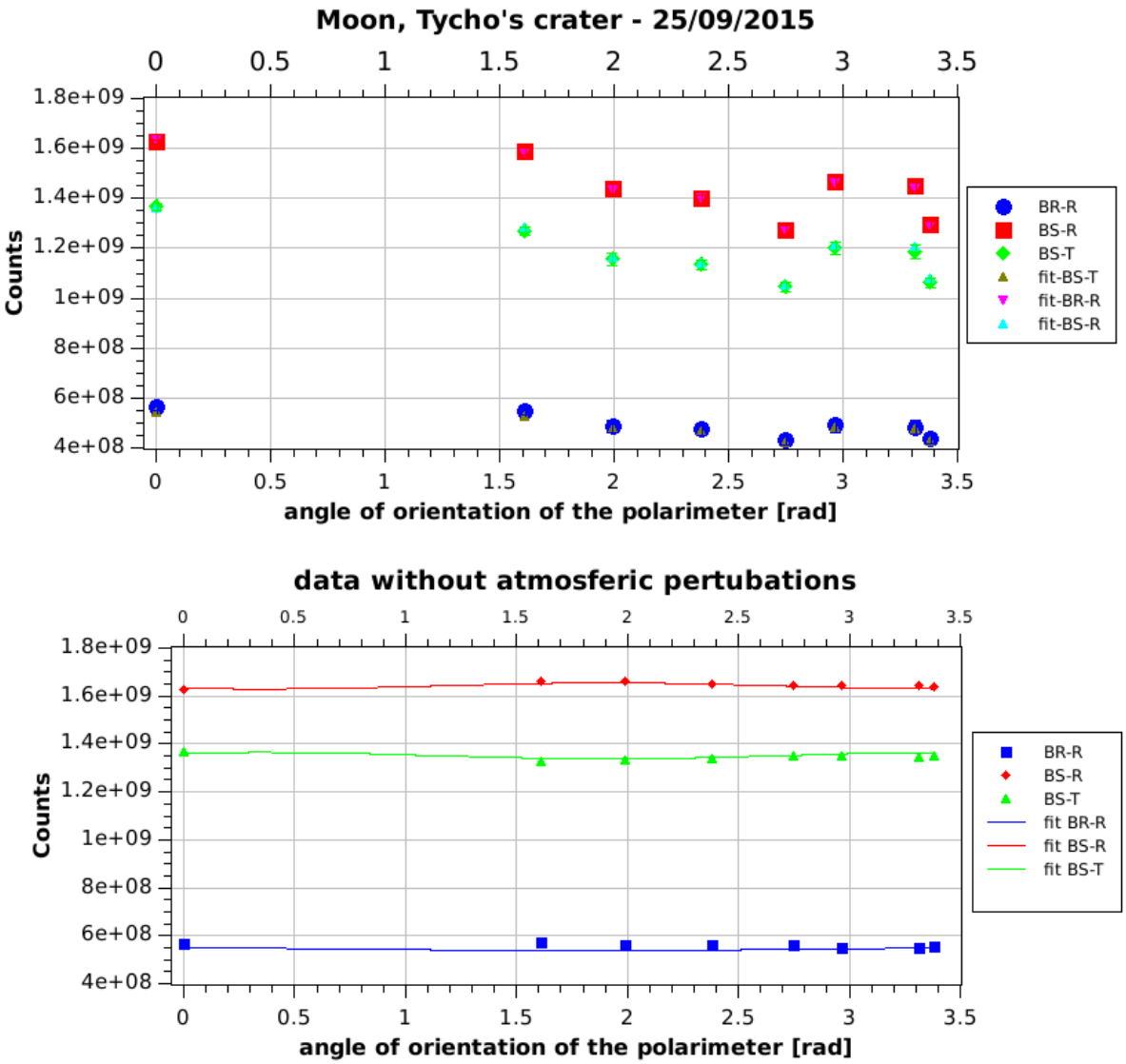

Figure 100: Measurement of the degree of polarization of the Moon's crater Tycho. Data acquired in the 25/09/2015 at 33° of Moon phase angle. The data are fitted by a custom software. In the lower graph is reported the same data without the atmospheric variation (the atmospheric influence is estimated by the same fitting software).

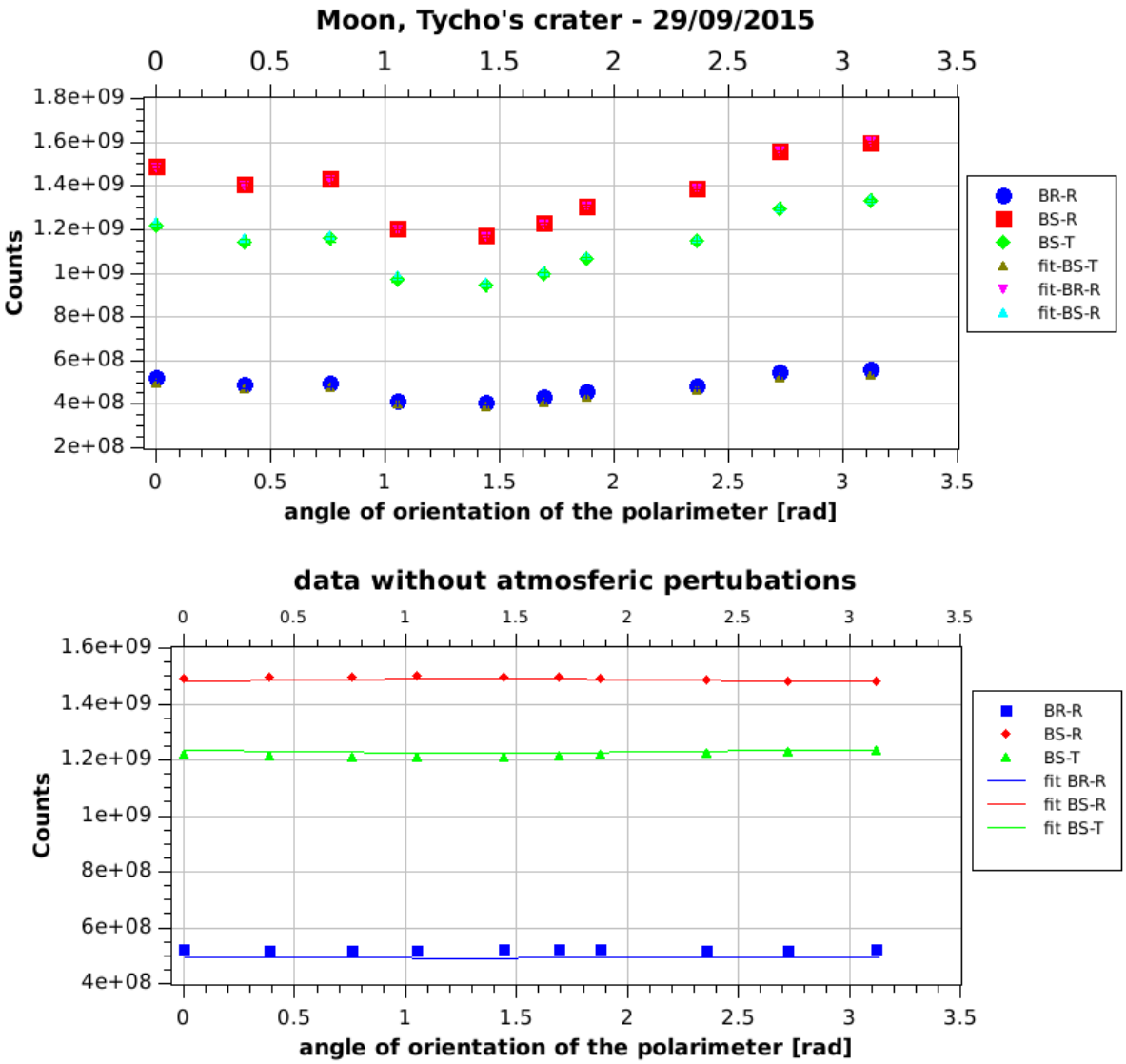

Figure 101: Measurement of the degree of polarization of the Moon's crater Tycho. Data acquired in the 29/09/2015 at 25° of Moon phase angle. The data are fitted by a custom software. In the lower graph is reported the same data without the atmospheric variation (the atmospheric influence is estimated by the same fitting software).

are fitted by the Malus law multplied to a coefficient of variation of the observing conditions between 0.3 and 2.0. This coefficient is the same for the 3 measurements made at specific angle, as they are temporally synchronous.

$$\begin{aligned} I_S &= \tfrac{1}{2} \cdot I_U + I_P \cdot \cos^2(\theta) \\ I_P &= \tfrac{1}{2} \cdot I_U + I_P \cdot \sin^2(\theta) \\ BRR(0) &= BR_{RS} \cdot I_S + BR_{RP} \cdot I_P \\ BSR(0) &= BR_{TS} \cdot BS_{RS} \cdot I_S + BR_{TP} \cdot BS_{RP} \cdot I_P \\ BST(0) &= BR_{TS} \cdot BS_{TS} \cdot I_S + BR_{TP} \cdot BS_{TP} \cdot I_P \end{aligned} \tag{97}$$

$$\begin{aligned} I_S &= \tfrac{1}{2} \cdot I_U + I_P \cdot \cos^2(\theta - \alpha) \\ I_P &= \tfrac{1}{2} \cdot I_U + I_P \cdot \sin^2(\theta - \alpha) \\ BRR(\alpha) &= AT(\alpha) \cdot [BR_{RS} \cdot I_S + BR_{RP} \cdot I_P] \\ BSR(\alpha) &= AT(\alpha) \cdot [BR_{TS} \cdot BS_{RS} \cdot I_S + BR_{TP} \cdot BS_{RP} \cdot I_P] \\ BST(\alpha) &= AT(\alpha) \cdot [BR_{TS} \cdot BS_{TS} \cdot I_S + BR_{TP} \cdot BS_{TP} \cdot I_P] \end{aligned} \tag{98}$$

where BRR, BSR and BST are the intensity of the three spots respectively reflected by Brewster, reflected by beamsplitter and transmitted by beamsplitter, α is the angle of orientation of the polarimeter, θ is the angle of the orientation of polarization vector, I_U is the intensity of unpolarized light, I_P is the intensity of polarized light and $AT(\alpha)$ is the atmosferic perturbation coefficient. Equations 97 are used to fit the first measurement at $\alpha = 0$ and equations 98 are used to fit the next measurements at $\alpha > 0$.
Once you have the set of coefficients of atmospheric transmission changes it will be found in independent curves by such perturbation. In order to obtain this, it is sufficient to divide the measures for the coefficients obtained and the result is represented in the lower part of the fig. 98, 99, 100 and 101.
This type of analysis shows that it is possible to find the trend of polarization even in measures affected by atmospheric disturbances are greater than those of polarization.
For 3 over 4 fits chi-square are well acceptable, as they are comparable to the degrees of freedom ($\chi^2 = 2.83$, dof=10; $\chi^2 = 10.75$, dof=10; $\chi^2 = 9.67$, dof = 12). The last fit (measurement of the 29/09/2015) has $\chi^2 = 93.08$ with 14 degrees of freedom, that is in rejection zone of statistic. Take into account that if the fit doesn't consider the atmospheric variations chi-square values are about a few hundred thousand. So, also for the latter measurement, this technique allows the analysis to obtain a much better result.

Fig. 102 reports the graph obtained for the degree of polarization in function of the phase angle. The red line in the graph is a cubic interpolation to drive the eye. The shape of the graph is correct (it agree with Moon polarization measurements of fig. 96), but the number of observations is small to make a strong confirmation of the shape of this graph.

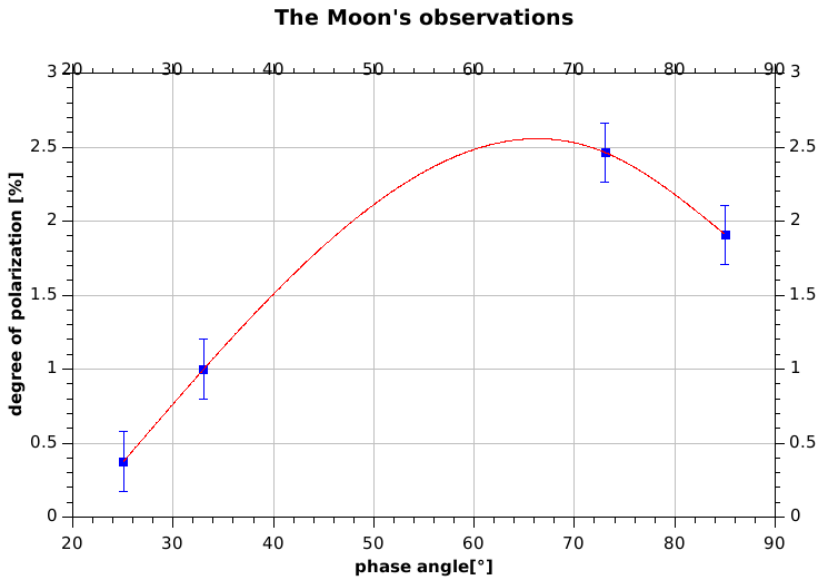

Figure 102: The four measurements of the Moon. The two smaller phases are the observation of the Thyco's Crater, the bigger one are the observation of Aliacensis's crater. The error bars are extracted from the difference of some analysis of the same data. The red line is a cubic interpolation to drive the eye. The modulation of the degree of polarization with the phase is compatible with expected behavior [63]

Conclusion

A project and a prototype of a polarimeter to observe exoplanets is developed in this thesis. The proposed polarimeter is designed to work in visible wavelengths, with a minimum sensitivity of 10^{-5} in polarization degree (better goal is 10^{-7}), and with the dynamic between 10^6 and 10^8. The main innovation of this polarimeter is a new optical scheme to split polarization with a spatial modulation. The optical scheme combines a Brewster window and a wire-grid polarizing beamsplitter.
The Brewster window has the advantage of selecting a polarization component without contamination of the other components, but selects only slightly more than 25 % (see chap. 5 for the counts) of incoming s-light. The polarizing beamsplitter has a high efficiency ($> 80\%$) but the components are partially contaminated (see chap. 5.2 for efficiency of the beamsplitter). The combined use of two optics allows taking advantage of both without having the disadvantages, leading to having a lower uncertainty on the final measurement (see chap. 5.3 for an analytical comparison of uncertainness).
The optical scheme has been successfully verified with a ray-tracing non sequential simulation.
A laboratory test is assembled on an optical bench to verify the optical patches and efficiency of the optics.
The behavior of the measured intensities of light is compatible with analytical computations. The intensities are a few different from expectation ones, but with a calibration of the instrument this is not a problem.
A project of a polarimeter's prototype based on this optical scheme has been developed.
The prototype has been realized with the INFN-RomaTre mechanical service by numeric control milling machines and with 3D-print techniques which have been necessary for some particular pieces (for example optical holders).
The polarimeter was equipped with 2 detector: a reflex camera for the first test and a low-noise cooled CCD (see chap. 7.3.7 for characteristics and a comparison of the detector).
The total weight of the prototype polarimeter is between 5 kg and 7 kg, hence it is compatible with the maximum load sustainable by a small commercial telescope, which is useful for the first stage of astrophysical polarimeter tests.

A calibration, with a telescope and a source of artificial light, has allowed to obtain the reflection and the transmission coefficients of the optical polarimeter in real operating conditions. The calibration is also a further test of the optical scheme, as the data are fitted by Malus law plus unpolarized light intensity. Calibration measurements and the polarimeter model is highly in agreement.
To achieve the best coefficients of the instrument, a suited software has been developed. The program implements the operation behavior of the optical scheme, changing the efficiency of the optics for the 2 components of polarization in a physical range (0.0 - 1.0). The program calculates a statistical function of the chi-square looking at its minimum, which is the best agreement among the calibration measurements and the analytical values of the calculated values.
Calibration also permits the verification of the reproducibility of a measure assuring an high intrinsic stability (better than 10^{-4}) of the instrument.

Some preliminary observations of celestial bodies have been performed.
It has been verified that stars produce a clear set of spots. By the control of the telescope's mount, it is possible to move the spots' position on the detector.
The extended sources, like the planet Saturn of our Solar System, are also observable, and it is possible to distinguish their shape. The polarimetric information of Saturn's images requires a complex analysis to distinguish the rings from the planet's body.
A series of observations of the Moon during different orbital phases have been made. In fact, for geometrical reasons, the polarization of the Moon is modulated by the position of the Moon in its orbit (in particular from the angle of reflection Sun-Moon-Earth) [63].
To analyze these measures, the already developed program to fit calibration measurements has been changed. It has been observed that the atmospheric transmission changes during a single observation which requires about an hour. Some coefficients have been introduced into the program to take into account the atmospheric transmission variations.
The instrument has proved capable of seeing the polarization signals also of astronomical sources (for example the moon).
As a next step it is possible to make some improvements of the data analysis methodology and some mechanical upgrades.
The possible improvements of software consists of a better selection of the light on the sensor to measure the intensity observed and a further refinement of data analysis technique such as taking account of a cross polarization induced by the sky.
To characterize the prototype better, systematic observations of a set of standard stars (polarized and not polarized) are required.
A field rotator must be introduced with high priority since it would stabilize the measurements and reduce the total time for technical operations.
After this tests you can define which mechanical parts optimize to achieve the definitive polarimeter. In particular, some parts can be reduced in size, to make easier handling the instrument. You can better balance the weights. The data analysis software has already reached a good optimization. In the definitive version of the instrument, the software will also mechanically control the rotation of the the polarimeter. With these improvements it is possible to design and realized the definitive version of the polarimeter optimized for a medium sized telescope of few meters class, to observe exoplanet's polarization.

***

Printed in May 2016.

Acknowledgments

A particular acknowledgment to my supervisors dott. Paolo Branchini and Enrico Bernieri who have supported me in all phases of my Ph.D. thesis.

A special acknowledgment to the mechanical service, in particular to Massimo Capponi for having programmed drilling machines. The mechanical support has also helped to fix and to optimize polarimeter's preliminary project.

A Special thank to dr. Riccardo Claudi for the suggestions he gave me during the making of the thesis and in particular for corrections and precious suggestions to improve the drafting of the written thesis.

I want to thank all people who have helped me in this work, in particular Emilio Favero (INFN / CNR), my aunt Laura Marchetti, my mother Vera Marchetti, Eva Francucci and prof. Massimo Santarsiero.

A APPENDIX

A.1 Table of acronyms used

- ADC = Analog to Digital Conversion
- AR = AntiReflecting coating
- BR = BRewster
- BS = BeamSplitter
- CAD = Computer Aided Design Software
- CCD = Charge Coupled Device
- DR = Dynamic Range
- ESA = European Space Agency
- FWC = Full Well Capacity
- FOV = Field Of View
- HWP = Half Wave Plate
- NASA = National Aeronautics and Space Administration
- NSC = Non-Sequential Component (in ray tracing simulation)
- p = parallel component of polaritation
- PEM = PhotoElastic Modulator
- PMMA = Poly-Methyl-MethAcrylate - acrylic glass
- PSF = Point Spread Function
- QWP = Quarter Wave Plate
- RGB =Red Green Blue (color model system)
- RN = Read Noise
- s = perpendicular component of polaritation
- S/N = Signal to Noise
- SLR = Single-Lens Reflex camera
- VLT = Very Large Telescope (at Cerro Paranal, Chile)

A.2 The geometric probability of a transit

The transit occurs if the orbit of the planet is in the angle θ:

$$\theta = \arctan\left(\frac{d_\star}{a}\right) \approx \frac{d_\star}{a} \tag{99}$$

Where $d_\star$ is the stellar diameter, a is semi mayor axis of planet orbit. Construct the celestial sphere centered on the star. the radius is the distance of the same from the observer (see fig. 103). In figure 103 the probability of observing a star being transited by a planet is the

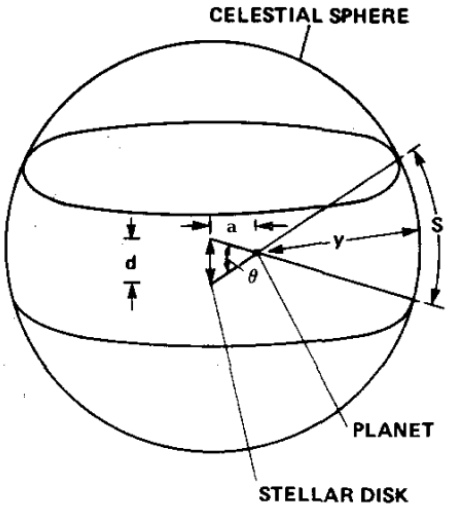

Figure 103: The celestial sphere used to compute the probability of a transit. Get from [64].

fraction of the area of the celestial sphere that is swept out by the shadow of the planet during one orbital period [64].

$$probability = \frac{2 \cdot \pi \cdot (a+y) \cdot s}{4 \cdot \pi \cdot (a+y)^2} = \frac{2 \cdot \pi \cdot \cancel{(a+y)} \cdot s}{4 \cdot \pi \cdot \cancel{(a+y)} \cdot (a+y)} \tag{100}$$

Where y is the distance between the planet and observer. s is the arc of circumference obtained by $s = y \cdot \theta \approx= y \cdot \frac{d_\star}{a}$ Substituting in 100

$$probability = \frac{y \cdot d_\star}{2 \cdot a \cdot (a+y)} \tag{101}$$

The distance between the planet and the observer is much greater than all other distances considered. So, it limits the y to infinity:

$$probability = \lim_{y \to \infty} \left(\frac{y \cdot d_\star}{2 \cdot a \cdot (a+y)}\right) = \frac{d_\star}{2 \cdot a} \tag{102}$$

A.3 Calculus of a light source with a degree of polarization equal to $2 \cdot 10^{-5}$

Next, the flux intensities are calculated to have a source of the degree of polarization $\alpha = 2 \cdot 10^{-5}$.

Suppose to have a light source with a degree of polarization of $\alpha = 2 \cdot 10^{-5}$ (coincidentally this is the polarization detected for exoplanet HD 189733b). By the definition of the degree of polarization:

$$P = \frac{\sqrt{Q^2 + U^2 + V^2}}{F} = \frac{Q}{F} = \frac{(F_0 - F_{90})}{\sqrt{F_0^2 + F_{90}^2}} = \alpha \tag{103}$$

The source is supposed without circular polarization ($V = 0$). The optics are supposed to be aligned with scattering plane ($U = 0$).

To have a significance of $3 \cdot \sigma$ it is needed that the difference between the two orthogonal components are measured at least for a time to accumulate 3 times the number of photon noise (that is the square root of the incident flux):

$$F_0 - F_{90} = 3 \cdot \sqrt{\sqrt{F_0^2 + F_{90}^2}} = 3 \cdot \sqrt[4]{F_0^2 + F_{90}^2} \tag{104}$$

Making a system of equations it is possible to obtain F_0 and F_{90}.

$$\begin{cases} \frac{(F_0 - F_{90})}{\sqrt{F_0^2 + F_{90}^2}} = \alpha \\ F_0 - F_{90} = 3 \cdot \sqrt[4]{F_0^2 + F_{90}^2} \end{cases} \tag{105}$$

Making a variables change: $F = \sqrt{F_0^2 + F_{90}^2}$ and $x = F_0 - F_{90}$. "F" is a physical quantity: the total flux.

$$\begin{cases} x = \alpha \cdot F \\ x = 3 \cdot \sqrt{F} \end{cases} \tag{106}$$

$$\begin{cases} x - \alpha \cdot \frac{x^2}{9} = 0 \\ F = \frac{x^2}{9} \end{cases} \tag{107}$$

From first equation is extract x. $x = 0$ is a solution of first equation, but it isn't a good physical solution.

$$x = \frac{9}{\alpha} \tag{108}$$

Substitute the value obtained for x in the second equation of system 107, then $F = \frac{9}{\alpha^2}$.

To find F_0 and F_{90} substitute the value obtained for x and F in their definitions.

$$\begin{cases} F_0 - F_{90} = \frac{9}{\alpha} \\ \sqrt{F_0^2 + F_{90}^2} = \frac{9}{\alpha^2} \end{cases} \tag{109}$$

$$\begin{cases} F_0 = \frac{9}{\alpha} + F_{90} \\ 2 \cdot F_{90}^2 + \frac{18}{\alpha^2} \cdot F_{90} + \left(\frac{81}{\alpha^2} - \frac{81}{\alpha^4}\right) \end{cases} \tag{110}$$

The second equation is a second order linear equation in F_{90}.

$$F_{90} = \frac{\frac{-9}{\alpha} \pm \sqrt{\frac{81}{\alpha} - 2 \cdot \left(\frac{81}{\alpha^2} - \frac{81}{\alpha^4}\right)}}{2} \tag{111}$$

Only the solution with plus sign has a physical sense and it is $F_{90} = 1.59097 \cdot 10^{10}$ Substituting in first equation of the system 110 $F_0 = 1.59101 \cdot 10^{10}$.

A.4 Matlab Script to analyze the image produced by ZEMAX optical scheme simulation

```
clc; clear all;
image = load ('Zemax_simulazione_sorgente_polarizzata_Jx_0_Jy_1.TXT');
Brewster = image(1:385,:);
BS_r = image(386:598,:);
BS_t = image(596:end,:);
disp('Source polarization: Jx = 0, Jy = 1')
Brewster_intensity = sum(sum(Brewster))
BS_r_intensity = sum(sum(BS_r))
BS_t_intensity = sum(sum(BS_t))
clear all;
image = load ('Zemax_simulazione_sorgente_polarizzata_Jx_1_Jy_0.TXT');
Brewster = image(1:385,:);
BS_r = image(386:598,:);
BS_t = image(596:end,:);
disp('Source polarization: Jx = 1, Jy = 0')
Brewster_intensity = sum(sum(Brewster))
BS_r_intensity = sum(sum(BS_r))
BS_t_intensity = sum(sum(BS_t))
clear all;
```

A.5 Mechanical project of optical supports

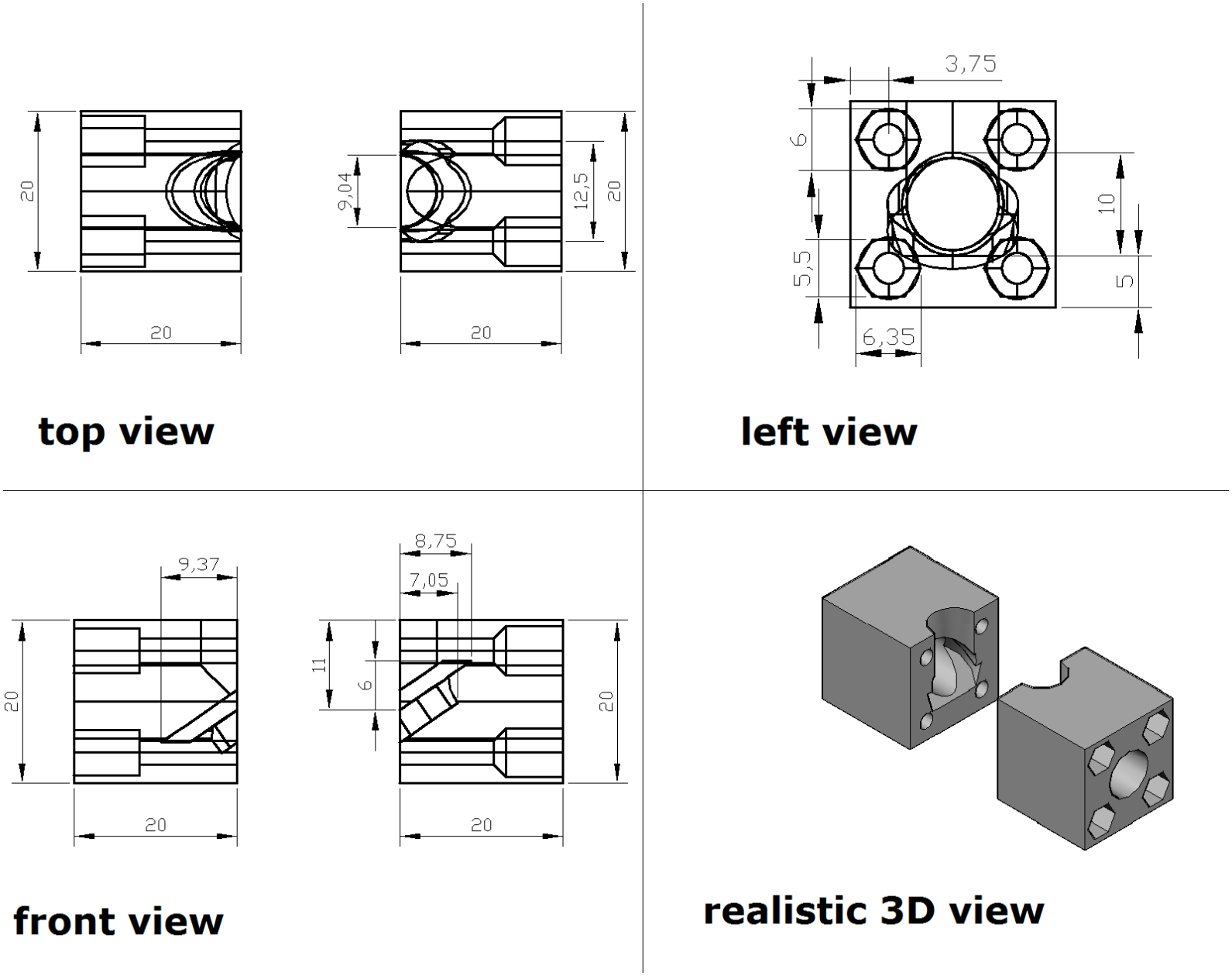

Figure 104: Preliminary support for the Brewster window. Dimensions are in millimeters.

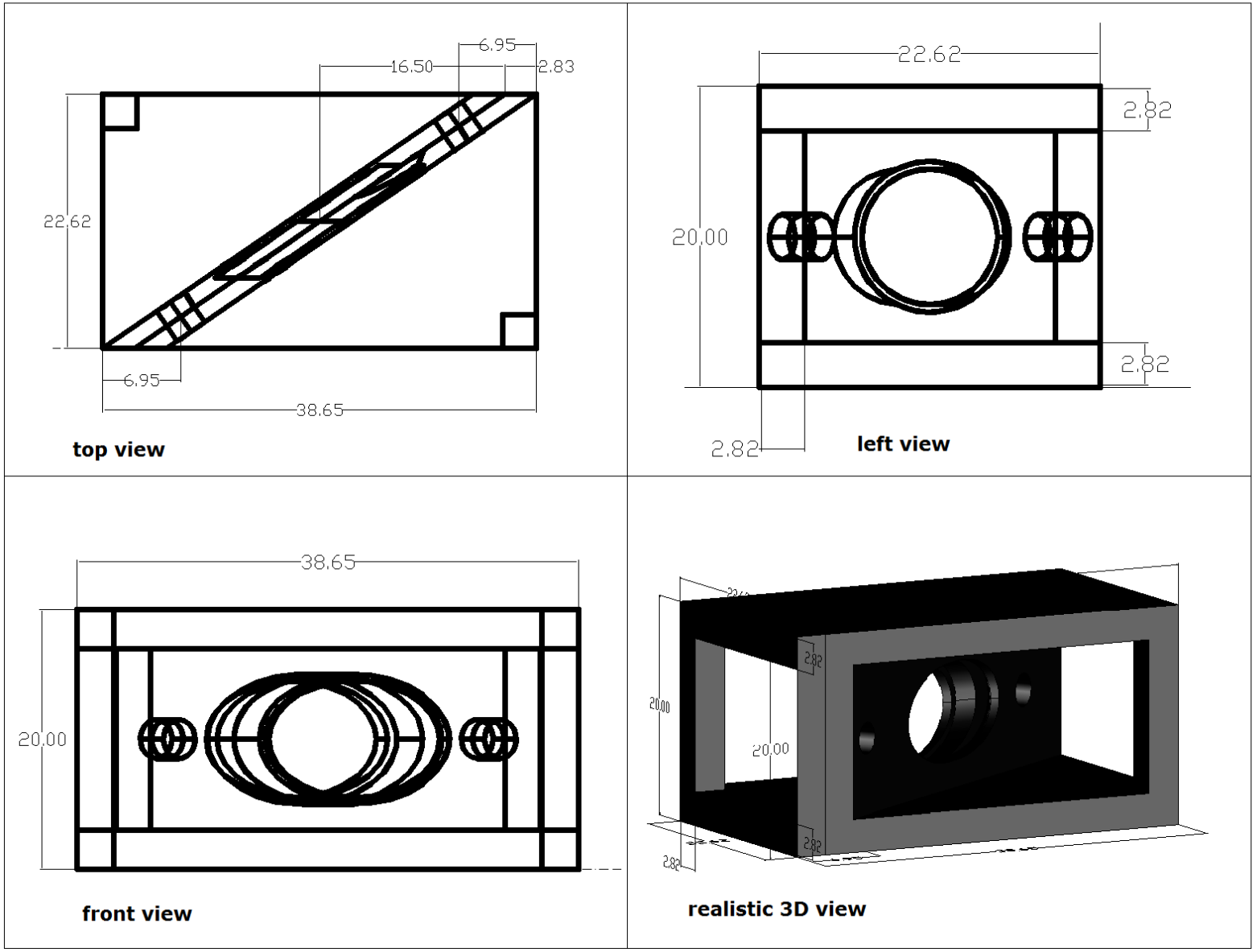

Figure 105: New support for the Brewster window. The support consists of 2 parts screwed with in the middle the glass. Dimensions are in millimeters.

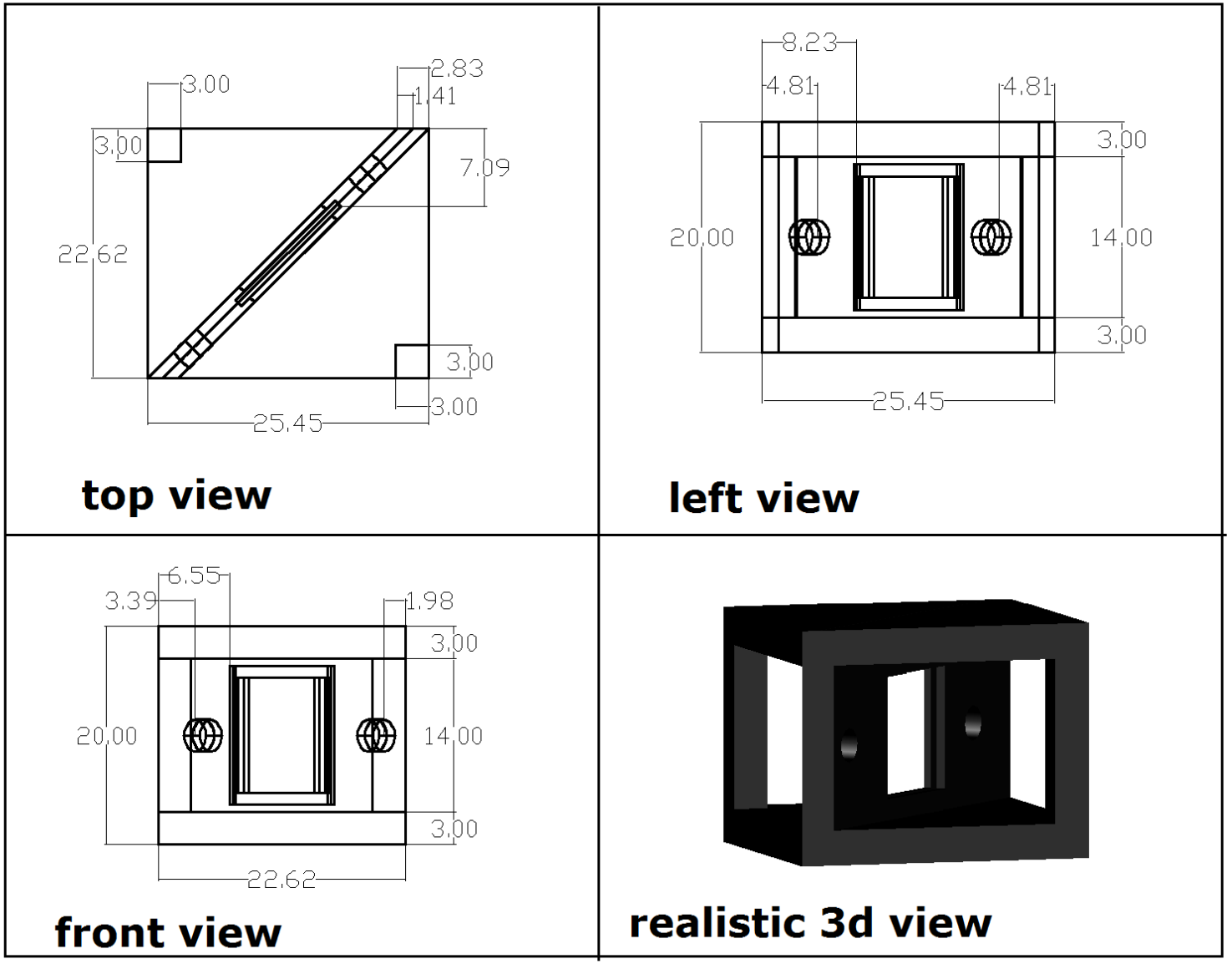

Figure 106: Support for the polarizing beamsplitter. The support consists of 2 parts screwed with in the middle the glass. Dimensions are in millimeters.

A.6 Brewster preliminary measurements

A simple measure of the transmission and reflection of the window of Brewster has been set up. To test the Brewster window with real measurement a very simple equipment was built up (see fig. 108). The source used is a red laser beam (intrinsic polarized), mounted on a cylindrical support to assure a rotation of the laser around its optical axis (to change the direction of oscillation of the electric field, i.e. the direction of polarization vector). After the Brewster window, two white rigid papers has been used as projection screens. A reflex photo camera has been used to measure the intensity of transmitted and reflected light. The setup is shown in fig. 107. The reflex is set to record the images in RAW mode: a commercial mode that doesn't compress the image preserving ADC counts information.

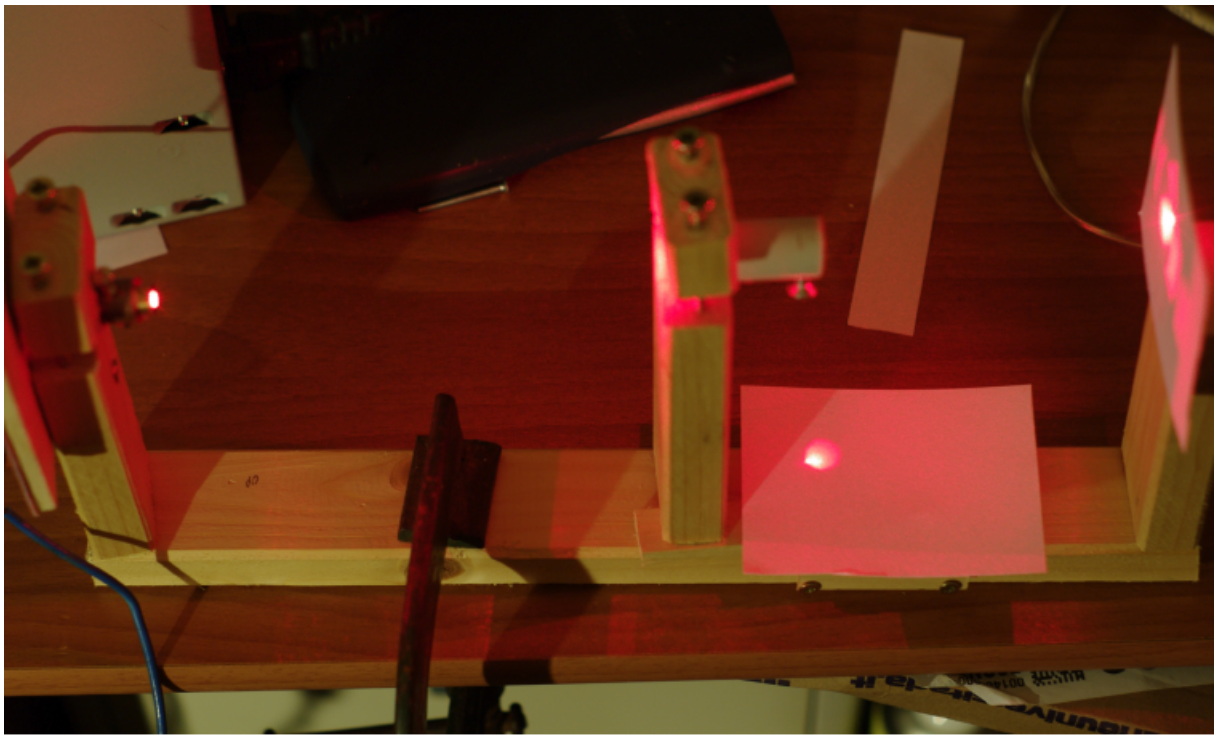

Figure 107: Simple setup to test the Brewster window

A first set of measurements have been acquired at different angles, and they are reported in fig. 109.a. This measure is a very preliminary test, and it is a rudimentary measure, in fact, its goal is only to assure the correct understanding of the general characteristics of the Brewster window. A computed theoretical graph of the reflectance and transmittance of a glass oriented at different angles is reported in the same figure. Note that the glass angle is fixed at Brewster angle in this measure. The goal of the measure is to reproduce only the values in vertical dot green line (at the Brewster angle) of the small theoretical graph reported in fig. 109.b. The cross-interpretation of these two graphs is not immediate.

The measurement was carried out by rotating a laser around its optical axis, so the polarization vector is rotated in the measurement.

The theoretical graph, instead, represents the transmission and reflection coefficients of a glass

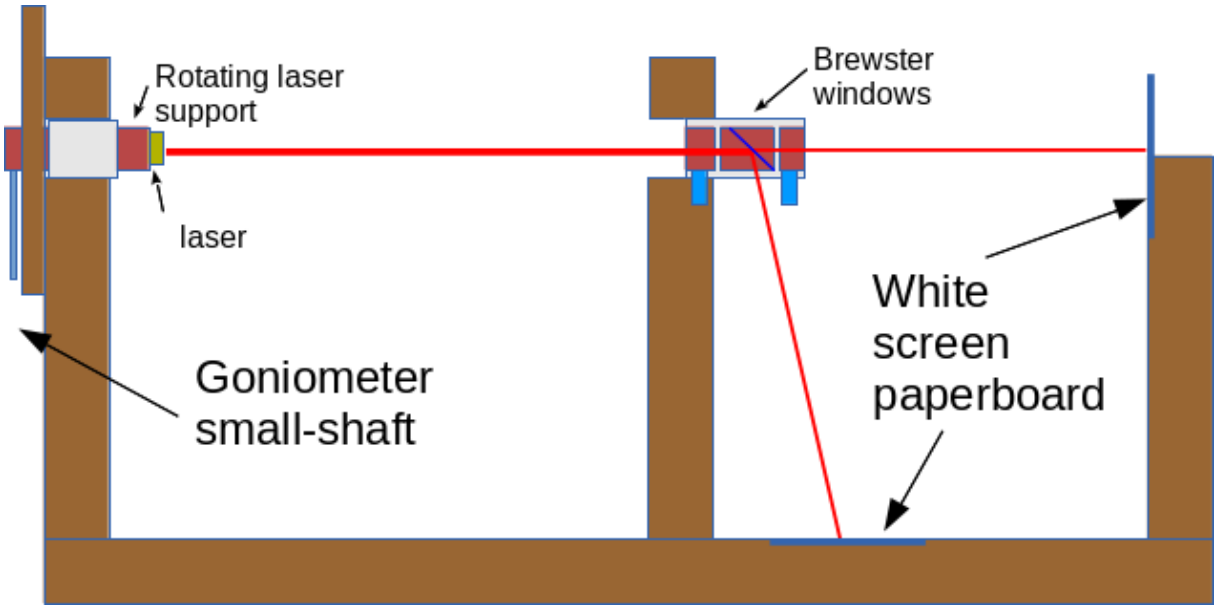

Figure 108: Scheme of the simple setup to test the Brewster window

window as a function of the angle of incidence light beam on the glass surface. The calculations of fig. 109.b are made for both polarization orthogonal components "p"and "s". In the measurement the angle of incidence was fixed at the Brewster angle, then you have to consider only the values on the vertical dashed green line.

At this angle the reflection coefficient of the parallel component is null, the reflection coefficient of the perpendicular component is equal to slightly less than 40%, the transmission coefficients are equal to about 70% with the parallel component with transmission coefficient slightly greater of that perpendicular.

Because the absolute direction of orientation of the polarization vector of the laser used as the source is not known it will try to extract it directly from the measured curves in fig. 109.a. The "spot-1"and "spot 2"(reflected light) vanishes at about 50°. Therefor it is assumed that at this angle the polarization vector of the laser is perpendicular to the plane of incidence. Since a rotation of 90° of the polarization vector is equivalent to an exchange of the components "p"and "s", shifting in the measured graph 109.a of 90°, the perpendicular component becomes the the parallel component to the plane of incidence.

Therefore at an angle of 50° in the graph 109.a the polarization vector of the laser is perpendicular to the plane of incidence and at the angle of 140° (50° + 90°) the vector of polarization is parallel to the plane of incidence. The measured intensities at these angles are compatible with the values of transmission and reflection for the Brewster angle in the theoretical graph 109.b. The superimposed arrows helps the reader to compare the two graphs. Pointing to read the yellow measured transmission curve it is possible to read the values at 50° and 140° and to compare them with the expected values. As the prediction, the value of 50° (magenta continuum line on lower graph) is slightly higher than 140° value (blue continuum line on lower graph).

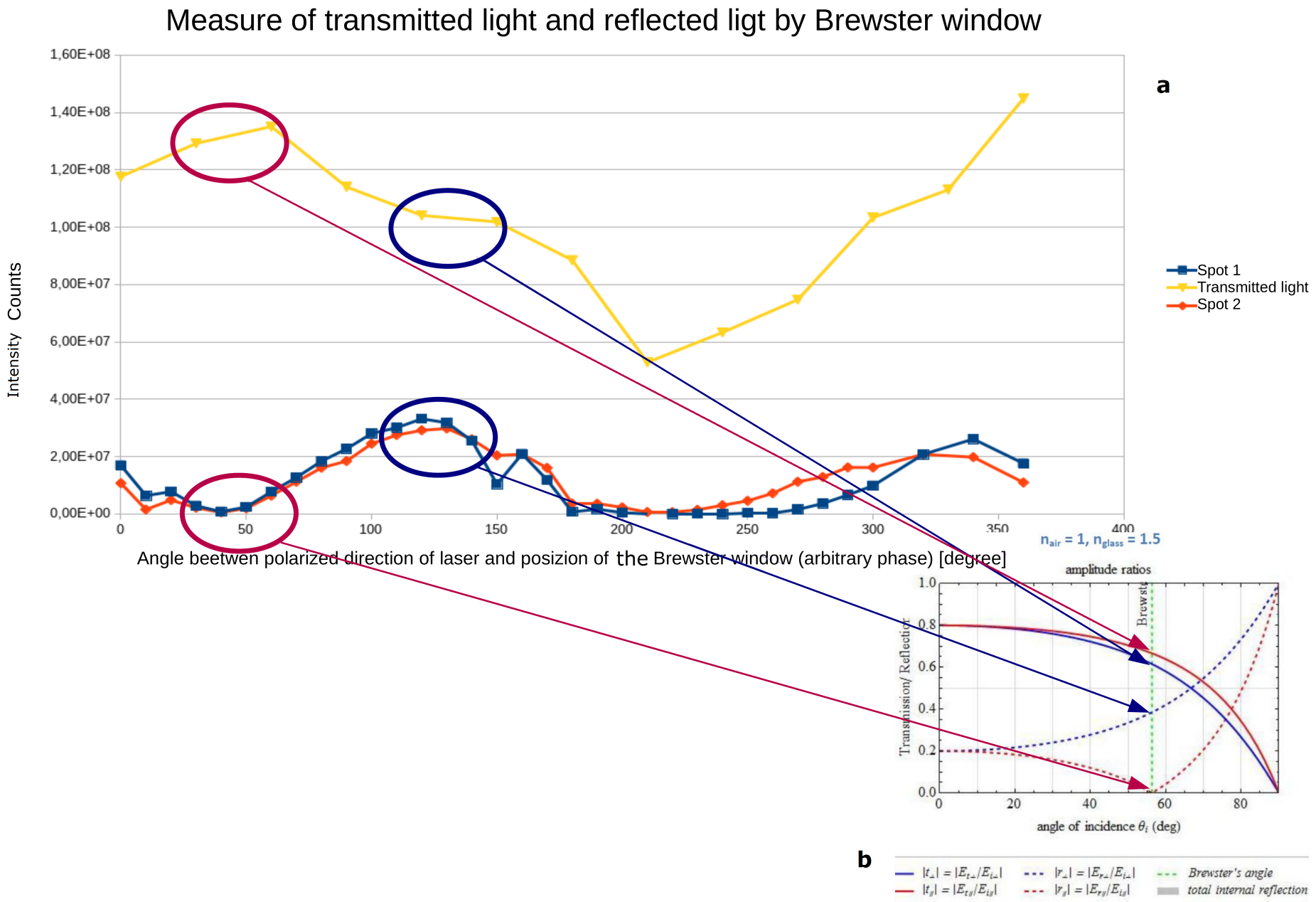

Figure 109: (a) Graph of the measure acquired with simple setup to test the Brewster window. "spot 1"and "spot 2"are the reflections spots that are formed on the horizontal paperboard, they are due to the first interface of the Brewster window (air → glass) and to the second interface (glass → air). (b) In lower right side of figure are reported a theoretical computed graph.

A.7 Mechanical project of prototype of polarimeter

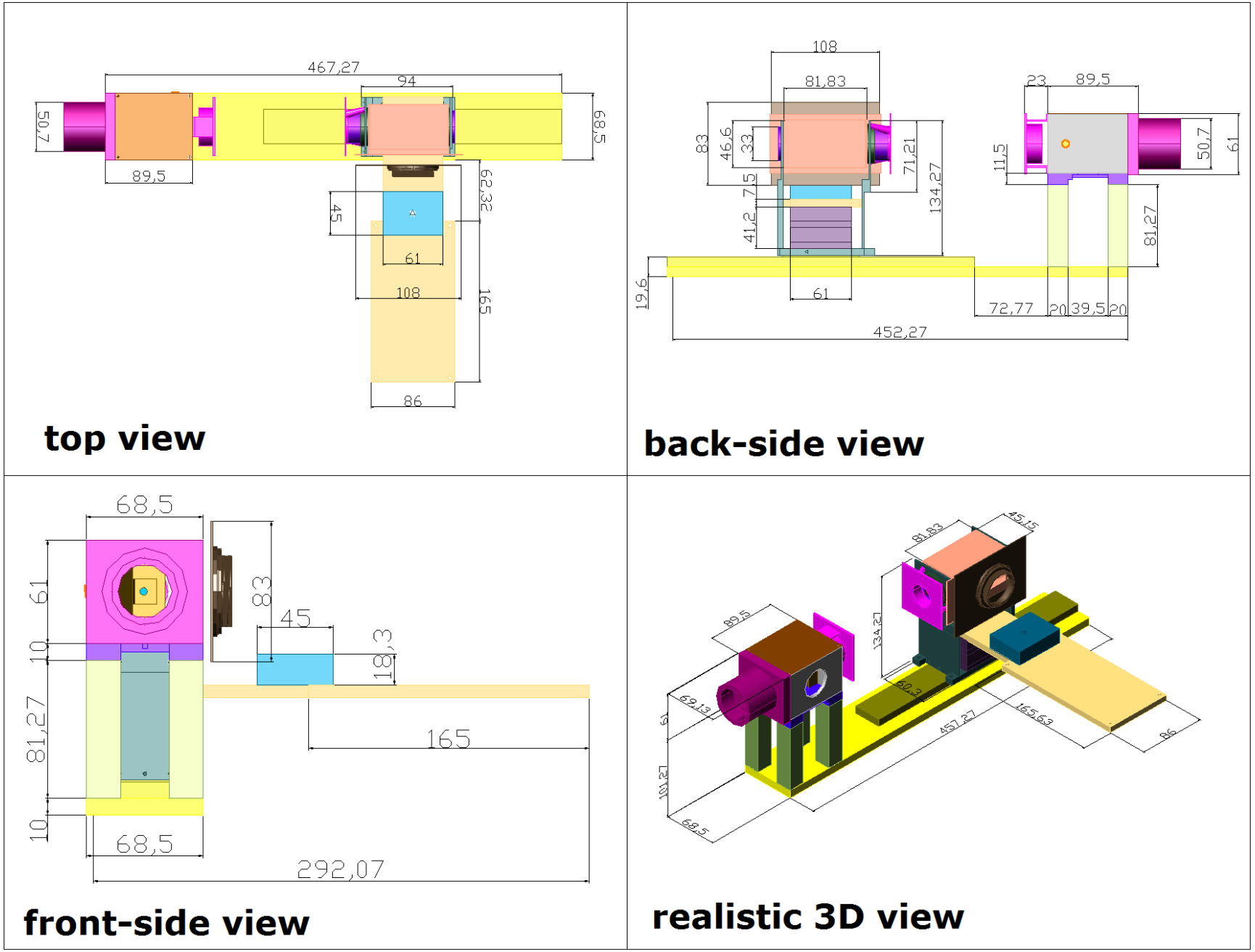

Figure 110: General project of the prototype of the polarimeter. Dimensions are in millimeters.

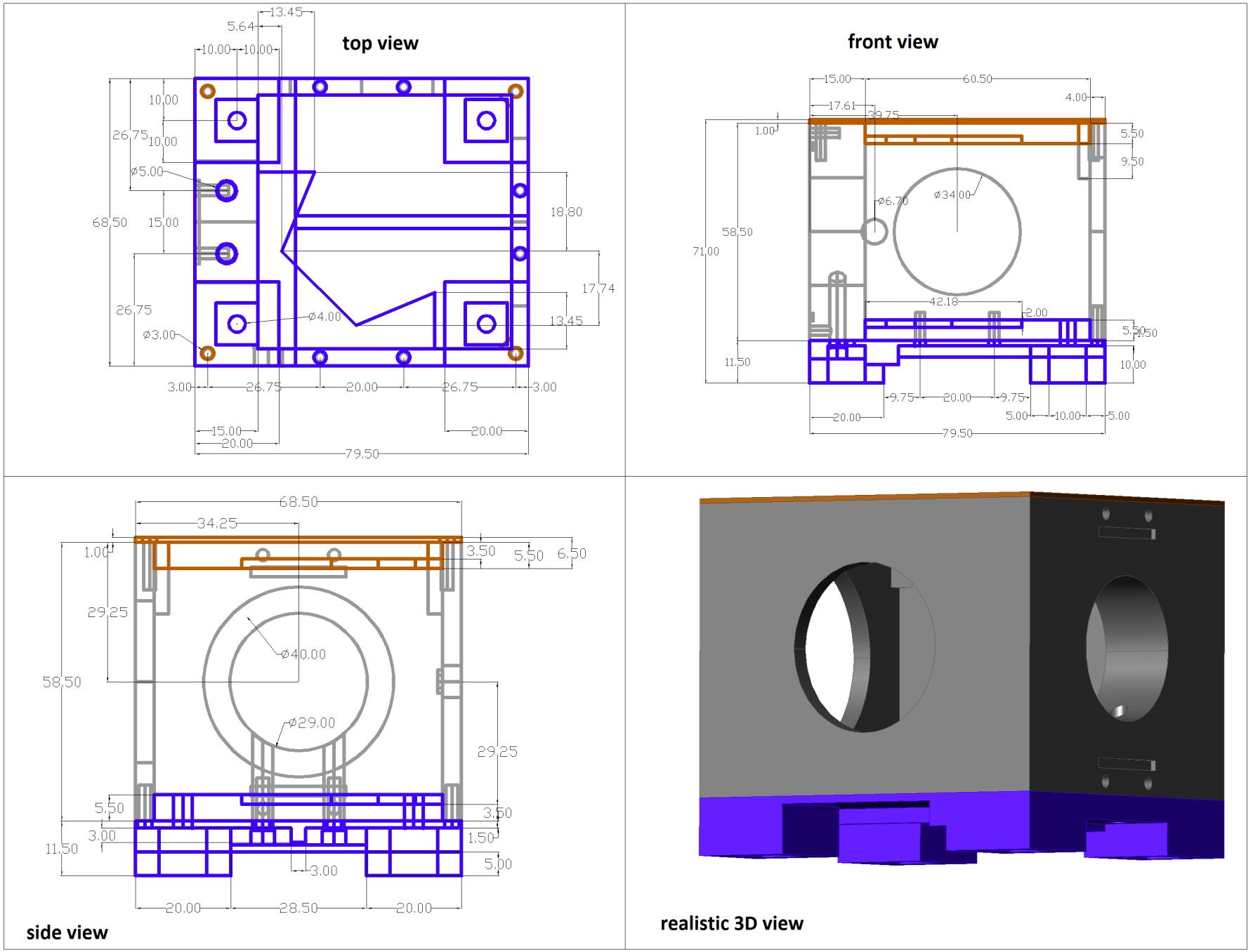

Figure 111: Project of “star selection box”. Dimensions are in millimeters.

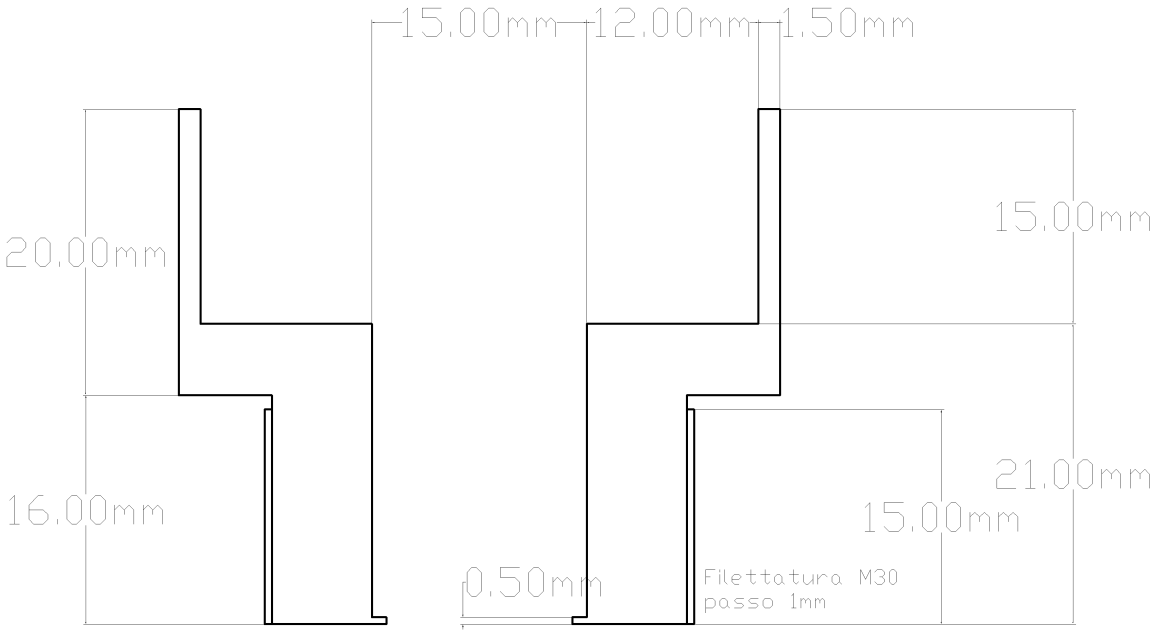

Figure 112: Mechanical support of the collimating lens. Section of the piece to be realized on a lathe.

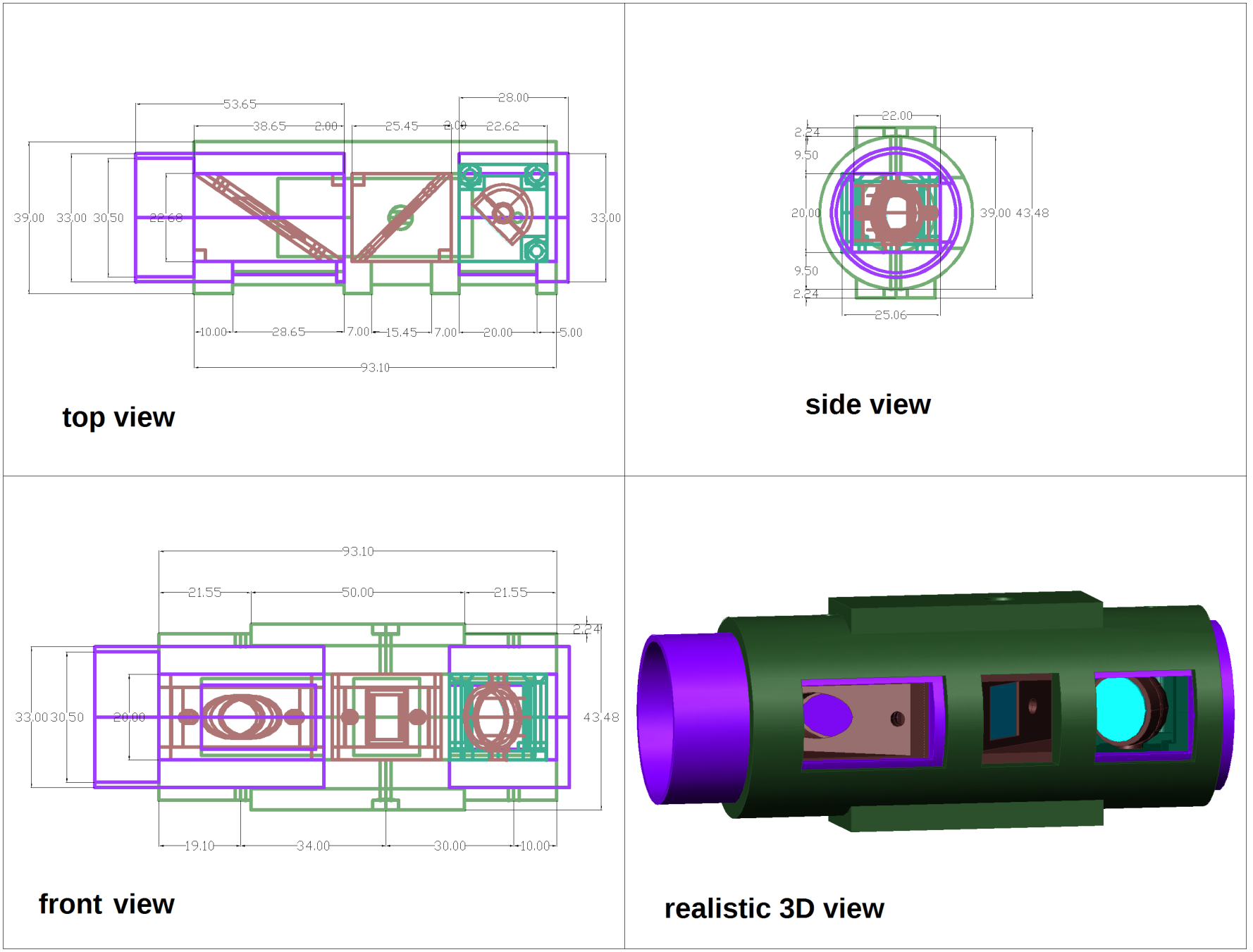

Figure 113: Project of “optical box”. This box contains the optics that split light according to its polarization. Dimensions are in millimeters.

A.8 Computation of the Moon's phase angle

From [62] are determined the Cartesian coordinate of the Earth and the Moon (the Sun is positioned at the origin of the reference frame) to determine the angle of phase between them at the date and time of the Moon observations. The 28th of July at 00:30 CEST Earth is in (x: 0.5764015 au, y: -0.8360830 au, z: 0.0 au), the Moon is in (x: 0.5758958 au, y: -0.8385769au, z: 0.0002185 au). The phase angle α can be determined by the scalene triangle whose vertexes are the Sun, The Earth, and the Moon. The length of triangle's sides is:

$$l = \sqrt{(x_2 - x_1)^2 + (y_2 - y_1)^2 + (z_2 - z_1)^2} \tag{112}$$

So the 3 sides of the triangle are:

$$l_{Earth-Moon} = \sqrt{(x_{Earth} - x_{Moon})^2 + (y_{Earth} - y_{Moon})^2 + (z_{Earth} - z_{Moon})^2} = 0.00255au \tag{113}$$

$$l_{Earth-Sun} = \sqrt{(x_{Earth})^2 + (y_{Earth})^2 + (z_{Earth})^2} = 1.01552au \tag{114}$$

$$l_{Moon-Sun} = \sqrt{(x_{Moon})^2 + (y_{Moon})^2 + (z_{Moon})^2} = 1.01728au \tag{115}$$

And the phase angle of the Moon is (with inverse "Law of cosines"):

$$\alpha_{Moon} = \arccos\left(\frac{(l_{Earth-Moon})^2 + (l_{Moon-Sun})^2 - (l_{Earth-Sun})^2}{2 \cdot l_{Earth-Moon} \cdot l_{Moon-Sun}}\right) = 47.2° \tag{116}$$

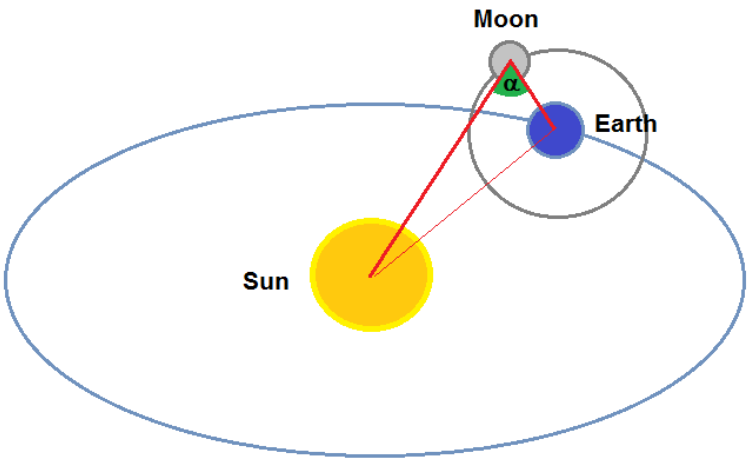

Figure 114: The scheme of the Moon phase α calculation. The distance and the celestial bodies diameters are not in scale.

A.9 Some examples of polarimetric measurements in Solar system

Small particles, like dust and regolith, are in many solar system bodies, in the interplanetary medium, and probably in the exoplanet atmosphere. They influence the climate of these planets.

Studying the properties of dust's particles in situ is often impossible in astrophysics. Only in our solar system there are some exceptions where the space exploration can analyze particles samples (example ESA Rosetta-Philae can analyze sample jetted from the surface of the comet 67/P Churyumov-Gerasimenko).

In astrophysics, it is possible to understand the properties of source and medium (inter-galaxy, interstellar and interplanetary medium) by analyzing the light received from one or more sources.

Analyzing polarimetric characteristic of the scattered radiation important proprieties of the particles as the size, the morphology, and the chemical composition can be deduced. [37]. The capability of understanding properties of particles is connected with the ability to simulate the theoretic measurement to make a correct inverse optical characterization problem.

The polarimetry is a good indicator to characterize **asteroids** of Solar System [38]. Only a few observations are reported in the literature (≈ 350 object observed polarimetric at least once) respect the number of known asteroids. The polarization is modulated with orbital phase angle as for other bodies. A zero phase angle is very difficult to occur for "main-belt asteroids" because the orbit of the asteroids is generally inclined respect to the Earth's orbit. The minimum angle of phase measurable for these asteroids is about 1° or 2°. The maximum phase angle is about 35°. TNOs (Trans-Neptunian Objects) are observable at maximum phase angle of a few degrees only.

The Intensity of polarization can be computed as:

$$P = \frac{(I_\perp - I_\parallel)}{(I_\perp + I_\parallel)} \tag{117}$$

Where"I" is the intensity measured by Polaroid filter parallel to scattering plane (the plane that contains Sun, Earth, and asteroid) and perpendicular at the same plane. From elementary physics, the light is expected to be polarized orthogonal to the scattering plane, but in real measurements this occurs only for the angle mayor than "inversion angle". The inversion angle is about 20° for main-belt asteroids. See fig. 115 for an example of real measurement of asteroids of the "Main-belt" of the Solar System. The negative branch of the degree of polarization curve indicates that the inclination of the polarization vector is near the scattering plane. The slope measured at the inversion angle is called **"polarimetric slope h"** and the minimum value of the degree of polarization in the negative branch is called **"**P_{min}**"**. P_{min} is useful to estimate the albedo of the asteroids. For the main-belt asteroids, it is impossible to measure P_{max} from the Earth, the maximum value of the degree of polarization, as it occurs at about 100° of phase angle. P_{max} was observed for some NEOs (Near Earth Objects) visible at very large phase angles.

Another astrophysical science target of polarimetry is the **Sun** [39]. The Sun is the only star resolved in great detail. The role of the solar magnetic field is important to understand the

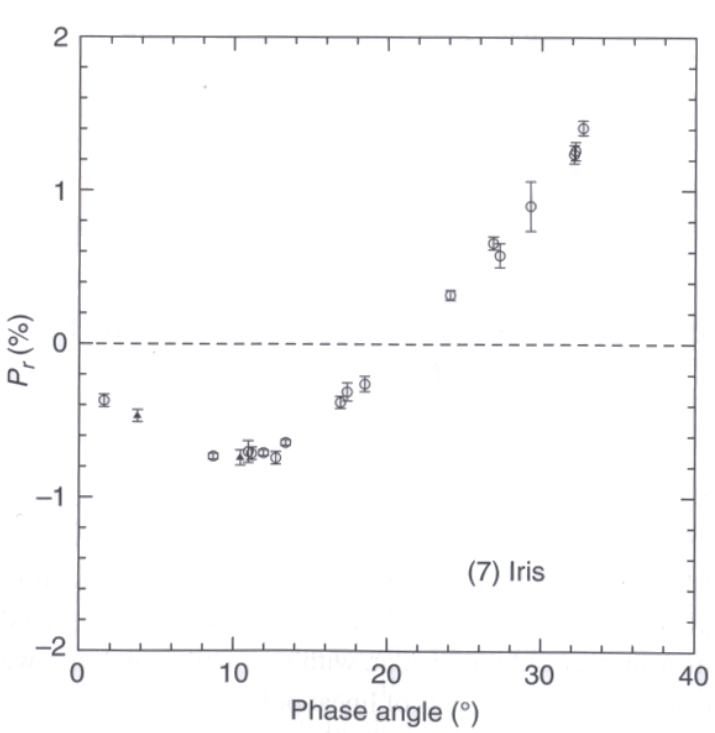

Figure 115: Degree of polarization of Iris asteroids of main-belt. Image taken from [38].

Sun's spot and solar cycles (like the 11 years activity cycle). The structure of the magnetic field has a scale smaller than max optically resolved structure with a solar telescope. So solar magnetic field models must compute sub-visible structures. To constrain this model, the polarimetric signature of Sun activity are fundamental. The data and instrumentation for solar spectropolarimetry are different from Solar System bodies (except the Sun) and stars polarimetry. The big flux collected with a solar telescope between 70cm and 150cm of diameter permits a spectral resolution for polarimetry analysis even of 10mÅ, impossible for stars and/or planets.

FTS interferometers were used to observe the Sun extracting the spectro-polarimetry information [42]. The instrument was developed starting from Michelson interferometer. Two mirrors can be moved by a system of oil and electrics motors. What is important is the position of these mirrors that must be known every time with very high precision (inferior to wavelength). To achieve this precision, a system of laser interferometry is used. The resolving power is limited by the maximum path of mirror's movement. A big advantage of this type of spectrograph is to cover a very wide range of wavelengths. A crystal polarization modulator at 10kHz was added in front of the spectrograph to transform the spectrograph in a spectro-polarimeter. A detail of a spectrum obtained with this technique is reported in fig. 116.

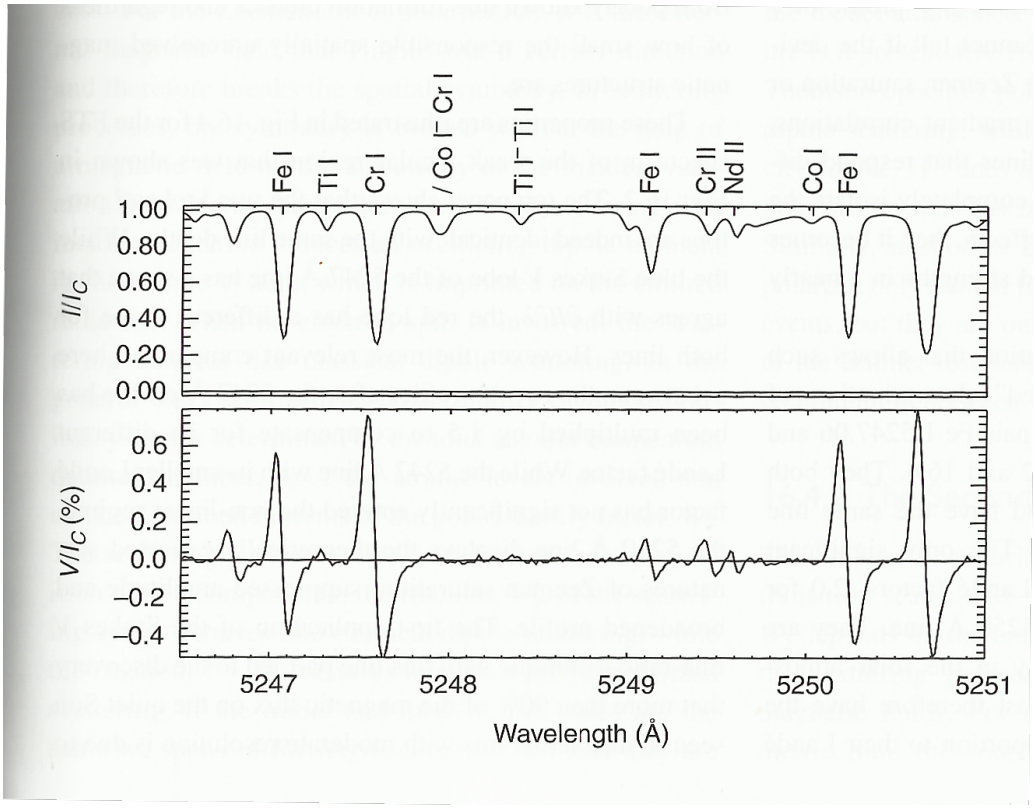

Figure 116: Spectrum of Sun light obtained by FTS in the wavelength of the line of Fe I ($\lambda = 5247.06$). Graph taken from [41].

A.10 Code of the program used to calibrate polarimeter and make a measure of the polarization

C Code of the program written to optimize the coefficients of transmission and reflection, the flux and polarization of the light.

```
#include <stddef.h>
#include <stdio.h>
#include <stdlib.h>
#include <math.h>
#include <nlopt.h>
#define ANGOLO_BR_BS 0.102
void dgetrf_(int* M, int *N, double* A, int* lda, int* IPIV, int*
    INFO);
void dgetri_(int* N, double* A, int* lda, int* IPIV, double* WORK,
    int* lwork, int* INFO);
double determinant(double[][10],double);
void cofactor(double[][10],double);
void transpose(double[][10],double[][10],double);
double determinant(double a[10][10],double k)
{
double s=1,det=0,b[10][10];
int i,j,m,n,c;
  if (k==1)
    {
     return (a[0][0]);
    }
  else
    {
     det=0;
     for (c=0;c<k;c++)
       {
        m=0;
        n=0;
        for (i=0;i<k;i++)
          {
            for (j=0;j<k;j++)
              {
                b[i][j]=0;
                if (i != 0 && j != c)
                 {
                   b[m][n]=a[i][j];
                   if (n<(k-2))
                    n++;
```

```
                    else
                     {
                      n=0;
                      m++;
                      }
                    }
                 }
               }
          det=det + s * (a[0][c] * determinant(b,k-1));
          s=-1 * s;
          }
     }
     return (det);
}
void cofactor(double num[10][10],double f)
{
 double b[10][10],fac[10][10];
 int p,q,m,n,i,j;
 for (q=0;q<f;q++)
 {
   for (p=0;p<f;p++)
    {
     m=0;
     n=0;
     for (i=0;i<f;i++)
     {
       for (j=0;j<f;j++)
        {
          if (i != q && j != p)
          {
            b[m][n]=num[i][j];
            if (n<(f-2))
             n++;
            else
             {
               n=0;
               m++;
               }
            }
        }
      }
      fac[q][p]=pow(-1,q + p) * determinant(b,f-1);
```

```
    }
  }
  transpose(num,fac,f);
}

/*Finding transpose of matrix*/


void transpose(double num[10][10],double fac[10][10],double r)
{
  int i,j;
  double b[10][10],inverse[10][10],d;
  for (i=0;i<r;i++)
    {
     for (j=0;j<r;j++)
       {
         b[i][j]=fac[j][i];
       }
    }
  d=determinant(num,r);
  for (i=0;i<r;i++)
    {
     for (j=0;j<r;j++)
       {
        inverse[i][j]=b[i][j] / d;
       }
    }
   printf("\n\n\nThe inverse of matrix is : \n");
   for (i=0;i<r;i++)
    {
     for (j=0;j<r;j++)
       {
         printf("\t%f",inverse[i][j]);
       }
    printf("\n");
     }
}



void inverse(double* A, int N)
{
```

```
    int *IPIV;
    double *WORK;
    int INFO;
    int LWORK;
    LWORK = N*N;
    IPIV = (int *)malloc((N+1)*sizeof(int));
    WORK = (double *)malloc((LWORK)*sizeof(double));
    dgetrf_(&N,&N,A,&N,IPIV,&INFO);
    dgetri_(&N,A,&N,IPIV,WORK,&LWORK,&INFO);
    free(IPIV);
    free(WORK);
}
/* Auxiliary routine: printing eigenvalues */
void print_eigenvalues( char* desc, int n, double* wr, double* wi ) {
        int j;
        printf( "\n %s\n", desc );
   for( j = 0; j < n; j++ ) {
      if( wi[j] == (double)0.0 ) {
         printf( " %6.2f", wr[j] );
      } else {
         printf( " (%6.2f,%6.2f)", wr[j], wi[j] );
      }
   }
   printf( "\n" );
}
/* Auxiliary routine: printing eigenvectors */
void print_eigenvectors( char* desc, int n, double* wi, double* v,
   int ldv ) {
        int i, j;
        printf( "\n %s\n", desc );
   for( i = 0; i < n; i++ ) {
      j = 0;
      while( j < n ) {
         if( wi[j] == (double)0.0 ) {
            printf( " %6.2f", v[i+j*ldv] );
            j++;
         } else {
            printf( " (%6.2f,%6.2f)", v[i+j*ldv], v[i+(j+1)*ldv] );
            printf( " (%6.2f,%6.2f)", v[i+j*ldv], -v[i+(j+1)*ldv] );
            j += 2;
         }
      }
```

```
        printf( "\n" );
    }
}
void eigenvalue(double *a, int N)
{
      int n = N, lda = N, ldvl = N, ldvr = N, info, lwork;
      double wkopt;
      double wr[N], wi[N], vl[N*N], vr[N*N];
      double* work;
      lwork=-1;
      dgeev_( "Vectors", "Vectors", &n, a, &lda, wr, wi, vl, &ldvl, vr
          , &ldvr,
           &wkopt, &lwork, &info );
      lwork = (int)wkopt;
      work = (double*)malloc( lwork*sizeof(double) );
/* Solve eigenproblem */
      dgeev_( "Vectors", "Vectors", &n, a, &lda, wr, wi, vl, &ldvl, vr
          , &ldvr,
            work, &lwork, &info );
/* Check for convergence */
      if( info > 0 ) {
                printf( "The algorithm failed to compute eigenvalues.\n
                    " );
                exit( 1 );
       }
/* Print eigenvalues */
        print_eigenvalues( "Eigenvalues", n, wr, wi );
/* Print left eigenvectors */
        print_eigenvectors( "Left eigenvectors", n, wi, vl, ldvl );
/* Print right eigenvectors */
        print_eigenvectors( "Right eigenvectors", n, wi, vr, ldvr );
/* Free workspace */
      free( (void*)work );

}
int numero_righe(FILE *);
double funzione_chi(unsigned, const double *, double *, void *);
double funzione_chi_stampa(unsigned, const double *, double *, void
    *);

struct dati_funzione {
int num_dati;
```

```
int numero_sorgenti;
int *num_misure;
double *angolo;
double *spot_1;
double *spot_2;
double *spot_3;
double *sigma_1;
double *sigma_2;
double *sigma_3;
int *N_mis_angolo;
}


main () {

/* spot sono le misure effettive, mis sono quelle aspettate*/

double F, alpha,  F_s, F_p, chi_quadro, chi_quadro1, mis_1, mis_2,
    mis_3, F_min, F_max, F_step, F_points, alpha_min=0.0, alpha_max =
    360.0, alpha_step, alpha_points, F_s_min, F_s_max, F_s_step,
    s_points, F_p_min, F_p_max, F_p_step, p_points, F_chi, alpha_chi,
    F_s_chi, F_p_chi, F_s_chi_1 = 0., F_p_chi_1 = 0.;
double BR_t_p, BR_t_s, BR_r_p, BR_r_s, BS_t_p, BS_t_s, BS_r_p, BS_r_s
    , M_p, M_s, BR_t_p_chi, BR_t_s_chi, BR_r_p_chi, BR_r_s_chi,
    BS_t_p_chi, BS_t_s_chi, BS_r_p_chi, BS_r_s_chi, M_p_chi, M_s_chi;
double *angolo, *spot_1, *spot_2, *spot_3, *sigma_1, *sigma_2, *
    sigma_3, *H,*EIGEN;
double matrix[10][10],inverse_matrix[10][10],det,num;
double m_Transpose[10][10];
FILE *input, *input_dati;
int ctrl, numero_dati, *N_mis, i, j, k, coef_numero_punti[10],
    numero_sorgenti, numero_coef, *N_mis_angolo, co;
double *coef_min, *coef_max, *coef, coef_risultati, coef_step[10];
double cos_an, sen_an;
void *puntatore;
struct dati_funzione dati;
double *tol;

puntatore = &dati;
/*Brewster_trasmitted_p  Brewster_trasmitted_s  Brewster_reflected_p
    Brewster_reflected_s
BS_trasmitted_p  BS_trasmitted_s  BS_reflected_p  BS_reflected_s
```

```
Mirror_reflected_p Mirror_reflected_s
immissione dei parametri*/

input_dati = fopen("dati.txt", "r");
/*osservabile_numero angolo spot1 spot 2 spot 3 delta_spot1
   delta_spot2 delta_spot3*/
numero_dati = numero_righe(input_dati);
printf ("numero righe: %d\n", numero_dati);
fclose(input_dati);

input = fopen("calibrazione.txt", "r");

printf ("\nNumero dati: %d\n", numero_dati);
printf("\nallocazione memoria per immagazzinare le misure");
N_mis = malloc(numero_dati * sizeof(int));
angolo = malloc(numero_dati * sizeof(double));
spot_1 = malloc(numero_dati * sizeof(double));
spot_2 = malloc(numero_dati * sizeof(double));
spot_3 = malloc(numero_dati * sizeof(double));
sigma_1 = malloc(numero_dati * sizeof(double));
sigma_2 = malloc(numero_dati * sizeof(double));
sigma_3 = malloc(numero_dati * sizeof(double));

printf("\ncaricamento dei valori delle misure");
fflush(0);
input_dati = fopen("dati.txt", "r");
for (i = 0; i < numero_dati; i++) {
        fscanf(input_dati, "%d %lf %lf %lf %lf %lf %lf %lf", (N_mis +
            i), (angolo + i), (spot_1 + i), (spot_2 + i), (spot_3 + i
           ), (sigma_1 + i), (sigma_2 + i), (sigma_3 + i));
        }
printf("\nFINE caricamento dei valori delle misure\n");
fflush(0);
numero_sorgenti = 1;
for (i = 0; i < numero_dati; i++) {
        printf("%d %lf %lf %lf %lf %lf %lf %lf\n", N_mis[i], angolo[i
           ], spot_1[i], spot_2[i], spot_3[i], sigma_1[i], sigma_2[i
           ], sigma_3[i]);
        if (N_mis[i] > (numero_sorgenti-1)) numero_sorgenti++;
        }
printf ("\nNumero di sorgenti individuate: %d\n", numero_sorgenti);
```

```
N_mis_angolo = malloc(numero_sorgenti * sizeof(int));

for (i=0; i<numero_sorgenti; i++) {
        N_mis_angolo[i] = 0;
        }

numero_coef = numero_sorgenti * 2 + 7;
co = 1;
k=0;
j=0;
for (i = 0; i < numero_dati; i++) {
        if (k<1) {
                if (angolo[i] > 0.) {
                        numero_coef++;
                        k = 1;
                        j = i;
                        N_mis_angolo[N_mis[i]] = co;
                        co++;
                        }
                }
        if (N_mis[i] > N_mis[j]) k = 0;
        }
printf ("Numero di coefficienti da ottimizzare: %d\n", numero_coef);

dati.num_dati = numero_dati;
dati.numero_sorgenti = numero_sorgenti;
dati.num_misure = N_mis;
dati.angolo = angolo;
dati.spot_1 = spot_1;
dati.spot_2 = spot_2;
dati.spot_3 = spot_3;
dati.sigma_1 = sigma_1;
dati.sigma_2 = sigma_2;
dati.sigma_3 = sigma_3;
dati.N_mis_angolo = N_mis_angolo;

coef_min = malloc((numero_coef) * sizeof(double));
coef_max = malloc((numero_coef) * sizeof(double));
coef = malloc((numero_coef) * sizeof(double));
tol = malloc((numero_coef) * sizeof(double));
```

```
/* coef 0 trasmissione Brewster, coef 1 trasmissione s BS, coef 2
   BR_r_, coef 3 BR_r_, coef 4 BS_r_, coef 5 BS_r_, coef 7 BS_t_p*/
coef_min[0] = 0.95; coef_min[1] = 0.75; coef_min[2] = 0.00; coef_min
   [3] = 0.22; coef_min[4] = 0.0; coef_min[5] = 0.83; /*coef_min[6] =
    0.6; coef_min[7] = 0.6; */
coef_max[0] = 1.00; coef_max[1] = 0.85; coef_max[2] = 0.05; coef_max
   [3] = 0.30; coef_max[4] = 0.05; coef_max[5] = 0.93; /*coef_max[6]
   = 1.00; coef_max[7] = 1.00; */
coef_min[0] = 0.97; coef_min[1] = -0.01; coef_min[2] = -0.01;
   coef_min[3] = -0.01; coef_min[4] = -0.01; coef_min[5] = -0.01;
   coef_min[6] = -0.01; /*coef_min[6] = 0.6; coef_min[7] = 0.6; */
coef_max[0] = 1.01; coef_max[1] = 1.0; coef_max[2] = 1.0; coef_max[3]
    = 1.0; coef_max[4] = 1.0; coef_max[5] = 1.0; coef_max[6] = 1.0;
   /*coef_max[6] = 1.00; coef_max[7] = 1.00; */

for (i = 7; i < 7 + numero_sorgenti * 2; i += 2) {
        coef_min[i] = 0;
        coef_min[i+1] = 0;
        coef_max[i] = 9000000000.0;
        coef_max[i+1] = 2.0 * M_PI;
        coef[i] = 50000;
//      coef[i+1] = 3.1;
        coef[i+1]=0.4;
        }
if (7 + numero_sorgenti * 2 < numero_coef) {
for (i = 7 + numero_sorgenti * 2; i < numero_coef; i++) {
        coef_min[i] = 0;
        coef_max[i] = 2000000000.0;
        coef[i] = 20000;
        }
}

for (i = 0; i < 10; i++) {
        tol[i] = 0.001;
        }
/* tol[7] = 50;
tol[8] = 0.1;
tol[9] = 50;
 */

/* calibrazione.txt is a file with calibration constant:
```

```
Brewster_trasmitted_p Brewster_trasmitted_s Brewster_reflected_p
    Brewster_reflected_s
BS_trasmitted_p BS_trasmitted_s BS_reflected_p BS_reflected_s
Mirror_reflected_p Mirror_reflected_s
*/


fscanf (input, "%lf %lf %lf %lf\n", &BR_t_p , &BR_t_s, coef + 2, coef
    + 3);
fscanf (input, "%lf %lf %lf %lf\n", &BS_t_p, &BS_t_s, coef + 4, coef
   + 5);
/*fscanf (input, "%lf %lf", coef + 6, coef + 7);*/
*coef = BR_t_p / (1 - *(coef + 2));
*(coef + 1) = BS_t_p / (1 - *(coef + 4));

coef[7] = 1000;
coef[8]= 200;
if (N_mis_angolo[0] == 1)  coef[9] = 50000;
coef[0] = 0.98; coef[1] = 0.096; coef[2] = 0.0; coef[3] = 0.26; coef
   [4] = 0.035; coef[5] = 0.88; coef[6] = 0.772;

printf ("\nchi quadro con valori forniti: %lf\n", funzione_chi_stampa
   (numero_coef, coef, NULL, &dati));

/*printf ("\nF %lf alpha %lf BR_t_p %lf, BR_t_s %lf, BR_r_p %lf,
   BR_r_s %lf, BS_t_p %lf, BS_t_s %lf, BS_r_p %lf, BS_r_s %lf, M_p %
   lf, M_s %lf, T_BR %lf, T_BS %lf chi_q: %lf\n", *(coef + 8) , *(
   coef + 9), BR_t_p, BR_t_s, *(coef + 2), *(coef + 3), BS_t_p,
   BS_t_s, *(coef + 4), *(coef + 5), *(coef + 6), *(coef + 7), *coef,
    *(coef+1), coef_risultati );*/

for (i = 0; i < numero_coef; i++) {
        coef[i] = (coef_max[i] + coef_min[i]) / 2.;
        }

nlopt_opt opt;
opt = nlopt_create(NLOPT_GN_ISRES, numero_coef);
printf ("\nSettaggio lower bounds %d\n", nlopt_set_lower_bounds(opt,
   coef_min));
printf ("\nSettaggio upper bounds %d\n", nlopt_set_upper_bounds(opt,
   coef_max));
```

```
BR_t_p = (1 - *(coef + 2)) * *coef;
BR_t_s = (1 - *(coef + 3)) * *coef;

printf ("\nchi quadro con valori medi: %lf\n", funzione_chi(
   numero_coef, coef, NULL, &dati));
{printf ("\nF %lf alpha %lf BR_t_p %lf, BR_t_s %lf, BR_r_p %lf, 
   BR_r_s %lf, BS_t_p %lf, BS_t_s %lf, BS_r_p %lf, BS_r_s %lf, M_p %
   lf, M_s %lf, T_BR %lf, T_BS %lf chi_q: %lf\n", *(coef + 8) , *(
   coef + 9), BR_t_p, BR_t_s, *(coef + 2), *(coef + 3), BS_t_p,
   BS_t_s, *(coef + 4), *(coef + 5), *(coef + 6), *(coef + 7), *coef,
    *(coef+1), coef_risultati );}

printf ("\nSettaggio funzione da minimizzare %d\n",
   nlopt_set_min_objective(opt, funzione_chi, &dati));

/*nlopt_set_xtol_rel(opt, 1e-4);*/
nlopt_set_maxtime(opt,30);
nlopt_set_stopval(opt, (double)numero_coef);
/* nlopt_result nlopt_set_xtol_abs(opt, tol); */

printf("\nNumero dati nel prog. principale: %d\n", numero_dati);
   fflush(0);

ctrl = nlopt_optimize(opt, coef , &coef_risultati);

BR_t_p = (1 - *(coef + 2)) * *coef;
BR_t_s = (1 - *(coef + 3)) * *coef;

if (ctrl < 0) {printf("\n OTTIMIZZAZIONE FALLITA\nCodice errore: %d"
   , ctrl);} else
{printf ("\nE_par %lf E_per %lf BR_t_p %lf, BR_t_s %lf, BR_r_p %lf, 
   BR_r_s %lf, BS_t_p %lf, BS_t_s %lf, BS_r_p %lf, BS_r_s %lf, chi_q:
   %lf\n", *(coef + 7) , *(coef + 8), BR_t_p, BR_t_s, *(coef + 2),
   *(coef + 3), *(coef + 6), *(coef + 1), *(coef + 4), *(coef + 5),
   coef_risultati );}

printf ("\nchi quadro con valori medi: %lf\n", funzione_chi_stampa(7
   + numero_sorgenti * 2, coef, NULL, &dati));



        H = (double *)malloc(10*10*sizeof(double));
        EIGEN = (double *)malloc(10*10*sizeof(double));
```

```
          for(i=0;i<10;i++){
            for(k=0;k<10;k++){
             H[i+k*10]= 0.;
             coef[i]+=tol[i];
             coef[k]+=tol[k];
             H[i+k*10]=funzione_chi(10, coef, NULL, &dati);
             coef[i]-=2*tol[i];
             coef[k]-=2*tol[k];
             H[i+k*10]+=funzione_chi(10, coef, NULL, &dati);
             coef[i]+=2*tol[i];
             H[i+k*10]-=funzione_chi(10, coef, NULL, &dati);
             coef[i]-=2*tol[i];
             coef[k]+=2*tol[k];
             H[i+k*10]-=funzione_chi(10, coef, NULL, &dati);
             coef[i]+=tol[i];
             coef[k]-=tol[k];
             H[i+k*10]=H[i+k*10]/(tol[i]*tol[k]*4);
        EIGEN[i+k*10]=H[i+k*10];
            }
           }

printf ("\nHessiano\n\n");
for (i = 0; i < 10; i++){
         for(k=0; k<10; k++){
                  printf("%.15lf ", H[i+k*10]);
                  }
         printf("\n");
}

         inverse(H,10);
printf ("\nmatrice errori\n\n");
for (i = 0; i < 10; i++){
         for(k=0; k<10; k++){
//                printf("%.15lf ", H[i+k*10]);
                  matrix[i][k]= H[i+k*10];
                  }
         printf("\n");
}



         det = determinant(matrix,10);
```

```
        if(det==0){
          printf("Error: inverse does not exist null determinant \n")
              ;
        }else{
            cofactor(matrix,10);
        }
        for (i = 0; i < 10; i++){
        printf("%lf +/- %.15lf | \n", coef[i], sqrt(fabs(H[11*i])));

}

       eigenvalue(EIGEN,10);

printf ("\nmatrice autovalori\n\n");
for (i = 0; i < 10; i++){
        for(k=0; k<10; k++){
                printf("%.15lf ", EIGEN[i+k*10]);
                }
        printf("\n");
}
        for (i = 0; i < 10; i++){
        printf("%lf +/- %.15lf | \n", coef[i], sqrt(2./fabs(EIGEN[11*
           i])));
        }


}




int numero_righe(FILE *input) {
int k = 0;
char a;

while ((a = fgetc(input)) != EOF ) {
        if (a == '\n') k++;
        }

return k;

}
```

```
double funzione_chi(unsigned n, const double *coef,double *grad, void
    *dati1) {
double *angolo, *spot_1, *spot_2, *spot_3, *sigma_1, *sigma_2, *
   sigma_3;
double *F_s, *F_p, mis_1, mis_2, mis_3, chi_quadro = 0.;
double BR_t_p, BR_t_s, BS_t_p, BS_t_s;
int i, numero_dati, *N_mis, k, numero_sorgenti, j, *N_mis_angolo;
struct dati_funzione *dati;
dati = dati1;

numero_dati = (*dati).num_dati;
numero_sorgenti = (*dati).numero_sorgenti;
N_mis = (*dati).num_misure;
angolo = (*dati).angolo;
spot_1 = (*dati).spot_1;
spot_2 = (*dati).spot_2;
spot_3 = (*dati).spot_3;
sigma_1 = (*dati).sigma_1;
sigma_2 = (*dati).sigma_2;
sigma_3 = (*dati).sigma_3;
N_mis_angolo = (*dati).N_mis_angolo;

BR_t_p = (1 - *(coef + 2)) * *coef;
BR_t_s = (1 - *(coef + 3)) * *coef;

F_s = malloc(numero_sorgenti * sizeof(double));
F_p = malloc(numero_sorgenti * sizeof(double));
/*printf("Prova prima del ciclo, numero dati: %d\n", numero_dati);
   fflush(0);*/
for (i = 0; i < numero_dati; i++){
        k = *(N_mis + i);
        j = *(N_mis_angolo + k);
        if (j == 0) {
                F_s[k] = *(coef + 7 + k*2) * pow(cos( *(coef + 8 + k
                   *2) - *(angolo + i) ), 2);
                F_p[k] = *(coef + 7 + k*2) * pow(sin( *(coef + 8 + k
                   *2) - *(angolo + i) ), 2);
                }
        if (j > 0) {
                F_s[k] = 0.5 * *(coef + 7 + numero_sorgenti * 2 + j -
                    1) + *(coef + 7 + k*2) * pow(cos( *(coef + 8 + k
```

```
                    *2) - *(angolo + i) ), 2);
                F_p[k] = 0.5 * *(coef + 7 + numero_sorgenti * 2 + j -
                    1) + *(coef + 7 + k*2) * pow(sin( *(coef + 8 + k
                    *2) - *(angolo + i) ), 2);
                }
/*printf("%d %lf %lf %lf %lf %lf %lf\n", *(N_mis + i), *(angolo +
    i), *(spot_1 + i), *(spot_2 + i), *(spot_3 + i), *(sigma_1 + i),
   *(sigma_2 + i), *(sigma_3 + i));*/
        mis_1 = F_s[k] * *(coef + 3) + F_p[k] * *(coef + 2);
        if (j == 0) {
                F_s[k] = *(coef + 7 + k*2) * pow(cos( *(coef + 8 + k
                    *2) - *(angolo + i) + ANGOLO_BR_BS), 2);
                F_p[k] = *(coef + 7 + k*2) * pow(sin( *(coef + 8 + k
                    *2) - *(angolo + i) + ANGOLO_BR_BS), 2);
                }
        if (j > 0) {
        F_s[k] = 0.5 * *(coef + 7 + numero_sorgenti * 2 + j - 1) + *(
            coef + 7 + k*2) * pow(cos( *(coef + 8 + k*2) - *(angolo +
            i) + ANGOLO_BR_BS), 2);
        F_p[k] = 0.5 * *(coef + 7 + numero_sorgenti * 2 + j - 1) + *(
            coef + 7 + k*2) * pow(sin( *(coef + 8 + k*2) - *(angolo +
            i) + ANGOLO_BR_BS), 2);
                }
        mis_2 = F_s[k] * BR_t_s * *(coef + 5) + F_p[k] * BR_t_p * *(
            coef + 4);
        mis_3 = F_s[k] * BR_t_s * *(coef + 1) + F_p[k] * BR_t_p * *(
            coef + 6);
/*      printf("prova nel mezzo mis_1 %lf mis_2 %lf mis_3 %lf\n",
    mis_1, mis_2, mis_3); fflush(0);
        printf("\nProva spot 2 %lf\n", *(spot_2 + i)); fflush(0);*/
        chi_quadro += (*(spot_1 + i) - mis_1) * (*(spot_1 + i) -
            mis_1) / *(sigma_1 + i) / *(sigma_1 + i) + (*(spot_2 + i)
            - mis_2) * (*(spot_2 + i) -mis_2) / *(sigma_2 + i) / *(
            sigma_2 + i) + (*(spot_3 + i) - mis_3) * (*(spot_3 + i) -
            mis_3) / *(sigma_3 + i) / *(sigma_3 + i);
/*printf ("mis_1 %lf mis_2 %lf mis_3 %lf chi2 %lf\n", mis_1, mis_2,
    mis_3, chi_quadro); fflush(0);*/
        }
/*printf ("mis_1 %lf mis_2 %lf mis_3 %lf chi2 %lf\n", mis_1, mis_2,
    mis_3, chi_quadro); fflush(0);*/
free(F_s);
free(F_p);
```

```
return chi_quadro;

}




double funzione_chi_stampa(unsigned n, const double *coef,double *
    grad, void *dati1) {
double *angolo, *spot_1, *spot_2, *spot_3, *sigma_1, *sigma_2, *
    sigma_3;
double *F_s, *F_p, mis_1, mis_2, mis_3, chi_quadro = 0.;
double BR_t_p, BR_t_s, BS_t_p, BS_t_s;
int i, numero_dati, *N_mis, k, numero_sorgenti, j, *N_mis_angolo;
struct dati_funzione *dati;
dati = dati1;

numero_dati = (*dati).num_dati;
numero_sorgenti = (*dati).numero_sorgenti;
N_mis = (*dati).num_misure;
angolo = (*dati).angolo;
spot_1 = (*dati).spot_1;
spot_2 = (*dati).spot_2;
spot_3 = (*dati).spot_3;
sigma_1 = (*dati).sigma_1;
sigma_2 = (*dati).sigma_2;
sigma_3 = (*dati).sigma_3;
N_mis_angolo = (*dati).N_mis_angolo;

BR_t_p = (1 - *(coef + 2)) * *coef;
BR_t_s = (1 - *(coef + 3)) * *coef;
BS_t_p = (1 - *(coef + 4)) * *(coef + 1);
BS_t_s = (1 - *(coef + 5)) * *(coef + 1);

F_s = malloc(numero_sorgenti * sizeof(double));
F_p = malloc(numero_sorgenti * sizeof(double));
/*printf("Prova prima del ciclo, numero dati: %d\n", numero_dati);
    fflush(0);*/
for (i = 0; i < numero_dati; i++){
        k = *(N_mis + i);
```

```
        j = *(N_mis_angolo + k);
        if (j == 0) {
                F_s[k] = *(coef + 7 + k*2) * cos( *(coef + 8 + k*2) -
                    *(angolo + i) ) * cos( *(coef + 8 + k*2) - *(
                   angolo + i) );
                F_p[k] = *(coef + 7 + k*2) * sin( *(coef + 8 + k*2) -
                    *(angolo + i) ) * sin( *(coef + 8 + k*2) - *(
                   angolo + i) );
                }
        if (j > 0) {
                F_s[k] = 0.5 * *(coef + 7 + numero_sorgenti * 2 + j -
                    1) + *(coef + 7 + k*2) * cos( *(coef + 8 + k*2) -
                    *(angolo + i) ) * cos( *(coef + 8 + k*2) - *(
                   angolo + i) );
                F_p[k] = 0.5 * *(coef + 7 + numero_sorgenti * 2 + j -
                    1) + *(coef + 7 + k*2) * sin( *(coef + 8 + k*2) -
                    *(angolo + i) ) * sin( *(coef + 8 + k*2) - *(
                   angolo + i) );
                printf("\nIu : %lf , Ip : %lf , Coeff costante sorgente
                   %d: %lf",*(coef + 7 + numero_sorgenti * 2 + j -
                   1) , *(coef + 7 + k*2), k, *(coef + 7 +
                   numero_sorgenti * 2 + j-1));
                }
printf("%d %lf %lf %lf %lf %lf %lf %lf\n", *(N_mis + i), *(angolo + i
   ), *(spot_1 + i), *(spot_2 + i), *(spot_3 + i), *(sigma_1 + i), *(
   sigma_2 + i), *(sigma_3 + i));
        mis_1 = F_s[k] * *(coef + 3) + F_p[k] * *(coef + 2);
        if (j == 0) {
                F_s[k] = *(coef + 7 + k*2) * cos( *(coef + 8 + k*2) -
                    *(angolo + i) + ANGOLO_BR_BS) * cos( *(coef + 8 +
                    k*2) - *(angolo + i) + ANGOLO_BR_BS);
                F_p[k] = *(coef + 7 + k*2) * sin( *(coef + 8 + k*2) -
                    *(angolo + i) + ANGOLO_BR_BS) * sin( *(coef + 8 +
                    k*2) - *(angolo + i) + ANGOLO_BR_BS);
                }
        if (j > 0) {
                F_s[k] = 0.5 * *(coef + 7 + numero_sorgenti * 2 + j -
                    1) + *(coef + 7 + k*2) * cos( *(coef + 8 + k*2) -
                    *(angolo + i) + ANGOLO_BR_BS) * cos( *(coef + 8 +
                    k*2) - *(angolo + i) + ANGOLO_BR_BS);
                F_p[k] = 0.5 * *(coef + 7 + numero_sorgenti * 2 + j -
                    1) + *(coef + 7 + k*2) * sin( *(coef + 8 + k*2) -
```

```
                        *(angolo + i) + ANGOLO_BR_BS) * sin( *(coef + 8 +
                        k*2) - *(angolo + i) + ANGOLO_BR_BS);
                }
        mis_2 = F_s[k] * BR_t_s * *(coef + 5) + F_p[k] * BR_t_p * *(
            coef + 4);
        mis_3 = F_s[k] * BR_t_s * *(coef + 1) + F_p[k] * BR_t_p * *(
            coef + 6);
/*      printf("prova nel mezzo mis_1 %lf mis_2 %lf mis_3 %lf\n",
    mis_1, mis_2, mis_3); fflush(0);
        printf("\nProva spot 2 %lf\n", *(spot_2 + i)); fflush(0);*/
        chi_quadro += (*(spot_1 + i) - mis_1) * (*(spot_1 + i) -
            mis_1) / *(sigma_1 + i) / *(sigma_1 + i) + (*(spot_2 + i)
            - mis_2) * (*(spot_2 + i) -mis_2) / *(sigma_2 + i) / *(
            sigma_2 + i) + (*(spot_3 + i) - mis_3) * (*(spot_3 + i) -
            mis_3) / *(sigma_3 + i) / *(sigma_3 + i);
printf ("mis_1 %lf mis_2 %lf mis_3 %lf chi2 %.15lf\n", mis_1, mis_2,
    mis_3, chi_quadro); fflush(0);
        }
free(F_s);
free(F_p);
/*printf ("mis_1 %lf mis_2 %lf mis_3 %lf chi2 %.15lf\n", mis_1, mis_2
    , mis_3, chi_quadro); fflush(0);*/
return chi_quadro;

}
```

List of Figures

References

[1] A. Wolszczan, D. A. Frail *A planetary system around the muillisecond pulsar PSR1257 + 12*. Nature, Vol. 355, 9 january 1992

[2] exoplanet team *Catalog of exoplanets*. www.exoplanets.eu

[3] Andrew Tribick, Christian Sturm, Ryan Varley, Hanno Rein, et al. *Open Exoplanet Catalogue*. www.openexoplanetcatalogue.com/

[4] NASA Exoplanet Science Institute *Nasa Exoplanet Archive*. http://exoplanetarchive.ipac.caltech.edu

[5] Michel Mayor, Didier Queloz *A Jupiter-mass companion to a solar-type star*. Nature, Vol. 378, 23 november 1995

[6] David Charbonneau, Timothy M. Brown, David W. Latham, Michel Mayor *Detection of planetary transit across a Sun-like star*. The Astrophysical Journal, vol 529, pages L45-L48, 20 January 2000

[7] Ram Sagar, *Discovery of a planetary system around 51 Pegasus*. Astronomical Society of india, 6 december 1995

[8] Gregory P. Laughlin, *Nuovi sistemi solari*. Le Scienze, 1 march 2007

[9] P. Barge et al., *Transiting exoplanets from the CoRoT space mission - I. CoRoT-Exo-1b: a low-density short-period planet around a G0V star*. Astronomy & Astrophysics, Vol. 482, L17-L20, 2008

[10] A. Baglin and all the CoRoT Team *CoRoT Highlights, 4S symposium Madeira May 2010, Scientific results of a minisatellite*, Observatoire de Paris, 2010

[11] Dr. Ingo Waldmann, *Lecture 10: Finding exoplanets with Astrometry and Radial velocities*. http://zuserver2.star.ucl.ac.uk/~ingo/Lecture_Notes_files/lect10.pdf, source Nasa, 11 may 2013

[12] Mayor M. et al. *Setting New Standards with HARPS* The Messanger, Vol. 114, pag. 20-24, December 2003

[13] A. Léger et al., *Transiting exoplanets from the CoRoT space mission - VIII. CoRoT-7b: the first super-Earth with measured radius*. Astronomy and Astrophysics, 506, 287-302, 2009

[14] W. J. Borucki et al. *Kepler Planet-Detection Mission: Introduction and First Results*. Science, vol 327, issue 5968, page 977-980, 19 February 2010

[15] Kepler Team (William Borucki, PI mission), *Kepler mission - A search for Habitable Planets*. kepler.nasa.gov

[16] S. B. Howell et al. *The K2 Mission: Characterization and Early Results*. The Astronomical Society of Pacific, vol 126, page 398-408, April 2014

[17] Kepler collaboration, *About transit, photometry, detection, planet size, Giant Planets and light curve.* http://kepler.nasa.gov/science/about/characteristicsOfTransits/

[18] PLATO Study Team *PLATO assessment study report* ESA/SRE(2013)5, 16 December 2013

[19] The CHEOPS Study Team *CHEOPS definition study report* ESA/SRE(2013)7, 01 November 2013

[20] Mark Clampin *Status of the James Webb Space Telescope (JWST)* Space Telescopes and Instrumentation, 2008 Optical, Infrared, and Millimeter, SPIE Proceedings, Vol 7010, 14 July 2008

[21] G. R. Ricker et at al. *Transiting Exoplanet Survey Satellite (TESS)* NASA Technical Report Server (NTRS) - Conference paper - Doc. ID: 20120011750 Jan 01 2012

[22] Michael Perryman, *Detection and characterization of Extra-Solar Planets.* Slides for Europen Space Agency from a book from the same author.

[23] Christian Marrois, Bruce Macintosh, Travis Barman, B. Zuckerman, Inseok Song, Jennifer Patience, David Lafreniére, René Doyon, *Direct Imaging of multiple Planets orbiting the Star HR 8799.* Science, vol. 322, pag. 1348 28 November 2008

[24] J. P. Gardner et al. *THE JAMES WEBB SPACE TELESCOPE* Space Science Reviews, vol. 123, pag. 485-606 April 2006

[25] G. Chauvin, A.-M Lagrange, C. Dumas, B. Zuckerman, D. Mouillet, I. Song, J.-L Beuzit, P. Lowrance *A giant planet candidate near a young brown dwarf - Direct VLT/NACO observations using IR wavefront sensing* Astronomy & Astrophysics, vol. 425, pag. L29-L32 2004

[26] C. Ducourant, R. Teixera, G. Chauvin, G. Daigne, J.-F Campion, I. Song, B. Zuckerman, *An accurate distance to 2M1207Ab* Astronomy & Astrophysics, vol. 477, pag. L1-L4 2008

[27] W. M. Keck Observatory, *Keck Telescope website.* http://www2.keck.hawaii.edu

[28] Jean-Luc Beuzit et al. *SPHERE: a 'Planet Finder' Instrument for the VLT* Telescope and Instrumentation - The Messanger, vol. 125, pag. 29 September 2006

[29] Adams S. Burrows, *Highlights in the study of exoplanet atmospheres.* Nature, Vol. 513, pages 345 - 352, 18 September 2014

[30] Drake Deming et al., *Infrared transmission spectroscopy of the exoplanets HD 209458b and XO-1b using the wide field camera-3 on the Hubble Space Telescope.* The Astrophysical Journal, Vol. 774, page 95, 10 September 2013

[31] Adams S. Burrows, *Spectra as windows into exoplanet atmospheres.* Proceedings of The National Academy of Science, Vol. 111, N. 35, page 12601-12609, 2 September 2014

[32] A. Vidal-Madajar, A. Lecavelier des Etangs, J.-M. Désert, G. E. Ballester, R.Ferlet, G. Hébrard, M. Mayor, *An extended upper atmosphere around the extrasolar planet HD209458b.* Nature, Vol. 422, page 143, 13 March 2003

[33] H. Knutson, D. Charbonneau, L.E. Allen, J. Fortney, E. Agol, N. Cowan, A. Showman, C. Cooper, T. Megeath, *A map of the day–night contrast of the extrasolar planet HD 189733b.* Nature, Vol. 447, page 183-186, 10 May 2007

[34] James P. Lloyd, *Habitable Planet Detection and Characterization with Far Infrared Coherent Interferometry.* arcXiv:1104.4112v1

[35] Stéphane Udry, Nuno C. Santos, *Statistical Properties of Exoplanet.* Annual Review of Astronomy & Astrophysics, Vol. 45, pag. 397-439, 2007

[36] Laurence R. Doyle et al. *Kepler-16: A transiting Circumbinary Planet.* Science, Vol. 333, pag. 1602-1606, 16 September 2011

[37] Michael I. Mishcenhenko, *Measurement and modelling of electromagnetic scattering by particles and particle groups.* from book "Polarimetry of star and planetary system", Cambridge University press, 2015

[38] Alberto Cellino, Ricardo Gil-Hutton, Irina Belskaya *Asteroids.* from book "Polarimetry of star and planetary system", Cambridge University press, 2015

[39] Jan o,. Stenflo, *The Sun.* from book "Polarimetry of star and planetary system", Cambridge University press, 2015

[40] George B. Rybicki, Alan P. Lightman, *Radiative Processes in Astrophysics.* Wiley-VCH Verlag GmbH & Co., 2004

[41] Jan o,. Stenflo, *Diagnostic of solar magnetic fluxtubes using a Fourier transform spectrometer.* Astronomy & Astrophysics, Vol 131, pag. 333-346 1984

[42] Claude Plymate, *A History of the MCMath-Pierce Solar Telescope.* http://nsokp.nso.edu 01 June 2001

[43] D. M. Stam, J. W. Hovenier, L. B. F. M. Waters *Using polarimetry to detect and characterize Jupiter-like extrasolar planets* Astronomy & Astrophysics, Vol. 428. pages 663-672, 2004

[44] D. M. Stam, *Spectropolarimetric signatures of Earth-like extrasolar planets* Astronomy & Astrophysics, Vol. 482. pages 989-1007, 2008

[45] S. V. Berdyugina, A. V. Berdyugin, D. M. Fluri, V Piirola *First detection of polarized scattered light from an exoplanetary atmosphere.* The Astrophysical Journal Letters, Volume 673, 20 January 2008

[46] S. V. Berdyugina, A. V. Berdyugin, D. M. Fluri, V Piirola *Polarized reflected light from the exoplanet HD 189733b: first multicolor observations and confirmation of detection.* The Astrophysical Journal Letters, Volume 728, Number 1, 18 January 2011

[47] P. Bastien, L. Drissen, F. Menard, A.F.J. Moffat, C. Robert, N. St-Louis *The variability of polarized standard stars.* The Astrophysical Journal, Volume 95, Number 3, March 1988

[48] Vilppu Piirola *A double image chopping polarimeter*. Astron. & Astrophys. volume 27, page 383-388, 1973

[49] Sloane J. Wiktorowicz *Nondetection of polarized, scattered light from the HD 189733b hot Jupiter.*. The Astrophysical Journal, volume 696, page 1116-1124, 2009 May 10

[50] Sloane J. Wiktorowicz, Larissa A. Nofi, Daniel Jontof-Hutter, Pushkar Kopparla, Gregory P. Laughlin, Ninos Hermis, Yuk L. Yung, Mark R. Swain *A ground-based albedo upper limit for HD 189733b from polarimetry.*. draft version submitted to The Astrophysical Journal, arXiv 1507.03588v1, 13 Jul 2015

[51] Sloane J. Wiktorowicz, Larissa A. Nofi, *Simultaneous linear and circular optical polarimetry of asteroid Vesta.*. The Astrophysical Journal Letter, Vol. 800, pag. L1 10 February 2015

[52] I. Pillitteri, A Maggio, G Micela, S. Sciortino, S.J. Wolk, T Matsakos *FUV Varaibility of HD 189733. Is the star accreting material from its hot Jupiter?*. The Astrophysical Journal, Volume 805, page 52, 20 May 2015

[53] G. Leyshon, *On the reduction and presentation of data in astronomical two-channel photopolarimetry*. Experimental astronomy, volume 8, issue 2, page 153-175 June 1998

[54] Yuriy Shkuratov, Nikolay Opanasenko, Viktor Korokhin, Gorden Videen, *The Moon*. from book "Polarimetry of star and planetary system", Cambridge University press, 2015

[55] N. Opanasenko, Y. Shkuratov, Viktor Korokhin, Gorden Videen, *Preliminary mapping negative polarization of the lunar nearside*. 44th Lunar and Planetary Science Conference, 2013

[56] Yu.I. Velikodsky, N. Opanasenko, L.A: Akimov, V.V. Korokhin, Yu.G. Shkuratov, V.G. Kaydash, G. Videen, Sh.A. Ehgamberdiev, N.E. Berdalieva. *New Earth-based absolute photometry of the Moon*. Icarus, 214, pag. 30-45 2011

[57] Michael F. Sterzik, Stefano Bagnulo, Enric Palle. *Biosignature as revealed by spectropolarimetry of Earthshine*. Letter to Nature, Vol .483, 1 march 2012

[58] Dr.Paschotta, RP Photonics Consulting GmbHm, *Encyclopedia for Photonics and Laser Technology*. www.rp-photonics.com

[59] Edmund Optics Inc., *Introduction to Polarization*. www.edmundoptics.com/technical-resources-center

[60] Christoph U. Keller, Frans Snik, David M. Harrington, Chris Packham *Instrumentation*. from book "Polarimetry of star and planetary system", Cambridge University press, 2015

[61] Weitenbeck, *Catalog of Stars with ISM Polarization Observed with HPOL*. 1999-2008

[62] Don Cross, *Solar System Calculator*. http://cosinekitty.com/solar_system.html

[63] T. Gehrels, T. Coffeen, and D. Owings *Wavelength dependance of polarization. III. The Lunar Surface*. The astronomical journal, Vol .69, number 10, December 1964

[64] William J. Borucki and Audrey L. Summers *The photometric Method of detecting Other Planetary Systems.* Icarus, Vol. 58, pag. 121-134, 1984

[65] Hansen, J.E., and L.D. Travis, *Light scattering in planetary atmospheres* Space Sci. Rev., Vol. 16, pag. 527-610, 1974

[66] P. Collins, G. Kyne, D. Lara, M. Redfern, A. Shearer, B. Sheehan, *The Galway astronomical Stokes polarimeter: an all-Stokes optical polarimeter with ultra-high time resolution* Experimental Astronomy, Vol. 36, pages 479-503, 2013

[67] P. Y. Deschamps, F.-M. Bréon, M. Leroy, A. Podaire, A. Bricaud, J.-C. Buriez, G. Séze, *The POLDER Mission: Instrument Characteristics and Scientific Objectives.* IEEE Transaction on Geoscience and remote sensing, Vol. 32, n. 3, 3 May 1994

[68] Pietro Giannone, *Esercizi e complementi di astronomia* Nuova Cultura, 2008

[69] Harvard University *Super-Earths and Life* online learning iniziative of Harvard University through edX https://courses.edx.org/courses/course-v1:HarvardX+SPU30x+2T2016

[70] Steve B. Howell, *Handbook of a CCD Astronomy* Cambridge University Press, Second version, 2006

[71] N. Kashikawa et al., *FOCAS: The Faint Object Camera and Spectrograph for the Subaru Telescope* Astronomical Society of Japana, Vol. 54, pag. 819-832, 2002 December 25

[72] Koji S. Kawabata *Subaru/FOCAS Spectropolarimetry of Supernovae* ASP Conference Series (Astronomical Polarimetry: Current Status and Future Directions), Vol. 343, December 2005

[73] I. Ilyin, K.G. Strassmeier, M. Woche, F. Dionies, I. Di Varano, *On the design of the PEPSI spectropolarimeter for the LBT* Astronomische Nachrichten, Vol. 332, Issue No. 8, pag. 753 – 758, 2011

[74] I. Ilyin, K.G. Strassmeier, M. Woche, A. Hofmann, *Spectropolarimetry with PEPSI at the LBT: accuracy vs. precision in magnetic field measurements* Proceedings IAU Symposium No. 259, 2008

[75] Paolo De Bernardis *Laboratory of astrophysics - course material* Ufficio dispense, Dipartimento di Fisica of La Sapienza University, Rome, Tecniche Sperimentali in Astrofisica

[76] J. Matsuoka, N. Kitamura, S. Fujinaga t, T. Kitaoka and H. Yamashita, *Temperature dependence of refractive index of SiO 2 glass* Journal of Non-Crystalhne Solids, Vol. 135, pages 86-89, 1991

[77] Ronald Roelfsema et al. *The ZIMPOL high contrast imaging polarimeter for SPHERE: design, manufacturing and testing* Ground-based and Airborne Instrumentation for Astronomy III, SPIE Vol. 7735, 77354B, 2010

[78] Daniel S. Sawyer, *"Refractive index database,"* http://refractiveindex.info

[79] K. G. Strassmeier et al. *PEPSI: The high-resolution échelle spectrograph and polarimeter for the Large Binocular Telescope* Astronomische Nachrichten, Vol. 336, Issue No. 4, pag. 324 – 361, 2015